Intermediate-Mass Black Holes in Globular Clusters

Nora Lützgendorf

München 2013

Intermediate-Mass Black Holes in Globular Clusters

Nora Lützgendorf

Dissertation
an der Fakultät für Physik
der Ludwig–Maximilians–Universität
München

vorgelegt von
Nora Lützgendorf
aus Zwenkau

München, den 27.05.2013

Erstgutachter: Dr. Markus Kissler-Patig
Zweitgutachter: Prof. Tim de Zeeuw
Tag der mündlichen Prüfung: 18.07.2013

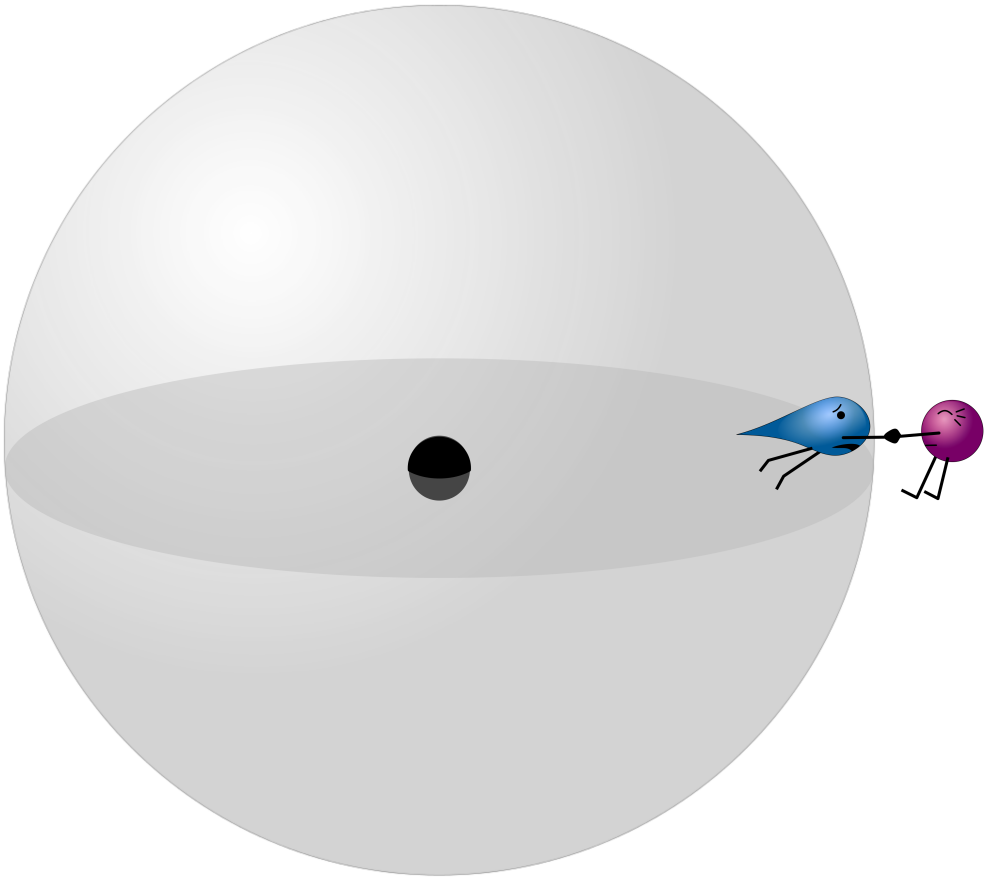

For all of those who asked:

"Science is not belief, but the will to find out."

- *anonymous*

Contents

List of Figures

List of Tables

Zusammenfassung

Die vorliegende Arbeit befasst sich mit der Suche nach mittelschweren Schwarzen Löchern in Kugelsternhaufen. In den letzten Jahren gab es bei zahlreichen Beobachtungen von supermassiven schwarzen Löchern Hinweise auf einen engen Zusammenhang zwischen ihren Massen ($M_\bullet$) und den charakteristischen Eigenschaften der Galaxien (z.B. Geschwindigkeitsdispersion σ). Die Betrachtung dieser Zusammenhänge trägt erheblich dazu bei, Bildung und Entwicklung massiver Schwarzer Löcher zu verstehen. Die Erforschung masseärmerer Schwarzer Löcher hat dabei eine zunehmende Bedeutung erlangt, um die Gültigkeit der für supermassive Schwarze Löcher entdeckten Zusammenhänge an ihnen zu testen. Desweiteren gelten sie als hervoragende Kandidaten als sogenannte Keime für den Wachstum supermassiver Schwarzer Löcher zu fungieren und das Rätsel ihrer rapider Massenzunahme zu lösen.

In den dieser Arbeit zugrunde liegenden Beobachtungen wurden kinematische Profile von neun galaktischen Kugelsternhaufen untersucht. Dabei wurde die integral-field spectroscopy verwendet, die zu den modernsten spektroskopischen Techniken gehört. Darüber hinaus vereinten wir photometrische Profile dieser Kugelsternhaufen, die mit den Hubble Space Telescope aufgenommen wurden, mit den spektroskopischen Aufnahmen und verglichen die Ergebnisse mit analytischen Modellen. Durch dieses Vorgehen wurde es möglich, für jeden Kugelsternhaufen die Masse oder die Obergrenze der Masse des zentralen Schwarzen Loches zu bestimmen. Steigt das kinematische Profil zum Zentrum des Haufens stärker an als aufgrund des photometrischen Profis zu erwarten wäre, so weist dies auf ein dunkles Objekt im Zentrum hin - ein Schwarzes Loch. Im Ergebnis zeigt sich, dass es sowohl Kugelsternhaufen mit starken Anzeichen für ein zentrales Schwarzes Loch (wie zum Beispiel NGC 6388) als auch Kugelsternhaufen mit sehr flachem Profil (NGC 2808) und damit kaum Anzeichen für zusätzliche Masse im Zentrum des Haufens gibt. Schließlich haben wir die Ergebnisse unserer Messungen mit Werten aus der Literatur zur $M_\bullet - \sigma$ - Relation superschwerer Schwarzer Löcher verglichen. Dabei konnte nachgewiesen werden, dass mittelschwere Schwarze Löcher eine ähnliche, allerdings flachere Korrelation aufweisen. Diese Abflachung könnte ihre Ursache im starken Masseverlust der Kugelsternhaufen während ihrer Lebensdauer haben.

Neben den Beobachtungen wurden sogenannte N-Körper Simulationen durchgeführt. Sie ermöglichen einen tiefen Einblick in die internen dynamischen Prozesse in Kugelsternhaufen. Sie geben Hinweise auf mögliche Fehlerquellen bei unseren Beobachtungsmethoden und bieten einen Vergleich zu den erhobenen Daten.

Die Zukunft der Erforschung mittelschwerer Schwarzer Löcher liegt in der Entwicklung immer hochauflösender und sensiblerer Instrumente, die es ermöglichen, noch weiter entfernte Objekte auf Schwarze Löcher zu untersuchen.

Summary

This work is focused on the search for intermediate-mass black holes (IMBHs) in the centers of globular clusters. It has been demonstrated that supermassive black holes (SMBHs) at the centers of galaxies show a tight correlation between their mass ($M_\bullet$) and the velocity dispersion (σ) of the galaxy. Investigating this $M_\bullet - \sigma$ and similar correlations is crucial to constrain scenarios of galaxy formation and evolution. If they formed by runaway collisions of massive stars in young and dense stellar clusters, IMBHs could still be present in the centers of globular clusters, today.

We measured the inner kinematic profiles for a sample of 9 galactic globular clusters using integral-field spectroscopy and combined them with existing outer kinematics and photometry obtained form HST archive images. In order to constrain the mass of a possible black hole we applied analytical Jeans models in combinations with varying M/L_V profiles to each of the clusters. The results of these fits range from strong hints towards an IMBH (e.g. NGC 6388) to globular clusters which do not show any indications of a rising velocity dispersion profile in their center (e.g. NGC 2808). Furthermore, the discovery of two high velocity stars in NGC 2808 opened another opportunity to study the internal kinematics of this particular cluster and indicates a high number of stellar-mass black holes in NGC 2808. We finally combined our results with measurements from the literature and investigated known scaling relations for SMBHs in galaxies (e.g. $M_\bullet - \sigma$) at the low-mass end by placing the results and upper limits of IMBH measurements on these correlations. We found that IMBHs follow similar, but more shallow correlations of their mass and the properties of their host systems. This might be caused with the severe mass-loss the cluster suffers during its life time.

In addition we ran numerical N-body simulations and compared globular clusters with different black-hole retention fractions, IMBH masses and binary fractions. We found that IMBHs lead to a higher ejection rate of massive stars so that clusters with less depleted mass functions might therefore be good candidates to host IMBHs at their centers. In the future more N-body simulations will be performed in order to reproduce our observations in a more sophisticated way and perform crucial tests to our observing and analysis methods. The search for IMBHs requires both high spatial and spectral resolution and will remain at the edge of feasibility. However, it is crucial to continue the investigations in order to shed light on black-hole formation and growth.

CHAPTER 1

Introduction

The human mind in its complexity is able to understand physical connections to high detail but when it comes to infinity we reach the limits of our imagination. Be it the infinity of the universe or the infinite gravitational force of a black hole, we struggle to grasp the meaning of a never ending quantity. But maybe it is exactly this inability which drives our fascination for these singularities. Black holes are singularities. They are points in space time where the mass, gravitation or curvature of the space become infinite. This is how we read it from our text books but understanding it is difficult. An easier description could be given by its property of not letting the light escape and a new definition of a black hole - an object, so massive that not even the light can escape, is given.

Ever since the theoretical discovery of these exotic objects, humanity was obsessed with the search for their existence, nature and origin. Black holes became the centers of science fiction stories and possible gates to time travel and wormholes. It was actually hard to believe that one would ever discover such an object in nature. But it happened! Nowadays, black holes are widely accepted among physicists, revealing their presence as one of the highest energy sources in the cosmos. Today, almost 50 years after the first discovery of a black hole, astronomers, physicists and amateurs still wonder about their complex nature. Many different kinds of black holes were discovered in the last decades, ranging from small companions of massive stars up to giant monstrosities in the centers of galaxies. But the hunt is by far not over yet. In this work we have set out to solve one of the key questions in the field of black hole observations: Do they exist at all masses?

In order to answer this question we look for a new kind of black holes whose mass range covers the gap between the stellar-mass black holes and the supermassive black holes. Because of the intermediate character compared to their extreme relatives, these objects were called intermediate-mass black holes and while supermassive black holes reside in galaxies and stellar-mass black holes are the end point of the evolution of massive stars, it is logical to search for intermediate-mass black holes in intermediate-sized environments. Stellar systems - no single stars, but also no entire galaxy. Fortunately, the universe contains a large number of these objects. We find them as satellites of massive galaxies and at the

lower end of the galaxy-mass distribution. The smaller ones are called globular clusters and are located mostly in the outer halos of galaxies such as our Milky Way. The more massive representatives have names like dwarf galaxies or ultra compact dwarf galaxies but are not considered in this work.

In order to understand the connection between globular clusters and intermediate-mass black holes, the following chapters introduce the two objects in detail and tell the tale from the first observations of black holes to the advanced technology of today and the extensive search for the small hints in the movements of stars in the centers of globular clusters that might reveal the presence of one of the last unknown 'species' of black holes.

1.1 Globular clusters

In the 19th century William Herschel discovered a new object on the sky when he resolved individual stars of an assumed spherical nebula and he realized that this nebula actually consists of a large number of stars. Today, we know that he observed one of the 150 almost spherical, densely packed stellar systems located in our galaxy that we call globular clusters. Figure 1.1 shows a typical representative of a globular cluster - Terzan 5. The image visualizes its high stellar density and spherical shape, two of the most distinct properties of globular clusters.

Located in the halo of almost every massive galaxy (see Figure 1.2), globular clusters are a common sight in our universe. Their masses range from $10^4 - 10^6\,M_\odot$ and so does the number of stars they contain. In contrast to their little brothers - the open star clusters - their high central densities of 100 - 1000 stars/pc^{-3} make them one of the densest stellar systems in the universe and very stable against tidal forces. This might also be the reason for their long lives. With an average age of $\sim$ 10 Gyr they belong to the oldest objects known, providing fossil records of the dynamical and chemical conditions when their host galaxies were in the process of formation. Therefore their formation process and evolution is of high interest for astronomers. The traditional scenario is that they emerge from giant molecular clouds (GMC) with a single chemical composition (e.g. Elmegreen & Efremov 1997; McLaughlin 1999). However, new observations and more accurate photometry have shown that almost all globular clusters consist of multiple stellar populations, indicating a much more complex formation process than previously assumed.

Due to their old ages, globular clusters can be considered as absolute gas-free objects. All gas that once formed the stars, is long gone, ejected by stellar winds, supernovae or accreted by stars. The only dominant force in a cluster is therefore the gravitational attraction between the stars. A globular cluster preserves the equilibrium between its self gravitation and the movements of the stars. The deeper the gravitational potential well, the higher the velocities of the stars. In this way, all the stars in the cluster are gravitationally bound to each other but prevent the cluster from collapsing. Due to their high densities, gravitational encounters between stars are common in globular clusters. The timescale

on which these encounters start affecting the overall structure of the system is called the relaxation time. It can be roughly estimated as the time a star needs to cross the system $\tau_{cross} \sim R/v$ multiplied by the total number of particles N. Typical globular clusters are about ten times older than their relaxation times ($\tau_{rlx} \sim 10^9$ yrs), implying an evolved dynamical state. The lifetime of such a system is governed by the external gravitational field it is located in, i.e. the galaxy. Due to two-body interactions stars with low masses gain high velocities and can escape the cluster when passing the critical point where the gravitational field of the galaxy is larger than the one of the cluster. In this way, every cluster in a tidal field evaporates after a certain amount of time. How long this is going to take is determined by the orbit and the distance of the cluster from the center of the host galaxy.

Another interesting fact about globular clusters is their negative heat capacity, a property valid for all gravitational bound systems but due to their short relaxation times very efficient in clusters. Through the analogy with gas particles, the temperature of the system can be determined by the velocities of the stars. While in a gas with positive heat capacity the temperature decreases when taking energy from it, a globular cluster increases its temperature. This arises from the energy stored in the gravitational field. A star that looses energy sinks deeper in the potential and is accelerated to higher velocities. The net energy is lost, but even more potential energy is lost causing the kinetic part of the energy to increase. In this way and because of energy exchange between particles, the core of the system loses energy and gets hotter, while the outskirts expand and cool down. Mathematically this leads to an infinite density in the core after a few relaxation times, a phenomenon known as core collapse. In practice, this is prevented by the generation of new energy sources in the center of the cluster such as binaries or an intermediate-mass black hole.

1.2 Black holes

The idea of objects with a gravity field so high that no light can escape can be traced back long before their observational evidence. In 1784 reverend John Michell argued that if light were indeed a stream of particles (as Newton's theory suggested), then it should be influenced by gravity. Following this assumption he predicted that a star with a gravity 500 times larger than the Sun, but with the Sun's average density, would have such a strong gravitational field that even light could not escape from it. Those objects could not be found by their radiation but rather by their gravitational effects on the environment. Many astronomers and physicists followed Michell's thoughts and developed theoretical predictions and possible observing strategies for the detection of black holes. With the advance of Einstein's theory of general relativity in 1916 it even became possible to describe the geometrical structure of space in the vicinity of a black hole in great detail (Einstein 1916; Schwarzschild 1916).

Figure 1.1: The globular cluster Terzan 5 as a representative of a typical Galactic globular cluster. With a mass of $\sim 10^6\,M_\odot$ it belongs to the most massive stellar clusters in our Milky Way. The images displays its spherical shape and high density in the center, overblended by bright, blue foreground stars.

1.2.1 Formation

But before going deeper into the complex nature of black holes, one has to understand how they were formed in the first place. To form a black hole, matter needs to be compressed to a point of total gravitational collapse. A star holds its equilibrium between its self-gravitation pressing inwards and its internal pressure produced by the thermonuclear reaction of fusing Hydrogen to Helium during its entire lifetime. The nuclear fusion in the core of every star heats the gas to high temperatures that prevent the giant gas ball to collapse under its own gravitational force. The remaining energy gets transported through the stars interiors and radiates into outer space - the star shines. However, the star cannot burn its content forever and soon the Hydrogen content is exhausted, the star starts contracting and increases its temperature. This is when the star starts burning heavier element such as Helium, Carbon, Neon, Oxygen and Silicon. The heavier the element, the hotter and faster the star burns in its center and the shorter is the burning time period. For a massive enough star, this goes on until the only element remaining in the core is Iron. Iron is the most stable element, fusing it to even heavier elements would not produce but require energy. This is when the star has no material left that can be transformed into energy, the gravitational pressure becomes the dominant inward directed force and the star collapses.

In principle, this is the process that can form a black hole, a star that exceeded its resources and collapses due to its self gravitation. However, the final end stadium of a star is dependent on its original mass. Figure 1.3 shows the evolution of a star for three different mass ranges. For stars with masses lower than $0.08\,M_\odot$ the temperature in the core does not

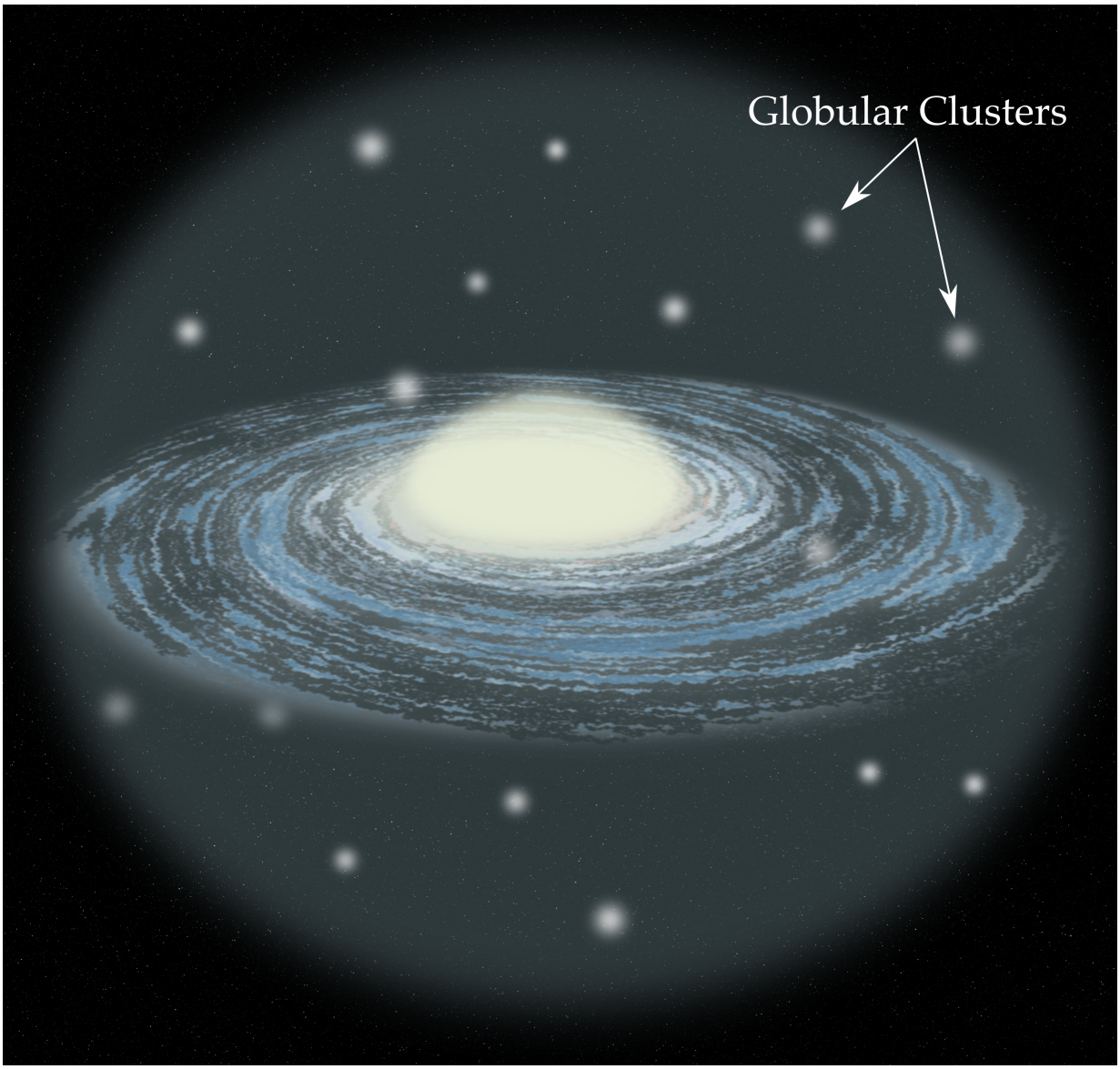

Figure 1.2: Schematic location of globular clusters in our Milky Way. The majority of these ancient objects is distributed in the halo of the galaxy.

reach the limit needed to burn Hydrogen. Therefore, it is not possible for those so called brown dwarfs to ignite the main Hydrogen burning process and so they remain "dark" for their entire life time. They reach their equilibrium between gravity and degeneracy pressure of the gas. Those stars do not form black holes and reside as brown dwarfs and continue to cool down and become black dwarfs.

The next category are low-mass, or sun-type stars ($1 - 10\,M_{\odot}$). After exhausting their burning material, they expand due to the higher temperatures of the heavy element burning and become so called red giants. In this stage the star is very unstable. Strong stellar winds and pulsations on the surface of the star cause the star to loose a high amount of its mass through the outer layers. In this way, the gravitational pressure from outside decreases and what remains is the Carbon and Oxygen rich core of the star supported by degeneracy pressure of its electrons and surrounded by the remnants of the ejected outer layers. These layers are excited by high-energy photons emitted from the central object and re-emit them to their environments. Due to their spherical and colorful appearance, those objects were named planetary nebula but they have nothing in common with planets. The hot and dense core inside these nebulas are white dwarfs which will follow a cooling sequence after their formation.

The last categories of stars are the so called blue giants. Hot stars with more than 10 $M_{\odot}$. Because of their high inner temperatures, these stars burn their reservoir of hydrogen and helium much faster than less massive stars. Therefore, their lifetimes are short and soon they reach the situation described above: An iron core in the center and no central fusion to oppose its own gravitational force. As a logical consequence of this situation the star starts to collapse, starting from the innermost layers. This leads to the formation of a very compact object in the center of the former star before the outer layers fall onto it. The crash produces a repulsive force and the outer material of the star bounces back and gets expelled in one of the most energetic events in our universe: a supernova. In the first scenario, no remnant stays behind. The explosion disrupted the entire star and even the temporary compact object in the center. The second scenario is the formation of a neutron star, i.e. when the compact core of the star survives. These objects are mainly made of iron but so highly compressed, that the nuclei of the atoms overlap and most of their protons decayed to neutrons through inverse beta processes. The stability of these objects, which have $\sim$ 10 km diameter, are given by the degeneracy pressure of the neutron 'sea'.

When the compact remnant is more massive than 3 solar masses (also called the Tolman - Oppenheimer - Volkoff limit), no force, not even the degeneracy pressure of the neutrons, can keep the balance with the gravitational force and the object finally collapses to a black hole. From this formation process it becomes clear, that not every star will form a black hole at the end of its life. Even for the most massive stars in our universe many factors such as mass loss and parameters of their supernova explosion are poorly known. It is therefore not straight-forward to predict the exact properties of the progenitors of black holes.

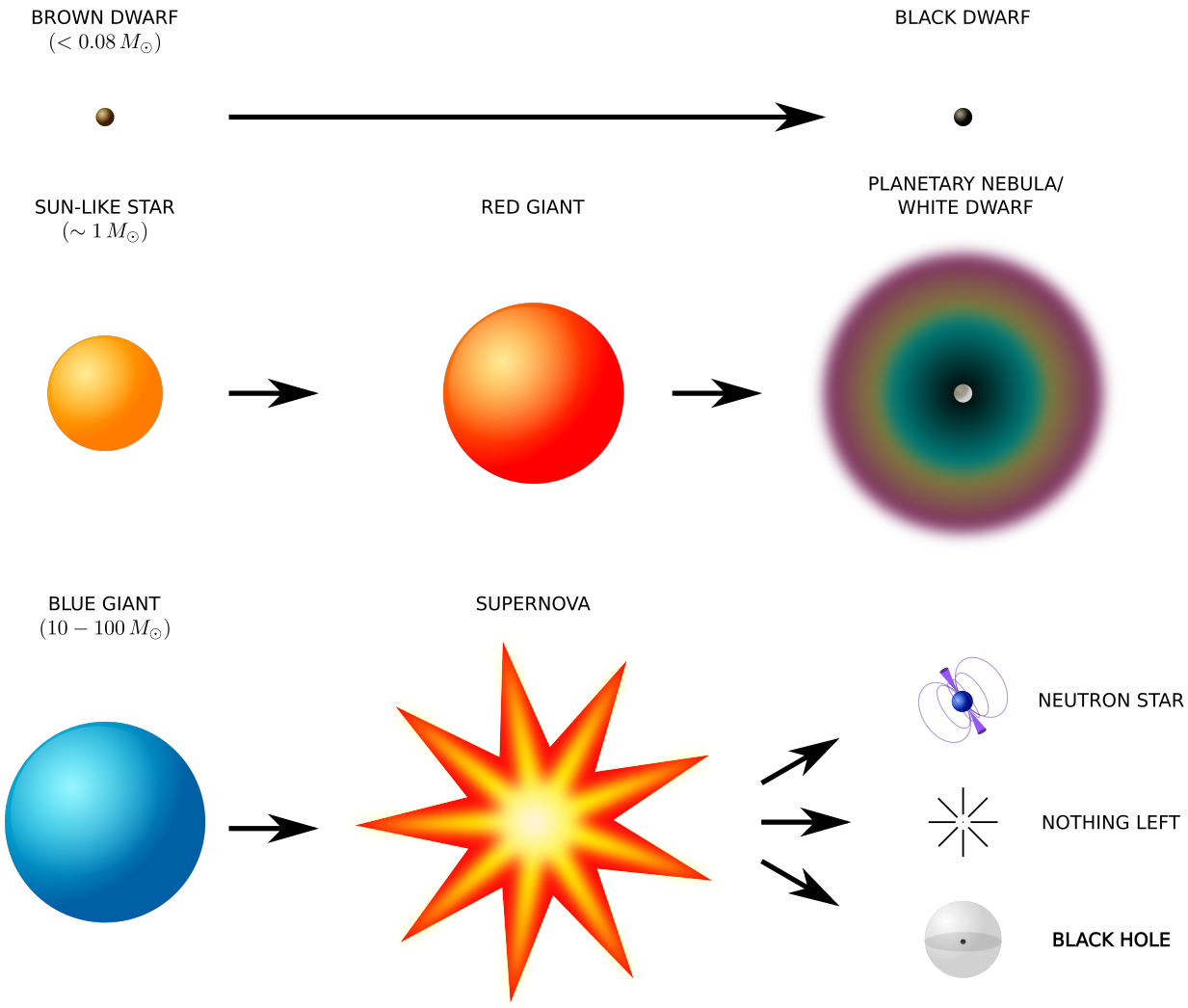

Figure 1.3: Stellar evolution dependent on the initial stellar mass and formation of a black hole.

1.2.2 Properties

Black holes are extreme physical objects. Mathematically speaking they are singularities in space time, i.e. a single point where its mass or density (and therefore its gravitational force) rises to infinity. Physically spoken this cannot be proven. There is a limit to our ability to study a black hole's properties, an invisible boundary which obscures any information within. This barrier is called the event horizon (or Schwarzschild radius) and it marks the distance to the black hole from which the escape velocity equals the speed of light. In other words: For radii smaller than the event horizon the gravitational force is so high that not even light and therefore - as stated by general relativity - nothing else can escape the gravitational field. Consequently no information can ever be extracted from this area.

By approaching this radius, space time is behaving in a remarkable way. As a direct consequence of general relativity where time passes slower in accelerated frames and every gravitational field is equivalent to such, time slows down by approaching the event horizon until it reaches a complete stop[1]. A direct consequence of the time dilatation in the vicinity of a black hole is the gravitational redshift, causing light emitted near a black hole shifted towards longer wavelengths. This arises from the increasing time intervals when departing from the black hole.

Figure 1.4 shows an artist impression of a black hole as it would be observed in nature. The black hole is surrounded by an accretion disc and its strong gravitational field acts as a gravitational lens on the accreted material. This leads to the bizarre shape of the accretion disk. In Figure 1.5 the geometry of this scenario is explained. Due to the deflection of the light through the black hole, even the back side of the accretion disk becomes visible. Another effect visible in Figure 1.4 is the one sided increase of intensity of the accretion disk. This arises from the fast rotating material near the black hole and the resulting blue-shift on the one side of the disk. Material which moves towards the observer at a high speed is shifted to shorter wavelengths and therefore increases its energy and intensity.

1.2.3 Observations

For a long time, black holes existed only in theory as a direct consequence of gravity. An observational evidence for the existence of these objects would have provided confirmation of gravitational theory and relativity. The first evidence of black holes came with the development of X-ray astronomy. In 1964 an X-ray rocket was launched in order to scan a small area of the sky. Among eight new X-ray sources the survey detected a bright source called Cygnus X-1 in a region where no prominent radio or optical emission was known (Bowyer et al. 1965). After more detailed follow-up studies on its variability and flux, Cygnus X-1 was the first stellar-mass black hole to be found. The X-ray emission originates

[1] In contrast to the physical singularity exhibited by the black hole itself, the time singularity exhibited by the Schwarzschild metric at the event horizon is a mathematical entity only. Choosing another coordinate system (Kruskal-Szekeres coordinates) would remove the divergence at the event horizon (Misner et al. 1973).

Figure 1.4: Artist impression of an accreting black hole observed from a small angle to the accretion disk. (Credits: J.A. Marck, J.P. Luminet)

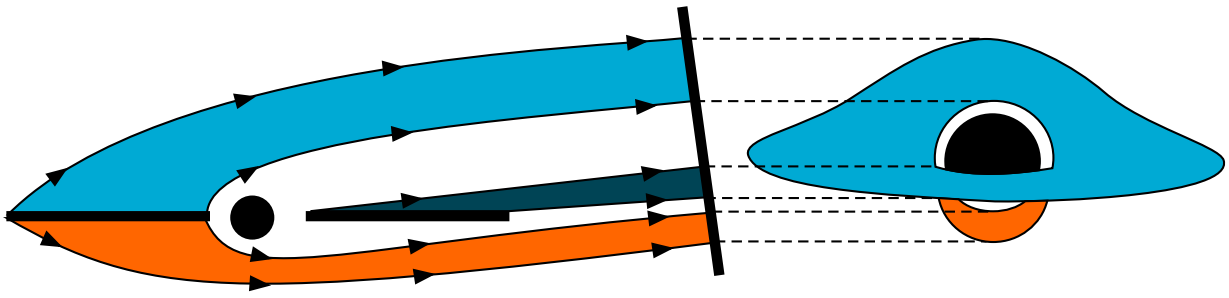

Figure 1.5: Geometry of a black hole explained through the bending of the light.

from a binary system of a blue supergiant and a black hole which accretes matter from its companion.

Black-hole binary systems such as Cygnus X-1 are common in our universe. As most of the massive stars are born in binaries, the connection between the stars can remain if it is not destroyed by the black-hole formation process. Today, X-ray observations can not only detect such a system but also provide information of the mass and spin of the black hole. Through the intensity (or hardness) of the X-ray radiation, astronomers can determine the innermost stable circular orbit, i.e. the marginal radius at which matter can circle the black hole before getting disrupted and accreted. This quantity is determined by the mass and the spin of the black hole. Through monitoring of the variability of the X-ray source, astronomers measure the light curve, which results from the partly eclipsing of the black-hole accretion disk by the black-hole companion star. From this data, crucial properties of the system can be determined.

While stellar-mass black holes like Cygnus X-1 can only be detected when located in a binary system, their large-scale equivalents - supermassive black holes - are hard to overlook. The discovery of these objects with masses reaching from 10^5 to $10^{10}\,M_\odot$, however, was not straight forward. In 1963 the radio source 3C 273, which until then was assumed to be a stellar object, was observed by Maarten Schmidt. He found that the spectrum of this source was redshifted, indicating that this object was much further away than previously assumed. As a consequence, he concluded that 3C 273 was not a star after all, otherwise it would not be visible to us in such a distance. He called this newly discovered object a quasi star, at term that is still used today: these objects are known as quasars. In 1969 Donald Lynden-Bell came to the conclusion that the energy source of these extremely bright galaxies could only be explained with an accreting supermassive black hole at the center (Lynden-Bell 1969). With increasing quality of observational techniques and telescopes, more and more quasars at farther distances are discovered. The most distant quasars have redshifts which indicate that they existed when the universe was younger than a Gyr. Until today, it is not understood how black holes could reach a mass of several billion solar masses in such a short time scale. This triggers the discussion about one of the biggest mysteries in modern astrophysics: the growth of supermassive black holes.

By the extensive search for quasars billions of light years away, we almost overlooked a giant black hole right in our back yard. The supermassive black hole in the center of our galaxy. The reason why it stayed unnoticed for such a long time is its quiet nature and the lack of strong accretion. Due to the lack of dense material in the center of our galaxy, the black hole cannot produce the X-ray and radio emission as expected from such a massive object. However, with the advance of observational techniques, the existence of the supermassive black hole could be proven by monitoring the movements of the stars in its vicinity over several years using adaptive optics (Schödel et al. 2002). These break-through observations were the first Keplerian orbits ever observed around a supermassive black hole and the best evidence for a supermassive black hole up to date.

1.3 Intermediate-mass black holes - The missing link?

Considering the observational evidence for black holes as described in the previous section, one could assume that they only come in two sizes: stellar-mass and supermassive. For many years after the first discovery of black holes, this concept was widely accepted. But why should nature form objects in such a discrete way? How do supermassive black holes grow from stellar-mass black holes and is there a connection at all between these distinct objects? The most commonly accepted scenario for the growth of a black hole is accretion. The black hole increases its mass by absorbing its surrounding material in the galaxy. However, even with the highest accretion rates possible (the limit is given by the radiation pressure of the accreted material) this mechanism is unable to explain the rapid growth up to several billion solar masses within one Gyr. Therefore, theorists start with so-called seed black holes with masses of the order of $10^3\,M_\odot$ which allow the accretion to proceed faster and the supermassive black holes to build up to the observed masses. The solution to all these problems could therefore be a new 'type' of black holes. Objects with masses between $10^2\,M_\odot$ (more massive than stellar-mass black holes) and $10^5\,M_\odot$ (less massive than supermassive black holes).

Those objects are called intermediate-mass black holes and are the center of interest of this thesis. In contrast to their smaller and bigger brothers they are not as easy to detect and their existence remains uncertain until today. On the search of possible environments for these massive black holes, astronomers used already known relationships between properties of the black hole and its host system. One of these so-called scaling relations (and probably the most famous) is the $M_\bullet - \sigma$ relation, where σ stands for the velocity dispersion, i.e. the second moment, of the stars in the galaxy [2]. As shown in Figure 1.6 these two quantities show a tight correlation for supermassive black holes and their host galaxies. Extrapolating this relation to lower mass ranges, the correlation predicts host systems for intermediate-mass black holes with velocity dispersion of $\sigma = 10 - 20\ \mathrm{km\,s^{-1}}$. This leads us to the velocity regime of globular clusters.

The search for intermediate-mass black holes was therefore mainly concentrated on small stellar systems such as globular clusters. The nature of globular clusters, however, makes the search for massive central objects rather difficult. While supermassive black holes and stellar-mass black holes can be observed through their X-ray and radio emission due to gas accretion, the lack of gas in these old stellar systems makes detection of accretion processes rather difficult. As we will see in the next chapter this does not prevent astronomers for searching for X-ray signals in globular clusters, but the most promising search method is based on stellar kinematics.

[2] This only holds if the rotational velocity of the cluster $\langle v \rangle$ is zero. Otherwise the second moment is defined as $\langle v^2 \rangle = \sigma^2 + \langle v \rangle^2$

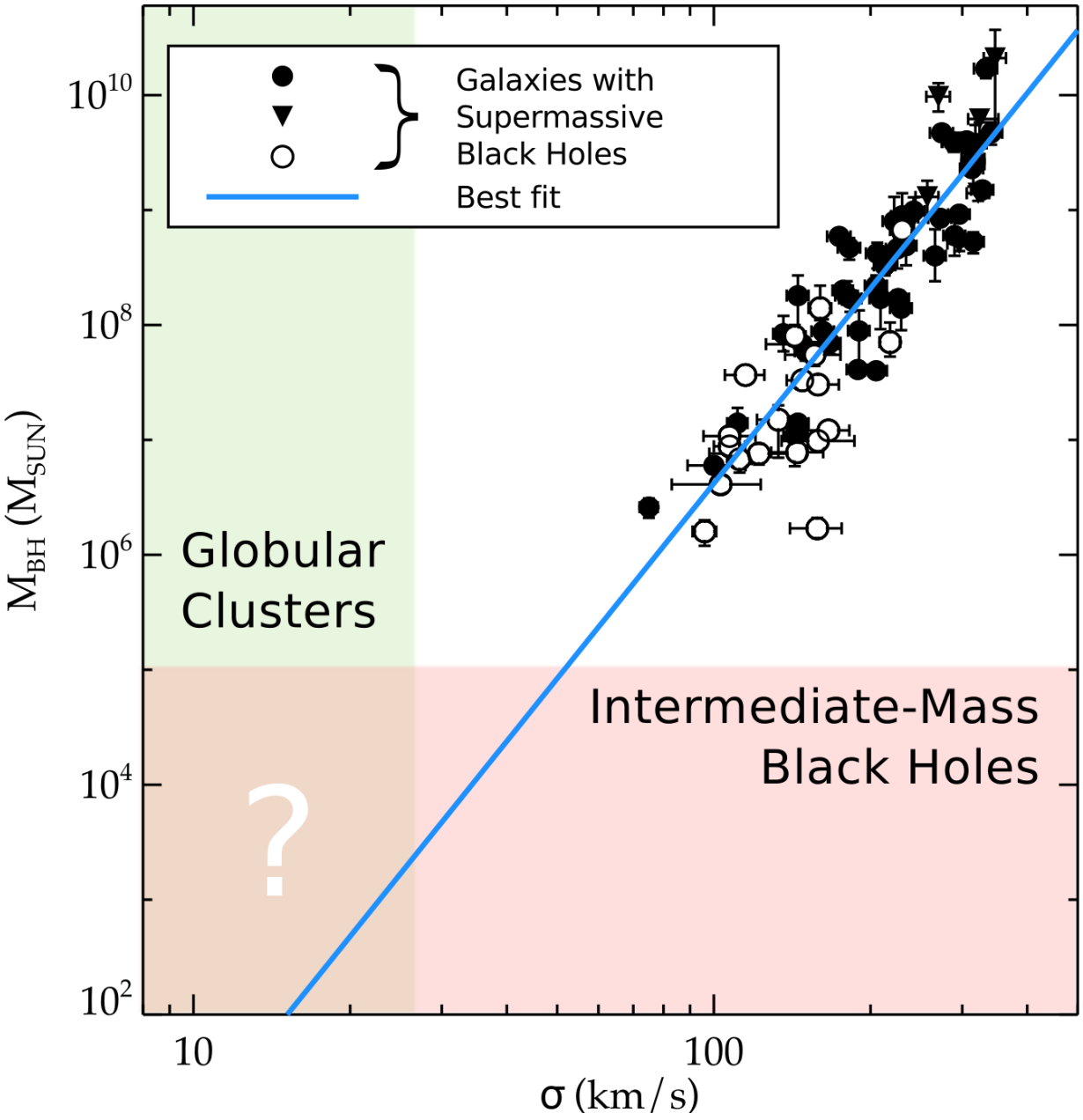

Figure 1.6: $M_\bullet - \sigma$ relation for galaxies with supermassive black holes. The different symbols indicate different types of galaxies such as: early type galaxies (filled circles), brightest cluster galaxies (filled triangles) and late type galaxies (open circles).

1.3.1 Possible Formation Scenarios

The first question that arises when thinking about intermediate-mass black holes is: Where did they come from? We know the origin of stellar-mass black holes and we also have an idea that supermassive black holes gain their enormous masses through accretion and mergers (without which the rapid speed of growth cannot be explained), but for intermediate-mass black holes a special formation process is required. Two possible scenarios are:

Remnants of Population III stars

The mass of a black hole resulting from a gravitational collapse of a massive object depends on the mass of its progenitor. This means, the more massive the star that collapsed, the more massive the black hole. A black hole with masses of the order of $10^2\,M_\odot$ can form through the collapse of a star with the same magnitude of mass. To form such a massive star, however, requires material with very low metallicity (since the higher the metallicity, the stronger the fragmentation of the gas cloud during star formation). In early stages of the universe, when the pristine gas was not enriched by supernovae or stellar winds, primordial stars with extremely low metallicity and high masses have formed. Today we call these ancient objects Population III stars and consider them as possible progenitors of very massive black holes of the order of $10^2\,M_\odot$ (Madau & Rees 2001).

Runaway merging in young star clusters

Another way of creating a massive star that can collapse to a massive black hole is merging many stars in a short time scale. Ideal environments for this to happen are young massive star clusters, i.e. the progenitors of today's globular clusters. Using N-body simulations, Portegies Zwart et al. (2004) found that in very dense environments such as young clusters, stars can collide with other stars in a runaway merging process. In a star cluster, massive stars sink to the center due to equipartition of energy and mass segregation. If this process does not take longer than the lifetime of a massive star, then the star reaches the center of the core before exploding in a supernova. There, the probability of colliding with another star is high and if two stars collide they form an even more massive star. This again increases the probability of collision since this more massive star has a larger cross section and gravitational drag. Therefore this process is self amplifying and is called runaway merging. After multiple mergers the outcome is a very massive star of $10^2 - 10^3\,M_\odot$. The collapse of this star then leads to a massive black hole near the center of the cluster.

This scenario is popular especially when searching for intermediate-mass black holes in globular clusters. However, it needs to be stated that this process does not include stellar evolution. Dynamically, the formation of a very massive star is possible but the resulting instabilities and stellar winds would most probably cause high mass loss before the star can collapse. It is therefore difficult to determine the final mass of the massive black hole that

can form in this way.

1.3.2 Hunting for intermediate-mass black holes

The hunt for intermediate-mass black holes in globular clusters has been challenging for X-ray astronomers and dynamicists in equal measure. The high complexity of their possible host systems makes the black-hole hunt in this mass regime difficult. While X-ray astronomers struggle with count rates, crowding and shotnoise errors dominate the dynamical approach. This section summarizes the past and ongoing search for intermediate-mass black holes and the motivation of this work.

Previous detections

The first suggestion of the existence of intermediate-mass black holes was made by Silk & Arons (1975) while studying X-ray sources in a large sample of globular clusters. For the globular cluster M15 they found high X-ray fluxes in the center of the cluster which could be explained with mass accretion onto a $100 - 1000\ M_\odot$ central black hole. Inspired by their work, Bahcall & Wolf (1976) measured the light profile of M15 and claimed the detection of an IMBH. This was the starting point for many follow-up observations and contradictory results on the globular cluster M15. For a long time, M15 was assumed to host an intermediate-mass black hole of a mass around $3 \times 10^3\ M_\odot$ due to the distinct rise in the central velocity dispersion profile (e.g. Peterson et al. 1989; Gebhardt et al. 1997, 2000b; Gerssen et al. 2002). However, more detailed analysis and modeling showed that the kinematic signature in M15 was more likely due to a high concentration of dark stellar remnants than due to one single massive object (e.g. Dull et al. 1997; Baumgardt et al. 2003, 2005; van den Bosch et al. 2006). The reason for this suggestion is the high concentration of stars in the cluster's core, suggesting a stage of high mass segregation, also known as core collapse (see Section 1.1). It also turned out that the previously detected X-ray source was a combination of many small contributions rather than one large emitter.

The misinterpretation of M15 did not stop the black-hole hunt. On the contrary, it was the start of a long search for intermediate-mass black holes in globular clusters in many different ways, lasting until today. The most promising candidates, ω Centauri in the Milky Way and G1 in M31 show kinematic signatures of black holes with masses of 20 000 to 40 000 solar masses (e.g. Noyola et al. 2008; Anderson & van der Marel 2010; Gebhardt et al. 2005). In the case of G1, a radio source was detected at the center of the cluster (Pooley & Rappaport 2006; Kong 2007; Ulvestad et al. 2007). Considering the fundamental plane, a relation between radio and X-ray fluxes as a function of black-hole mass, the observations were consistent with a $20\ 000\ M_\odot$ black hole. However, follow-up observations made by Miller-Jones et al. (2012) did not detect radio emission, suggesting that either a variable accretion mechanism or strong biases in either one of the observations are present.

Further radio observations were performed in order to find the critical signature of a black hole. Strader et al. (2012) tested several Galactic globular clusters for the presence of possible intermediate-mass black holes and found upper limits of the order of 10^2 $M_\odot$. Also for ω Centauri and the massive Galactic globular cluster NGC 6388 radio observations were made and compared with X-ray detections. Despite the signatures found by kinematic studies, no strong evidence for accretion by a massive black hole was found (e.g. Maccarone et al. 2005; Ulvestad et al. 2007; Bash et al. 2008; Cseh et al. 2010). However, a non-detection in radio emission does not imply the non-existence of an intermediate-mass black hole. In order to transform radio fluxes into black-hole masses, one has to make various assumptions about the gas accretion process such as gas distribution and accretion efficiency in order to derive those limits.

Observing strategy

Besides X-ray and radio observations there is only one other method to detect massive black holes in complex environments such as globular clusters - the kinematic approach. Even with no material to accrete, a black hole acts on its environment due to its strong gravitational field. It affects stars in its vicinity whose velocities and trajectories can be observed.

The observing strategy of this work is divided into two parts: 1) measuring the light and 2) measuring the mass. The first part is done using high-resolution images obtained with the Hubble Space Telescope (HST). Besides adaptive optics from the ground, which involves highly complicated atmospheric corrections using lasers, the HST is the only telescope that can resolve every star in a Galactic globular cluster. Using images from the HST, we are able to determine the total light contained in a cluster, which is used to estimate the total gravitational potential produced by the stars. The second step is to measure the actual gravitational potential in the cluster. This is done by analyzing the spectra of many stars in the cluster, determining their velocities using the Doppler shift of their spectra. The velocity dispersion σ, can then be transformed into a total mass using simple gravitational theories.

Each star in the cluster has an individual velocity with three components. From the point of view of an observer these are two tangential components (along the plane of the sky) and one radial component (along the line of sight). While the tangential motions can be measured over many years, monitoring the cluster and measuring the change of position of each star on the sky (also known as proper motions), the radial velocities can be measured instantaneously through spectroscopy. Due to the Doppler effect, the spectrum of each star is shifted by a small amount. If the star approaches us, its spectrum becomes blue shifted, a star receding results in a red shift. By measuring these shifts with respect to the vacuum position of the lines in the spectrum, one derives a velocity. But what happens when it is not possible to measure every individual spectrum? The separations between the stars in the center of the cluster are small and due to the atmospheric distortions (so-called seeing)

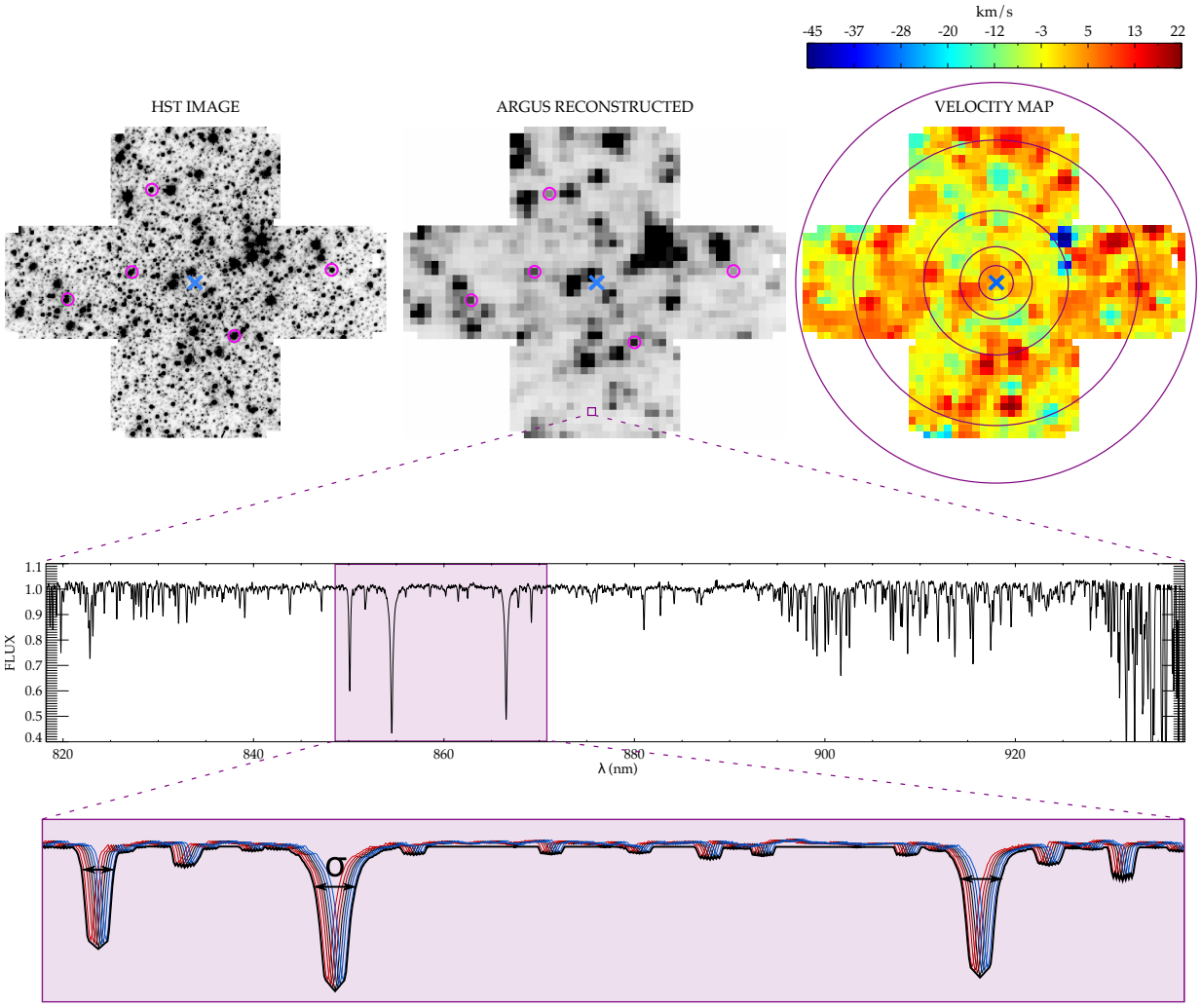

Figure 1.7: Observing strategy with integral-field units. The velocity dispersion σ is determined by measuring the broadening of the spectral lines which is caused by the superposition of several velocity shifted lines (lower panel).

the light of one bright star can overlap with the light of adjacent fainter stars, which makes the extraction of individual velocities impossible. However, since we are not interested in the individual velocities themselves but the velocity dispersion, a different technique, called integral-field spectroscopy, can also be applied. When measuring individual velocities the standard approach is to position a slit on top of the object of interest which allows only the light of this one star into the dispersing instrument. Integral-field spectroscopy, uses in our case small microlenses located next to each other on an array, allowing to scan an entire region of the sky instead of individual objects. The light of several stars is collected in each microlens and led by optical fibers into the disperser. In this way, the final spectrum is a superposition of several individual spectra. Figure 1.7 shows what happens when spectra of stars with different velocities get superposed. The velocities randomly shift the spectra to either the blue or red side of the wavelengths which results in a broadened line in the summed spectrum. This broadening can now be measured by comparing it to a spectrum of a single star. The width of this broadening is nothing else but the velocity dispersion of all the stars contributing to the spectrum. As shown in Figure 1.7, the individual stars are still visible in the velocity map. This is different compared to the velocity maps observed for galaxies where no single star can be resolved and the velocity map appears to be a smooth distribution. This makes integral-field spectroscopy for globular clusters more difficult since an additional factor of low-number statistics, i.e. shotnoise, is introduced. It also differes from the direct orbital measurement of the supermassive black hole in our galaxy, as the stars in this case are fully resolved. Our technique for measuring masses of intermediate-mass black holes can therefore also be seen as an intermediate observational strategy.

The velocity dispersion is measured in concentric bins in order to derive a velocity dispersion profile. As mentioned before this can now be directly compared to the velocity-dispersion profile derived from the visible light. In order to transform the light profile into a velocity-dispersion profile (that can be compared to the observed data) we use anayltical models to describe collisionless, self-gravitating stellar systems such as globular clusters. In reality, collisions (or close encounters) play a critical role in the dynamical evolution of a globular cluster (see Section 1.1). However, since this only affects processes over several relaxation times and we are interested in the momentary dynamical stage of the cluster, the globular cluster can be assumed to be collisionless. In this regime, a good description of the stellar system is given by the 6-dimensional phase space $(\vec{x}, \vec{v})$ where each star in the cluster is represented as a datapoint with three spacial and three velocity components. By assuming no collisions, the phase space distribution function follows a continuity equation[3]. As a direct consequence of the phase space continuity follows the collisionless Bolzmann equation, connecting velocities and positions of every star. As the distribution function in the collisionless Boltzmann equation depends on independent variables, the equation is usually very difficult to solve. Therefore it is useful to concentrate on the moments of the equation, i.e. integrated quantities such as velocity dispersion and density. This finally leads to a group

[3]As each data point can only move on a continuous path through phase space, in contrast to collisions where the particles can "jump".

of equations known as the Jeans equations which describe the connection between density and velocity dispersion at every point in the cluster. From this, a model velocity-dispersion profile is derived and compared to the observed profile.

Without a black hole, these two profiles should agree with each other. With a black hole at the center, however, the stars in its vicinity will move faster than the stars outside, causing the velocity dispersion profile to rise at the very center. In summary, if the measured velocity dispersion profile shows a rise at the center which is not explained by the visible light, an additional dark mass has to be present. The question whether this dark mass is actually a black hole or rather a collection of many stellar-mass black holes is still a point of debate that will also be addressed in this work.

1.4 N-body simulations

Simulations have been a valuable tool for astronomers ever since (and even before) computers were powerful enough to perform numerical calculations. As astronomers are limited to observations only (in contrast to sciences where experiments dominate) they need another way of testing their hypotheses and theories. One of the first simulations ever was performed by Holmberg (1941) using a set of light bulbs instead of a computer. He replaced the gravitational force with the intensity of the light since both follow the same $1/r^2$ law. Every time step the light bulbs were moved according to the net flux at its position. In this way, Holmberg performed a gravitational simulations with $N = 76$ particles.

With the advance of computational technology in the early 60s, simulations became faster and easier to handle on computers and a new research field in astronomy opened up. Nowadays we are able to simulate the entire 13.8 billion years history of our universe, interacting galaxies and even supernova explosions in high detail. N-body simulations, i.e. simulations with N particles only influenced by their own gravity, still belong to the most computational expensive simulations. Due to the long-range character of gravity, all particles have to be considered contributing to the net force of all the remaining particles, leading to $\propto N^2$ calculations each time step. The calculations have to be repeated until the cluster dynamically evolves, i.e. undergoes core collapse. As described in Section 1.1 this occurs roughly after 10 - 15 relaxation times which can be estimated as $\tau_{rlx} \sim N\tau_{cross}$.This gives a third factor of N, increasing the CPU cost of N-body simulations to $\propto N^3$. Nevertheless, in order to describe the evolution of self gravitating systems without any further components such as globular clusters, direct N-body computation remains the best tool.

The basic principle of N-body simulations of globular clusters is outlined in Figure 1.8. First, one has to decide how many stars to use. An old globular cluster has on average 10^5 stars. If one wants to simulate the evolution of a cluster including its mass loss, one has to start with almost 10 times more stars. This slows down the computational time drastically so that one has to find a compromise between including enough stars to make a realistic simulation

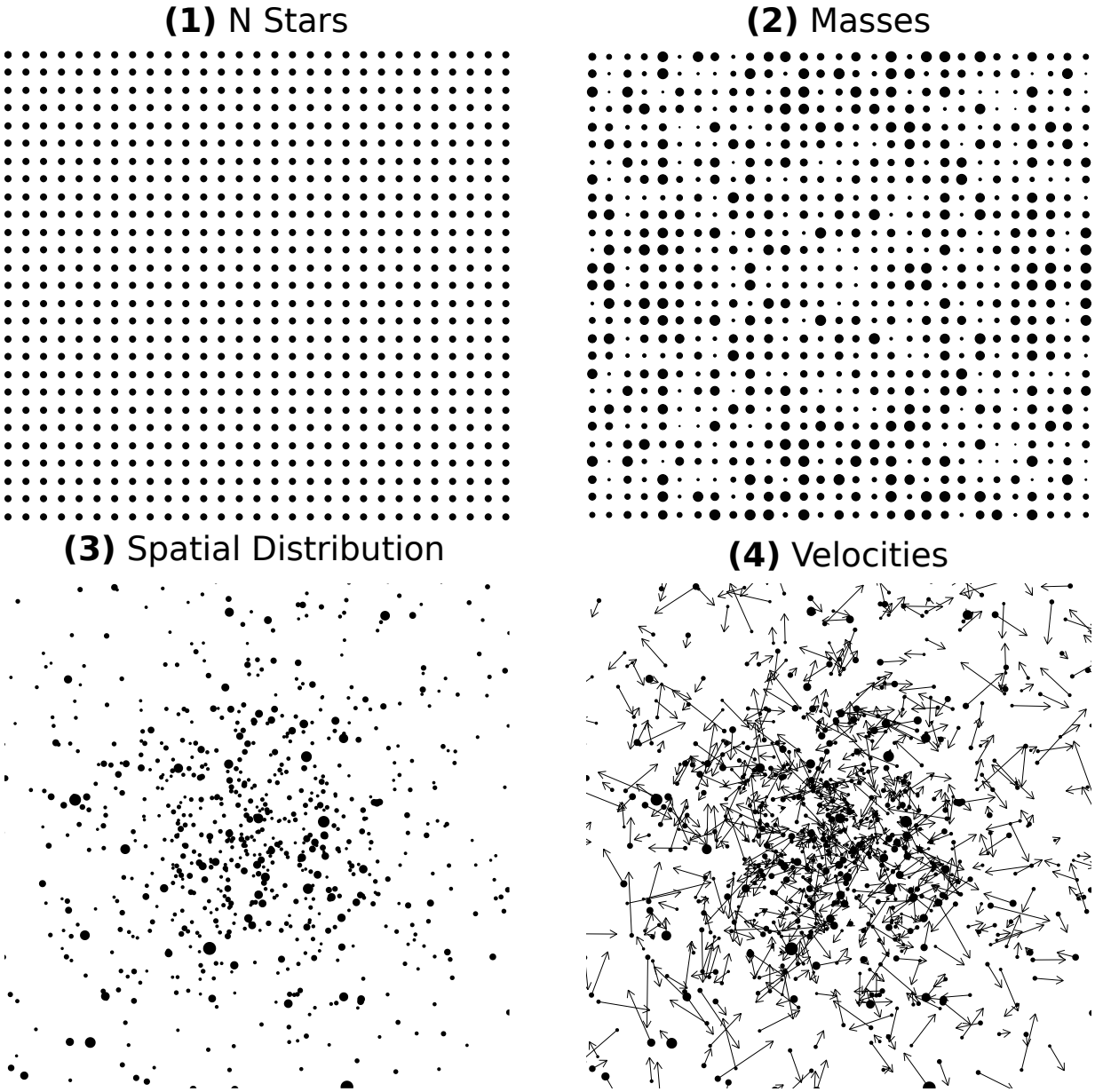

Figure 1.8: The N-body principle. Before starting a simulation the initial parameters such as mass and spatial distribution are critical.

and not using too many stars, slowing down the calculations. With modern computers, simulations with $N = 100\ 000 - 500\ 000$ are possible. Once the number of particles is fixed, each particle gets assigned a mass. The masses are drawn from mass-distributions as observed in real clusters. One of these, and the most commonly used, was found by Kroupa (2001). Given their masses, the stars are now distributed in three-dimensional space also using common mass-density distributions such as King (1966) profiles. As a last step, the initial velocities are calculated according to the mass and position of each star, and the overall gravitational potential. Here, the Virial theorem is used to start with the cluster in equilibrium between its stellar velocity and gravitational attraction. Although most of the N-body codes are public and free to use, finding the right starting parameters is not trivial and requires detailed knowledge of the dynamics of globular clusters. Once the starting parameters are determined the N-body code starts calculating the new position and velocity of each star for every time step.

What looks simple at first sight is actually a highly complex code in order to minimize computational time and numerical round-off errors. The code used in this work was developed by Aarseth (1999) and evolved from the first version NBODY1 to the sophisticated and detailed code today NBODY6, NBODY7 and NBODY8. In order to integrate individual time steps the code uses a Hermite scheme which allows fast calculations and individual time steps for each particle. In addition it treats binaries as perturbed harmonic oscillators by performing a coordinate transformation in order to reduce the number of time steps that have to be calculated to trace such close encounters. This and many more tricks of smart coding make NBODY6 one of the fastest direct N-body codes to date. Furthermore, these codes allow for stellar evolution and stellar mass-loss to be included, allowing for the formation of massive remnants and white dwarfs.

1.5 This Work

This work concentrates on the search of intermediate-mass black holes in globular clusters through kinematic observations and N-body simulations. The following chapters cover the observing strategies outlined in the previous chapter using state-of-the art integral field spectroscopy. In total, a sample of nine Galactic globular clusters (eight are discussed in this work) was analyzed and black-hole masses or upper limits determined. The results were compared to other cluster properties and set into context with scaling relations of supermassive black holes in galaxies. The observations are supported by a large number of N-body simulations of globular clusters in tidal fields in order to study the clusters' dynamical processes when including intermediate-mass black holes and to constrain new obervables.

CHAPTER 2 As a pilot project we investigated the globular cluster NGC 6388, one of our best candidates for the presence of an intermediate-mass black hole. Using integral-field units of the Very Large Telescope in combination of high-resolution images of the Hubble

Space Telescope, we obtained the central velocity dispersion profile and found a steep rise that indicates a black-hole mass of $\sim 10^4\,M_\odot$. In order to exclude observational biases we performed Monte-Carlo simulations and measured the uncertainties caused by shotnoise. We used N-body simulations to test for radial anisotropy in the center of the cluster which could mimic the black-hole signature. We found that after a few relaxation times, all radial anisotropy is smoothed out in the center.

CHAPTER 3 NGC 2808 shows a flattened shape and strong rotation in its outer parts. Therefore we used this cluster to test our kinematic modeling in extreme cases. In the same way as in the previous Chapter, the inner kinematics of this cluster were extracted and compared to photometric data from the HST. Outer kinematics were taken from archival data observed with a Fabry-Perot instrument. The highly flattened shape of the kinematic profile of NGC 2808 required axisymmetric Jeans models instead of spherical ones to account for rotation, but also a variable mass-to-light (M/L) profile. In this work, we used the M/L profile derived from N-body simulations and included it in the Jeans models. We found that none of the various models we compared to our data required an intermediate-mass black hole for NGC 2808.

CHAPTER 4 During our analysis of NGC 2808, we discovered the presence of stars with unusually high velocities. In this Chapter we discuss possible origins of their high velocities and exclude alternative explanations. Using three-body scattering simulations, we conclude that the fast stars most likely originate from encounters with massive remnants and binaries in the stage as main-sequence stars and generalize these results to previously detected high-velocity stars in other globular clusters. The results agree with the non-detection of an intermediate-mass black hole in NGC 2808, since the coexistence of massive stellar remnants and a central black hole is unlikely.

CHAPTER 5 The remaining six clusters NGC 1851, NGC 1904, NGC 5694, NGC 5824, NGC 6093 and NGC 6266 were analyzed all together by applying methods developed for NGC 2808 and NGC 6388. When available, the velocity-dispersion profiles were completed with outer kinematics from various sources. All profiles were compared to analytic Jeans models allowing for variable M/L profiles and different black-hole masses. Only NGC 6266 and NGC 1904 show signatures of an intermediate-mass black hole in their center.

CHAPTER 6 Using all the data obtained in the previous studies, this paper finalizes the observational work. We take the measured black-hole masses and upper limits from our sample, and add data from the literature to obtain a total sample of 14 globular clusters that were tested for a central black hole through kinematics. Out of these, six clusters have an actual black-hole detection. We collect cluster properties from various sources and compare our sample with the three major scaling relations observed for globular clusters: $M_\bullet - \sigma$, $M_\bullet - L_{tot}$ and $M_\bullet - M_{tot}$. We applied several statistical methods in order to

quantify correlation coefficients and to apply a linear fit. For all three relations, we find a correlation for the globular cluster sample, but with a slope that is more shallow than what is measured for the supermassive black holes. We suggest that this might be due to the rapid mass loss in globular clusters and therefore the fast change of their structural properties. We also tested for further correlations between black-hole masses and cluster properties, but did not find significant connections.

CHAPTER 7 The N-body work described in this Chapter is the beginning of a series of N-body simulations. We performed N-body simulations for globular clusters with 32 000, 64 000, and 128 000 stars in a tidal field. To study the detailed dynamical effect of each property, we varied three qualities of the cluster: The black-hole retention fraction (i.e. the fraction of stellar-mass black holes that stays in the cluster after formation), the primordial binary fraction and the mass of the intermediate-mass black hole. We studied the effect of these variations on characteristics of the model clusters such as lifetime, mass-function slope, remnant fraction and concentration. We found that an intermediate-mass black hole at the center of the cluster increases the ejection of massive stars and leads to a lower remnant fraction and a low-mass star depletion.

1.6 Future

The field of intermediate-mass black holes is still young and our sample small. To date we are limited to observations of globular clusters in our own galaxy which most probably only shows the tip of the iceberg. However, in order to search for intermediate-mass black holes in extragalactic globular clusters, our technology still has to advance.

1.6.1 Observations

From formation scenarios, only 10% of all globular clusters are expected to have the initial conditions that are needed to form a massive black hole. Therefore, a large sample of globular clusters is crucial in order to detect a useful number of intermediate-mass black hole candidates and make statistics about their properties. Our galaxy hosts 150 globular clusters and most of them are less massive than $10^5\,M_\odot$. Not the best environment to search for massive black holes. Moreover, without adaptive optics that drastically enhances the resolution of ground-based telescopes or the help of space telescopes, it is impossible to resolve the sphere of influence of an intermediate-mass black hole in an extragalactic globular cluster. In the future there will be many instruments, supported by adaptive optics as well as new space telescopes (e.g. James Webb Space Telescope) but high spatial resolution is not enough. In order to perform the technique of integral-field spectroscopy, also a high spectral resolution is needed, otherwise the broadening of the line, which is small for small velocity dispersions in systems such as globular clusters, can not be measured.

The only hope for testing IMBHs in extragalactic sources lies therefore in next-generation telescopes such as the 40 meter Extremely Large Telescope (ELT) and its near-infrared integral-field spectrograph HARMONI that will allow adaptive optics observations with high spectral resolution. However, this remains a far future project.

This unfortunate situation requires new observing techniques that allow the search for intermediate-mass black holes to be continued. Furthermore, independent mass determinations are needed in order to remove the doubt of the existence of the already detected black holes. One solution might be provided by the new interferometry instrument GRAVITY, built by a consortium composed of the European Southern Observatory (ESO), the Max Planck Institute for Extraterrestrial Physics (MPE), and collaborators. It is planned to start operations in 2014. This instrument combines all four Unit Telescopes of the VLT and will reach an astrometric accuracy of 10 microarcseconds. With this, the direct measurement of acceleration of individual stars and therefore the direct determination of the potential the star is moving in, becomes possible.

1.6.2 Simulations

In contrast to the observations, the simulations are not limited in their possibilities. With the rapid growth of CPU power, it will soon be possible to simulate realistic clusters with particle numbers up to 10^7. But even now, we can already address many key questions in the dynamical evolution of globular clusters and pin down new observables. Three main goals that we want to achieve with N-body simulations in the near future are:

Reproduce observations

Jeans models are a good first approximation to describe and reproduce the observational dynamical data of globular clusters. However, too many processes such as mass-segregation and remnant retention fraction are not covered by this kind of models. Therefore, more sophisticated models are needed. By running a large grid of N-body simulations with different initial conditions and environmental properties, we will be able to pin down these simulations that fit our observed data the best. If we are able to reproduce both the kinematic and the photometric profiles, we can constrain the possible black-hole mass in addition to many more cluster properties, such as initial size and mass, anisotropy, retention fraction and binary fraction.

Test analysis methods

As mentioned earlier, the method of integrated light for semi-resolved stellar populations brings many uncertainties. One of the goals we are aiming with N-body simulations is to create mock datasets of globular clusters and to 'observe' them with the same techniques

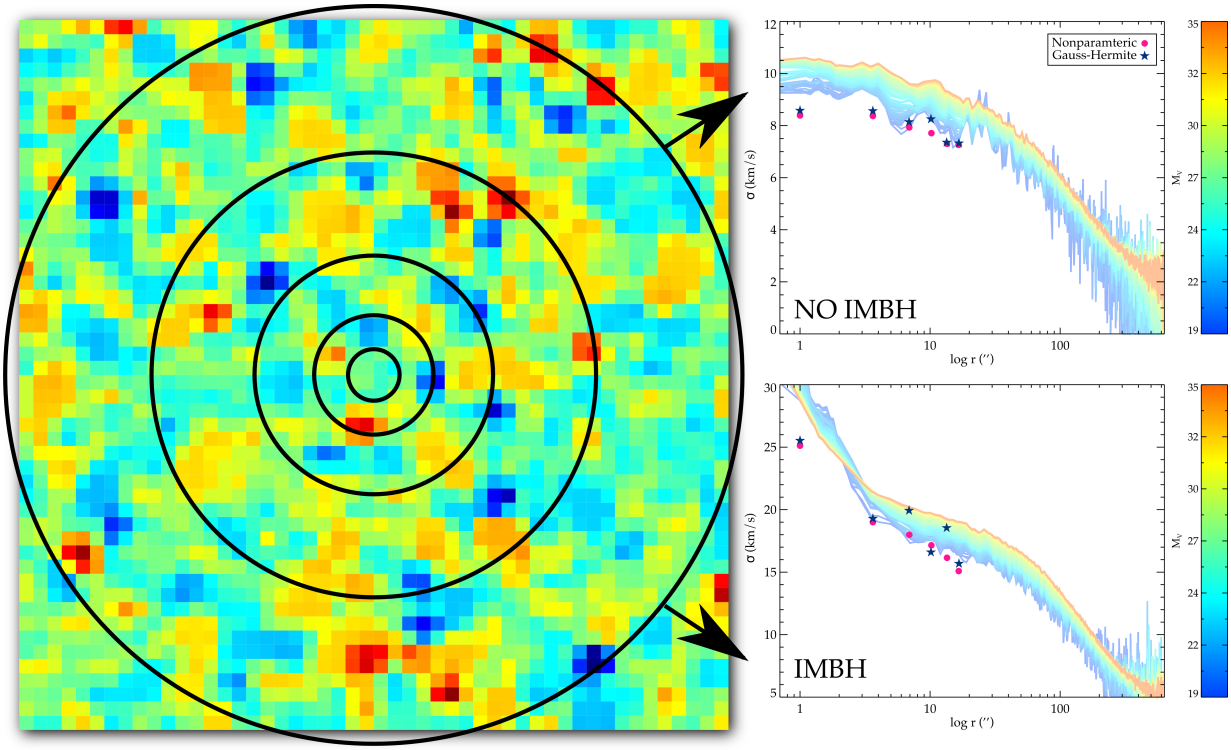

Figure 1.9: Simulated IFU from N-body simulations and the resulting velocity-dispersion profile for a cluster with (lower panel) and without (upper panel) an IMBH.

as we use for our data. In this way we will be able to detect problems and biases in our methods that allows us to correct our measured quantities and estimate their uncertainties.

Figure 1.9 shows the velocity map of a simulated cluster IFU observation. The map was derived from a simulated data cube produced from luminosities, velocities and spectral types of the stars in an N-body simulation. The future goal is to produce datacubes for simulations with different intrinsic properties and to test how well these are reproducible.

Explore dynamical processes

N-body simulations allow us to study and understand the physics of globular clusters and their internal dynamics. During the next years we want to address several open questions of globular cluster science using N-body simulations. One of the major caveats in the search for IMBHs is the unknown amount of dark remnants in the core of globular clusters which are expected in the cluster core due to two-body relaxation and mass segregation. The question whether the rise in the velocity-dispersion profile is really due to one single massive object rather than a number of compact objects, such as white dwarfs or neutron stars in the cluster core, is crucial in the search for IMBHs. N-body simulations will shed light onto this topic by measuring the velocity-dispersion profiles of highly mass segregated cluster simulations and searching for signs in the kinematic profile which could be mistaken for an IMBH signature.

Related to this is the population of Blue Straggler Stars (BSSs) in globular clusters which are good tracers for mass segregation and evolutionary state of the cluster. Many observational attempts to discover their nature have been performed and can be tested with simulations. One example is the discovery of two distinct BSS populations in post core collapse clusters Ferraro et al. (2009). Also kinematic anisotropy in clusters can influence the black hole measurements. If the cluster is highly radially anisotropic in the center this produces a rising velocity dispersion profile, thus mimicking the effect if an IMBH. Understanding the origin and evolution of anisotropy and, related to this, the effects of primordial rotation in the cores of globular clusters is crucial in order to model the cluster accurately and constrain the black-hole mass. Combining our radial velocity measurements with HST proper motions, will give us the full 3D kinematic information, crucial to constrain anisoptropy and to compare with N-body simulations.

1.6.3 Black-hole evolution

In Chapter 6 we have investigated the positions of the IMBHs on the $M_\bullet - \sigma$ relation that is observed for SMBH in massive galaxies. We found the slope for IMBH being much more shallow than the one measured for the SMBHs. In ongoing work, not included in this thesis (Kruijssen & Lützgendorf, 2013 in press), we are investigating the possibility that globular clusters originally were on the $M_\bullet - \sigma$ relation and moved away from it where they are

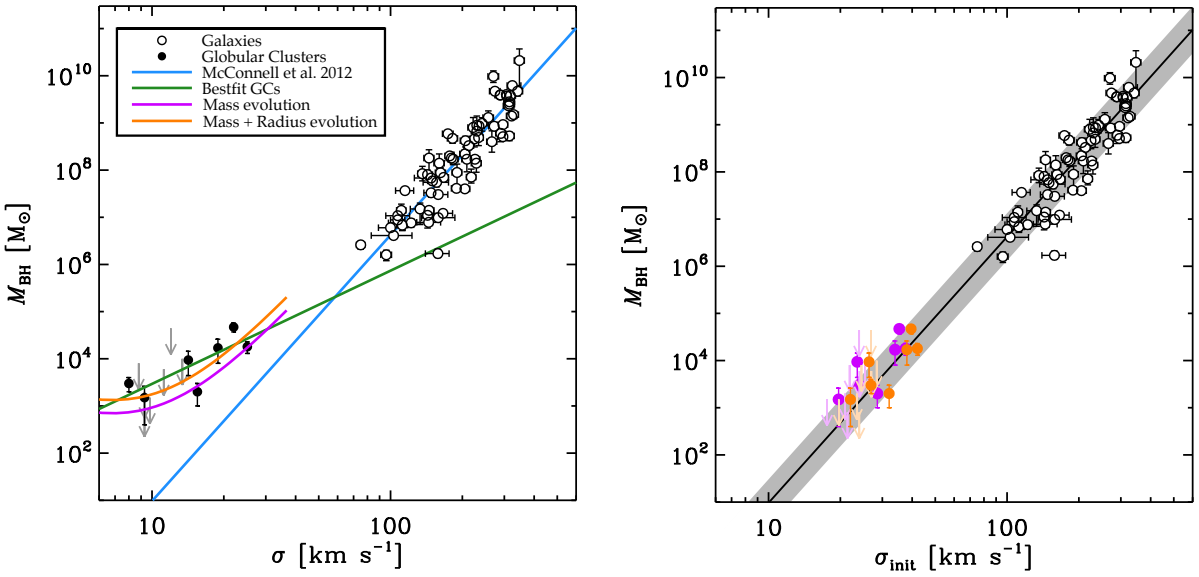

Figure 1.10: The current and initial $M_\bullet - \sigma$ relation for IMBHs using mass evolution and radius evolution of the globular clusters.

today due to mass-loss. In Figure 1.10 we show the result of the cluster evolution model SPACE (Kruijssen & Lamers 2008; Kruijssen 2009) that allows us to determine the amount of mass that was lost by the cluster. This can be directly translated into the amount of decrease of the velocity dispersion using the Virial theorem. In addition to the mass loss, the cluster also expanded during its dynamical evolution in a tidal field. This again affects the velocity dispersion and causes an additional decrease besides the effect of mass loss. In Figure 1.10 we show both effects and note that the difference is not crucial and the mass evolution is the major effect.

The agreement between IMBH and SMBH scaling relations is both intriguing and suggestive. However, it is only valid under a few crucial assumptions. The first one is that the major growing process of intermediate-mass black holes took place before the cluster started its dynamical evolution the calculations shown in Figure 1.10 do not include further black-hole growth. This is plausible since after all the gas is gone, the black hole can only grow by capturing individual stars. The second assumption is that the scaling relation for SMBH on galaxies did not change, i.e. was the same at the time of cluster formation. Only under these assumptions, the comparison of unevolved globular clusters and galaxies would be meaningful.

The origin of the $M_\bullet - \sigma$ scaling relation and therefore the process of co-evolution of black hole and its host galaxy is still under debate. Recent observations have revealed black-hole masses that lie far away from the known scaling relations (e.g. van den Bosch et al. 2012) and raise the question under which circumstances they hold. Populating the low-mass end of this relation with objects such as intermediate-mass black holes in globular clusters or dwarf

galaxies will help to constrain its validity in this mass regime and might help to distinguish between different black-hole growth mechanisms and evolution scenarios. Also its high-mass end is of interest. In the next years, more extreme black-hole mass detections are required in order to distinguish between outliers or an actual different behavior of scaling relations at higher masses. For this, new observing techniques and high performance telescopes and instruments are required to continue the hunt of black holes on all scales.

We have investigated a sample of Galactic globular clusters for the presence of a possible intermediate-mass black hole in the center using integral-field spectroscopy. The results show, that one third of the clusters in our sample show kinematic signatures of a central massive black hole and that they follow similar, but more shallow scaling relations of black-hole mass and properties of the host system as observed for supermassive black holes in galaxies. This intriguing finding could be explained by the severe mass-loss of globular clusters due to two-body relaxation and the tidal field of the galaxy. This again would imply that IMBHs in globular clusters and SMBHs in massive galaxies originally followed the same scaling relations, which would be remarkable considering their different formation processes and environments. In summary, the study of the low-mass end of the black-hole scaling relation as it was carried out in this work has revealed new aspects of connection of black-hole growth in very different host systems.

CHAPTER 2

Kinematic signature of an intermediate-mass black hole in the globular cluster NGC 6388

Nora Lützgendorf, Markus Kissler-Patig, Eva Noyola, Behrang Jalali, Tim de Zeeuw, Karl Gebhardt, and Holger Baumgardt
Astronomy & Astrophysics, Volume 533, id.A36 (2011)

Abstract We present results from ground based VLT/FLAMES spectroscopy in combination with HST data for the globular cluster NGC 6388. The aim of this work is to probe whether this massive cluster hosts an intermediate-mass black hole at its center and to compare the results with the expected value predicted by the $M_\bullet - \sigma$ scaling relation.The spectroscopic data, containing integral field unit measurements, provide kinematic signatures in the center of the cluster while the photometric data give information of the stellar density. Together, these data sets are compared to dynamical models and present evidence of an additional compact dark mass at the center: a black hole. Using analytical Jeans models in combination with various Monte Carlo simulations to estimate the errors, we derive (with 68% confidence limits) a best fit black-hole mass of $(17 \pm 9) \times 10^3 M_\odot$ and a global mass-to-light ratio of $M/L_V = (1.6 \pm 0.3)\ M_\odot/L_\odot$.

2.1 Introduction

For a long time, only two mass ranges of black holes were known. On the one hand, we have stellar mass black holes, which are remnants of massive stars, and can be observed in binary systems. On the other hand, there are supermassive black holes at the centers of galaxies, some of them accreting at their Eddington limit and producing the brightest objects known (quasars). It has been demonstrated that supermassive black holes show a tight correlation between their mass and the velocity dispersion of the galaxy in which they reside (e.g. Ferrarese & Merritt 2000; Gebhardt et al. 2000a; Gültekin et al. 2009). Extrapolating this relation to the lower velocity dispersions of globular clusters, with $\sigma \sim 10 - 20$ km s^{-1}, predicts central black holes in these objects with masses of $10^3 - 10^4 M_\odot$.

Due to the small amount of gas and dust in globular clusters, the accretion efficiency of a potential black hole at the center is expected to be low. Therefore, the detection of IMBHs at the centers of globular clusters through X-ray and radio emissions is challenging (Miller & Hamilton 2002c; Maccarone & Servillat 2008). Nevertheless, there is another way to detect IMBHs in globular clusters: exploring the kinematics of these systems in the central regions. This method, proposed forty years ago (Bahcall & Wolf 1976; Wyller 1970), has long been limited by the quality of observational datasets, since it requires velocity dispersion measurements at a spatial resolution comparable to the size of the gravitational sphere of influence for plausible IMBH masses ($1-2''$ for large Galactic globular clusters). However, with existence of the Hubble Space Telescope (HST) and with high spatial resolution ground based integral-field spectrographs, the search for IMBHs was revitalized.

Gebhardt et al. (1997, 2000b) and Gerssen et al. (2002) claimed the detection of a black hole of $(3.2 \pm 2.2) \times 10^3 M_\odot$ in the globular cluster M15 from photometric and kinematic observations. After more investigations this cluster no longer appears as a strong IMBH candidate (e.g. Dull et al. 1997; Baumgardt et al. 2003, 2005; van den Bosch et al. 2006), but new detections of IMBH candidates in other clusters followed. Gebhardt et al. (2002, 2005) used the velocity dispersion measured from integrated light near the center of the M31 cluster G1 to argue for the presence of a $(1.8 \pm 0.5) \times 10^4 M_\odot$ dark mass at the cluster center. The possible presence of an IMBH in G1 gained further credence with the detection of weak X-ray and radio emission from the cluster center (Pooley & Rappaport 2006; Kong 2007; Ulvestad et al. 2007). Also, the globular cluster ω Centauri (NGC 5139) has been proposed to host a black hole at its center (Noyola et al. 2008, 2010). The authors measured the velocity-dispersion profile with an integral field unit and used orbit based dynamical models to analyze the data. Anderson & van der Marel (2010) studied the same object using proper motions from HST images. They found less compelling evidence for a central black hole, but more importantly, they found a location for the center that differs from previous measurements. Both G1 and ω Centauri have been suggested to be stripped nuclei of dwarf galaxies (Freeman 1993; Meylan et al. 2001) and therefore may not be the best representatives of globular clusters. The key motivation of this work is to probe more globular clusters for the presence of IMBHs.

Further evidence for the existence of IMBHs is the discovery of ultra luminous X-ray sources at non-nuclear locations in starburst galaxies (e.g. Fabbiano 1989; Colbert & Mushotzky 1999; Matsumoto et al. 2001; Fabbiano et al. 2001). The brightest of these compact objects (with $L \sim 10^{41}$ erg s^{-1}) imply masses larger than $10^3 M_\odot$ assuming accretion at the Eddington limit. Several realistic formation scenarios of black holes in globular clusters have been developed. The two main formation theories are: a) IMBHs would be Population III stellar remnants (Madau & Rees 2001), or b) they would form in a runaway merging of young stars in sufficiently dense clusters (Portegies Zwart et al. 2004; Gürkan et al. 2004; Freitag et al. 2006). In addition Miller & Hamilton (2002c) presented scenarios for the capture of clusters by their host galaxies and accretion in the galactic disk in order to explain the observed bright X-ray sources.

Table 2.1: Properties of the globular cluster NGC 6388 from the references: NG=Noyola & Gebhardt (2006), H= Harris (1996), M= Moretti et al. (2009), L=Lanzoni et al. (2007) and PM=Pryor & Meylan (1993).

Parameter	Value	Reference
RA (J200)	17h 36m 17s	NG
DEC (J200)	-44° 44′ 08″	NG
Galactic Longitude l	345.56	H
Galactic Latitude b	-6.74	H
Distance from the Sun R_{SUN}	11.6 kpc	M
Core Radius r_c	7.2″	L
Central Concentration c	1.8	L
Heliocentric Radial Velocity V_r	81.2 ± 1.2 km/s	H
Central Velocity Dispersion σ	18.9 km/s	PM
Age	(11.5 ± 1.5) Gyr	M
Metallicity [Fe/H]	-0.6 dex	H
Integrated Spectral Type	G2	H
Reddening E(B-V)	0.38	M
Absolute Visual Magnitude M_{Vt}	-9.42 mag	H

Our goal in this paper is to study the globular cluster NGC 6388. This cluster is located 11.6 kpc away from the Sun, in the outer bulge of our Galaxy. White & Kraft (1972) assigned it a high metallicity after studying its color magnitude diagram. Later, Illingworth & Freeman (1974) determined the dynamical mass of the cluster: with $\sim 1.3 \times 10^6 M_\odot$ it belongs to the most massive clusters in the Milky Way. In addition, its high central velocity dispersion of 18.9 $\mathrm{km\,s^{-1}}$ (Pryor & Meylan 1993), and assuming a black-hole mass correlation with velocity dispersion, make NGC 6388 a good candidate for detecting an intermediate-mass black hole. Besides the kinematic properties, the photometric characteristics are also quite interesting. Noyola & Gebhardt (2006, hereafter NG06) found a shallow cusp in the central region of the surface brightness profile of NGC 6388. N-body simulations showed that this is expected for a cluster hosting an intermediate-mass black hole (Baumgardt et al. 2005). For that reason, Lanzoni et al. (2007) investigated the projected density profile and the central surface brightness profile with a combination of HST high-resolution and ground-based wide-field observations. They found the observed profiles are well reproduced by a multimass, isotropic, spherical King model, with an added central black hole with a mass of $\sim 5.7 \times 10^3 M_\odot$. Also, the work of Miocchi (2007) suggests the presence of an intermediate-mass black hole in NGC 6388 as a possible explanation for the extended horizontal branch.

Another interesting fact about NGC 6388 is that it appears to contain multiple stellar populations (e.g. Yoon et al. 2000; Piotto 2008). This fact makes the scenario of merging

clusters plausible, leading to potentially complicated dynamics in the center. Recently, X-ray observations for NGC 6388 showed no significant signatures for an accreting IMBH (Cseh et al. 2010). But as already mentioned, this does not rule out a quiescent black hole. In summary, this cluster was chosen as it presents many interesting features. We measured the kinematics of the central regions, allowing us to probe the result of Lanzoni et al. (2007) with a different method, taking the kinematic properties as well as the photometric properties into account.

The basic approach of this work is to first study the light distribution of the cluster. Photometric analysis, such as the determination of the cluster center and the measurement of a surface brightness profile, is described in section 3.2. De-projecting this profile gives an estimation of the gravitational potential produced by the visible mass. The next step is to study the dynamics of the cluster. Section 4.5 gives an overlook of the FLAMES observations and data reduction and section 3.4 describes the analysis of the spectroscopic data. With the resulting velocity-dispersion profile, it is possible to estimate the actual dynamical mass. The next step is to compare the data to dynamical Jeans models (section 3.5). These models take the light profile and predict a velocity-dispersion profile, which is scaled to the data in order to obtain the mass-to-light ratio. This is done for models containing different black-hole masses until the best fit to the observed profile is found. In section 3.6 we summarize our results, list our conclusions and give an outlook for further studies.

2.2 Photometry

The photometric data, retrieved from the archive, were obtained with the Advanced Camera of Surveys (ACS) of the Hubble Space Telescope (HST) in the Wide-Field Channel (under the HST program SNAP-9821, PI: B.J. Pritzl) between October 2003 and June 2004. This data set is composed of six B (F435W), V (F555W) and I (F814W) images with exposure times of 11, 7 and 3s, respectively. It gives a complete coverage of the central region of the cluster out to a radius of 110″. The data were calibrated, geometrically corrected and dither-combined as retrieved from the European HST-Archive (ST-ECF, Space Telescope European Coordinating Facility[1]).

2.2.1 Color magnitude diagram (CMD) of NGC 6388

The CMD was obtained using the programs *daophot II*, *allstars* and *allframes* by P. Stetson, applied to our HST image. For a detailed documentation of these routines see Stetson

[1]Based on observations made with the NASA/ESA Hubble Space Telescope, and obtained from the Hubble Legacy Archive, which is a collaboration between the Space Telescope Science Institute (STScI/NASA), the Space Telescope European Coordinating Facility (ST-ECF/ESA) and the Canadian Astronomy Data Centre (CADC/NRC/CSA).

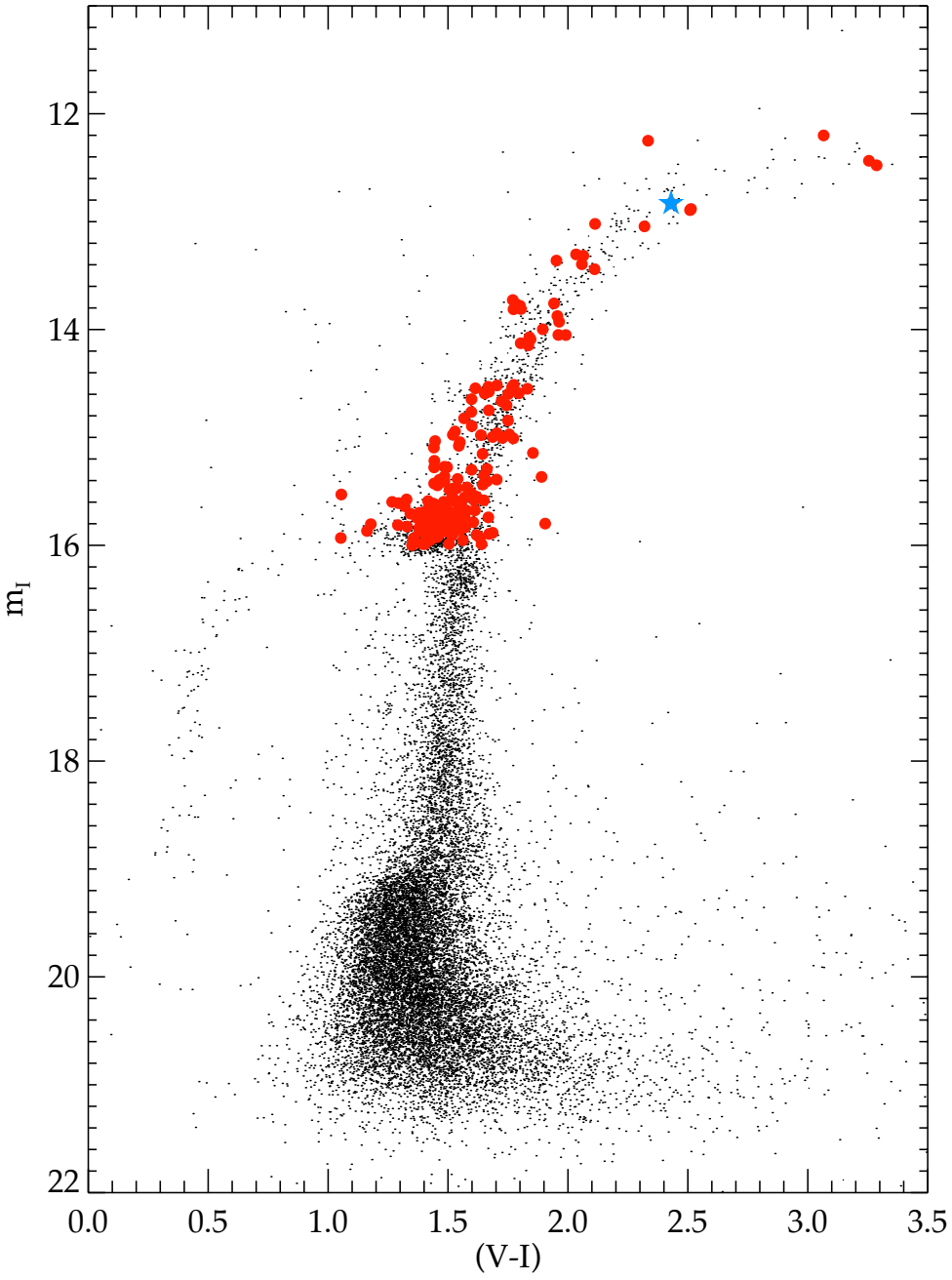

Figure 2.1: Color-magnitude diagram of NGC 6388. Overplotted are the brightest stars identified in the ARGUS field of view (red circles), and the template star used (star symbol).

(1987). These programs were especially developed for photometry in crowded fields and therefore ideally suited for the analysis of globular clusters. The routines *find*, *phot* and *psf* identify the stars, perform aperture photometry and compute the average point spread function (PSF) over the image, respectively.

Once the PSF has been defined, the next step is to group the neighboring stars to apply the multiple-profile-fitting routine simultaneously by the task *allstars*. Afterwards, the *find* task is applied again to find, in the star-subtracted image, stars which were not found in the first run. The entire procedure was performed on the V- and I-band images independently. As a next step the programs *daomaster* and *allframes* were used to combine both images and to create the final catalog containing all stars, their positions and magnitudes in the two bands. At the end, we calibrated the final catalog to the Johnson magnitude system by following the steps described in Sirianni et al. (2005).

In order to get better quality at the faint end of the CMD, one final step was applied to the catalog. The program *separation* (Bruntt et al. 2003) computes a separation index for every star in a catalog. This index is calculated by, first, evaluating a local surface brightness at the position of a given star. Second, the local surface brightness is compared to the sum of the surface brightnesses produced by the PSF of all the other stars in the field at the position of the centroid of that star. The ratio of these two surface brightness values expressed in magnitudes determines the separation index. Thus, the stars could be selected considering background-light contamination and not only by magnitude. Figure 4.4 shows the final CMD of stars with a separation index ≥ 5 overplotted with the positions of the brightest stars in the ARGUS pointing and the spectroscopic template star (see section 4.5).

2.2.2 Center of the cluster

Using the star catalog generated with *daophot*, the center of the cluster can be determined. Precise knowledge of the cluster center is important since the shape of the surface brightness and the angular averaged line-of-sight velocity distribution (LOSVD) profiles depend on the position of that center. Using the wrong center typically produces a shallower inner profile. For example determining the center for ω Centauri is not trivial (Noyola & Gebhardt 2006; Noyola et al. 2010; Anderson & van der Marel 2010). Fortunately, NGC 6388 is not as extended and has a steeper light profile than ω Centauri so that the center is easier to determine. NG06 determined the center of this cluster to be at $\alpha = 17:36:17.18$, $\delta = -44:44:07.83$ ($J2000$), with an uncertainty of $0.5''$, by minimizing the standard deviation of star counts in eight segments of a circle. In view of the discrepancies about the center location for ω Centauri, we decided to recompute the center of NGC 6388 and to evaluate how precisely the center can be determined. NG06's center on our I-band image was used as a first guess for the following methods to determine the center in the ACS images, i.e. our reference frame for the spectroscopy.

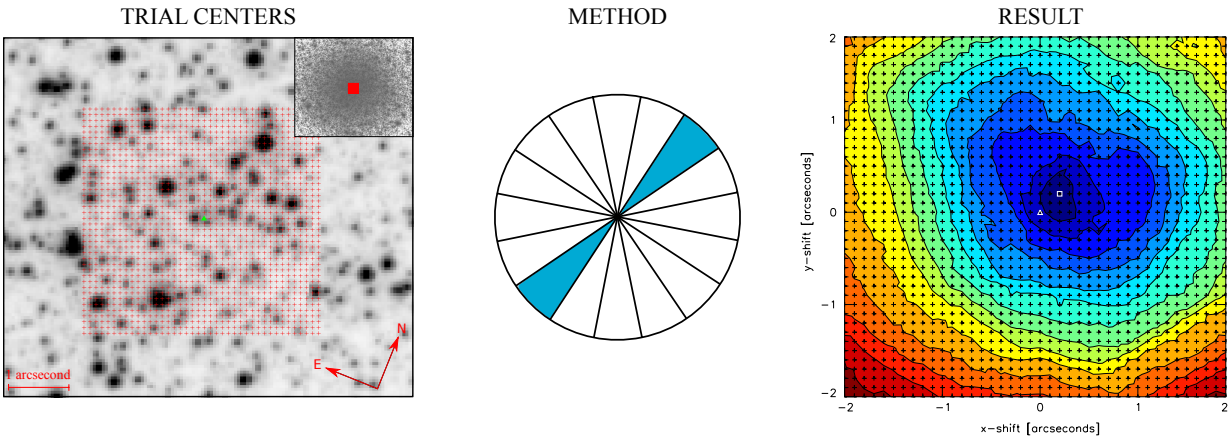

Figure 2.2: Method to determine the globular cluster center. From left to right: a zoom into our HST/ACS image of NGC 6388 (used to derive the CMD and luminosity profile for the cluster) with the over-layed grid of trial centers. Around each trial center, differential stellar counts and stellar luminosity were computed in two opposite wedges extending 15" in radius [middle panel]. A minimization of the residuals, as shown in the contour plot [right panel] determines the center to within 0.2″. The distances between the contours vary between 40 - 70 stars for the star count methods.

The first method is a simple star count as described in McLaughlin et al. (2006). The catalog generated with *daophot* (see section 5.2.1) contains 88,406 stars. In a field of $4'' \times 4''$ a grid of trial centers was created, using a grid spacing of 2 ACS pixels (0.1″). Around each trial center a circle of 300 pixels (15″) was considered and divided into 16 wedges as shown in Figure 3.2. The stars in each wedge were counted and compared to the opposite wedge. The differences in the total number of stars between two opposing wedges were summed for all 8 wedge pairs. The coordinates that minimized the difference defined a first guess of the center of the cluster. This center was refined as described in the next sections. We compared our result to the center obtained by NG06. The two centers are only 0.32″ apart and thus coincide within the error bars of 0.5″ (as determined by NG06 performing artificial image tests).

The second method that we used is also described in McLaughlin et al. (2006). Instead of comparing the total number in pairs of opposite wedges, a cumulative radial distribution for each wedge in 4 bins was generated. This time 8 wedges were used instead of 16 to avoid too large stochastic errors due to insufficient numbers of stars in each bin. The bins were placed at equidistant radii. Again the absolute value of the integrated difference between the radial distributions in any two opposing wedges was calculated and the minimum used to determine the new center of the cluster. The so derived center lies within 0.1″ of the one derived with the previous method and within 0.3″ of NG06's location.

We present a last method in which the light of the stars instead of their number, is considered. Similar to the first method, 16 wedges without any radial bins were generated, but this time not the stars were counted but the luminosities of the stars were summed up in

each wedge. In order to avoid a bias by the contamination of a few bright stars, only stars from the lower giant branch and the horizontal branch (between $m_V = 15$ and $m_V = 19$) were used. This approach reproduces NG06's center within the error bars (0.28″) as well. The method is illustrated in Figure 3.2. Shown are the grid of trial centers, the 16 wedges we applied to each of them, and the final contour plot.

For the subsequent analysis, we used the center derived from our ACS catalog. To estimate the error of our center determination we took the scatter from the three different methods as well as an additional test where only eight wedges where used. For these eight wedges we repeated the routine by only using the cardinal wedges and the semi-cardinal wedges separately. For this dataset (HST J8ON08OYQ, also used as position reference coordinates) we derived a final position of the center of:

$$(x_c, y_c) = (2075.5, 2548.5) \pm (3.1, 2.1) \text{ pixel} \tag{2.1}$$

$$\alpha = 17:36:17.441,\ \Delta\alpha = 0.2'' \text{ (J2000)} \tag{2.2}$$

$$\delta = -44:43:57.33,\ \Delta\delta = 0.1'' \tag{2.3}$$

All the derived centers lie within a few tenths of an arcsecond ($\sim 10^{-2}$ pc) radius. However, it must be considered that all the methods are using the same catalog derived by DAOPHOT. This catalog most likely suffers from incompleteness since the bright stars are covering the fainter stars underneath. This could bias the center towards the bright stars even if they are excluded in the counts. Our center agrees within the error bars with the one determined in NG06 on WFPC2 images. It also coincides with the center found by Lanzoni et al. (2007) which, according to them, lies $\sim 0.5''$ northwest of the NG06 center and therefor closer to ours.

2.2.3 Surface brightness profile

The last step of the photometric analysis was to obtain the surface brightness profile. This is required as an input for the Jeans models described in the following section. To obtain the profile, a simple method of star counts in combination with an integrated light measurement from the ACS image was applied. The fluxes of all stars brighter than $m_V = 18$ were summed in radial bins of equal width (50 pix) around the center and divided by the area of each bin. Since there are no stars in the gap between the two ACS CCD chips this area was subtracted from each affected bin.

In addition, the integrated light for stars fainter than $m_V = 18$ was measured directly from the HST image. Using the same radial bins as in the star count method, we measured the

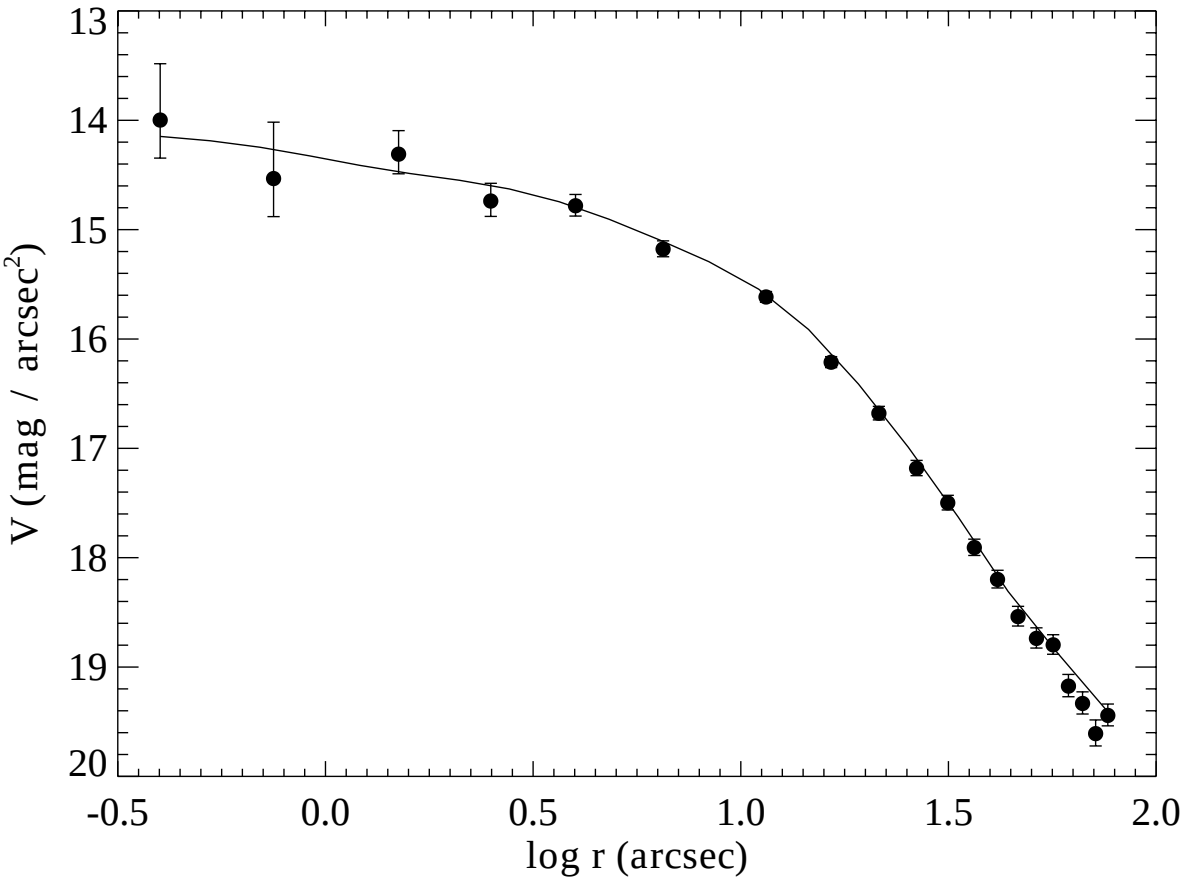

Figure 2.3: Surface brightness profile of NGC 6388. The profile shows a clear cusp for the inner 10 arcseconds. Also shown is the MGE fit (solid line) which was used to parametrize our profile (see section 2.8.)

statistical distribution of counts per pixel excluding regions with stars with $m_V < 18$. After trying different methods to derive the “average" of the distribution of counts, we applied a simple average that takes into account the faintest pixels i.e. stars. At the end, the flux per pixel was transformed back into magnitude per square arcseconds and added to the star counts profile.

We compared our profile with Trager et al. (1995), Lanzoni et al. (2007) and NG06. The latter was derived by measuring the integrated light using a bi-weight estimator while Lanzoni et al. (2007) derived their points by taking the average of the counts per pixel in each bin. We were able to reproduce the shape in the outer regions, but due to the method and data that we used our profile in the innermost region has a high uncertainty. The errors on our profile were obtained by Poisson statistics of the number of stars in each bin. With a linear fit inside the core radius ($\sim 7''$) we derived a logarithmic slope of $\beta = 0.7 \pm 0.2$

Table 2.2: Derived surface brightness profile in the V-band. ΔV_h and ΔV_l are the high and low values of the errors, respectively.

$\log r$ [arcsec]	V [mag/arcsec^2]	ΔV_l [mag/arcsec^2]	ΔV_h [mag/arcsec^2]
- 0.40	14.00	0.52	0.35
- 0.12	14.53	0.52	0.35
0.18	14.31	0.21	0.18
0.40	14.74	0.16	0.14
0.60	14.78	0.10	0.09
0.81	15.18	0.07	0.07
1.06	15.62	0.05	0.05
1.22	16.21	0.05	0.05
1.33	16.68	0.06	0.06
1.42	17.18	0.07	0.07
1.50	17.50	0.07	0.07
1.56	17.91	0.08	0.07
1.62	18.20	0.08	0.08
1.67	18.54	0.09	0.09
1.71	18.74	0.10	0.09
1.75	18.80	0.09	0.09
1.79	19.17	0.11	0.10
1.82	19.33	0.11	0.10
1.85	19.61	0.13	0.11
1.88	19.44	0.10	0.10

(where β corresponds to $\mu_V \sim \log r^\beta$ with the surface brightness μ_V), which results in a slope of the surface luminosity density $I(r) \propto r^\alpha$ of $\alpha = -0.28 \pm 0.08$. This value is steeper (but consistent within the errors) than the slope of $\alpha = -0.13 \pm 0.07$ derived by NG06 and also consistent with the slope derived by Lanzoni et al. (2007) of $\alpha = -0.23 \pm 0.02$.

To derive the SB profile, we used a calibrated catalog but we also combined this with measurements that we obtained from counts per pixel. It is possible that the transformations from counts into magnitudes do not match the calibrations of the catalog and therefore would cause an offset in our profile. The fact that we used all the light in the image, including the background light could also shift the profile to higher magnitudes than the intrinsic brightness. For that reason, we scaled our profile to the outer parts of the profile by Trager et al. (1995). This profile was obtained with photometrically calibrated data and provides a good reference for the absolute values of the profile. The final result of the surface brightness profile is shown in Figure 2.3.

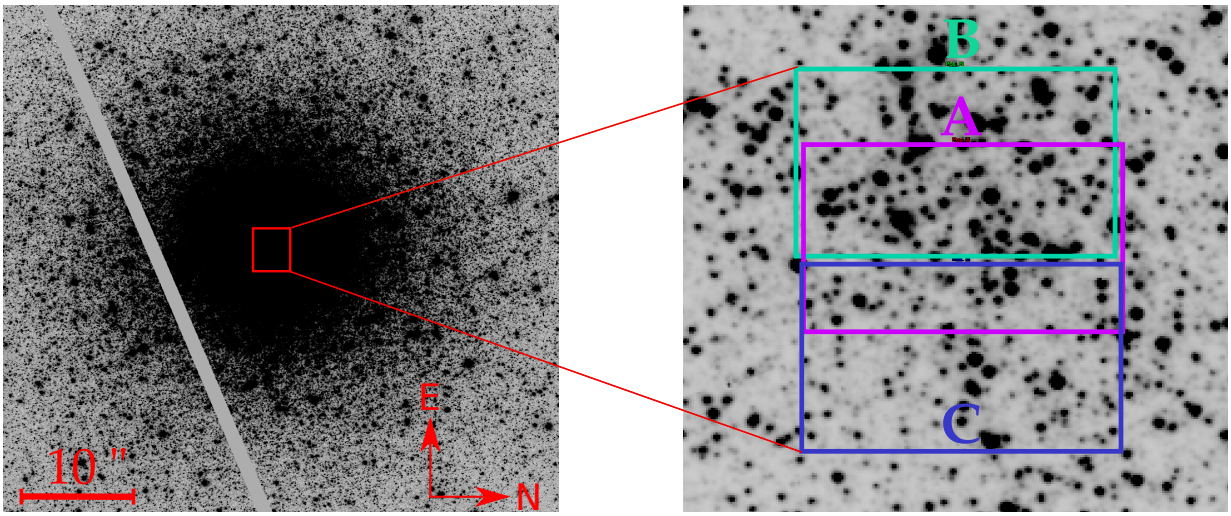

Figure 2.4: Positions of the three ARGUS pointings (A, B and C) reconstructed on the HST/ACS image.

2.3 Spectroscopy

2.3.1 Observations

The spectroscopic data were observed with the GIRAFFE spectrograph of the FLAMES (Fiber Large Array Multi Element Spectrograph) instrument at the Very Large Telescope (VLT) in ARGUS (Large Integral Field Unit) and IFU (Integral Field Unit) mode. The set contains spectra from the center (ARGUS) and the outer regions (IFU) for the globular cluster NGC 6388. The observations were performed during two nights (2009-06-14/15). The ARGUS unit was set to the 1 : 1 magnification scale (pixel size: 0.3″, 14×22 pixel array) and pointed to three different positions (exposure times of the pointings: A: $3 \times 480\,\mathrm{s} + 3 \times 1500\,\mathrm{s}$, B: $3 \times 1500\,\mathrm{s}$, C: $1 \times 1500\,\mathrm{s}$) to cover the sphere of influence of the potential black hole (see Figure 2.4). The IFU fibres were placed around the core radius of the cluster to obtain velocity dispersions in the outer regions.

The kinematics were obtained from the analysis of the Calcium Triplet ($\sim 850\,\mathrm{nm}$) which is a strong feature in the spectra. The expected velocity dispersions lie in the range 5-20 $\mathrm{km\,s^{-1}}$ and need to be measured with an accuracy of 1-2 $\mathrm{km\,s^{-1}}$. This implied using a spectral resolution around 10000, available in the low spectral resolution mode set-up LR8 ($820 - 940\,\mathrm{nm}$, R = 10400).

2.3.2 Data reduction

We reduced the spectroscopic data with the GIRAFFE pipeline programmed by the European Southern Observatory (ESO). This pipeline consists of five recipes which are briefly

described below.

First, a master bias frame was created by the recipe *gimasterbias* from a set of raw bias frames. Next, a master dark was produced by the recipe *gimasterdark* which corrected each input dark frame for the bias and scaled it to an exposure time of 1 second. The recipe *gimasterflat* was responsible for the detection of the spectra on a fiber flat-field image for a given fiber setup. *Gimasterflat* located the fibers, determined the parameters of the fiber profile by fitting an analytical model of this profile to the flat-field data and created an extracted flat-field image. This image was later used to apply corrections for pixel-to-pixel variations and fiber-to-fiber transmission.

The pipeline recipe *giwavecalibration* computed a dispersion solution and a slit geometry table for the fiber setup in use. This was done by extracting the spectra from the bias corrected ThAr lamp frame, using the fiber localization (obtained through the flat-field), selecting the calibration lines from the line catalog, and predicting the positions of the ThAr lines on the detector using an existing dispersion solution as an initial guess. The quality of the calibration was checked in two ways. The first one was by measuring the centroid of one dominating sky emission line in all 14 sky spectra and the second was a cross-correlation in Fourier-space of all sky spectra.

Both methods did not show any systematic shift of the spectra and resulted in an RMS of 0.03 Å, which corresponds to a velocity of 1 $\mathrm{km\,s^{-1}}$. The last recipe, *giscience* combined all calibrations and extracted the final science spectra. A simple sum along the slit was applied as extraction method. The input observations were averaged and created a reduced science frame, the extracted and rebinned spectra frame. At the end, the recipe also produced a reconstructed image of the respective field of view of the IFU and the ARGUS observations.

The most important parts of our reduction are the sky subtraction and an accurate wavelength calibration to avoid artificial line broadenings due to incorrect line subtractions. The program we used was developed by Mike Irwin and described in Battaglia et al. (2008). To subtract the sky, the program first combined all (14) sky fibers using a 3-sigma clipping algorithm and computed an average sky spectrum. Using a combination of median and boxcar, it then split the continuum and the sky-line components in order to create a sky-line template mask. For the object spectra, the same method of splitting the continuum from the lines was applied. In the process, the sky-lines were masked out to get a more accurate definition of the continuum. Afterwards, the sky-line mask and the line-only object spectra were compared to find the optimum scale factor for the sky spectrum in order to subtract the sky-lines from the object spectra. The continuum was added back to the object spectra and the sky continuum subtracted by the same scaling factor as obtained for the lines (assuming that lines and continuum have the same scaling factor).

After applying the sky subtraction program, the last step in the reduction of the data was to remove the cosmic rays from the spectra. This was done using the program LA-Cosmic developed by van Dokkum (2001) and based on a Laplacian edge detection. In order to avoid bright stars dominating the averaged spectra when they were combined, we applied

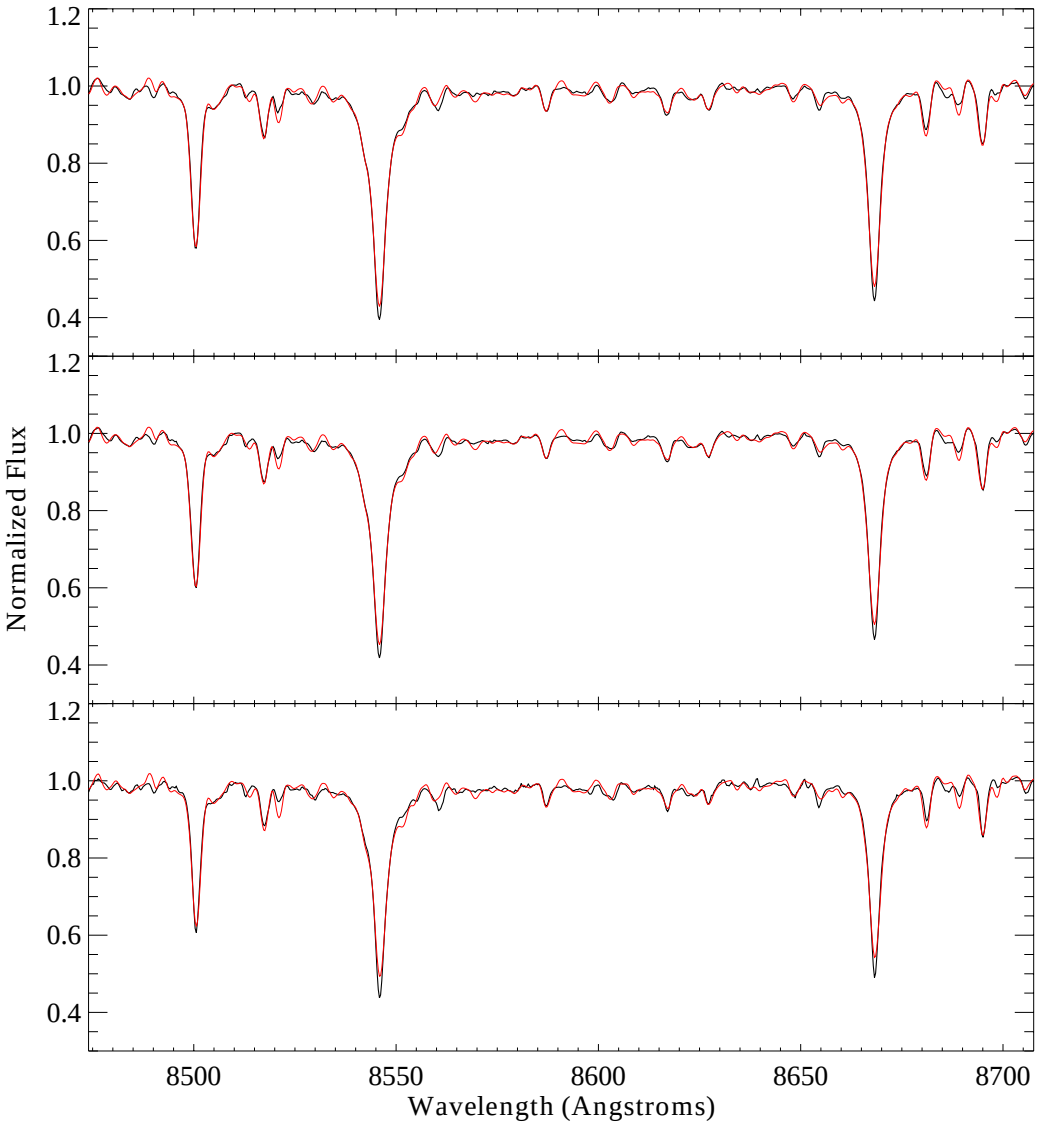

Figure 2.5: Combined spectra of the first, third and sixth bin overplotted by their best fit (red line). Due to the binning, the spectra show a high signal-to-noise ratio.

a simple normalization by fitting a spline to the continuum and dividing by it.

For the small IFUs, we applied the same reduction steps as for the large integral-field unit, except for the cosmic ray removal, since LA-Cosmic did not give a satisfying result. However, we were able to average all exposures applying a sigma clipping method in order to remove the cosmic rays, due to the fact that these pointings were not dithered.

2.4 Kinematics

This section describes how we created a velocity map in order to check for rotation or other peculiar kinematic signals and how we derived a velocity-dispersion profile. This profile is then used to fit analytic models, described in the next section.

2.4.1 Velocity map

The reconstructed images of the three ARGUS pointings were matched to the HST image. With this information, the pointings were stitched together and each spectrum correlated to one position in the field of view. The resulting catalog of spectra and their coordinates allowed us to combine spectra in different bins. The combined pointing contains 24×29 spaxels.

For each spaxel, the penalized pixel-fitting (pPXF) program developed by Cappellari & Emsellem (2004) was used to derive the kinematics in that region. Figure 2.6 shows a) the field of view of the three pointings on the HST image, b) the field convolved with a Gaussian and resampled to the resolution of the ARGUS array and c) the reconstructed and combined ARGUS image. The corresponding velocity map is shown in Figure 4.1. For every ARGUS pointing, a velocity map was derived before combining. The C pointing is a bit more noisy due to the fact that it only had one exposure. To check for systematic wavelength offsets we compared the derived velocities of the different pointings and exposures at overlapping spaxels. We found offsets of up to 1 $\mathrm{km\,s.^{-1}}$ We checked for systematic wavelength offsets between the pointings by cross-correlating their averaged sky spectra. The rms of the shifts measures 0.006 pixel (0.0018 Å) which corresponds to a velocity shift of ~ 0.1 $\mathrm{km\,s.^{-1}}$ We conclude that the velocity offsets are not due to uncertainties in the wavelength calibration and do not cause problems for our further analysis. Instead, the offsets are explained as follows:

i) Different pointings were dithered about half an ARGUS spaxel. This means that in every pointing a slightly different combination of stars contributes to the different spaxel, which could cause a different velocity measurement. ii) Errors in the reconstruction of the pointing positions could also cause velocity offsets between two positions. If the spaxels do not point at the exact same position we measure, similar to point i), different velocities. iii) Not all pointings had the same exposure time. This causes different signal-to-noise ratios

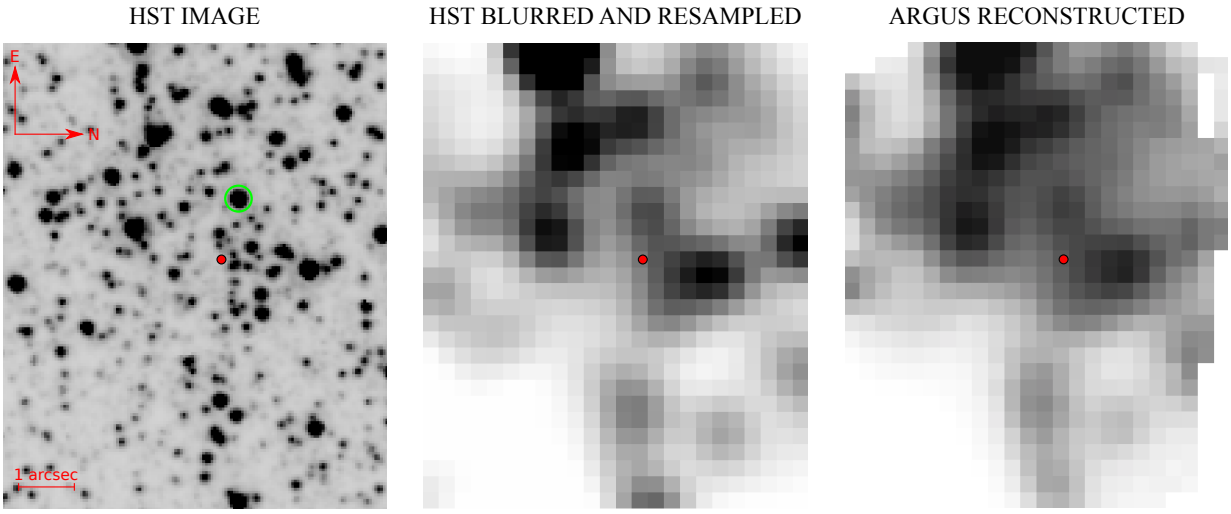

Figure 2.6: ARGUS field of view: the HST image is shown on the left. The red circle marks the center, the green one the template star which was used. The same image but convolved with a Gaussian and resampled to the 0.3âĂİ pixel scale of the ARGUS array [center]. Compared to the actual reconstructed ARGUS pointing [right], it is clear that they are pointing to the same region.

for different pointings. This could also explain some variations in the velocity measurements with the pPXF routine. Note that for the velocity dispersion measurements, we grouped the individual spectra in large annuli. For that reason, the position offsets do not cause a problem for the further analysis as the “error" in position is not propagated into the velocity dispersion measurement as a systematic shift.

We used a star from the central pointing (pointing A) as a velocity template. This has the advantage that it went through the same instrumental set-up as well as the same reduction steps as all other spectra and therefore the same sampling and wavelength calibration. The green circle in the HST image in Figure 2.6 (left panel) and the blue star in the color magnitude diagram (Figure 4.4) marks the star which was used. We also identified the brightest stars form the pointing in the CMD to make sure that the template and other dominating stars are not foreground stars (see Figure 4.4). In order to derive an absolute velocity scale, the line shifts of the templates were measured by fitting a Gaussian to each line and deriving the centroid. This was compared with the values of the Calcium Triplet in a rest frame and the average shift was calculated. We then corrected the radial velocity for the heliocentric reference frame.

2.4.2 Shot noise corrections

An obvious feature of the velocity map in Figure 4.1 is the bright blue spot in the middle left of the pointing which seems to dominate the blue (approaching) part of the map. We investigated whether we see a real rotation around the center or just one or a few bright stars

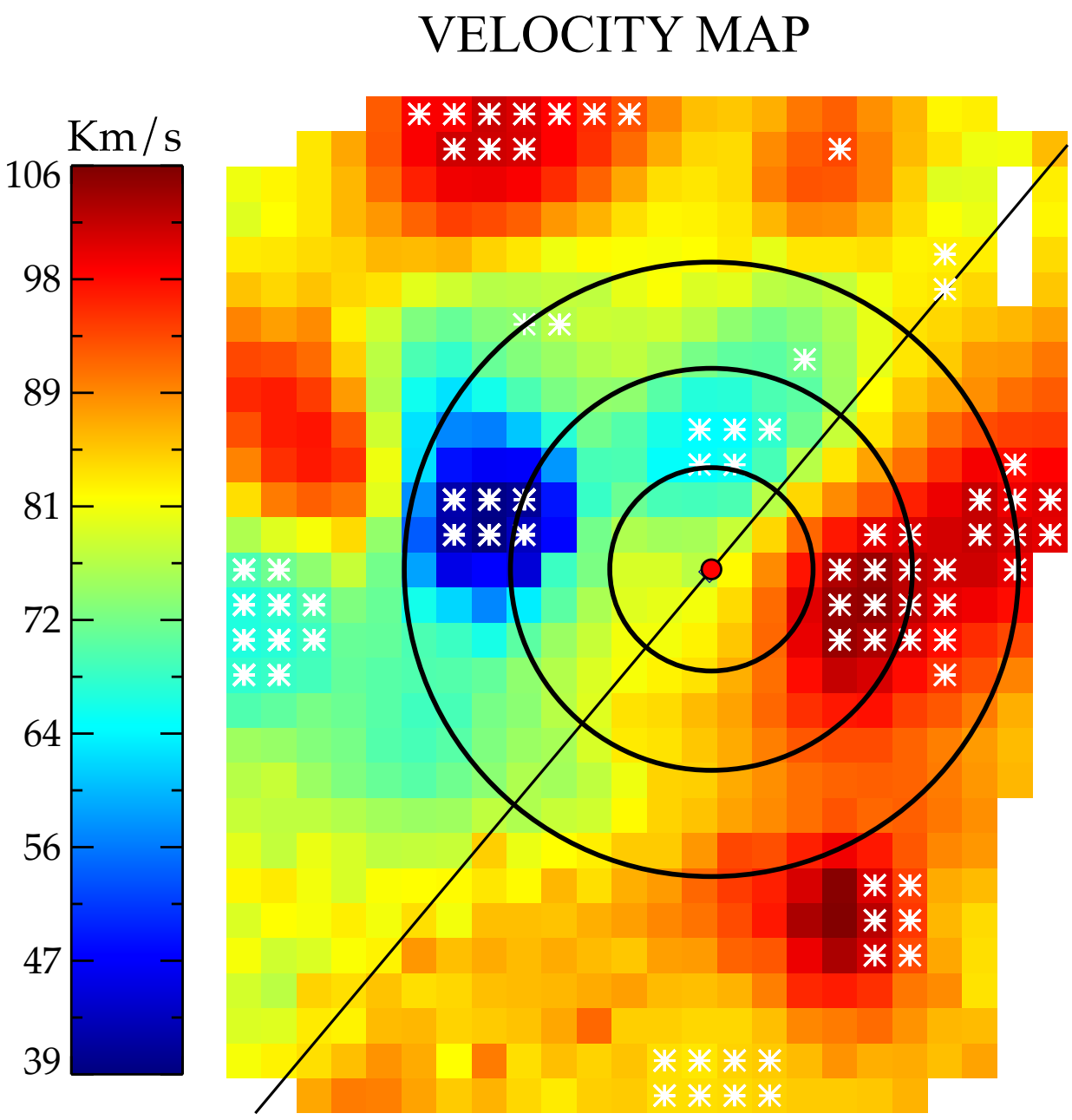

Figure 2.7: Velocity map of NGC 6388. As shown on the velocity scale, the blue spaxels indicate approaching velocities and the red ones receding. The white stars mark the spaxels which we excluded from the velocity dispersion measurement as they might suffer from shot noise. Also shown are the first three velocity dispersion bins to help visualize the binning method.

with a peculiar velocity dominating their environment and with their light contaminating neighboring spaxels. Therefore, we tested the influence of each star on the adjacent spaxels. This allowed us to test if the derived velocity dispersion is representative of the entire population at a given radius or whether it is biased by a low number of stars, i.e. dominated by shot noise.

To perform this test, we considered our photometric catalog (described in section 3.2) for the field of view covered by the ARGUS pointings. At every position of a star in the catalog, a two dimensional Gaussian was modeled with a standard deviation set to the seeing of the ground based observations (FWHM = 0.9″) and scaled to the total flux of the star. The next step was to measure the absolute amount and fraction of light that each star contributes to the surrounding spaxels. After computing these values for every star in the pointing, we had the following information for each spaxel: a) how many stars contribute to the light of that spaxel, and b) which fraction of the total light is contributed by each star, i.e. we determined whether the spectrum in a given spaxel was dominated by one or a few stars. The test showed that most of the spaxels contained meaningful contributions by more than 10 stars. Some spaxels, however, were dominated by a single star contributing more than 50 % to the spaxel's light. For this reason, the contribution in percent of the brightest star was also derived by the program. We found out that the blue area in the left side of the velocity map of Figure 4.1 is not due to a single star. In fact this area in the velocity map corresponds to a group of at least 10 stars moving with 10 - 40 $\mathrm{km\,s^{-1}}$ with respect to the cluster systemic velocity.

2.4.3 Velocity-dispersion profile

To derive a radial velocity-dispersion profile for the stellar population of NGC 6388 it is necessary to bin the spectra accordingly. We divided the pointing into six independent angular bins, each of them with the same width of three ARGUS spaxels (0.9″, 0.04 pc). To check the effect of the distribution of the bins on the final result, we tried different combinations of bins and bin distances as well as overlapping bins. We found no change in the global shape of the profile when using different bins. Therefore the choice of the bins was not critical, but in order to make an accurate error estimation, independent bins are more useful.

In each bin, all spectra of all exposures where combined with a sigma clipping algorithm to remove any remaining cosmic rays. Velocity and velocity-dispersion profiles were computed using the pPXF method applied to the binned spectra. The velocity map in Figure 4.1 shows the dynamics in the cluster center. A rotation-like or a shearing signature is visible, but it seems to be a very local phenomenon (within 3″, 0.15 pc). In earlier attempts, we split the pointing in two halves (tilted line in figure 4.1) in order check for consistency and symmetry on both sides. The velocity dispersion was then derived separately for the binned spectra on each side. Both sides show a rise in the velocity-dispersion profile but differ in their

Table 2.3: Moments of the velocity distribution of NGC 6388.

log r [arcsec]	V [km/s]	V_{RMS} [km/s]	$h3$	$h4$
-0.05	-1.6 ± 2.9	23.3 ± 3.1	-0.05 ± 0.16	-0.16 ± 0.13
0.26	-2.2 ± 0.6	25.7 ± 1.8	-0.07 ± 0.01	-0.10 ± 0.01
0.43	-0.1 ± 0.6	24.0 ± 1.3	-0.08 ± 0.02	-0.07 ± 0.02
0.56	2.9 ± 0.6	22.2 ± 1.1	-0.09 ± 0.02	-0.09 ± 0.02
0.65	6.4 ± 0.6	20.5 ± 0.9	-0.08 ± 0.02	-0.07 ± 0.02
0.78	4.6 ± 0.8	18.6 ± 0.8	-0.03 ± 0.04	-0.01 ± 0.03
1.04	3.5 ± 0.8	16.8 ± 2.9	-0.12 ± 0.03	-0.14 ± 0.02
1.26	6.7 ± 1.0	13.6 ± 2.9	-0.07 ± 0.04	-0.03 ± 0.04

shape and absolute values from each other. However, treating both sides separately would not properly take into account a possible rotation at the center and therefore not exactly represent the observed data. We decided to use the total radial profile over the 360 degree bins and measure the second moment $V_{RMS} = \sqrt{{V_{rot}}^2 + \sigma^2}$, with the rotation velocity V_{rot} and the velocity dispersion σ. The reason why we chose to analyze V_{RMS} instead of σ is twofold. First, the Jeans models require the V_{RMS} rather than the pure velocity dispersion as an input. Second, the broadening of the line we measured represents V_{RMS} and not σ. The velocity dispersion can be obtained by subtracting the rotation velocity from this quantity. Determining the rotation is difficult due to the large shot noise introduced by the small number of spatial elements in the central region. The second moment, however, is robustly measured since we average over all angles. For simplicity we refer to the V_{RMS} profile as the velocity-dispersion profile in our study.

In addition to the central pointings, we derived kinematics for regions further out using the small IFU measurements, which were scattered at larger radii around the cluster. Unfortunately, the surface brightness of the cluster drops quickly with radius resulting in a low signal-to-noise ratio for the IFUs most distant from the center. These could therefore not be used for further analysis. Only the two innermost positions showed reasonable signal, so that these two pointings could be used as two separated data points at 11″ and 18″ radius, respectively. The disadvantage of the small IFU fields (20 spaxels for a total field-of-view of $3'' \times 2''$) is that these values are very affected by shot noise since only a few stars fall into the small field-of-view. Consequently, these points show larger errors than the rest of the profile.

Further, we estimated the radial velocity of the cluster in the heliocentric reference frame. We combined all spectra in the pointing and measured the velocity relative to the velocity of the template. This value was then corrected for the motion of the template and the heliocentric velocity and results in a value of $V_r = (80.6 \pm 0.5)\ \mathrm{km\,s^{-1}}$ which is in good agreement with the value from Harris (1996) $V_r = (81.2 \pm 1.2)\ \mathrm{km\,s^{-1}}$.

We ran Monte Carlo simulations to estimate the error on V_{RMS} due to shot noise. From the routine described in section 2.4.2, we knew exactly how many stars are contributing (*nStars*) and how many spaxels are summed (*nSpax*) in each bin. We took all stars detected in each bin and their corresponding magnitude. Each of the stars was then assigned a velocity chosen from a Gaussian velocity distribution with a fixed dispersion. We used our template spectrum and created *nSpax* spaxel by averaging *nStars* flux weighted and velocity shifted spectra. The resulting spaxels were then normalized, combined and the kinematics measured with pPXF (as for the original data). After 1000 realizations for each bin, we obtained the shot noise errors from the spread of the measured velocity dispersions. For the outer IFU pointings, we extrapolated the surface density to larger radii and performed the same Monte Carlo simulations as for the inner pointing, with random magnitudes drawn from the magnitude distribution in this region. The errors for the velocity and the higher moments were derived by applying Monte Carlo simulations to the spectrum itself. This was done by repeating the measurement for 100 different realizations of data by adding noise to the original spectra. (see Cappellari & Emsellem 2004, section 3.4)

The resulting profile is displayed in Figure 2.8. The plot shows the second moment of the velocity distribution V_{RMS}. Except for the innermost point, a clear rise of the profile towards the center is visible. The highest point reaches more than 25 $\mathrm{km\,s^{-1}}$ before it drops quickly below 20 $\mathrm{km\,s^{-1}}$ at larger radii. In table 3.3 we list the results of the kinematic measurements. The first column lists the radii of the bins. The following columns show the central velocities of each bin in the reference frame of the cluster, the second moment V_{RMS} as well as higher velocity moments h3 and h4. It is conspicuous that all h4 moments tend to have negative values. This hints at a lack of radial orbits in the central region of the globular cluster.

For general purposes we also determined the effective velocity dispersion σ_e as described in Gültekin et al. (2009). This is defined by:

$$\sigma_e^2 = \frac{\int_0^{R_e} \mathrm{V_{RMS}^2\, I(r)\, dr}}{\int_0^{R_e} I(r)\, dr} \tag{2.4}$$

Where R_e stands for the half light radius ($\sim 40''$) and $I(r)$ the surface brightness profile. We extrapolated our kinematic data to the half light radius since our furthest out data point only reaches a radius of $18''$. This results in an effective velocity dispersion of $\sigma_e = (18.9 \pm 0.3)$ $\mathrm{km\,s^{-1}}$ which is in perfect agreement with the value derived by Pryor & Meylan (1993) listed in table 2.1.

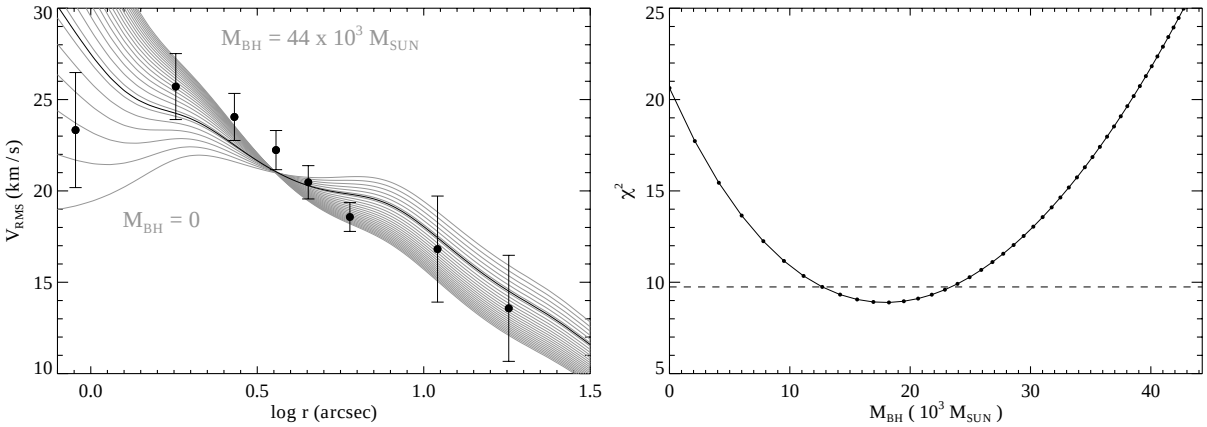

Figure 2.8: Different isotropic ($\beta = 0$ fixed) Jeans models applied to the kinematic data from our pointing. The M/L is fitted to the data by scaling the profile to the data points. The final values are obtained by finding the minimum of χ^2 while varying the black-hole mass: $\beta = 0.0$, $M_{BH} = 18.24 \times 10^3 M_\odot$, $M/L_V = 1.65$, $\chi^2_{min} = 8.89$. The plot on the left panel shows the models together with the data and the best fit. Labeled are also the black holes masses of the two enclosing models. The solid black line marks the best fit. The right panel shows the χ^2 values of every model as well as the $\Delta\chi^2 = 1$ line (dashed line).

2.5 Dynamical models

The main goal of this work is to compare the derived kinematics and light profile with a set of simple analytical models in order to test whether NGC 6388 is likely to host an intermediate-mass black hole in its center. We used Jeans models as implemented and described in Cappellari (2008).

2.5.1 Isotropic and anisotropic models

The first input for the Jeans models is the surface brightness profile in order to estimate the 3-D density distribution in the cluster. Given the fact that the density can only be observed in a projected way, the profiles have to be deprojected. One way of doing this is by applying the multi-Gaussian expansion (MGE) method developed by Emsellem et al. (1994). The basic approach of this method is to parametrize the projected surface brightness with a sum of Gaussians since the deprojection of a Gaussian function results again in a Gaussian.

To apply this parametrization and to compare results of the Jeans equation to our data, we used the Jeans Anisotropic MGE (JAM) dynamical models for stellar kinematics of spherical and axisymmetric galaxies, as well as the multi-Gaussian expansion implementation developed by Cappellari (2002, 2008). The IDL routines provided by M. Cappellari[2] enable

[2]Available at http://purl.org/cappellari/idl

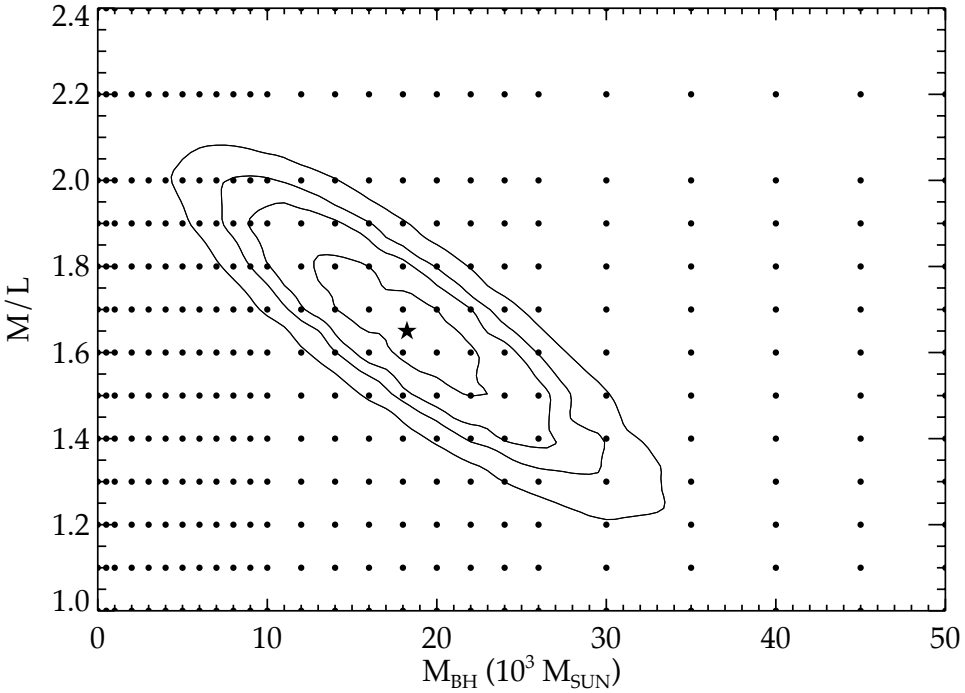

Figure 2.9: Contours of the χ^2 as a function of black-hole mass and mass-to-light ratio. Each point represents a particular isotropic model. The plotted contours are $\Delta\chi^2 = 1.0, 2.7, 4.0$ and 6.6 implying a confidence of 68, 90, 95 and 99 percent.

the modeling of the surface brightness profile and fitting the observed velocity data and the mass-to-light ratio at the same time. We used our surface brightness profile in combination with a spherical model with different values of anisotropy and constant M/L_V setups along the radius of the cluster.

In Figure 2.8, we plot the isotropic model data comparison for our velocity-dispersion profile. The JAM program does not actually fit the model to the data but rather calculates the shape of the second moment curve from the surface brightness profile, deconvolves the profile with the PSF of the IFU observations, and then scales it to an average value of the kinematic data in order to derive the M/L_V. This explains why all trial models meet in one point. The thick black line marks the model with the lowest χ^2 value and therefore the best fit.

With the given surface brightness profile and without a central black hole, the models predict a drop in velocity dispersion towards the central region. As a final result, we used the χ^2 statistics of the fit to estimate an error. This results in: $M_\bullet = (18 \pm 6) \times 10^3 M_\odot$ and $M/L_V = (1.7 \pm 0.2)\ M_\odot/L_\odot$. Figure 2.9 shows the contour plot of χ^2 as a function of black-hole mass and mass-to-light ratio over a grid of isotropic models (black points). The contours represent $\Delta\chi^2 = 1.0, 2.7, 4.0$ and 6.6 which correspond to a confidence of 68, 90, 95 and 99 percent for 1 degree of freedom (marginalized). This implies that for an

isotropic model and this specific surface brightness profile the models predict a black hole of at least $M_\bullet = 5 \times 10^3 M_\odot$ with a confidence of 99 percent.

We also tested whether anisotropic Jeans models would result in a significantly better fit. To do this, we repeated the model fitting with $\beta \neq 0$ values. We found a decrease of χ^2 for a rising β down to $\chi^2 = 4.21$ for $\beta = 0.5$ with a lower black-hole mass of $M_\bullet = 5.3 \times 10^3 M_\odot$. However, this requires a very high anisotropy of $\beta = 1 - \overline{V_\vartheta^2}/\overline{V_r^2} = 0.5$ which is expected to be unstable in the center of a relaxed globular cluster such as NGC 6388. The anisotropy will be discussed in more detail in section 2.5.3.

2.5.2 Error estimation

In section 5.2.3 we introduced the different surface brightness profiles for NGC 6388. The Trager et al. (1995) profile contains the most data points and extends to large radii ($\sim 4'$). However, the inner regions (important for our dynamical purposes) are not as well sampled by the ground based observations used by Trager et al. The profile by NG06 was derived by measuring integrated light on a WFPC2 image using a bi-weight estimator and covers the inner regions of the cluster very well. To calibrate the profiles to the correct absolute values NG06 also adjusted it to the Trager et al. profile. The third profile was obtained by Lanzoni et al. (2007) by computing the average of the counts per pixel in each bin of their ACS/HRC images. Since it was not clear in the paper how they calibrated their photometry, this profile was also shifted (by a small amount of 0.09 mag) to overlap with the Trager et al. profile. As a test, we used each of these profiles as an input for the Jeans models and found similar black-hole masses varying from $M_\bullet = (25 \pm 6) \times 10^3 M_\odot$ for the Trager et al. (1995) profile to $M_\bullet = (11 \pm 5) \times 10^3 M_\odot$ for the Lanzoni et al. (2007) data. The result from the profile provided by NG06 is identical to the fit of our profile in black-hole mass and slightly lower in the mass-to-light ratio ($M/L_V = (1.5 \pm 0.2)\ M_\odot/L_\odot$). Again we find the lowest χ^2 value (and therefore the best fit) for an anisotropic model of $\beta = 0.5$. In this case the observations can be explained without any black hole for all profiles. As mentioned in the previous section this rather unlikely configuration will be discussed in more detail in the next subsection.

From our studies of the surface brightness profiles, we see that they yield similar, but not identical results. The shape of the SB profile predicts the shape of the velocity-dispersion profile. Therefore, it is crucial to test the effect of variation of the surface brightness profile in the inner regions. To perform this, we run Monte Carlo simulations on the six innermost points of the profile. We used 1000 runs and a range of β between -0.5 and 0.5. The results are displayed in figure 2.10. The black points mark the mean value of the derived black-hole masses. The shaded contours represent the 68, 90 and 95 percent confidence limits. The mean black-hole mass decreases at higher β values since a radial anisotropy can mimic the effect of a central black hole. Nevertheless, for an isotropic case, we have a black hole detection within a mass range of $17^{+8}_{-7} \times 10^3 M_\odot$ and a global mass-to-light

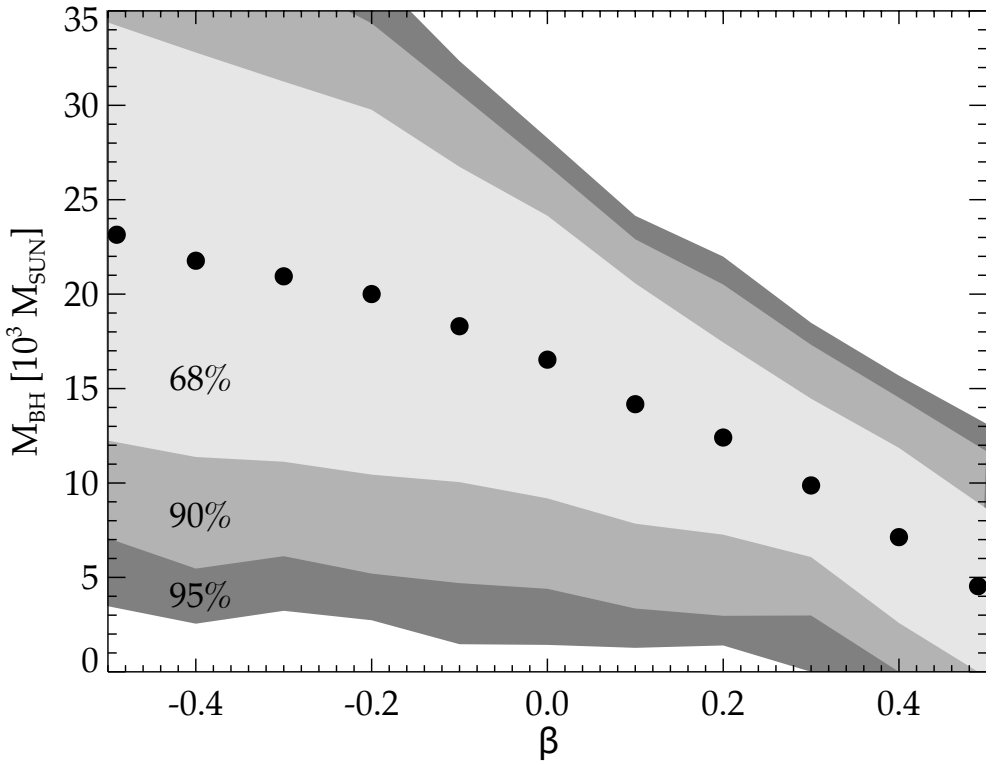

Figure 2.10: Result of the Monte Carlo simulations of the surface brightness profile. For each fixed β value 1000 realizations of the light profile have been performed. The black dots mark the average value of the best fit black-hole mass. The shaded contours represent the 68, 90 and 95 percent confidence limits.

ratio of $M/L_V = 1.6^{+0.2}_{-0.2}\ M_\odot/L_\odot$ (errors are the 68 percent confidence limits). We derived the total error (resulting from kinematic and photometric data) by again, running Monte Carlo simulations and varying both, the velocity-dispersion profile and the surface brightness profile at the same time. As a final result for the uncertainties of our method we derived $\delta M_\bullet = 9 \times 10^3 M_\odot$, $\delta M/L_V = 0.3\ M_\odot/L_\odot$. This shows, that a significant percentage of the error ($\sim 75\%$) in the context of isotropic Jeans models results from the uncertainties of the surface brightness profile.

2.5.3 Anisotropy in relaxed globular clusters

In the previous sections we have shown, that the strong significance for a black hole with isotropic models vanishes when using anisotropic models. The anisotropic Jeans models show a better fit for a model with much lower black-hole masses or without a black hole requiring an anisotropy of $\beta = 0.5$ or higher. Thus, it is necessary to investigate the probability of such a kinematic configuration in our cluster. We run N-body simulations for 30000 equal-mass stars, distributed according to a Plummer model. The initial anisotropy

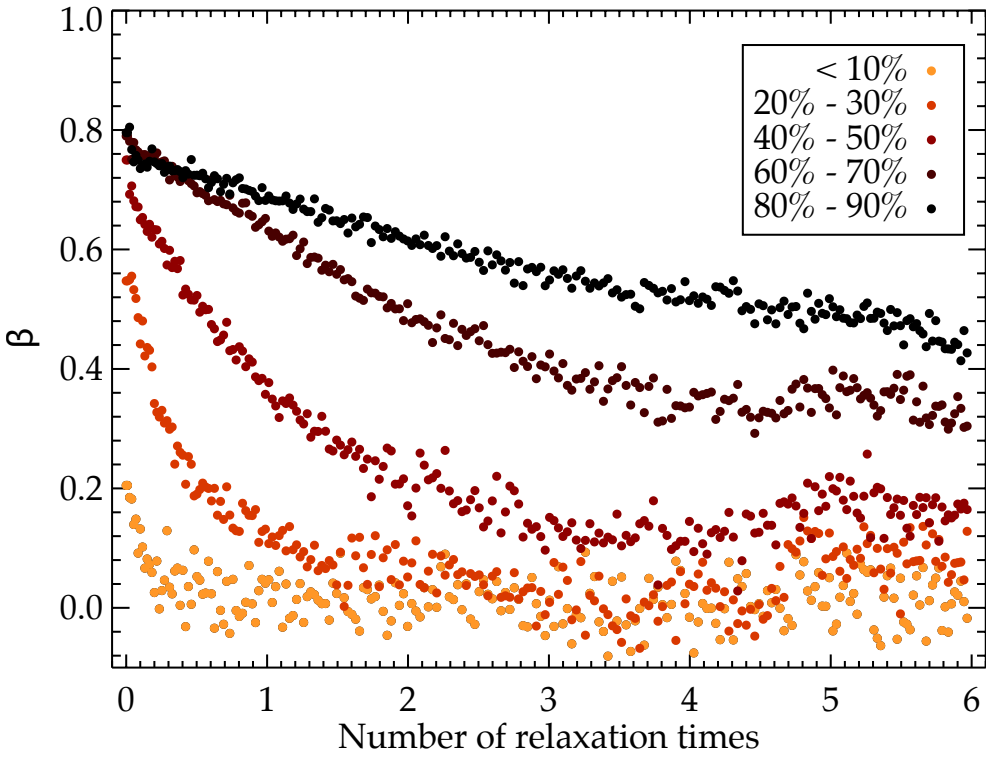

Figure 2.11: Anisotropy β as a function of time for different regions in the cluster. The different colors represent different percentages of the cluster total light/mass going from the inner part of less than 10% to the outskirts of the cluster with 90% light/mass enclosed.

was created by a cold collapse, which resulted in a cluster that was slightly anisotropic in its core and had increasing anisotropy further out rising to $\beta = 0.9$ outside the half-mass radius. Furthermore, we took the tidal field of the galaxy into account by letting the cluster move on a circular orbit around a point-mass galaxy. The ratio between tidal radius and core radius was set to 1:10 as it is the case for most globular clusters as well as for NGC 6388. We then let the cluster evolve over a time scale of several relaxations times and calculated the anisotropy for snapshots of the model.

Figure 2.11 shows the result of these tests. The different colors represent different areas in the cluster. Important for our case are the kinematics inside the half-light radius (curves with $< 50\%$ light/mass enclosed in figure 2.11). The system relaxes very quickly in the central regions. After six relaxation times the inner regions of the cluster are almost isotropic with β values below 0.2. The relaxation time of NGC 6388 is of order $10^9 yrs$ (at the half-mass radius, Harris 1996) which implies that the cluster is about 10 relaxation times old. This shows, that high anisotropies (such as the the ones needed from our best fit models) in NGC 6388 are not stable and would have vanished over a short time scale. Therefore, we limit our discussion to the results from our isotropic models.

2.5.4 Remaining concerns

In our analysis we used the assumption of a constant M/L_V for the entire cluster. In reality, this ratio can vary with radius and it may not be well described with a single value if the cluster is mass segregated. The rise in the velocity-dispersion profile could then be mimicked by a dark remnant cluster at the center. Such a scenario is expected in core collapsed clusters which display surface brightness profiles with logarithmic slopes of -0.8 or higher (Baumgardt et al. 2005). We looked at the deprojected light-density and mass-density profiles resulting from the surface brightness profile and the velocity-dispersion profile. The mass-density profile from the kinematics drops with $\propto r^{-2}$ which would be expected from a core collapsed cluster. But the light profile is shallow and does not support that hypotheses: with a concentration of $c = 1.7$ and a logarithmic slope of the surface brightness profile of $\alpha = -0.28 \pm 0.08$ NGC 6388 does not show any signs of core collapse in the distribution of the visible stars. We compared these profiles with simulated core collapsed or mass segregated clusters (described in Baumgardt & Makino 2003) and were not able to find a good agreement with either shape of the light profile or slope of the mass density of the cluster. We currently consider the presence of a dark remnant cluster unlikely but we will perform detailed n-body simulations with a variable M/L in the near future.

2.6 Summary and conclusions

We derived the mass of a potential intermediate-mass black hole at the center of the globular cluster NGC 6388 by analyzing spectroscopic and photometric data. With a set of HST images, the photometric center of the cluster was redetermined and the result of NG06 confirmed. Furthermore, a color magnitude diagram as well as a surface brightness profile, built from a combination of star counts and integrated light, were produced. The spectra from the ground-based integral-field unit ARGUS were reduced and analyzed in order to create a velocity map and a velocity-dispersion profile. In the velocity map, we found signatures of rotation or at least complex dynamics in the inner three arcseconds (0.15 pc) of the cluster. We derived a velocity-dispersion profile by summing all spectra into radial bins and applying a penalized pixel fitting method.

Using the surface brightness profile as an input for spherical Jeans equations, a model velocity-dispersion profile was obtained. We ran several isotropic models with different black-hole masses and scaled them to the observed data in order to measure the mass-to-light ratio. Using χ^2 statistics, we were able to find the model which fits the observed data best. We run Monte Carlo simulations on the inner points of the surface brightness profile in order to estimate the errors resulting from the particular choice of a light profile. From this, we determined the black-hole mass and the mass-to-light ratio as well as the scatter of these two results. The final results, with 68% confidence limits are: A black-hole mass of $(17 \pm 9) \times 10^3 M_\odot$ and a global mass-to-light ratio of $M/L_V = (1.6 \pm 0.3)\ M_\odot/L_\odot$. In

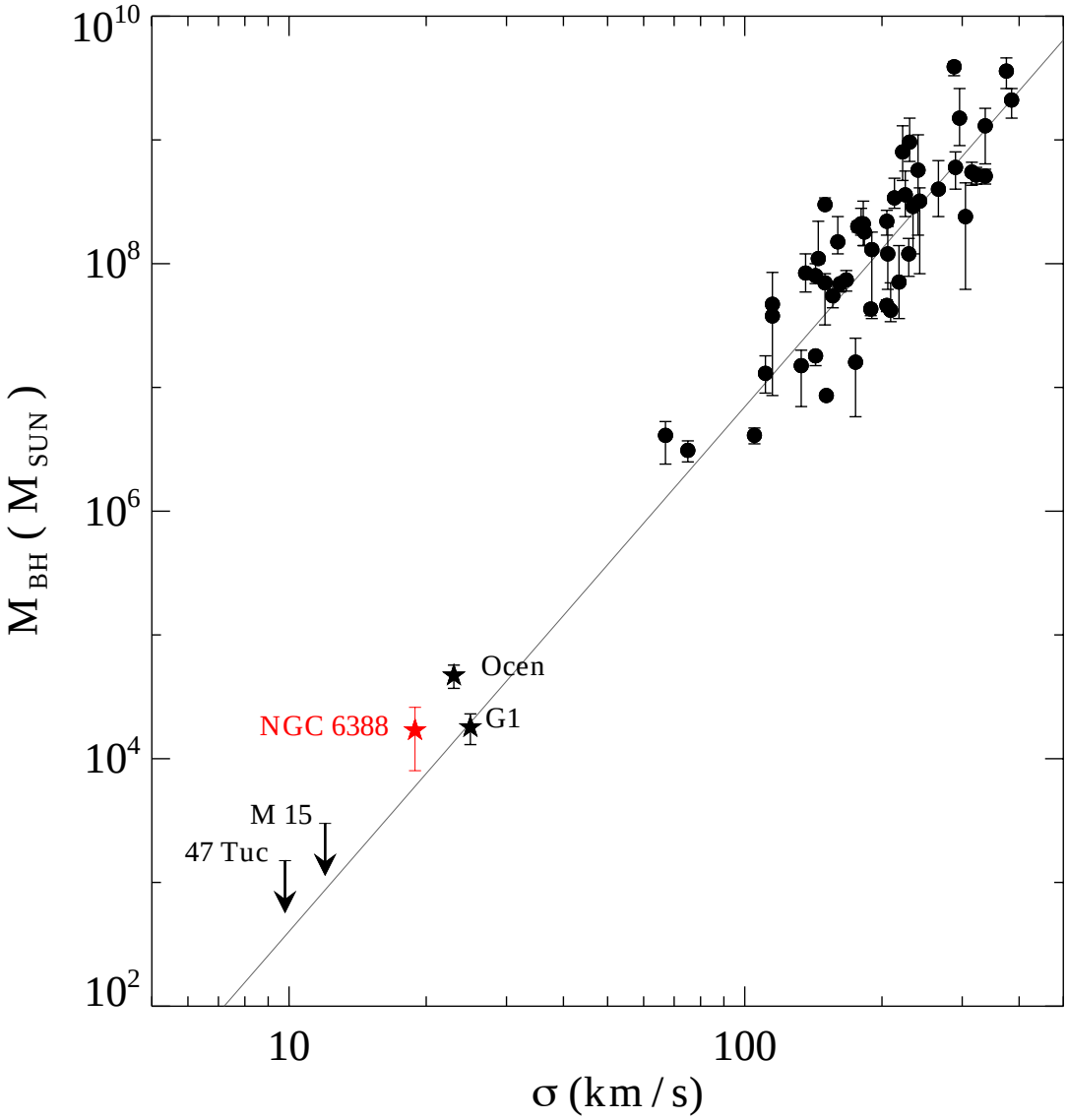

Figure 2.12: The $M_\bullet - \sigma$ relation for galaxies at the high mass range (filled circles) and the first globular clusters with potential black hole detection (filled stars). The slope of the line $\log(M_\bullet/M_\odot) = \alpha + \beta \log(\sigma/200\mathrm{km\,s^{-1}})$ with $(\alpha, \beta) = (8.12 \pm 0.08, 4.24 \pm 0.41)$ was taken from Gültekin et al. (2009). The mass of the black holes of ω Centauri, G1 and the upper limits of M15 and 47 Tuc were obtained by Noyola et al. (2010), Gebhardt et al. (2005), van den Bosch et al. (2006) and McLaughlin et al. (2006), respectively. Overplotted is the result of NGC 6388 with our derived effective velocity dispersion $\sigma_e = 18.9$ km s^{-1}.

addition, we run anisotropic models. The confidence of black hole detection is decreasing rapidly with increasing radial anisotropy. However, using N-body simulations, we found that in a relaxed cluster such as NGC 6388 an anisotropy higher than $\beta = 0.2$ inside the half mass radius will be erased within a few relaxation times.

With respect to the black-hole mass estimate of $5.7 \times 10^3\ M_\odot$ by Lanzoni et al. (2007), which they derived from photometry alone, our derived black-hole mass is larger by a factor of three with our surface brightness profile profile. Using their light profile, we obtained a black-hole mass of $M_\bullet = (11 \pm 5) \times 10^3 M_\odot$ which includes their value within one sigma error. Cseh et al. (2010) obtained deep radio observations of the inner regions of NGC 6388 and discussed different accretion scenarios for a possible black hole. They found an upper limit for the black-hole mass of $\sim 1500 M_\odot$ since no radio source was detected at the location of any Chandra X-ray sources. However, inserting our black-hole mass in equation 5 of Cseh et al. (2010) and using their assumptions as well as the Chandra X-ray luminosity of the central region, results in minimal but possible accretion rates and conversion efficiency ($\varepsilon\eta \sim 10^{-7}$). Considering the fact that supermassive black holes have masses not much higher than 0.2 % of the mass of their host systems (Marconi & Hunt 2003; Häring & Rix 2004), our mass with 0.9% seems to be higher than the predictions for larger systems. Globular clusters in contrast lose much of their mass during their evolution. This could naturally result in higher values of black-hole mass - host system mass ratios. Due to the complicated dynamics, the 1σ uncertainties are 40 % for our black-hole mass and 10 % for the derived M/L_V. Figure 2.12 shows the position of NGC 6388 in the black-hole mass velocity dispersion relation. With our derived effective velocity dispersion of $\sigma_e = (18.9 \pm 0.3)\ \mathrm{km\,s^{-1}}$ the results for NGC 6388 seem to coincide with the prediction made by the $M_\bullet - \sigma$ relation.

The mass-to-light ratio of $M/L_V = (1.7 \pm 0.3)\, M_\odot/L_\odot$ derived in this work is consistent within the error bars with the dynamical results of McLaughlin & van der Marel (2005, $M/L_V \sim 1.8$) but slightly lower than the value predicted by stellar population models. According also to McLaughlin & van der Marel (2005), we would expect a value of $M/L_V = (2.55 \pm 0.28)\, M_\odot/L_\odot$ for [Fe/H] $= -0.6$ dex and (13 ± 2) Gyr. Baumgardt & Makino (2003) have shown that dynamical evolution of star clusters causes a depletion of low-mass stars from the cluster. Since these contribute little light, the M/L_V value drops as the cluster evolves. Dynamical evolution could therefore explain part of the discrepancy between theoretical and observed M/L_V values.

Summarizing, it can be said that the globular cluster NGC 6388 shows a variety of interesting features in its photometric properties (e.g. the extended horizontal branch) as well as in its kinematic properties (e.g. the high central velocity dispersion or the rotation like signature in the velocity map). In this work we investigated the possibility of the existence of an intermediate-mass black hole at the center. With simple analytical models we were already able to reproduce the shape of the observed velocity-dispersion profile very well if the cluster hosts an IMBH. Future work would be to compute detailed N-body simulations of NGC 6388 in order to verify whether a dark cluster of remnants at the center would be an alternative.

Additionally, it is crucial to obtain kinematic data at larger radii to constrain the mass-to-light ratio and the models further out. Also proper motions for the central regions would further constrain the black hole hypothesis.

The study of black holes in globular clusters is currently limited to a handful of studies. For this reason, it is necessary to probe a large sample of globular clusters for central massive objects in order to move the field of IMBHs from “whether" to “under which circumstances do" globular clusters host them. Thus tying this field to the one of nuclear clusters and super-massive black holes. From the experience we gathered with NGC 6388, we can say that the dynamics of globular clusters is not as simple as commonly assumed and by searching for intermediate-mass black holes, we will also be able to get a deeper insight into the dynamics of globular clusters in general.

Acknowledgements: *This research was supported by the DFG cluster of excellence Origin and Structure of the Universe (www.universe-cluster.de). We also thank Nadine Neumayer for constructive feedback and inspiring discussions, Annalisa Calamida for her support in the photometric analysis and Giuseppina Battaglia for helping with the sky subtraction. H.B. acknowledges support from the Australian Research Council through Future Fellowship grant FT0991052. We thank the anonymous referee for constructive comments and encouraging further analysis concerning anisotropy and error estimation.*

CHAPTER 3

Central kinematics of the globular cluster NGC 2808: Upper limit on the mass of an intermediate-mass black hole

Nora Lützgendorf, Markus Kissler-Patig, Karl Gebhardt,Holger Baumgardt, Eva Noyola, Behrang Jalali, Tim de Zeeuw, and Nadine Neumayer
Astronomy & Astrophysics, Volume 542, id.A129 (2012)

Abstract We determine the central velocity-dispersion profile of the globular cluster NGC 2808 using VLT/FLAMES spectroscopy. In combination with HST/ACS data our goal is to probe whether this massive cluster hosts an IMBH at its center and constrain the cluster mass to light ratio as well as its total mass. We derive a velocity-dispersion profile from integral field spectroscopy in the center and Fabry Perot data for larger radii. High resolution HST data are used to obtain the surface brightness profile. Together, these data sets are compared to dynamical models with varying parameters such as mass to light ratio profiles and black-hole masses. Using analytical Jeans models in combination with variable M/L profiles from N-body simulations we find that the best fit model is a no black hole solution. After applying various Monte Carlo simulations to estimate the uncertainties, we derive an upper limit of the back hole mass of $M_{BH} < 1 \times 10^4\ M_\odot$ (with 95% confidence limits) and a global mass-to-light ratio of $M/L_V = (2.1 \pm 0.2)\ M_\odot/L_\odot$.

3.1 Introduction

Kinematics of globular clusters have long been a field of interest in observational and computational astronomy. In the last years, a new aspect, searching for the signature of central intermediate-mass black holes (IMBHs) was added to the picture. The specific mass range of black holes ($10^2-10^5 M_\odot$) had not been observed before and for a long time intermediate-mass black holes even thought not to exist. However, recent observations (eg. Gebhardt et al. 2000a; Gerssen et al. 2002; Gebhardt et al. 2005; Noyola et al. 2008, and Chapter 2)

have shown that the velocity-dispersion profiles of some globular clusters and dwarf galaxies are consistent with hosting a massive black hole at their center.

Numerical simulations have demonstrated (Portegies Zwart et al. 2004; Gürkan et al. 2004; Freitag et al. 2006) that intermediate-mass black holes can form in dense young star clusters by runaway merging. However, taking into account mass loss through stellar winds, Yungelson et al. (2008) found that super-massive stars with initial masses up to 1000 $M_{\odot}$ reduce to objects less massive than $\sim$ 150 $M_{\odot}$ by the end of their lives. An other scenario was presented by Miller & Hamilton (2002c) who discussed the formation of intermediate-mass black holes through mergers of stellar-mass black holes in globular clusters when starting with a $M \gtrsim 50$ $M_{\odot}$ seed black hole. Further, they presented scenarios for the capture of clusters by their host galaxies and accretion in the galactic disk in order to explain the observed bright X-ray sources. In addition, remnants of massive Population III stars could have formed intermediate-mass black holes in the early universe (Madau & Rees 2001).

If the velocity dispersion - black-hole mass scaling relation observed for supermassive black hole in galaxies (e.g. Ferrarese & Merritt 2000; Gebhardt et al. 2000a; Gültekin et al. 2009) holds at the lower end, intermediate-mass black holes would be expected in systems with velocity dispersions between 10-20 km/s like for globular clusters. Radio and X-ray detection of gas in the central regions is also employed either to provide a black hole mass estimate or an upper limit (e.g. Maccarone et al. 2005; Ulvestad et al. 2007; Bash et al. 2008; Cseh et al. 2010; Strader et al. 2012). While the current flux limits of Strader et al. (2012) are impressively low, in order to provide an upper limit on a possible black hole mass, they must make various assumptions about the gas accretion process. Some of the more uncertain assumptions include 1) the distribution of the gas, since a clumpy distribution will lead to time variability which significantly lowers the detection probability, 2) the efficiency of the accretion process, which may be particularly important if these systems are dominated by advection or convection, and 3) uncertainties in translating X-ray fluxes to bolometric fluxes to black hole masses. Thus, non-detection in X-ray and radio can be difficult to interpret in terms of a black hole mass upper limit.

So far the best candidates for hosting an IMBH are the most massive globular clusters in the local group. One of them is ω Centauri (NGC 5139) where Noyola et al. (2008, 2010) and Jalali et al. (2012) detect the kinematic signature of a 40 000 $M_{\odot}$ black hole based on radial velocities from integrated light. The results were however challenged by van der Marel & Anderson (2010), who find a lower value of the black-hole mass via HST proper motions. Jalali et al. (2012) perform N-body simulations and show that the current kinematic and light profile with respect to a kinematic center found in Noyola et al. (2010) are consistent with presence of a 5×10^4 $M_{\odot}$ IMBH assuming a spherical isotropic model for this cluster. Another good candidate is G1 in M31. It is the most massive globular cluster in the Local Group and is found to host a black hole of 20 000 $M_{\odot}$ (eg. Gebhardt et al. 2005) by kinematic measurements. In addition Pooley & Rappaport (2006); Kong (2007); Ulvestad et al. (2007) detected X-ray and radio emission at its center which is consistent with a black hole of the same mass.

A third good candidate is NGC 6388, a massive globular cluster in our Galaxy. In Chapter 2 we detected a rise in its central velocity-dispersion profile which is consistent with a black hole of $\sim$ 20 000 $M_{\odot}$ at its center. The understanding of the formation and evolution of intermediate-mass black holes is crucial for the understanding of the evolution and formation of supermassive black holes. Seed black holes are needed in order to explain the fast formation process of these massive black holes which are observed at very high redshift, i.e. at early times in the Universe Fan (2006). Intermediate-mass black holes formed in globular clusters and accreted by their host galaxy could be these seeds (eg. Ebisuzaki et al. 2001; Tanaka & Haiman 2009).

We chose to observe the globular cluster NGC 2808 as it shows a variety of interesting features. As known for some globular clusters by now, NGC 2808 has multiple stellar populations. So far only one other cluster (ω Centauri) shows more than two distinguishable populations (eq. Bedin et al. 2004). As observed by Piotto et al. (2007), NGC 2808 shows a triple main sequence, which indicates the existence of three sub-populations, all with an age of $\sim$ 12.5 Gyr, but with different metallicities. Also, its complex extended horizontal branch morphology (Harris 1974; Ferraro et al. 1990) shows puzzling discontinuities in the stellar distribution along its blue tail. Maccarone & Servillat (2008) analyze deep radio observations of NGC 2808 and found no sources detected within the core radius. This places an upper limit on a possible intermediate-mass black hole of $370-2100 M_{\odot}$ assuming a uniform gas density and the accretion rate to be different fractions of the Bondi rate. This limit can increase if one assumes even lower Bondi accretion rates or non-uniform gas content in the cluster.

Noyola & Baumgardt (2011) analyze N-body simulations of star clusters with and without central black holes. These reveal that the presence of an IMBH induces a shallow central cusp in the radial density profile. Hence, clusters showing shallow cusps are the best candidates for harboring an IMBH. Further, Miocchi (2007) investigate the effect of an IMBH on horizontal branch morphologies. A central black hole that strips enough stars of their outer envelope during close passages, could be one avenue for producing an extended horizontal branch (EHB). NGC 2808 displays a shallow cusp as well as an EHB, making it an excellent candidate for harboring a central black hole. Given its measured central velocity dispersion of $\sigma = 13.4$ km/s (Pryor & Meylan 1993) an extrapolation of the $M_{BH} - \sigma$ relation predicts a black-hole mass of $\sim 3 \times 10^3 M_{\odot}$. This translates into a radius of influence of $1'' - 2''$ at a distance of ~ 9.6 kpc, which would induce clear kinematic signatures inside the $\sim 12''$ core radius. Further main characteristics of NGC 2808 are listed in table 3.1.

This work aims at investigating whether the globular cluster NGC 2808 hosts an intermediate - mass black hole at its center. We first study the light distribution of the cluster. Photometric analysis, including the determination of the cluster center and the measurement of a surface brightness profile, is described in section 3.2. De-projecting this profile gives an estimate of the gravitational potential produced by the visible mass. The next step is to study the dynamics of the cluster. Section 4.5 summarizes our FLAMES observations and data reduction and section 3.4 describes the analysis of the spectroscopic data. With

Table 3.1: Properties of the globular cluster NGC 2808 from the references: NG=Noyola & Gebhardt (2006), H= Harris (1996) and PM=Pryor & Meylan (1993).

Parameter	Value	Reference
RA (J2000)	09h 12m 03s	NG
DEC (J2000)	-64° 51′ 49″	NG
Galactic Longitude l	282.19	H
Galactic Latitude b	-11.25	H
Distance from the Sun R_{SUN}	9.6 kpc	H
Core Radius r_c	12.4″	NG
Central Concentration c	1.77	H
Heliocentric Radial Velocity V_r	101.6 ± 0.7 km/s	H
Central Velocity Dispersion σ	13.4 km/s	PM
Metallicity [Fe/H]	-1.15 dex	H
Integrated Spectral Type	F7	H
Reddening E(B-V)	0.22	H
Absolute Visual Magnitude M_{Vt}	-9.39 mag	H

the resulting velocity-dispersion profile, it is possible to estimate the dynamical mass of the cluster. We then compare the data to Jeans models in section 3.5. Finally, we summarize our results, list our conclusions and give an outlook for further studies in section 3.6.

3.2 Photometry

The photometric data were taken from the archive of the Hubble Space Telescope (HST). They were obtained with the Wide Field and Planetary Camera 2 (WFPC2) in May 1998 (GO-6804, PI: F. Fusi Pecci) and are composed of a set of two exposures. The deep exposure dataset contains three images each in the filters I (F814W) and V (F555W) with exposure times of 120 and 100 s, respectively. In addition we use a set of two shallow images per filter with exposure times of 3 s in the I filter and 7 s in the V filter obtained in the same run. For both datasets the images cover the cluster center with the central 20″ on the PC chip. The data were calibrated using the WFPC2-specific calibration algorithm, as retrieved from the European HST-Archive (ST-ECF, Space Telescope European Coordinating Facility[1]).

[1]Based on observations made with the NASA/ESA Hubble Space Telescope, and obtained from the Hubble Legacy Archive, which is a collaboration between the Space Telescope Science Institute (STScI/NASA), the Space Telescope European Coordinating Facility (ST-ECF/ESA) and the Canadian Astronomy Data Centre (CADC/NRC/CSA).

3.2.1 Color magnitude diagram (CMD) of NGC 2808

The CMD is obtained using the programs *daophot II*, *allstar* and *allframe* by P. Stetson, applied to the HST images. For a detailed documentation of these routines, see Stetson (1987). These programs are especially developed for photometry in crowded fields and are therefore ideally suited for the analysis of globular clusters. For the description of the individual steps we refer to our previous paper (Chapter 2).

We obtain two catalogs with V and I magnitudes from the two datasets with different exposure times. We match and combine the catalogs using the routines *CataXcorr* and *CataComb* in order to obtain a complete star catalog over a wide magnitude range. All coordinates are transformed to the reference frame of the first I band image of the shallow exposure (*u4fp010br*). Figure 4.4 shows the final CMD with the positions of the brightest stars in the ARGUS pointing and the spectroscopic template stars (see section 4.5) overplotted.

3.2.2 Cluster center determination

A crucial step is the determination of the cluster's center. Precise knowledge of the center is important since the shape of the surface brightness and the angular averaged line-of-sight velocity distribution (LOSVD) profiles depend on the position of that center. Using the wrong center typically produces a shallower inner profile. Previous attempts have shown that the larger the core radius of the cluster, the more difficult it is to determine the exact position of the center. For example, the exact position of the center of the globular cluster ω Centauri is still under debate and differs by up to $12''$ in different analyses (e.g. Noyola et al. 2010; Anderson & van der Marel 2010). In contrast, NGC 6388, with a core radius 10 times smaller than ω Centauri, turned out to have a well defined center when applying various methods to determine the center of the cluster (Chapter 2).

Noyola & Gebhardt (2006, hereafter NG06) determined the center of NGC 2808 to be at $\alpha = 09{:}12{:}03.09$, $\delta = -64{:}51{:}48.96$ ($J2000$), with an uncertainty of $0.5''$, by minimizing the standard deviation of star counts in eight segments of a circle. NGC 2808 has a small core radius ($12''$) in comparison to ω Centauri (NG06; Noyola et al. 2010; Anderson & van der Marel 2010). In order to get an estimate of how accurately the center can be derived, we apply various routines to our catalog.

The field of view of our dataset is very small because we are limited to the $34'' \times 34''$ field of the PC ship. In such a small field of view, it is difficult to determine the center given the large errors arising from the Poisson statistics, i.e. shot noise. Also, if the core is extended, we might not be able to see the stellar concentration decreasing. However, we compensate for this by using different techniques and by estimating the error from their scatter. All techniques are applied for stars brighter than $m_V = 20$ in order to account for the incompleteness effect for faint stars.

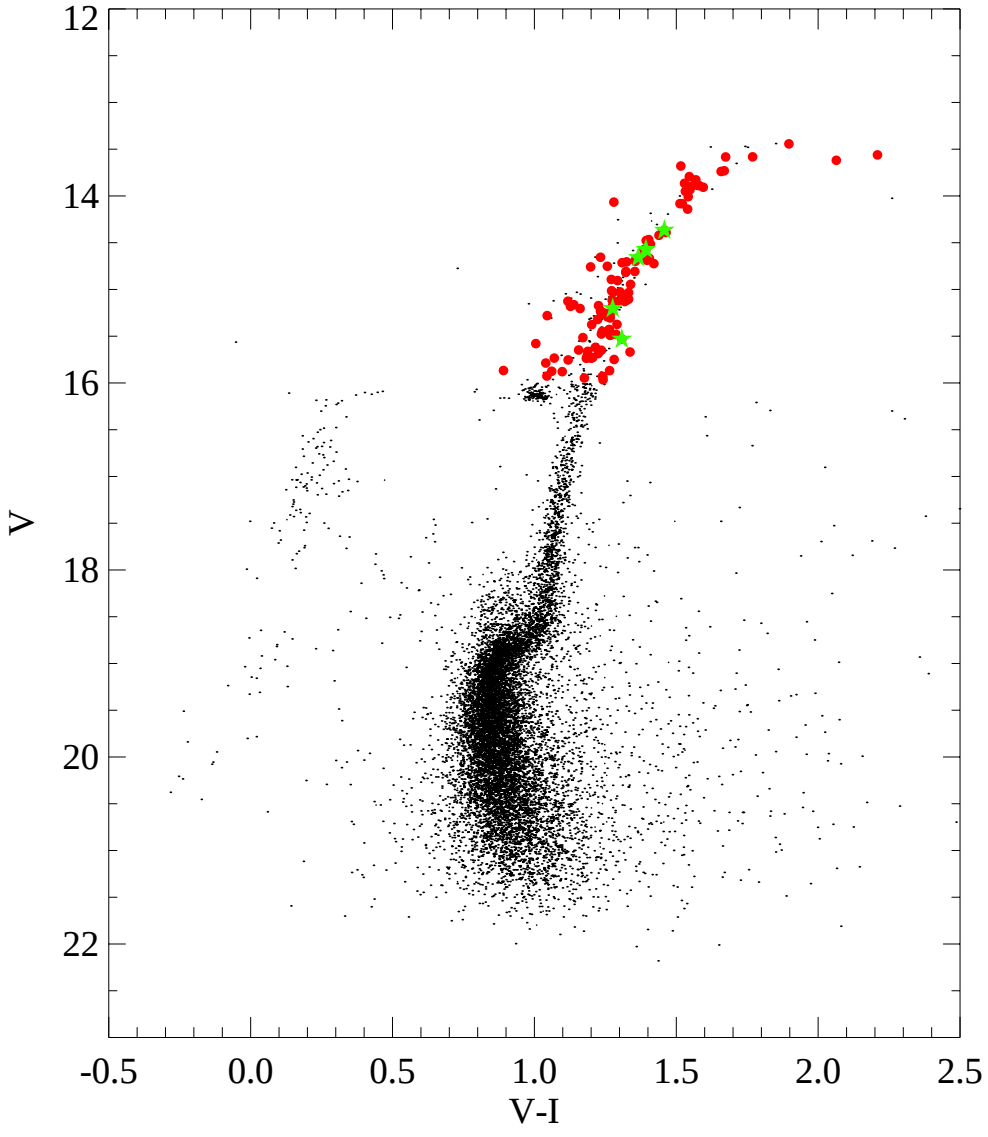

Figure 3.1: Color-magnitude diagram of NGC 2808. Overplotted are the brightest stars identified in the ARGUS field of view (red circles), and the used template stars (green stars).

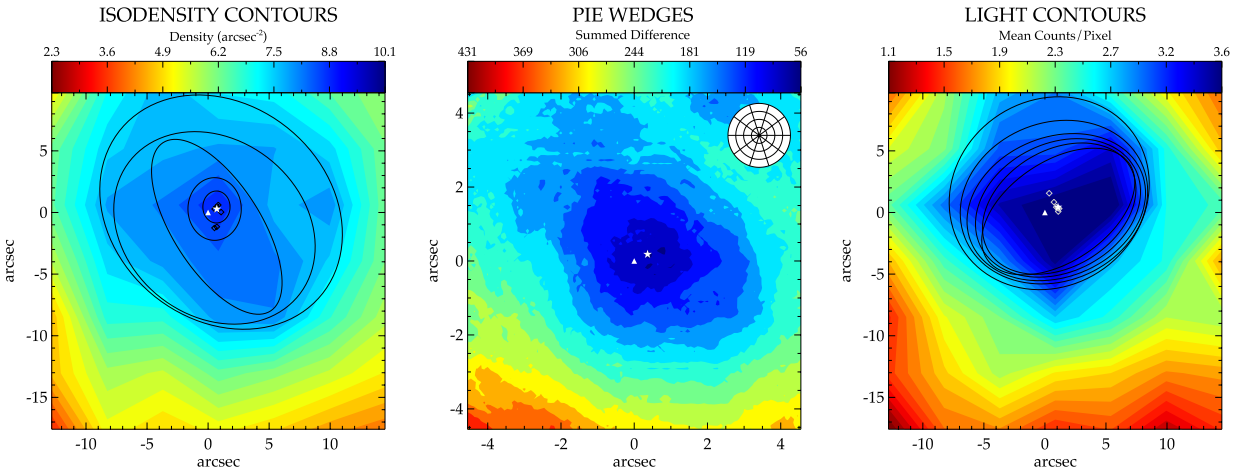

Figure 3.2: Method to determine the globular cluster center. Left, ellipses fitted to isodensity contours. Middle panel, the contours of the cumulative pie wedges method. The wedges are shown in the upper right of the plot. The right panel shows the contours of the pixel analysis of the mapped image. Contours in blue mark areas of either high stellar density in the left panel, high symmetry (i.e. low differences between the wedges) in the central panel or high light density in the right panel. In every plot the triangle marks the center adopted by NG06 and the white star the newly derived center.

The first technique uses isodensity contours as described in Anderson & van der Marel (2010). The field of view is divided into boxes of equal size of 100×100 pixels ($4.6'' \times 4.6''$). This size is the best compromise between having too few stars in each box and therefore large shot noise errors (boxes too small), and having not enough points and therefore a very noisy contour plot (boxes too large). The boxes contain about 100 stars on average. In each box, the stars are counted and the density is derived. The innermost isodensity contours, which were not disturbed by geometrical incompleteness are fitted by ellipses and their central points are determined. From the average of these points and their scatter we determine the central position and its error.

The second method is very similar to the one described in McLaughlin et al. (2006) and in Chapter 2. It uses a symmetry argument to determine the cluster center. In our field of view a grid of trial centers is created, using a grid spacing of 2 PC pixels ($\sim 0.1''$). Around each trial center, a circle is traced and divided into wedges as shown in Figure 3.2. In order to increase the number of stars, we vary the size of the circle depending on its position on the image. That is, the circle is always as big as the image borders allow it. The stars in each wedge are counted and the numbers compared to the opposite wedge. The differences in the total number of stars between two opposing wedges are summed for all wedge pairs and divided by the area of the circle. The coordinates that minimize the differences define the center of the cluster. We use different numbers of wedges from 4 to 16. We repeat the procedure by rotating the wedges so that their bisector is matching the x-y axis. This method is refined by comparing the cumulative stellar distribution of the

stars in the opposing wedges instead of the star counts alone.

The third and last method is based on the HST/WFPC2 image instead of the star catalog. This method computes the light distribution of the cluster. For this we map out the brightest stars with circular masks in order to prevent a bias towards these stars. We divide the resulting image into boxes of 100×100 pixel and derive the mean value of the counts per pixel in each box. From this we compute a contour plot and fit ellipses to determine the center. Despite our attempt to not get biased by the brightest stars, we find that in comparison to the previous two methods, the center obtained with the light distribution is shifted towards a clump of bright stars north-east of the center. However, due to its large errors it does not bias the final center position.

Figure 3.2 shows the contour plots of the different methods and Figure 3.3 presents a finding chart of our final center position. As a final result we obtain

$$(x_c, y_c) = (344.4, 441.6) \pm (9.9, 3.7) \text{ pixel} \tag{3.1}$$

$$\alpha = 09:12:03.107,\ \Delta\alpha = 0.5'' \text{ (J2000)} \tag{3.2}$$

$$\delta = -64:51:48.45,\ \Delta\delta = 0.2'' \tag{3.3}$$

which uses as reference image *u4fp010br*. We compared our result to the center obtained by NG06. The two centers are $0.32''$ apart and thus coincide within the error bars of $0.5''$ (as determined by NG06 performing artificial image tests). This center also coincides within $0.3''$ with the one derived by Goldsbury et al. (2010) using ellipse fitting applied to the density distribution on ACS/WFC images.

3.2.3 Surface brightness profile

The surface brightness (SB) profile is required as an input for the Jeans models described in the following section. As in Chapter 2 we use a simple method of star counts in combination with an integrated light measurement from the WFPC2 image to derive the SB profile. For our analysis we do not use stars brighter than $m_V = 17$ to avoid contamination by very bright stars in the center. The fluxes of all stars brighter than $m_V = 20$ are summed in radial bins around the center and divided by the area of the bin. In addition, the integrated light for stars fainter than $m_V = 20$ is measured directly from the HST image. Using the same radial bins as in the star count method, we measure the statistical distribution of counts per pixel excluding regions containing stars with $m_V < 20$ by mapping out these stars in the image using a circular mask with a radius of $0.3''$ (6 HST pixels). We use a robust bi-weight estimator to derive the mean counts-per-pixel for every bin. Finally, the flux per pixel is transformed into magnitudes per square arcseconds and added to the star count profile. Due to the small field of view of the PC chip we are only measuring points inside a radius of $10''$. The errors of our profile are obtained by Poisson statistics of the

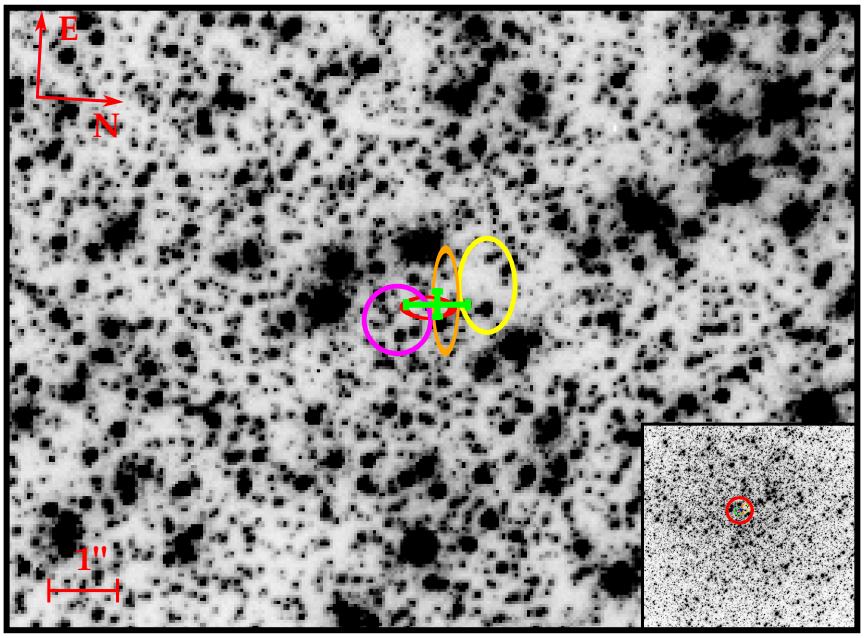

Figure 3.3: Finding chart for the center of NGC 2808. The magenta circle marks the center of NG06, the red ellipse the results from the pie wedges method, the orange ellipse is for the isodensity contour method and the yellow one shows the position and error of the method measuring the light distribution. The final adopted center and its error bar are displayed in green.

number of stars in each bin. With a linear fit to the innermost points ($r < 10''$) we derive a slope of the surface luminosity density $I(r) \propto r^{\alpha}$ of $\alpha = -0.16 \pm 0.08$. This value is steeper (but consistent within the errors) than the slope of $\alpha = -0.06 \pm 0.07$ derived by NG06. The final inner profile is listed in Table 3.2 and shown in Figure 3.4.

For the outer regions we use the profile obtained by Trager et al. (1995) for our spherical models and a two-dimensional profile obtained from ground based (2MASS) images (see Section 3.5.2) for the axisymmetric models. The two 2MASS images in J-band which cover the entire cluster were received from the public archive and combined to a single pointing. Using routines provided in the package of the anisotropic Jeans models we obtain a two-dimensional surface brightness profile by fitting isophotes to the image. The final profile is constructed by combining the inner profile obtained with the HST with the outer profile from the 2MASS image. Since the two images are taken in different bands, it is necessary to scale the images to a common flux. For this purpose we simply scale the data points of the 2MASS image to the HST profile. Here we neglect stellar population effects and assume a constant color within the cluster. Figure 3.4 shows the final combined profile with the minor and major axis of the two-dimensional profile colored in blue and red, respectively.

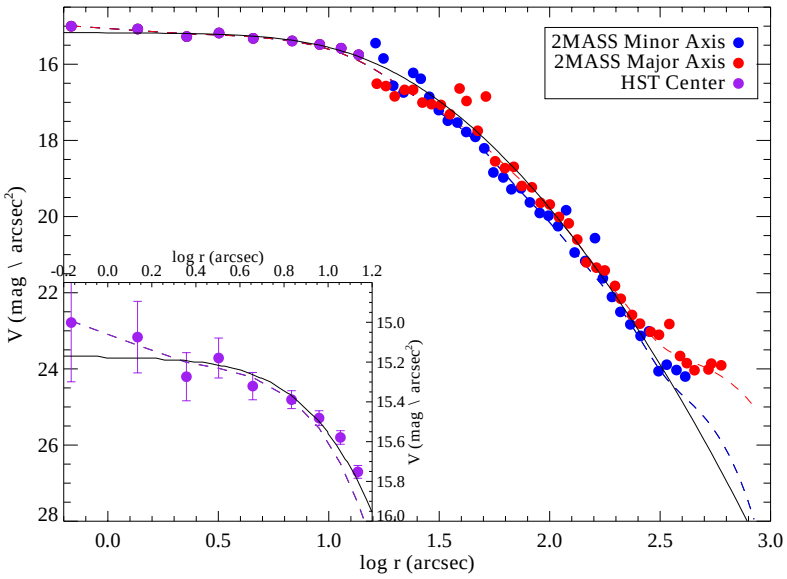

Figure 3.4: Surface brightness profile of NGC 2808. The red and the blue circles mark the measurements from the 2MASS image along the major and minor axis, respectively, as well as their MGE parametrization (dashed lines). The profile obtained from the HST star catalog is shown in purple. Overplotted is the profile obtained by Trager et al. (1995) with a solid black line.

3.3 Spectroscopy

The spectroscopic data were obtained with the GIRAFFE spectrograph of the FLAMES (Fiber Large Array Multi Element Spectrograph) instrument at the Very Large Telescope (VLT) using the ARGUS mode (Large Integral Field Unit). The observations were performed during two nights (2010-05-05/06). The ARGUS unit was set to the 1 : 1.67 magnification scale (pixel size: 0.52″, 14 × 22 pixel array) and pointed to six different positions, each of them containing three exposures of 600s with 0.5″ dithering to cover the entire core radius. The position angle of the integral field unit remained at 0 degrees (long axis parallel to the north-south axis) during the entire observation.

The kinematics are obtained from the analysis of the Calcium Triplet ($\sim 850\,\mathrm{nm}$), which is a strong feature in the spectra. The expected velocity dispersions lie in the range 5-20 $\mathrm{km\,s^{-1}}$ and had to be measured with an accuracy of 1-2 $\mathrm{km\,s^{-1}}$. This implied using a spectral resolution around 10 000, available in the low spectral resolution mode set-up LR8 ($820 - 940\,\mathrm{nm}$, R = 10 400).

We reduce the spectroscopic data with the GIRAFFE pipeline programmed by the European Southern Observatory (ESO). This pipeline consists of five recipes (*gimasterbias, gimasterdark, gimasterflat, giwavecalibration, giscience*) which are described in Chapter 2. From the input observations, the final routine *giscience* produces a reduced science frame as

Table 3.2: Derived surface brightness profile in the V-band. ΔV_h and ΔV_l are the high and low values of the errors, respectively

$\log r$ [arcsec]	V [mag/arcsec^2]	ΔV_l [mag/arcsec^2]	ΔV_h [mag/arcsec^2]
−0.17	15.00	0.30	0.24
0.14	15.07	0.18	0.16
0.36	15.27	0.12	0.11
0.50	15.18	0.10	0.09
0.66	15.32	0.07	0.06
0.83	15.39	0.04	0.04
0.96	15.48	0.04	0.04
1.06	15.58	0.03	0.03
1.14	15.75	0.03	0.03

well as the extracted and rebinned spectra frame. At the end, the recipe also produces a reconstructed image of the respective field of view of the ARGUS observations.

For sky subtraction, we use the program developed by Mike Irwin and described in Battaglia et al. (2008). The program combines all 14 sky fibers using a 3-sigma clipping algorithm and computes an average sky spectrum. It splits the continuum and the line components for both the averaged sky spectrum and the object spectrum, using a combination of median and boxcar. The sky-line mask and the line-only object spectra are compared finding the optimum scale factor for the sky spectrum and the sky-lines are subtracted from the object spectra. The continuum is added back to the object spectra after subtracting the sky continuum by the same scaling factor.

As a next step we use the program LA-Cosmic developed by van Dokkum (2001) to remove the cosmic rays from our spectra. In order to avoid bright stars dominating the averaged spectra when they are combined, we apply a normalization to the spectra by fitting a spline to the continuum and divide the spectra by it.

3.4 Kinematics

In this section we describe how we compute the velocity map in order to check for peculiar kinematic signals. Further, we measure the velocity-dispersion profile which is used to fit analytic models, described in the next section.

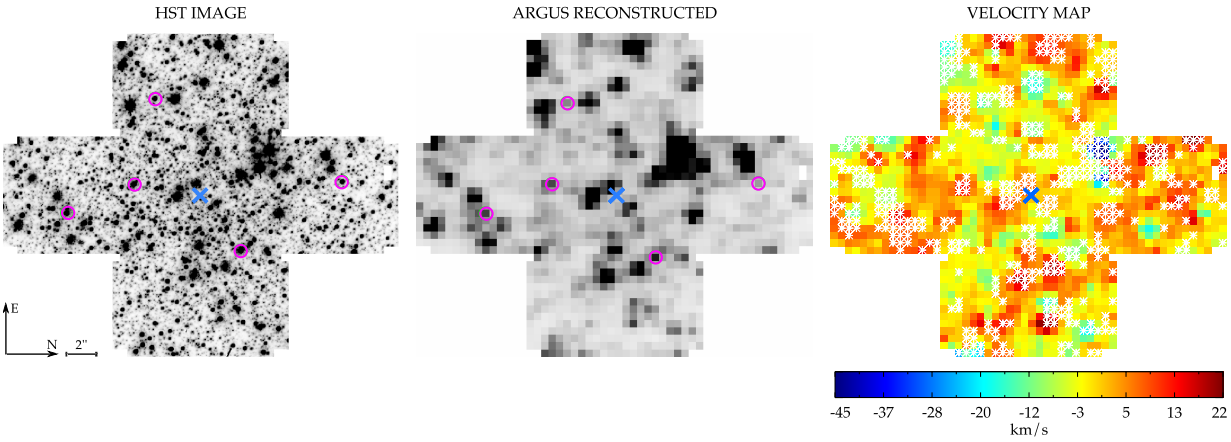

Figure 3.5: The velocity map of NGC 2808. Shown are the ARGUS field of view reconstructed on the WFPC2 image (left panel), the combined reconstructed ARGUS pointings (middle panel), and the resulting velocity map. Magenta circles mark the template stars used to derive the kinematics and the blue cross marks the center of the cluster. The white crosses on the velocity map mark the spaxel which are not used in deriving the velocity-dispersion profile.

3.4.1 Velocity map

To construct the velocity map, we use the relative shifts of the pointings to stitch them together and create a catalog with each spectrum correlated to one position in the field of view. The resulting catalog of spectra and their coordinates allow us to combine spectra in different bins. The combined pointing contains 54 $\times$ 44 spaxels and is cross shaped. We also reconstruct the ARGUS pointing on top of the HST image in order to obtain a direct connection between spaxel positions and our star catalog.

Using the penalized pixel-fitting (pPXF) program developed by Cappellari & Emsellem (2004), a velocity is derived for each spaxel. In regions of overlap the spectra are first averaged before being analyzed. Figure 4.1 shows a) the field of view of the six ARGUS pointings on the HST image, b) the reconstructed and combined ARGUS image and c) the corresponding velocity map. For every ARGUS pointing, an individual velocity map is derived. The velocities of overlapping spaxels are in agreement with each other to 1 km s^{-1}, which is expected as discussed in Chapter 2.

In order to test individual spaxels for shot noise, we apply the same routines as described in Chapter 2. At every position of a star in the catalog, a two dimensional Gaussian is modeled with a standard deviation set to the seeing of the ground based observations (FWHM = 0.8″) and scaled to the total flux of the star. We measure the absolute amount and fraction of light that each star contributes to the surrounding spaxels. For each spaxel we then have the following information: a) how many stars contribute to the light of that spaxel, and b) which fraction of the total light is contributed by each star. The test shows that NGC 2808 is less concentrated in the center than NGC 6388 (in fact NGC 6388 has 1.5 times the central stellar density of NGC 2808) and therefore fewer stars contribute to

individual spaxel. Also, more spaxels are dominated by a single star by 60 % or higher. As in the case of NGC 6388, we map out spaxels in which either less than 10 stars contribute to the light or a single star contributes more than 60 % of the light. This leaves us with 1080 spectra out of the 1514 spectra sample.

The velocity template used in the kinematic analysis is important to consider carefully given the strong changes in the intrinsic line widths in a globular cluster. In order to find an optimal velocity template we first collect all stars which dominate a spaxel by more than 80% via the shot noise routine described above. We plot these stars on our CMD in order to check for non-cluster members. We choose the five faintest stars and combine them after shifting them to the same velocity. We also try kinematic fits with individual stars with high signal-to-noise from the upper giant branch. We do not find as good a fit to the integrated light using the stars from the upper giant branch as templates; this result is expected since the integrated light comes primarily from the fainter stars. The kinematics, however, are similar using both templates.

The positions of the template stars are marked in the HST image (Figure 5, left panel) with magenta circles and in the CMD (Figure 1) with green stars. We also identify the brightest stars from the pointing in the CMD to make sure that none of the dominating stars is a foreground star (see Figure 1, red dots). In order to derive an absolute velocity scale, the line shifts of the template are measured by fitting a Gaussian to each Ca-triplet line of the template spectrum, and deriving the centroid. This is compared with the values of the Calcium Triplet in a rest frame and the average shift is calculated. The derived radial velocity is transformed to the heliocentric reference frame. This results in a template velocity of $v_{\mathrm{temp}} = (122.3 \pm 2.3)\ \mathrm{km\,s^{-1}}$.

As a conspicuous feature in the velocity map we recognize two blue spots in the upper right, indicating two stars with high approaching velocities. Considering the velocity scale, also plotted in Figure 4.1, these features refer to velocities of -40 and $-45\ \mathrm{km\,s^{-1}}$ relative to the cluster, respectively. This corresponds to 3.1 and 3.5 times the velocity dispersion (if one assumes the value of Pryor & Meylan 1993). High velocity stars have been discovered in only a few globular clusters up to now (Gunn & Griffin 1979; Meylan et al. 1991) and require a detailed analysis in terms of membership, the tails of the velocity distribution, and ejection mechanisms. We discuss the two high-velocity stars in a separate paper (Chapter 4).

3.4.2 Inner velocity-dispersion profile

For the radial velocity-dispersion profile of NGC 2808, we bin the spectra in the following way. The pointing is divided into five independent angular bins, with radii of 2, 5, 10, 20 and 28 ARGUS spaxels corresponding to $1.0'', 2.6'', 5.2'', 10.4''$ and $15.6''$ ($\sim 0.05, 0.12, 0.24, 0.48, 0.68$ pc). We try different combinations of bins and bin distances as well as overlapping bins and find no change in the global shape of the profile. In each

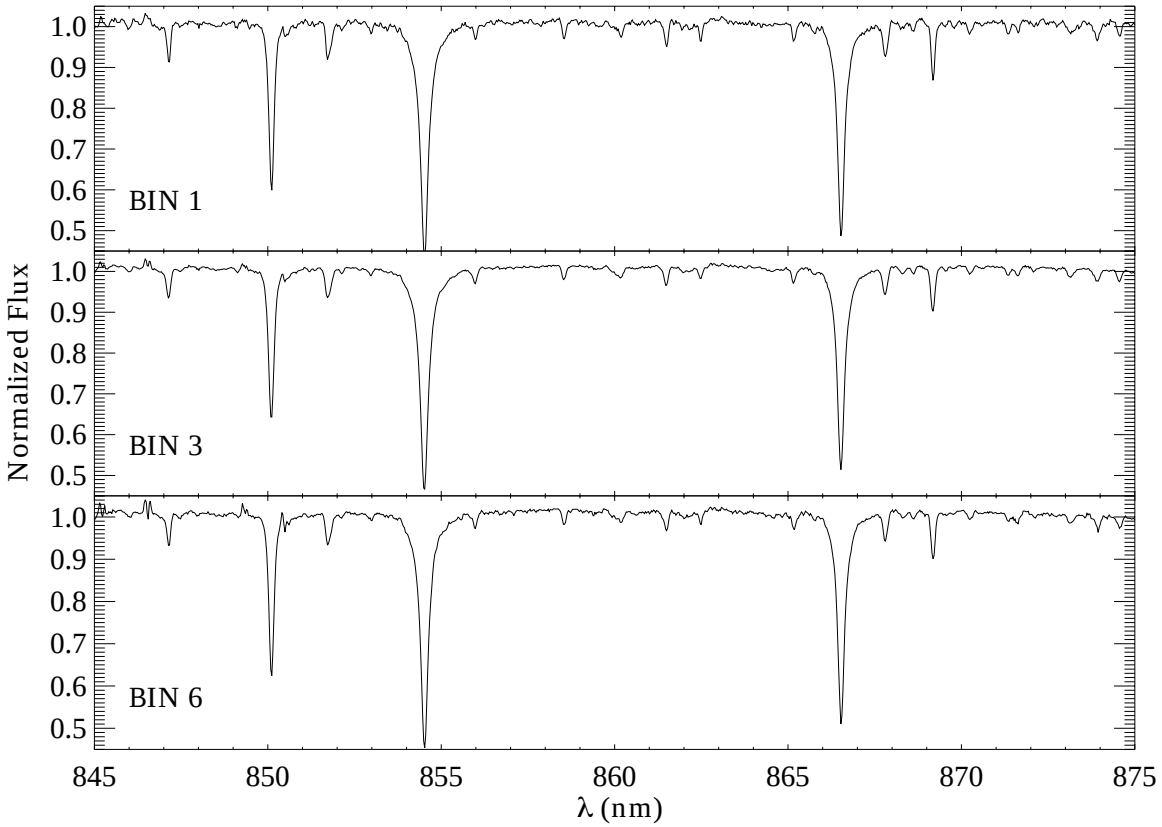

Figure 3.6: Combined spectra for the bins 1, 3 and 6 from which the kinematic measurements are taken.

bin, all spectra of all exposures are combined with a sigma clipping algorithm to remove any remaining cosmic rays. Velocity and velocity-dispersion profiles are computed by applying pPXF to the binned spectra using the same template as for the velocity map. We compare the results of pPXF with a non-parametric fit. We obtain the best agreement of these two methods by fitting four moments of the Gauss-Hermite parametrization. The final parameters (V, σ, h_3, h_4) are transformed to the "true" moments of the LOSVD $(\tilde{V}, \tilde{\sigma}, \xi_3, \xi_4)$ by applying equations (17) of van der Marel & Franx (1993).

We estimate the radial velocity of the cluster in a heliocentric reference frame and the effective velocity dispersion σ_e. We combine all spectra in the pointing and measure the velocity relative to the velocity of the template. This value is corrected for the motion of the template and the heliocentric velocity and results in a value of $V_r = (104.3 \pm 2.3)$ $km\,s^{-1}$ which agrees within the errors with the value from Harris (1996) $V_r = (101.6 \pm 0.7)$ $km\,s^{-1}$. The effective velocity dispersion is derived using equation (1) in Chapter 2 and results in $\sigma_e = (13.4 \pm 0.2)$ $km\,s^{-1}$. This is in very good agreement with the central velocity dispersion $\sigma_c = (13.4 \pm 2.6)$ $km\,s^{-1}$ of Pryor & Meylan (1993).

Table 3.3: Kinematics of NGC 2808 obtained from the VLT/FLAMES data.

log r [arcsec]	$\tilde{V}$ [km/s]	$\tilde{\sigma}$ [km/s]	V [km/s]	σ [km/s]	h_3	h_4	S/N
FLAMES MEASUREMENTS							
1.09	0.6 ± 0.3	11.4 ± 2.5	0.3 ± 0.3	13.0 ± 0.6	0.00 ± 0.01	-0.15 ± 0.06	128
2.60	-0.0 ± 0.3	13.0 ± 1.3	-0.5 ± 0.3	14.7 ± 0.6	0.02 ± 0.00	-0.16 ± 0.07	165
5.20	-1.6 ± 2.9	13.8 ± 0.7	-2.4 ± 2.9	15.5 ± 0.4	0.04 ± 0.22	-0.12 ± 0.03	188
7.80	-0.1 ± 0.4	13.6 ± 0.5	-0.5 ± 0.4	15.4 ± 0.6	0.01 ± 0.00	-0.14 ± 0.06	184
10.40	0.9 ± 0.4	13.9 ± 0.5	0.4 ± 0.4	15.7 ± 0.5	0.02 ± 0.02	-0.14 ± 0.00	157
14.56	0.9 ± 0.4	13.1 ± 0.6	0.5 ± 0.4	14.8 ± 0.7	0.02 ± 0.00	-0.17 ± 0.09	154
FABRY-PEROT MEASUREMENTS							
57.42	-0.2 ± 0.4	10.7 ± 0.3					
89.27	-1.4 ± 1.3	9.4 ± 0.9					
108.02	1.5 ± 0.9	8.2 ± 0.7					
157.58	1.3 ± 1.0	8.1 ± 0.7					

For the error estimation we run Monte Carlo simulations for each bin. From the routine described in section 3.4.1, we know how many stars contribute to what amount to each spaxel, and how many spaxels are added up in each bin. Each of the stars in one bin is assigned a velocity chosen from a Gaussian velocity distribution with a fixed dispersion of 10 $\mathrm{km\,s^{-1}}$. Using our template spectrum we shift the spectra by their velocity and weight them according to their contribution before combining them in to one spaxel. The resulting spaxels are normalized, combined and the kinematics measured with pPXF (as for the original data). After 1000 realizations for each bin, we obtain the shot noise errors from the spread of the measured velocity dispersions. The errors for the velocity are derived by applying Monte Carlo simulations to the spectrum itself. This is done by repeating the measurement for 100 different realizations, adding noise to the original spectra (see Cappellari & Emsellem 2004, section 3.4).

The resulting profile is displayed in Figure 3.7. The innermost point drops down to a dispersion of 11.4 $\mathrm{km\,s^{-1}}$, which is lower than the outermost point of the IFU data, but it is also severely affected by shot noise, as seen by its large error bar. In Table 3.3, we record the results of the kinematic measurements. The first column lists the radii of the bins. The following columns show the central velocities of each bin in the reference frame of the cluster, the corrected velocity dispersion $\tilde{\sigma}$ (V_{RMS}), as well as the parameters from the Gauss-Hermite parameterization V, σ, h_3 and h_4.

3.4.3 Outer kinematics

In addition to the inner kinematics we use the dataset of Gebhardt et al. (2012, in preparation) for larger radii. This data was obtained in three epochs (1995, 1997, 1998) with the Rutgers Fabry Perot on the Blanco 4-m telescope at Cerro Tololo Inter-American Observatory (CTIO). The data set contains over 3600 velocities of individual stars out to 4′. For reduction and more detailed information we refer to Gebhardt et al. (2012, in preparation).

The Fabry-Perot velocities come from a very similar set of observations and reductions as presented in Gebhardt et al. (1997). These spectra are centered on a small region around the H-alpha absorption line, with absolute velocity calibration derived from comparison with published radial velocities. We exclude the Fabry-Perot data in the central regions where crowding is important; whenever measuring radial velocities of individual stars in clusters, one must be careful to limit contamination by other cluster members, otherwise potentially biasing the velocity dispersion measurement.

A closer look at the outer velocities shows a clear rotation at larger radii. We derive the rotation velocity and orientation in the following way: Different radial bins of 10", 30", 50", 70" and 90" are divided into 12 angular bins and the velocity of each of these wedges is derived. The rotation curve (the velocity as a function of position angle) is fitted by a sine function and orientation as well as rotation velocity is extracted for each of the bins. We obtain an average orientation angle of of maximum positive rotation of $\theta = 132^\circ \pm 9^\circ$ (measured from

North to East). The rotation velocity increases from no rotation within the core radius to ~ 5 km s^{-1} in the outskirts of the cluster.

In order to obtain the velocity-dispersion profile, we apply the maximum likelihood method introduced by Pryor & Meylan (1993). The iterative scheme used to solve the maximum likelihood equations is very similar to that used by Gunn & Griffin (1979) to fit the velocity scale parameter of King models. This approach is necessary especially when the uncertainties of the individual velocities are different. The data is divided into radial bins and the velocity dispersion derived for each bin. Due to crowding in the cluster center, fainter stars get contaminated from background light which biases their measured velocities towards the cluster mean velocity. This results in a lower velocity dispersion for points measured in the central regions of the cluster. For this reason we only used measurements for radii larger than 50″ ($\sim r_h$). The resulting velocity-dispersion profile is shown in Figure 3.7 together with the points of the IFU measurements and the best fit Jeans model (see section 3.5).

3.5 Dynamical Models

After having extracted the velocity dispersion profile over a large radial range, the next step is to compare this data, together with the photometric profiles, to dynamical models. This section describes the different types of models which we compare to our data. We start with a spherical isotropic Jeans model, increase the complexity of the models to axisymmetric models, and radial varying M/L_V profiles.

3.5.1 Isotropic spherical Jeans models

Assuming spherical symmetry is a good approximation for most globular clusters and a valid first order assumption for NGC 2808. To compute the models, we use the Jeans Anisotropic multi-Gaussian expansion (JAM) dynamical models implementation for stellar kinematics of spherical and axisymmetric galaxies developed by Cappellari (2002, 2008) [2]. The routines take a one dimensional surface brightness profile as an input and use the multi-Gaussian expansion (MGE) method Emsellem et al. (1994) to fit and deprojects the light profile. This is then fed into the spherical Jeans equations and a second-moment profile ($V_{RMS} = \sqrt{(\sigma^2 + V_{rot}^2)}$, hereafter referred to as velocity-dispersion profile) is computed. The modeled velocity-dispersion profile is scaled by a constant factor to fit the kinematic data. This scaling factor is adopted as the global M/L_V value. In Figure 3.7, the black line in the left panel represents the spherical Jeans model with a $M/L_V = 1.4$.

The comparison of the spherical model with our data in Figure 3.7 shows already good agreement. However, a constant M/L_V profile over a larger radial range is not a good assumption for a globular cluster. N-body simulations have shown that the M/L_V increases

[2] Available at http://www-astro.physics.ox.ac.uk/∼mxc/idl

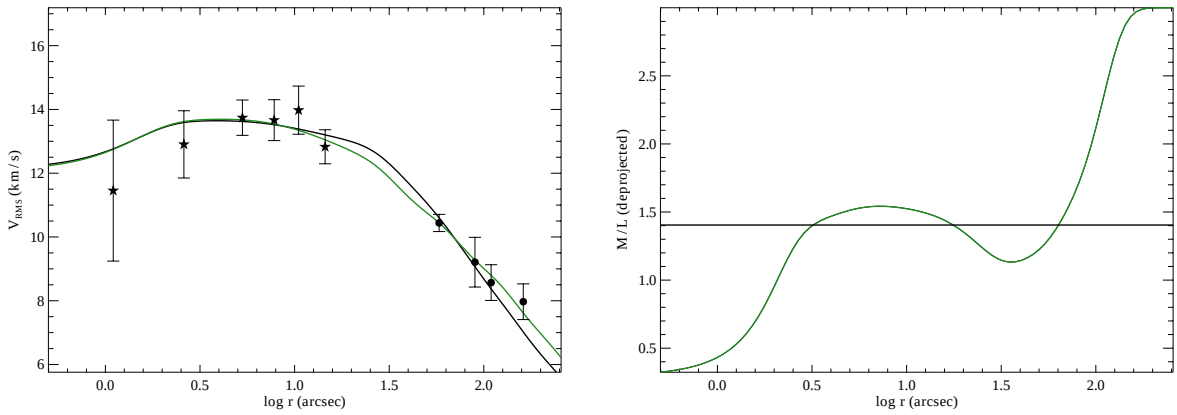

Figure 3.7: Isotropic spherical Jeans models compared to the kinematic data of NGC 2808. Stars correspond to the inner kinematic profile obtained with integral-field spectroscopy and bullets represent the data obtained with the Fabry-Perot instrument. Shown are a model with a constant M/L_V over the entire radius of the cluster (black line) as well as the model where we fit an M/L_V profile (green line). The resulting M/L_V profile is shown in the right panel together with the constant value of the previous model.

for larger radii due to mass segregation and migration of low-mass stars towards the outskirts of the cluster. The underestimation of the model for the outer points might be caused by this effect. Therefore, it is necessary to allow for a varying M/L_V profile in the models. For this, we apply two methods: the first one is to let the model fit the M/L profile to the data. This can be done by multiplying each of the MGE Gaussians of the fitted surface brightness profile with different factors p (Williams et al. 2009). These factors are varied over a physical range ($p \in \{0, 3\}$). For every combination, the Jeans model is computed and the quality of the fit calculated via a least square statistic. With this technique, we find the M/L_V profile which best reproduces the data. The disadvantage of this method is the degeneracy of the problem. There are many combinations of the factors p that return similar quality of the fit to the kinematic data. In addition, without constraining the parameters of the M/L_V profile to a physical limit, the best fit would favor unrealistic high values in the outer regions to fit the flat velocity-dispersion profile beyond 100″. The resulting M/L_V profile is shown in the right panel of Figure 3.7 as a green line.

The second method takes an already existing M/L_V profile obtained from N-body simulations and is explained in the next Section.

3.5.2 Isotropic axisymmetric Jeans models

The Fabry-Perot dataset shows a clear rotation in the outer regions with rotation velocities up to 5 $\mathrm{km\,s^{-1}}$. The shape of NGC 2808 reveals the rotation character of that cluster with a flattening of $\epsilon = 1 - b/a = 0.12$ (White & Shawl 1987). For that reason we compute

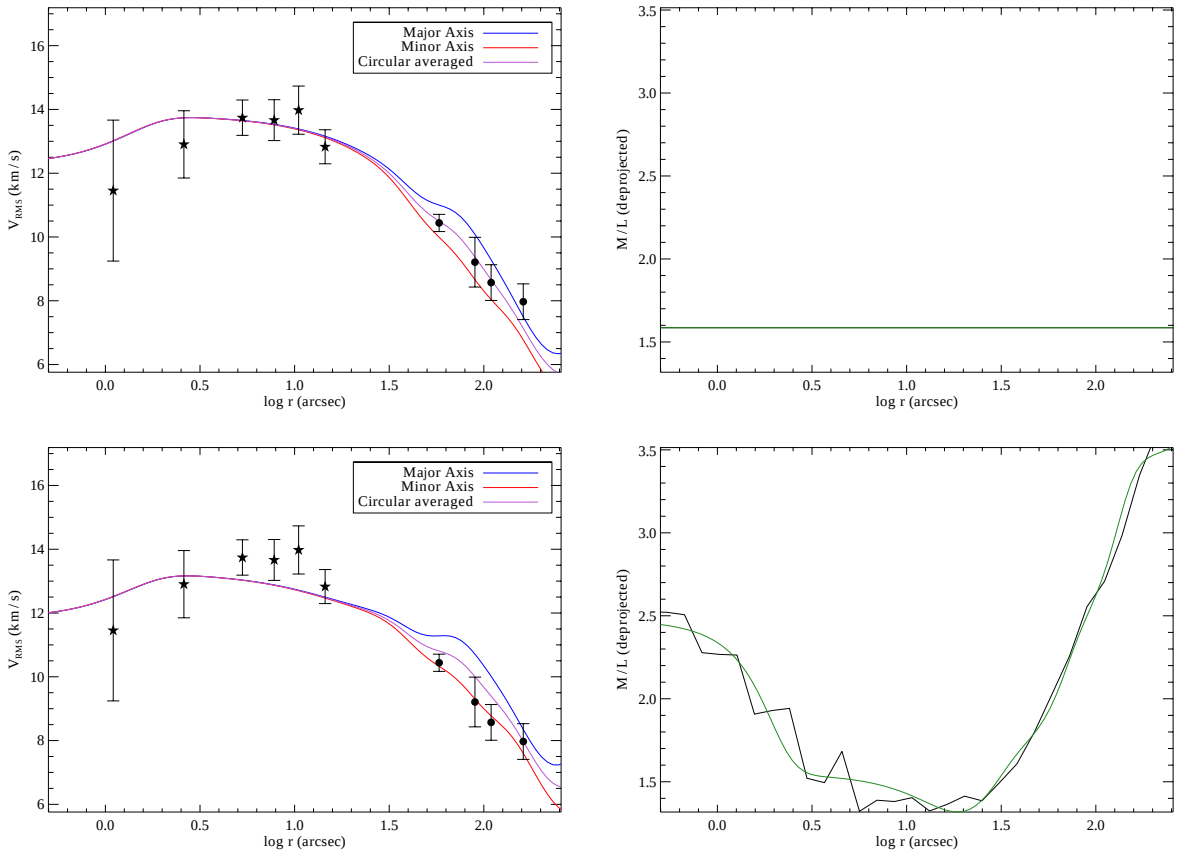

Figure 3.8: Axisymmetric Jeans models for NGC 2808 for a constant (upper panel) and a varying M/L_V profile (lower panel). The used M/L_V profiles/values are shown in the right panels. The black line marks the inserted profile from N-body simulations and the green line its parametrisations with the MGE Gaussians.

axisymmetric Jeans models in addition to the spherical models described in the previous section. These models assume an axial symmetry of the velocity ellipsoids rather than a spherical symmetry and are ideally suited for rotating systems. By applying the general axisymmetric Jeans equations (3) and (4) in Cappellari (2008), the Jeans models provide good descriptions of the two-dimensional shape of the velocity (V) and its velocity-dispersion (V_{RMS}), once a surface brightness profile is given.

Instead of using an one-dimensional surface brightness profile the axisymetric models (also present in the JAM package) perform a two-dimensional fit to the surface brightness obtained from an image of the object. For globular clusters, determining a 2D surface brightness profile is challenging since the individual stars are resolved and the routine has difficulties in fitting isophotes to a discontinuous image. Images with a lower resolution are better suited for this purpose. We use a combination of a ground based image in J-band taken from publicly available data of 2MASS and of our inner one-dimensional surface brightness

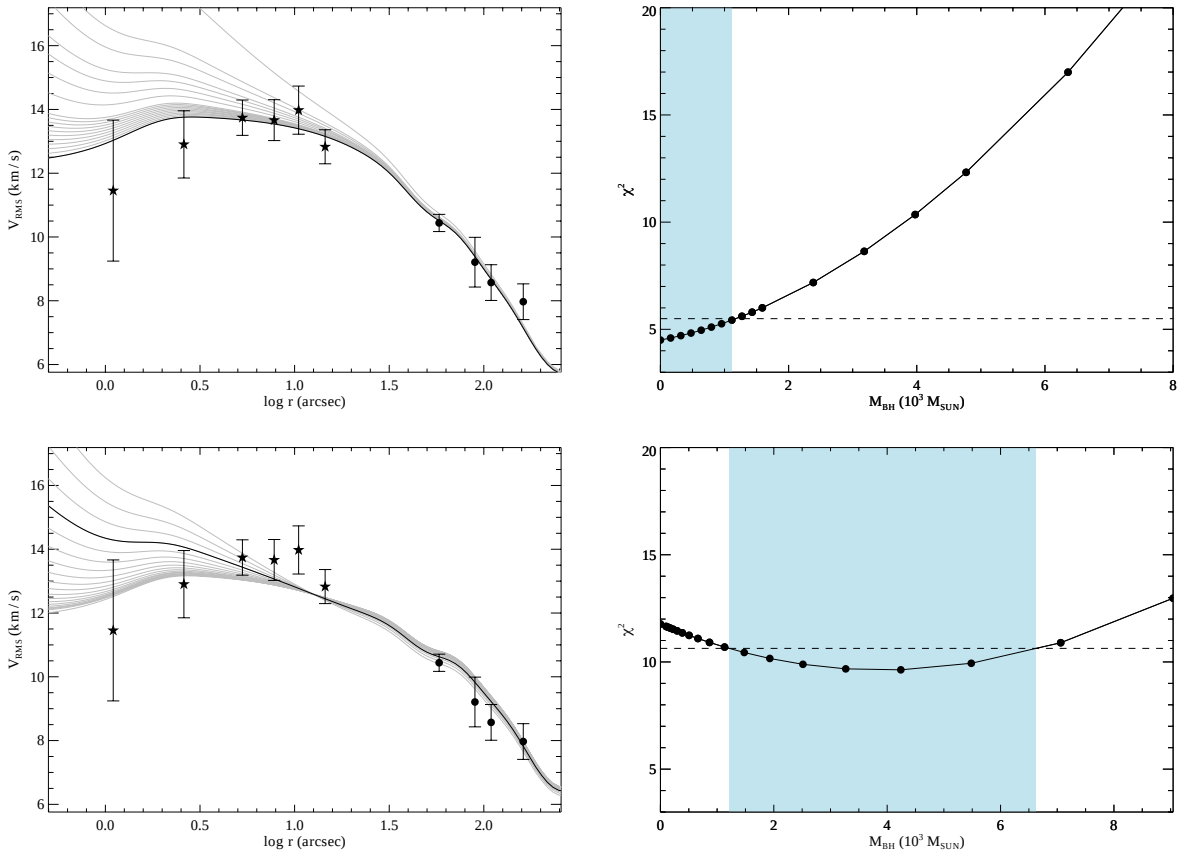

Figure 3.9: Axisymmetric Jeans models with different black-hole masses for NGC 2808. Upper panel: The model with the constant M/L_V (same as in Figure 3.8). Lower panel: The model with an M/L_V profile. The $/chi^2$ values as a function of black-hole mass are shown in the right panels. Blue shaded areas mark the black-hole mass range where $\Delta\chi^2 < 1$, thus the 1σ error.

profile obtained from the HST image (see Section 5.2.3). Since the high resolution of the HST does not allow a two-dimensional fit on the image itself and because we do not measure any rotation within the core radius, we assume spherical symmetry inside a radius of $r \sim 15''$(the size of the combined ARGUS field of view). This assumption is further supported by the results of Chapter 2 where we found that any anisotropy in a globular cluster is smoothed out within a few relaxation times inside the core radius of the cluster.

For the outer region of the cluster the routine *find_ galaxy.pro*, which is also included in the JAM package, measures an ellipticity of $\epsilon = 1 - b/a = 0.11$ and an orientation of $\theta = 104°$. This orientation differs from the one that we obtain from the kinematic studies ($\theta = 132°$) and from the results of White & Shawl (1987) of $\theta \sim 121°$. Because of the large uncertainties of the photometric measurement (due to shot noise of single stars), we decide to adopt the orientation from the kinematics as our final result $\theta = 132° \pm 9°$. The next step is to determine the two-dimensional surface brightness profile from the 2MASS image.

This is done by the routine *sectors_ photometry.pro*. The routine performs photometry of an image along sectors equally spaced in angle. The result is converted into magnitudes per squarearcsecond and combined with the inner surface brightness profile obtained with the HST.

The JAM code calculates a two dimensional V_{RMS} map by using the surface brightness profile. To compare with our one dimensional kinematic profile we extract the profile along the major axis and the minor axis. In addition, we derive a third profile by averaging the two-dimensional V_{RMS} map over concentric radial bins and call it the averaged profile. Figure 3.8 shows these three profiles on top of the data. The models differ only in the outer region since the inner part is assumed to be spherical.

In order to use the most realistic M/L_V profile, we use an M/L_V profile obtained by running N-body simulations and comparing them to our data points using the N-body code NBODY6 (Aarseth 1999). Starting from a King (1962) model the simulations run with varying initial central concentrations c, half-mass radii r_h, and IMBH masses with $N = 50\ 000$ particles. We use a metallicity of $[Fe/H] = -1.18$ and model a stellar evolution according to the stellar evolution routines of Hurley et al. (2000). The simulations start with stars distributed according to a Kroupa (2001) mass function in the mass range $0.1 < m/M_{\odot} < 100$. Binaries can form during the evolution of the cluster, but are not included primordially. For more informations about these simulations we refer to McNamara et al. (2012) and Baumgardt & Makino (2003). We use a grid of computed models with different initial conditions and find the model which fits the observed kinematic and light profile the best. The M/L of this model is then computed as a function of radius by only using the brightest stars. This allows an independent determination of the M/L profile of NGC 2808. This is fed into the Jeans model, which parametrizes the input M/L profile with an MGE fit and applies it to the resulting velocity-dispersion profile. The lower right panel of Figure 3.8 shows the used M/L_V profile from the N-body simulations (black line) as well as its parametrization with the MGE Gaussians (green line). Also shown is the resulting model compared to the data (lower left panel). Model provides a worse fit then the model with a constant M/L_V profile. This comes probably from overestimating the M/L_V profile in the outer regions of the cluster.

Both methods of deriving an M/L_V profile show similar results. Figure 3.8 in the upper panel shows the Jeans model for the major axis, minor axis and circular averaged on top of our data points. The model of the major axis seems to reproduce the data best. This might be due to the fact that the data set of the Fabry-Perot observations is asymmetric and spatially biased towards the major axis. The right panel of the figure shows the deprojected M/L profile from the N-body simulations (black line) together with the fit of the M/L profile from the Jeans model (red line). The M/L profile in the lower panel of Figure 3.8 has an interesting shape. The steep rise at the center implies a high concentration of stellar remnants and therefore an advanced stage of mass segregation. Beyond the half-light radius ($\sim 48''$) the M/L profile rises again, which can also be explained by the process of mass segregation. Low mass stars move towards the outer regions while the cluster evolves.

That explains the higher M/L ratio in the outskirts of the cluster.

The next step in terms of modeling is to include a central black hole in our Jeans models and to test if we obtain a better fit to our data. Figure 3.9 shows the result of these models. For both cases, with and without a M/L_V profile, we compute models with black-hole masses between $M_{BH} = 0$ and $M_{BH} = 8 \times 10^3\ M_\odot$. The black solid line shows the best fit of the model with a zero mass black hole. Higher black-hole masses predict higher central V_{RMS} than seen in our data. The χ^2 curves in the right panel of the figure shows this result. The blue shaded areas define the 1σ limit of the best fit. For the model with the constant M/L_V profile, no black hole is needed in order to reproduce the data with a 1σ uncertainty of $M_\bullet = 1 \times 10^3 M_\odot$. The second model, however, exhibits a flatter profile and therefore is better fit by a model with a non-zero black-hole mass. The best fit model returns a black-hole mass of $M_\bullet = 4 \times 10^3 M_\odot$ and a 1σ upper limit of $M_\bullet \sim 6 \times 10^3 M_\odot$. Also the total M/L_V values of both models differ. The model with the constant M/L_V results in a total value of $M/L_V = 1.6 M_\odot/L_\odot$ while the model with the M/L_V increasing in the outskirts of the cluster predicts a M/L_V of $\sim 2.1 M_\odot/L_\odot$.

We run Monte Carlo simulations on both the surface-brightness profile and the velocity-dispersion profile in order to get an estimate of how much the individual errors from the two profiles influence the result. We find that by only changing the inner surface-brightness profile, 90 % of the cases result in the same black-hole mass as the fit with the original light profile. This indicates that the error on the black-hole mass is only dependent on the uncertainties of the velocity-dispersion profile. We therefore adopt the 95% confidence upper limit of $M_\bullet < 1 \times 10^4 M_\odot$ of the model with the varying M/L_V profile. We note that the model with the constant M/L_V fits the data slightly better and results in a lower upper limit of $M_\bullet < 3 \times 10^3 M_\odot$. However, a constant M/L_V profile is very unrealistic for a globular cluster like NGC 2808 and therefore the results from the model with the M/L_V profile more reliable. From the Monte Carlo simulations we also derive a 1σ error on the total mass and the global mass to light ratio of ~ 10 %.

3.6 Summary and Conclusions

We examine the central kinematics of the globular cluster NGC 2808 in order to constrain the mass of a possible intermediate-mass black hole at its center. With a set of HST images, the photometric center of the cluster is determined. Furthermore, a color magnitude diagram as well as a surface brightness profile, built from a combination of star counts and integrated light, are produced. The spectra from the VLT ground-based integral-field unit ARGUS are reduced and analyzed in order to create a velocity map and a velocity-dispersion profile. We derive a velocity-dispersion profile by summing all spectra into radial bins and applying a penalized pixel fitting method. In addition, we use radial velocities measured with the Rutgers Fabry Perot by Gebhardt et al. (2012, in preparation) to derive the velocity-dispersion profile in the outer regions.

We compare the data to spherical and axisymmetric isotropic Jeans models using different M/L_V profiles and black-hole masses. We include a radius dependent M/L_V profile obtained from N-body simulations in order to account for mass segregation in the cluster. This does not improve the fit of the velocity dispersion profile, but still coincides with the data within the error bars. The best fitting Jeans model is the axisymmetric case with a constant M/L_V profile and no black hole. The 95% error of that fit predicts an upper limit of $M_\bullet = 3 \times 10^3 M_\odot$ on the black-hole mass. However, assuming a non constant M/L_V profile the model upper limit on the black-hole mass increases to $M_\bullet = 1 \times 10^4 M_\odot$.

Our result on the upper limit of the black-hole mass in NGC 2808 is higher with the results of the radio observations of Maccarone & Servillat (2008) and their upper limit of 370 - 2100 $M_\odot$. With the uncertainties in gas content and accretion rates, however it is plausible for the limit derived by the radio observations to increase. We stress that the result is dependent on the choice of the M/L_V profile and needs to be treated carefully since different M/L_V profiles bring different results on black-hole mass and total mass of the cluster.

Our derived mass to light ratio of $M/L_V = (2.1 \pm 0.2)\ M_\odot/L_\odot$ is higher than the M/L of ~ 1.3 derived by McLaughlin & van der Marel (2005). This results from the fact that our total luminosity is lower than the one derived by Harris (1996) by $\sim 22\%$ which results from the slightly steeper drop of the surface brightness profile compared to the profile obtained by Trager et al. (1995) in the outskirts of the cluster. Also the total mass of $M_{TOT} = (8.2 \pm 0.8) \times 10^5 M_\odot$ is higher than the total mass derived with the values of Harris (1996) and McLaughlin & van der Marel (2005) of $M_{TOT} \sim 6.4 \times 10^5 M_\odot$ which results from the shape of our M/L_V profile.

So far, Jeans models allow us a crude first guess on the dynamic state of a globular cluster. Nevertheless, the result of the black hole-mass depends strongly on the M/L_V profile used. We find that using different profiles with lower M/L values at the center but still high values in the outskirts result in models which fit the data with a black-hole mass up to 5000 $M_\odot$. However, due to the high degeneracy we encounter when fitting the M/L profile with Jeans models, we have to choose the profile which is derived from N-body simulations. Therefore, it is crucial to run specific N-body simulations for all our globular cluster in order to get an accurate M/L_V profile and constraints on the anisotropy and mass segregation. This is an important factor especially for mass segregated clusters such as NGC 2808.

The dynamical models presented here include Jeans isotropic modeling and comparison with N-body simulations. We do not present results from orbit-based models. These axisymmetric models are significantly more general than the isotropic models since they have no assumption about the velocity anisotropy. They are also more general than the N-body simulations, since the N-body models rely on a limited set of initial conditions; the orbit models encompass all available phase space configurations, at the expense of producing a dynamical model that does not take the evolutionary processes into account. Thus, the orbit models will provide larger uncertainties, and hence a large upper limit on the black hole mass. For this analysis, however, we rely on the N-body simulations which should be

a fair representation of the current dynamical state of the cluster.

The study of black holes in globular clusters has drawn the attention of the astronomy community. Not only radial velocities are observed and analyzed, also, observations and analysis of proper motions for many clusters are in progress. A desired future project would be the combination of all these data sets and a detailed analysis via N-body and orbit based models which would allow a deeper insight into the dynamics of globular clusters, revealing their hidden secrets.

Acknowledgements: *This research was supported by the DFG cluster of excellence Origin and Structure of the Universe (www.universe-cluster.de). H.B. acknowledges support from the Australian Research Council through Future Fellowship grant FT0991052. We thank an anonymous referee whose fast comments and suggestions have helped a lot to improve this paper. We also thank Mike Irwin for making available to us his proprietary code for sky-subtraction and Giuseppina Battaglia for providing assistance.*

CHAPTER 4

High-velocity stars in the cores of globular clusters: The illustrative case of NGC 2808

Nora Lützgendorf, Alessia Gualandris, Markus Kissler-Patig, Karl Gebhard, Holger Baumgardt, Eva Noyola,J. M. Diderik Kruijssen, Behrang Jalali, Tim de Zeeuw, and Nadine Neumayer

Astronomy & Astrophysics, Volume 543, id.A82 (2011)

Abstract We report the detection of five high-velocity stars in the core of the globular cluster NGC 2808. The stars lie on the red giant branch and show total velocities between 40 and 45 $\mathrm{km\,s^{-1}}$. For a core velocity dispersion $\sigma_c = 13.4\ \mathrm{km\,s^{-1}}$, this corresponds to up to $3.4\sigma_c$. These velocities are close to the estimated escape velocity ($\sim 50\ \mathrm{km\,s^{-1}}$) and suggest an ejection from the core. Two of these stars have been confirmed in our recent integral field spectroscopy data and we will discuss them in more detail here. These two red giants are located at a projected distance of $\sim 0.3\,\mathrm{pc}$ from the center. According to their positions on the color magnitude diagram, both stars are cluster members. We investigate several possible origins for the high velocities of the stars and conceivable ejection mechanisms. Since the velocities are close to the escape velocity, it is not obvious whether the stars are bound or unbound to the cluster. We therefore consider both cases in our analysis. We perform numerical simulations of three-body dynamical encounters between binaries and single stars and compare the resulting velocity distributions of escapers with the velocities of our stars. If the stars are bound, the encounters must have taken place when the stars were still on the main sequence. We compare the predictions for a single dynamical encounter with a compact object with those of a sequence of two-body encounters due to relaxation. If the stars are unbound, the encounter must have taken place recently, when the stars were already in the giant phase. After including binary fractions and black-hole retention fractions, projection effects, and detection probabilities from Monte-Carlo simulations, we estimate the expected numbers of detections for all the different scenarios. Based on these numbers, we conclude that the most likely scenario is that the stars are bound and were accelerated by a single encounter between a binary of main-sequence stars and a $\sim 10\,M_\odot$ black hole. Finally, we discuss the origin of previously discovered fast stars in globular clusters, and conclude that the case of NGC 2808 is most likely a

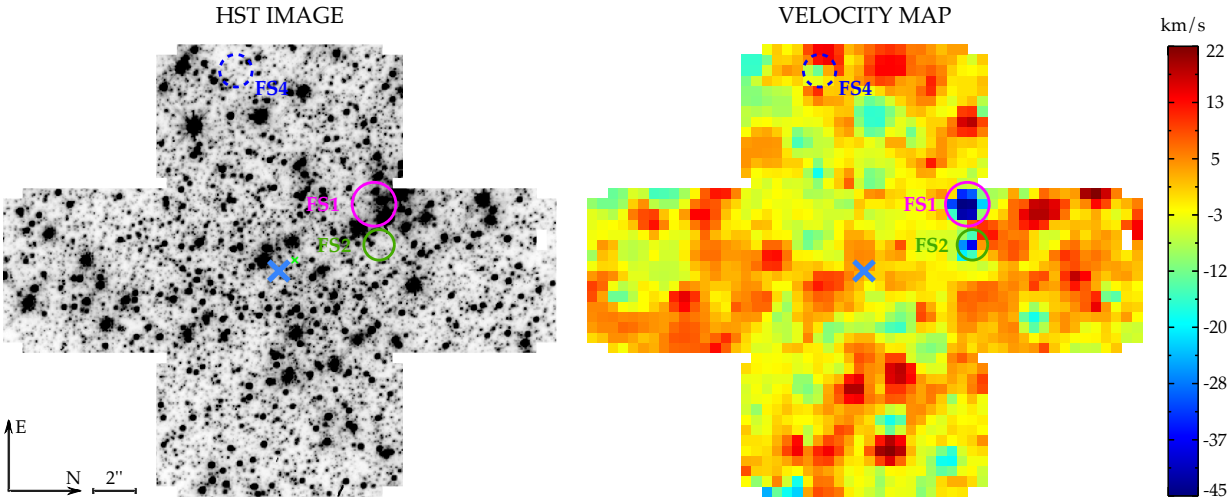

Figure 4.1: ARGUS field of view (left) and velocity map of NGC 2808 (right). Visible as bright blue spots are the two high-velocity stars FS1 and FS2. Marked with the dashed blue line is FS4, the star which does not dominate its spaxel and therefore is not detectable. The blue cross marks the center of the cluster.

representative case for most other detections of fast stars in globular clusters. We show that with the present analysis we are able to explain high-velocity stars in the clusters M3 and 47 Tucanae with simple dynamical encounters.

4.1 Introduction

High-velocity stars in globular clusters have been a puzzle to astronomers since the beginning of velocity measurements. Especially finding fast giant stars in the core of globular clusters has drawn attention. Gunn & Griffin (1979) found two fast stars which they called “interlopers" in the globular cluster M3. The stars are located in the core of the cluster, both at a projected distance of about 20″ from the center. With radial velocities of 17.0 $\mathrm{km\,s^{-1}}$ and $-22.9\ \mathrm{km\,s^{-1}}$ relative to the cluster, they move with 3.5 and 4.5 times the central velocity dispersion ($\sigma_c = 4.9\ \mathrm{km\,s^{-1}}$), respectively. Due to the high systemic velocity of the cluster itself ($V_r \sim -147\ \mathrm{km\,s^{-1}}$) the possibility of these stars being field stars is rather low. Meylan et al. (1991) found a similar case for the globular cluster 47 Tucanae. The stars which they found have radial velocities of $-36.7\ \mathrm{km\,s^{-1}}$ and $32.4\ \mathrm{km\,s^{-1}}$ in the reference frame of the cluster which corresponds to 4.0 and 3.6 times the core velocity dispersion $\sigma_c = 9.1\ \mathrm{km\,s^{-1}}$. Despite the fact that the low systemic velocity of the cluster does not allow for an accurate kinematic statement on the membership of these two stars, their position in the color-magnitude diagram and the high Galactic latitude of 47 Tucanae ($b = -44°$) both argue for membership.

Plausible mechanisms to explain these high-velocity stars are ejection from the core by

recoil from an encounter between a single star and a binary, between two binary stars, between a binary and an intermediate-mass black hole (IMBH) at the center or even from encounters of stars with an IMBH binary (e.g. Gualandris et al. 2004, 2005; Baumgardt et al. 2006; Gvaramadze et al. 2009; Mapelli et al. 2005). It has been recently suggested that globular clusters may contain central black holes in the mass range of $10^3 - 10^4\,M_\odot$ (Miller & Hamilton 2002c; Baumgardt et al. 2005) which fall on top of the relation between the velocity dispersion and black hole mass seen for galaxies (e.g. Ferrarese & Merritt 2000; Gebhardt et al. 2000a). Kinematic signatures for intermediate-mass black holes have been found in the globular clusters ω Centauri (Noyola et al. 2008, 2010), G1 in M31 (Gebhardt et al. 2002, 2005) and NGC 6388 (Chapter 2). High velocity stars are predicted in globular clusters which host intermediate-mass black holes. Therefore it is important to study such stars in more detail when observed in a globular cluster.

The globular cluster NGC 2808 is of high interest in many regards. From the photometric side, it has a complex extended horizontal branch (Harris 1974; Ferraro et al. 1990) which shows puzzling discontinuities in the stellar distribution along its blue tail. Furthermore, Piotto et al. (2007) found a triple main sequence after accurate photometric and proper motion analysis with deep Hubble Space Telescope (HST) data. This indicates the existence of three sub-populations with an age of ~ 12.5 Gyr and different metallicities. The kinematic properties of NGC 2808 are also unusual. By analyzing Fabry-Perot data, Gebhardt et al. (2011) found rotation in the outer parts of the cluster with a maximum rotation velocity of $V_{rot} \sim 5\ \mathrm{km\,s^{-1}}$. The latest radial velocity measurements of the cluster core in Chapter 3 have shown that NGC 2808 most probably does not host an intermediate-mass black hole: the best fit model is consistent with no IMBH and gives an upper limit of $M_{BH} < 1 \times 10^4\,M_\odot$.

In this work we report on the discovery of five high-velocity stars in NGC 2808 and discuss several explanations and ejection scenarios for the two stars found in our integral field spectroscopy observations. In Section 4.2 we explain the observations and the method of obtaining single star velocities with integral field spectroscopy. Further, we introduce a second data set used for velocity measurements taken from a Fabry-Perot instrument. At the end of the first Section we determine the escape velocity of NGC 2808. Section 4.3 is dedicated to the discussion of alternative explanations for the observed high velocities including foreground stars, binaries and atmospheric active stars. Section 4.4 describes the analysis of the Maxwellian velocity distribution and the probabilities of these stars resulting from relaxation while Section 4.5 describes the dynamical three-body simulations in order to find the most likely acceleration scenario for the two fast stars. In Section 4.6 we briefly discuss other cases of fast star detections in globular clusters. Finally, we summarize our results and list our conclusions in Section 7.5.

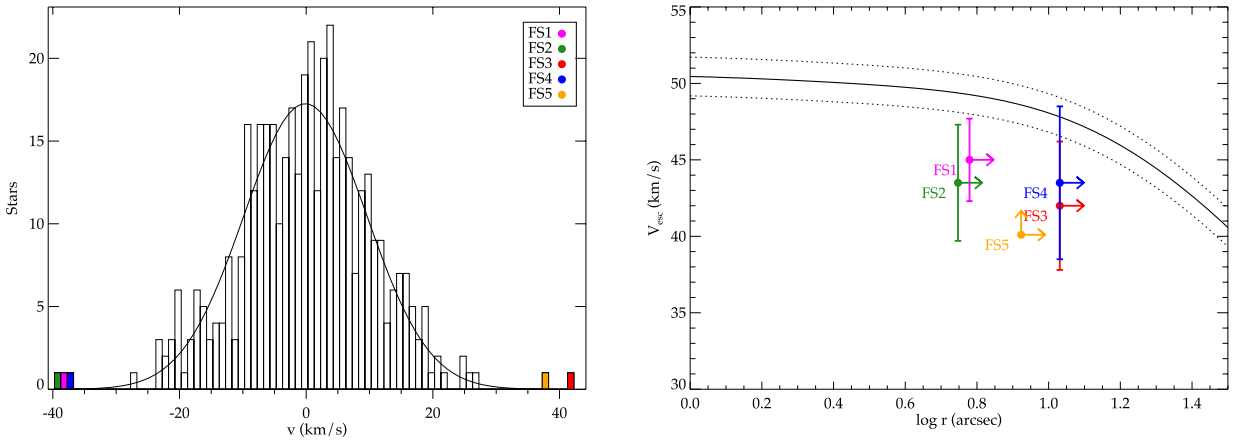

Figure 4.2: Kinematic properties of the five high-velocity stars. Left: The histogram of the Fabry-Perot data in the core of NGC 2808. Marked with colors are five high velocity stars FS1 to FS5. Right: The escape-velocity profile (solid line) and its uncertainties (dotted line) obtained from the density profile overplotted by the total velocities and projected positions of the five fast stars.

4.2 Radial velocities

The data we use were obtained with the GIRAFFE spectrograph of the FLAMES (Fiber Large Array Multi Element Spectrograph) instrument at the Very Large Telescope (VLT) in ARGUS (Large Integral Field Unit). For more details on the observations and reductions we refer to Chapter 3. From these data we construct a velocity map which is shown in Figure 4.1 together with the corresponding field of view from the HST image. The two fast stars are visible as bright “blue" spots and are labeled with FS1 and FS2 in the maps. To estimate their velocities, we use the output of a shot noise routine described in Chapter 3. This routine computes for every spaxel the number of stars that contribute to the light of the spaxel and indicates which spaxels are dominated by a single star. With this information we find the spaxel to which our two (bright) fast stars contribute with more than 80% of the light and use the radial velocities derived for these spaxels as the ones of the stars. These velocities are corrected for the systemic velocity of the cluster ($V_r = 93.6\ km\,s^{-1}$ see Chapter 3).

A second measurement is obtained from the dataset observed by Gebhardt et al. (2011) with the Rutgers Fabry Perot on the Blanco 4-m telescope at Cerro Tololo Inter-American Observatory (CTIO). This dataset contains 3634 stars and covers the center of the cluster as well as regions up to 4 arcmin radius. We match this dataset with our photometric catalog from the HST image and identify the two fast stars. Despite crowding in the inner regions, the two stars are resolved and can be identified in the Fabry-Perot dataset. In addition to FS1 and FS2, we find three more stars with velocities values between 36.0 $km\,s^{-1}$ and 42.0 $km\,s^{-1}$ inside the core radius labeled with FS3, FS4 and FS5. Table 4.1 lists the velocity measurements of all the stars as well as other properties derived from

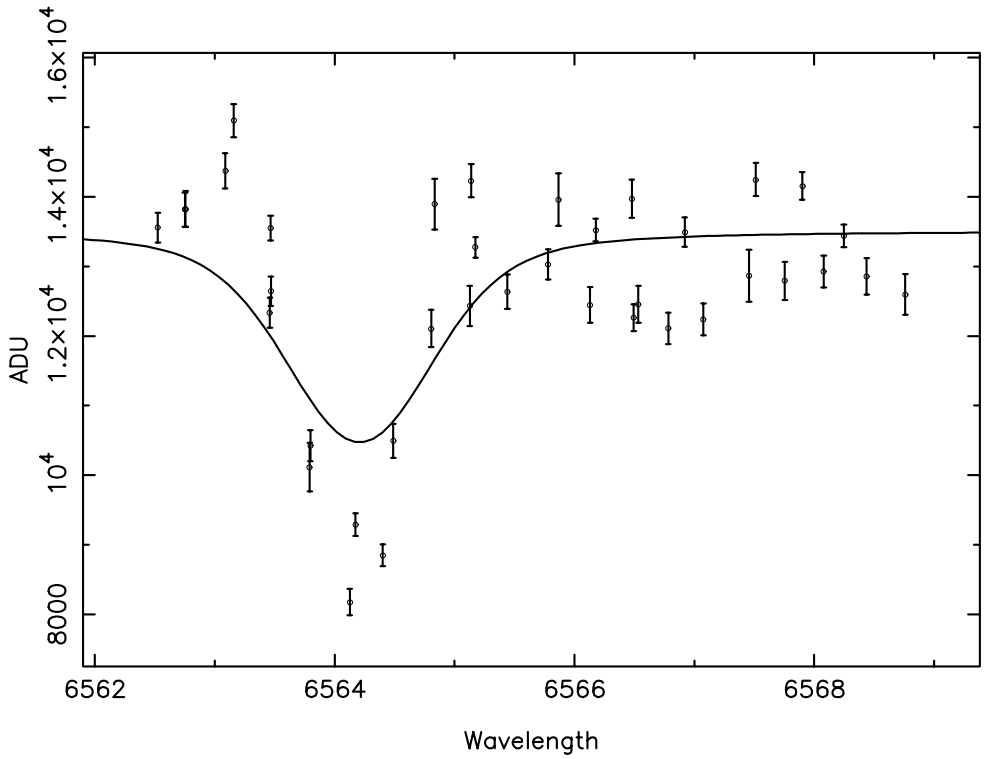

Figure 4.3: Fabry-Perot photometric points for FS1. Overplotted is the best fit of the model for the Hα line.

the HST data. Besides FS1 and FS2 only FS4 is also located inside the field of view of the combined ARGUS pointing (see Figure 4.1). However, due to its low contribution of ~ 55 % to the single spaxel we measure a much lower velocity in the IFU data than with the Fabry-Perot. The remaining stars lie outside the IFU pointing. Figure 4.2 shows the histogram of the radial velocities inside the core from the Fabry-Perot data set. The five fast stars are color-coded and visible as outliers of the distribution.

In addition to the spectroscopic data sets we also received proper motions for four out of the five stars (private communication, Jay Anderson). As listed in Table 4.1 the proper motions indicate that all stars are cluster members and increase the total velocities up to $40 - 45$ km s^{-1}. FS3, unfortunately, lies outside the proper motion dataset and therefore can only be assigned a lower limit of velocity. Since our measurements are only complete for FS1 and FS2 we decided to limit the following analysis to these two stars.

Figure 4.3 shows the photometric data points of the Fabry-Perot for FS1 and the best fit to its spectrum. The data of FS1 is not well reproduced by the model (solid line). In order to compare velocities from both datasets the velocities are corrected for the systemic motion of the cluster by computing the average velocity of the central region. The results from both data sets show high velocities for these stars. However, for FS1 the two measurements differ by 7 km s^{-1}, i.e. more than 1σ, from each other. The star is close to the saturation limit

and therefore causes difficulties when measuring the velocity. Also, measuring individual velocities with integrated light can lead to larger errors since other stars always contribute some amount of light to the analyzed spectrum. For FS2 the measurements agree within the error bars. Thus, the difference for FS1 is probably not due to a systematic shift. The discrepancy for FS1 can have several reasons: a) the velocity of this star is variable. This suggests a binary or long period variable and is discussed in more detail in Section 4.3. b) At least one of the measurements is affected by a large error. Considering the quality of the fit of the Fabry-Perot data we consider the spectroscopic measurement more accurate.

As a next step, we calculate the escape velocity of the cluster as a function of radius. This value gives the information needed to decide whether the stars are bound or unbound. We obtain an escape velocity profile by parametrizing our surface-brightness profile with a multi-gaussian expansion (MGE, Emsellem et al. 1994) as implemented in the Jeans Anisotropic Models (JAM) by Cappellari (2008). The parametrization allows an easy way of deprojecting the profile after multiplying it with the derived M/L profile from our kinematic fits (see Chapter 3). The gravitational potential generated by the deprojected density of stars is given by Equation (39) of Emsellem et al. (1994):

$$\Phi(R,z) = -\sqrt{2/\pi}\; G \int_0^1 \sum_{j=1}^{N} \frac{M_j \mathcal{H}_j(u)}{\sigma_j} \mathrm{d}u, \tag{4.1}$$

where G is the gravitational constant, M_j and σ_j the enclosed mass and the dispersion of each of the N Gaussians, respectively and with

$$\mathcal{H}_j(u) = \frac{\exp\left\{\frac{-u^2}{2\sigma_j^2}\left[R^2 + \frac{z^2}{1-(1-q_j^2)u^2}\right]\right\}}{\sqrt{1-(1-q_j^2)u^2}}, \tag{4.2}$$

a function of the integration variable u, the deprojected axial ratio $0 \leq q_j \leq 1.$, and the cylindrical coordinates R and z.

The escape-velocity profile is then evaluated by calculating the difference in the potential at a radius of r and the potential at the tidal radius ($r_t = 35\,\mathrm{pc}$, Harris 1996) as given by the equation:

$$\mathrm{V}_{esc}(r) = \sqrt{2\,(\Phi(r_T) - \Phi(r))} \tag{4.3}$$

The resulting profile is shown in Figure 4.2. Overplotted are the velocities of the five stars at their projected radii. Since the radii are projected, they only give a lower limit on the actual distance from the center. Considering the uncertainties of the stellar velocities and of the escape velocity from the cluster, we find that star FS4 is consistent with being both bound and unbound. The remaining stars appear to be bound,but given the large velocity uncertainties we will also investigate ejection mechanisms in the unbound regime.

Table 4.1: Radial velocities and photometric properties of the two fast stars FS1 and FS2. The table lists the radial velocity measurements from the IFU dataset (V_{IFU}) and the velocities measured from the Fabry-Perot data (V_{FP}). m_V and m_I are the V and I magnitudes of the stars and r_{cen} is the projected distance from the cluster center.

		FS1	FS2	FS3	FS4	FS5
α		−09 : 12 : 03.620	09 : 12 : 03.346	09 : 12 : 01.783	09 : 12 : 04.746	09 : 12 : 03.928
δ		−64 : 51 : 43.47	−64 : 51 : 43.16	−64 : 51 : 41.64	−64 : 51 : 50.79	−64 : 51 : 41.93
r_{cen}	[pc]	0.28	0.26	0.50	0.50	0.39
m_V	[mag]	13.56 ± 0.01	14.47 ± 0.01	14.25 ± 0.01	15.02 ± 0.01	15.68 ± 0.01
m_I	[mag]	11.35 ± 0.02	13.06 ± 0.02	15.51 ± 0.02	16.02 ± 0.02	16.78 ± 0.01
$V_{z,\mathrm{IFU}}$	[km s^{-1}]	−44.0 ± 1.8	−37.4 ± 0.3	-	−12.0 ± 6.0	-
$V_{z,\mathrm{FP}}$	[km s^{-1}]	−38.0 ± 2.3	−39.7 ± 2.4	42.0 ± 4.2	−36.0 ± 6.3	38.0 ± 3.9
$V_{x,\mathrm{PM}}$	[km s^{-1}]	8.6 ± 10.3	17.8 ± 7.0	-	22.4 ± 1.3	−12.6 ± 2.4
$V_{y,\mathrm{PM}}$	[km s^{-1}]	4.0 ± 5.0	13.2 ± 8.0	-	−9.6 ± 1.5	2.7 ± 1.5
V_{tot}	[km s^{-1}]	45.0 ± 2.7	43.5 ± 3.8	> 42	43.5 ± 5.0	40.1 ± 0.8

4.3 Possible explanations

Despite the uncertainties in the exact velocity, both stars lie more than $3\sigma_c$ above the systemic velocity of the cluster, where $\sigma_c = (13.4 \pm 0.2)\,\mathrm{km\,s^{-1}}$ (Chapter 3) represents the central velocity dispersion. Before investigating dynamical acceleration scenarios for the stars, we consider possible alternative explanations for the high velocities.

4.3.1 Foreground stars

The first possibility we consider is that the two stars are field stars and therefore moving with a different velocity than the cluster. We identify the two stars in our HST image (see Figure 4.1) and study their position on the color-magnitude diagram (CMD) which was obtained in Chapter 3. Figure 4.4 shows the position of all the stars in the CMD. Both stars are located on the giant branch, which suggests cluster membership. The three other stars are also most likely cluster members. FS1 is the brightest star in our pointing and sits at the top of the giant branch. The fact that the brightest star in our dataset is also the fastest is suspicious. This star is most likely a long period variable star and will be discussed in more detail in Section 4.3.3. The second star (FS2), however, lies in the central part of the giant branch about one magnitude fainter than FS1 and does not seem to show any peculiar photometric properties.

The fact that both stars lie on the giant branch of the cluster does not strictly exclude them from being foreground stars. Stars at a distance of a few hundred pc may also appear superposed on the giant branch of NGC 2808. In the case of FS2, a lower main sequence foreground star would be projected up on the giant branch if its apparent magnitude was increased by 8 to 9 magnitudes. This would imply that the star is located 40 - 60 times closer than a giant of similar apparent magnitude. That is, at a distance of $240 - 150\,\mathrm{pc}$ from us. FS1 is even more extreme. With a color $(B - V) \sim 1.9$, an equivalent dwarf star would have an apparent brightness increased by more than 12 magnitudes. This would mean that the star is 240 times closer to the sun than its giant equivalent and therefore at 40 pc distance from us.

In general the probability of contamination through galactic field stars is rather low. According to a galactic model by Ratnatunga & Bahcall (1985), the estimated number of field stars per square arcminute projected onto the central regions of NGC 2808 is 3.4×10^{-2} for $0.8 < (B - V) < 1.3$ (FS2) and 1.8×10^{-3} for $(B - V) > 1.3$ (FS1). The stellar population synthesis model of the Milky Way by Robin et al. (2004) can also be used to predict the number of foreground stars expected in this part of the sky. For a field of view of $0.5\,\mathrm{arcmin}^2$ at the position of $l = 282.19°$, $b = -11.25°$, the model does not predict any stars in the observed magnitude ranges ($m_V = 13.5 - 14.5$ mag, $m_I = 11.5 - 13.0$ mag). Also, the high radial velocity of NGC 2808 makes it easier to distinguish between field stars and cluster members.

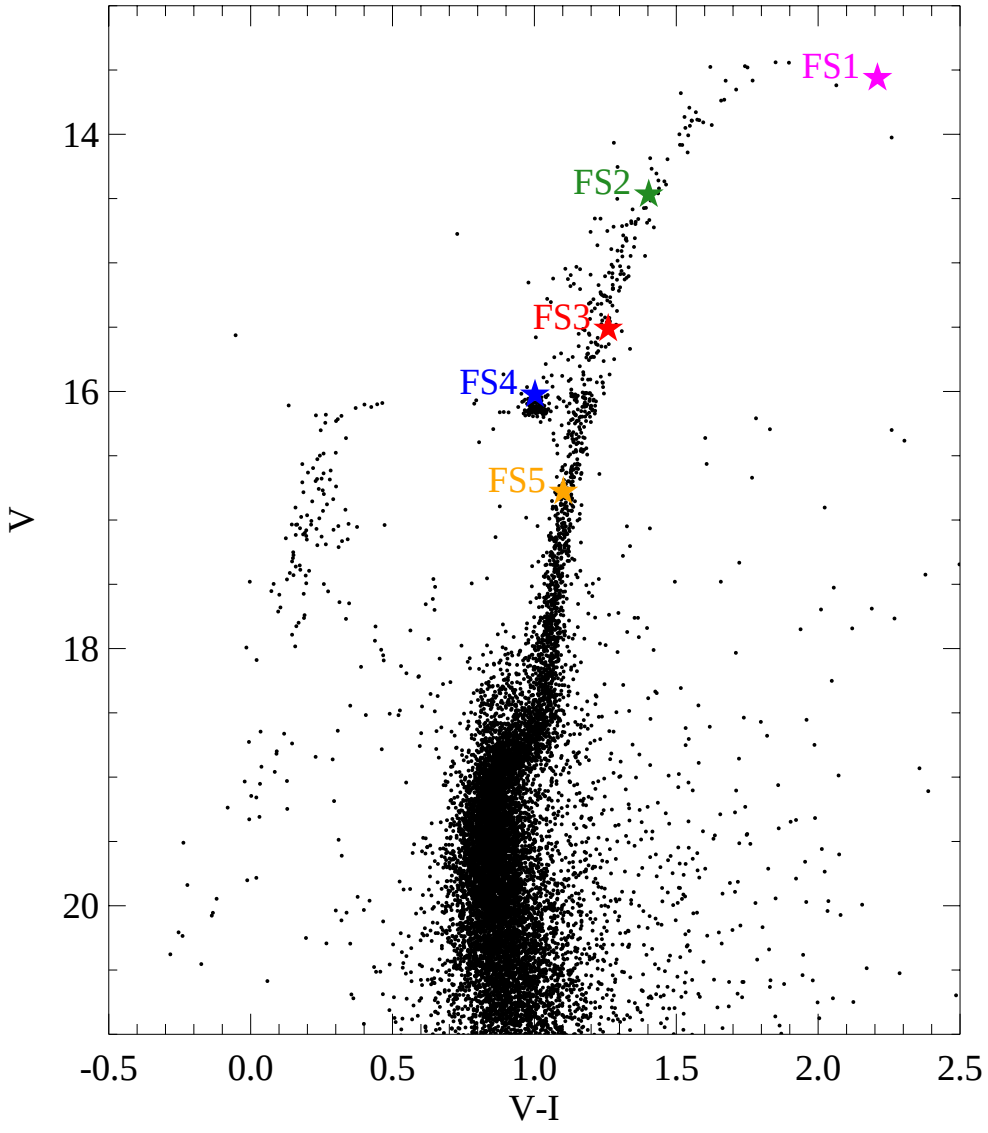

Figure 4.4: Color-magnitude diagram of NGC 2808 overplotted with the positions of the high-velocity stars FS1 to FS4. All of them are located on the red giant branch or the horizontal branch and therefore most likely cluster members.

Finally, neither star shows peculiar motions in the plane of the sky and the tangential velocities fall inside the velocity distribution of the cluster (see Table 4.1). This strongly argues for membership and a dynamical connection between the stars and cluster. Considering all these facts, we conclude that both stars are giants and associated to the cluster.

4.3.2 Binaries

The binary fraction in typical globular clusters is about 10 % (e.g. Rubenstein & Bailyn 1997; Davis et al. 2008; Dalessandro et al. 2011). Due to their higher dynamical mass, binaries tend to sink to the cluster center and become more concentrated in that region. This is why it is likely that binaries are present in our field of view. The possibility that these two fast stars are binaries, however, is rather low.

The fact that we measure very similar radial velocities at different epochs (IFU and Fabry-Perot datasets) with a time difference of 15 years already speaks against a binary scenario. Within this time period we should have seen large differences between the two measurements if the velocities were periodical. If we assume that the radial velocities that we measure for our two stars are their orbital velocities, a $\sim 1\,M_{\odot}$ companion would imply a separation of $\sim 0.5\,\mathrm{AU}$. The two stars are located on the giant branch and their radii are of about $7\,R_{\odot}$ (FS1) and $70\,R_{\odot}$ (FS2) (most likely lower limits), which are comparable to the presumed separation. This would indicate that these systems are in deep contact and that we should see signatures of accretion and mass transfer in the form of X-ray and UV excesses. Servillat et al. (2008) obtained X-ray observations with Chandra for the core of NGC 2808. Comparing their observations with our image, we see no match between our two stars and any of the X-ray sources detected. We also investigate a near and a far UV image obtained with the Space Telescope Imaging Spectrograph (STIS) on board the Hubble Space Telescope (Program ID: 8511). The stars are visible in the near UV but no source was detected in the far UV image. We conclude that these stars show no excess in either X-ray and UV which excludes almost all scenarios of contact binaries.

Sommariva et al. (2009) investigate the binary fraction of the globular cluster M4 via spectroscopy. They find 57 binary star candidates out of 2469 observed stars with 4 candidates inside the core radius. Looking at their table of candidates we find 7 binaries which show velocities $> 20\ \mathrm{km\,s^{-1}}$ in one of their orbital phases. Since the velocity dispersion of NGC 2808 is over twice as high as the one of M4 ($\sim 4\ \mathrm{km\,s^{-1}}$), total velocities around $40\ \mathrm{km\,s^{-1}}$ would be possible if the binary itself approached with a velocity $> 20\ \mathrm{km\,s^{-1}}$. However, all high velocity binaries in M4 lie in the upper main sequence and the turn-off region. There is no high velocity binary observed on the giant branch. To make a quantitative statement, we estimated the expected fraction of binaries with these properties and velocities higher than $45\ \mathrm{km\,s^{-1}}$ with binary population synthesis.

We assume a binary fraction of 10 % and use a log-normal orbital period distribution with a mean of $\langle \log\,(\mathrm{P/days}) \rangle = 4.8$ and a sigma of 2.3 as obtained by Duquennoy & Mayor

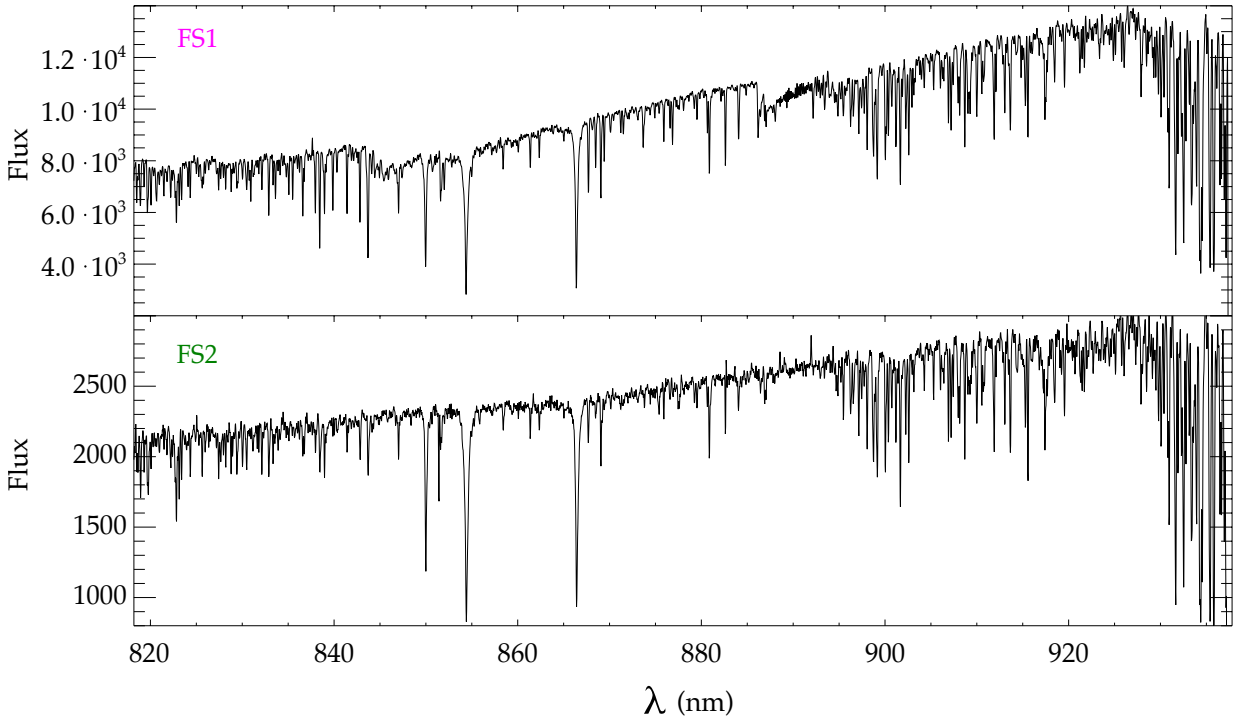

Figure 4.5: Spectra of the two fast stars extracted from the ARGUS integral field unit in the Calcium Triplet region. The lines of both stars are narrow and confirm the assumption that both stars are giants.

(1991). The binary components are chosen randomly from an evolved (over 12 Gyr) Kroupa initial mass function (IMF) to account for the age of NGC 2808. For the eccentricities we assume a thermal distribution of $f(e) = 2e$. Thus, for every binary we compute M_1, M_2, P and e. From P we derive the semi-major axis a and place both components (M_1, M_2) at random positions in their orbits. We then distribute the binary orientation randomly in space and add systemic velocities drawn from a velocity distribution with $\sigma = 13.4\ \mathrm{km\,s^{-1}}$. Finally we observe the binaries from a random position and count how often a giant star or main-sequence star with $M > 0.8\,M_\odot$ has velocities $|\mathrm{V}| > 45\ \mathrm{km\,s^{-1}}$. As additional boundary conditions we required that the pericenter distance of the binary is larger than the sum of the stellar radii, i.e. $a(1e) > (R_{*1} + R_{*2})$

Among the 1000 bright stars in our pointing we expect 0.0054 stars like FS2 ($R_* \sim 7\,R_\odot$) and only 0.00012 stars like FS1 ($R_* \sim 70\,R_\odot$) if their velocities originate from orbital binary velocities. To summarize, it is possible but highly unlikely that the high velocities we observe are due to orbital velocities in binary systems.

4.3.3 Atmospheric active stars

Another possibility is that these stars have active atmospheres, such as strong stellar winds or expanding shells which we would see as approaching velocities. According to its location in the CMD, FS1 is most likely a Mira star. Studies have shown that the amplitudes of Mira pulsations do not exceed 30 $\mathrm{km\,s^{-1}}$ (e.g. Hinkle 1978; Hinkle et al. 1982; Hinkle et al. 1997; Lebzelter et al. 2000; Lebzelter et al. 2005; Lebzelter & Wood 2011). Our stars show velocities faster than this limit. However, an explanation could be that these stars have radial velocities of about 20 $\mathrm{km\,s^{-1}}$ on top of their Mira pulsations.

Lebzelter & Wood (2011) recently investigated the long period variables of NGC 2808. Unfortunately, they had to exclude the inner regions of the cluster due to crowding. We identify their long period variable stars in our pointing and found two matches. The first one is LW 15 with a period of 332 days while the second one, LW 7, does not have a precise position and is therefore an uncertain candidate with a period of 21 days. We use the matches in our pointing to compare these spectra with our two fast stars. The spectra of the fast stars are shown in Figure 4.5. No conspicuous features were found in the Mira spectra nor in the spectra of the fast stars. The lack of studies of Mira spectra in the optical range, especially in the Calcium Triplet region, prevents us from making comparisons with other measurements.

Another argument against the pulsation velocities is the fact that optical lines usually form in the upper atmospheres where no shock waves can be observed. Also, these optical velocities are nearly always directed inward relative to the stellar center-of-mass as found by Wood (1979).

It is worth mentioning that we found no asymmetry in any of the lines used to measure the radial velocity. Assuming that the high velocity would come from an atmospheric effect, such as winds or expanding shells, one would expect the lines to be either asymmetric like p-Cygni profiles or even split into two parts which is often observed in Mira variables (eg. Scholz 1992; Lamers & Cassinelli 1999).

We conclude that thermal pulsations are an explanation for the high velocities of our two stars seem rather unlikely. The range of velocities reached by these pulsations is not high enough to explain the peculiar motions of the stars and unlikely to be strongly represented in optical lines.

4.4 The bound case - Maxwellian distribution

Having established that the most likely scenario is that the two stars do indeed have velocities exceeding more than three times the velocity dispersion of the cluster, we investigate possible acceleration mechanisms of dynamical nature. We first consider the case in which we assume that the stars are bound to the cluster. Under this assumption, the stars could have been accelerated either through encounters as giants or in their main-sequence stage.

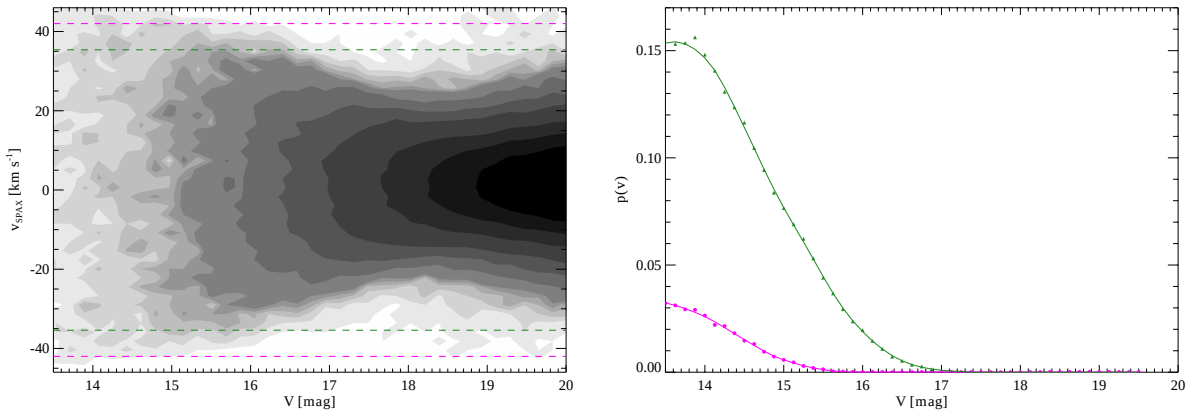

Figure 4.6: Monte Carlo simulations of recovering the radial velocities of v= 44 km s^{-1} and v= 37 km s^{-1} as a function of the magnitude of the star. The left panel shows the measured velocities of every spaxel from the 10^6 realizations as a density contour plot. The magenta and green lines mark the detection limits of 42 km s^{-1} and 35 km s^{-1} for FS1 and FS2 respectively. A spaxel with a velocity lower than 2 km s^{-1} (which corresponds to the error bars) minus the actual radial velocity is not considered to be a detection anymore. The right panel visualizes the probability of detecting a star with a radial velocity of 44 km s^{-1} (magenta) and 37 km s^{-1} (green) as well as their smoothed curves.

For the latter the acceleration can occur through either many two-body encounters or a single encounter with a more massive object. In this Section we discuss the first scenario and the likelihood of observing such an event.

4.4.1 Acceleration through uncorrelated two-body encounters

The first possibility we consider is that the stars acquired their high velocities through relaxation, i.e. a sequence of uncorrelated, distant encounters with other cluster stars over long timescales. In such a case they would be bound to the cluster and belong to the tail of the three-dimensional Maxwellian velocity distribution which is established by relaxation. However, stars with velocities $\sim 3.5\sigma$ are quite rare. The chance of detection decreases even more if one also considers the probability of detecting the high-velocity star in an integral-field unit (IFU) since the star has to be very bright to be detected. The final probability is composed of the probability of a Maxwellian velocity distribution with a certain velocity dispersion producing a high velocity star, the number of stars in our pointing and the probability of detecting such a star in our pointing.

In order to make a quantitative statement we calculate these probabilities in the following way. We use the velocity dispersion profile obtained in Chapter 3 to estimate σ at the position of the two fast stars. From this, we find that the stars have velocities of 3.2 and 3.1 times their local velocity dispersion. The probability of finding a star with a total velocity

V or higher from a three-dimensional Maxwellian velocity distribution is then given by:

$$p(x) = 1 - \left[\mathrm{erf}\left(\frac{x}{\sqrt{2}}\right) - \sqrt{\frac{2}{\pi}} x \mathrm{e}^{-x^2/2} \right], \tag{4.4}$$

with $x = \mathrm{V}/\sigma$.

With this information we can calculate how many stars we would expect among all the stars in the pointing using the stars which have been found in the HST image. In order to obtain the detection probability we run Monte Carlo simulations for 10^6 spaxels. For each simulated spaxel we draw 10 stars from the luminosity function. For 9 of them, we assign random total velocities from a Maxwellian velocity distribution with $\sigma = 13.4$ km s^{-1} as well as a random spatial orientation. The tenth star is always assigned a velocity value of 44 km s^{-1}. We build the spaxel in the following way: for each star we take the template spectrum, scale it with the flux of the star, and shift it with the amount of its projected radial velocity. Then we combine all 10 spectra to a single spaxel spectrum. The velocity of each spaxel is measured using the penalized pixel-fitting (pPXF) program developed by Cappellari & Emsellem (2004) as described in Chapter 3. Figure 4.6 shows the result of the Monte Carlo simulations. Plotted are all the 10^6 measured spaxel velocities as a function of the magnitude of the star with V = 44 km s^{-1} in the form of a density contour. This shows that the probability of detecting a high velocity star strongly decreases with the magnitude of the star.

In order to calculate the detection probability, we set the detection limit equal to the minimal velocities within the error bars (2 km s^{-1}), 42 km s^{-1} for FS1 and 35 km s^{-1} for FS2. Spaxel with velocities below this limit are not considered to be a detection anymore. The probability is obtained by deriving the fraction of stars which are faster than these limits in overlapping bins of 100 stars each. The right panel of Figure 4.6 shows the smoothed curve of the probability for FS1 (magenta) and FS2 (green). The plot shows that the probability to detect a star with a radial velocity of 37 km s^{-1} in the IFU is higher by almost a factor of 5 than a star with 44 km s^{-1} in the radial component and that for stars fainter than $m_V = 17$ both velocities are not detectable anymore.

To derive the expected number of stars with this configuration we multiply the luminosity function of stars in our pointing with the probability from the Maxwellian distribution and the detection probability from the Monte Carlos simulations and integrate over all magnitudes for both stars. As a final result we derive:

$$N_{r,\mathrm{FS1}} = 0.02 \text{ stars} \tag{4.5}$$

$$N_{r,\mathrm{FS2}} = 0.30 \text{ stars} \tag{4.6}$$

For further analysis we also derive the pure detection probability f_b, which accounts for (1) the geometric probability that the velocity component along the line of sight exceeds a

certain threshold velocity, and (2) the probability that the star is massive and bright enough to be detected in the IFU. The probabilities are derived in the same way as described above but without multiplying by the probability from the Maxwellian distribution. Thus we integrate only the probability function from the Monte Carlo simulations multiplied by the number of stars over the entire magnitude range. The derived detection probabilities for stars like FS1 and FS2 are $f_{b,\mathrm{FS1}} = 4 \times 10^{-4}$ and $f_{b,\mathrm{FS2}} = 4 \times 10^{-3}$, respectively.

We conclude that neither FS1 nor FS2 is likely to originate from the Maxwellian velocity distribution. The probability for a star such as FS2 is higher than that for FS1 by an order of magnitude but still too low to explain the observations with this mechanism. It is therefore unlikely that FS1 and FS2 acquired their high velocities through relaxation and we study other acceleration scenarios in the following Sections.

4.5 Dynamical encounters

The numbers we derive from the analysis of the Maxwellian distribution and observational effects are too small to explain the observed stars. Therefore we test for alternative acceleration scenarios due to dynamical three-body encounters of two different types of stars (main-sequence stars and giants) as described in this Section.

4.5.1 Acceleration in the main-sequence stage

Here we study a scenario in which FS1 and/or FS2 were accelerated by a single dynamical encounter at some time during the main-sequence stage. To test this possibility we perform numerical three-body scattering experiments (e.g. Hills & Fullerton 1980; Hut & Bahcall 1983; Sigurdsson & Phinney 1993; Heggie et al. 1996; Gvaramadze et al. 2008, 2009; Gvaramadze & Gualandris 2011) involving main-sequence stellar binaries and single stars/compact objects of different kinds. The simulations are carried out with the `sigma3` package included in the STARLAB software environment (McMillan & Hut 1996).

We adopt a mass of $m = 0.8\,M_\odot$ and a radius of $R = 0.8\,(M/\,M_\odot)^{0.7}\,R_\odot$ (Habets & Heintze 1981) for both stars, and we set the characteristic ejection velocity to $V_{\mathrm{ej}} = 45\,\mathrm{km\,s^{-1}}$.

We consider four types of binary-single star encounters, which are detailed in Table 4.2: (1) encounters with a main-sequence star of the same mass, (2) encounters with a $0.8\,M_\odot$ white-dwarf, (3) encounters with a $1.4\,M_\odot$ neutron star and (4) encounters with a $10\,M_\odot$ black hole. We consider a fifth type of encounters, between a binary containing a main-sequence star and a stellar mass black hole and single stars. Such binaries originate from the encounters of stellar binaries with single black holes.

We first discuss the simulations involving stellar binaries. As is typical in three-body scatterings, we use a Monte Carlo approach to randomly generate the angles that define the spatial orientation of the binary with respect to the incoming star. The binary eccentricity is

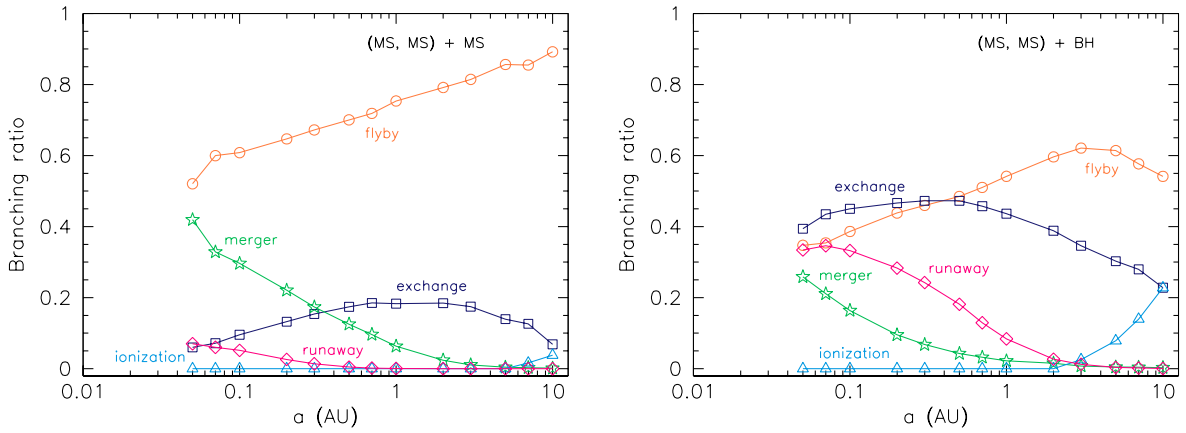

Figure 4.7: Branching ratios versus initial binary separation for the outcomes of encounters between a stellar binary and a main-sequence star E1 (left) or a stellar mass black hole E4 (right). The label "runaway" refers to encounters that produce an escaper with velocity larger than $45\,\mathrm{km\,s^{-1}}$.

randomly drawn from a thermal distribution (Heggie 1975), having set a maximum value to guarantee that the binary components do not come into contact at the first pericenter passage. The impact parameter b is randomized according to an equal probability distribution for b^2 with a maximum value that is determined automatically for each set of experiments (see Gualandris et al. 2004, for a detailed description). The relative velocity between the single star and the binary center of mass is set equal to the cluster velocity dispersion. We vary the initial semi-major axis of the binary from a minimum value $a_{\mathrm{min}} = 0.05\,\mathrm{AU}$ set by the radii of the stars to a maximum value $a_{\mathrm{max}} = 10\,\mathrm{AU}$.

While stars are treated as point particles in the integrations, all inter-particle distances are monitored to identify physical collisions when the distance between any two stars becomes equal to the sum of their radii. Since we are interested in the ejection of stars with high velocity, we neglect all encounters that result in a physical collision. While it is a priori possible to eject collision products during dynamical encounters, the fact that stars FS1 and FS2 lie precisely on the color-magnitude diagram of the cluster strongly argues against such a scenario.

Possible outcomes of three-body encounters include: flybys of the single star past the binary (F), exchanges of the incoming star into the binary (E), with ejection of one of the binary components, ionization (I) of the binary where three single stars get ejected, and collisions. For each type of encounter listed in Table 4.2, we consider all outcomes resulting in the ejection of (at least) one main-sequence star, and record the ejection velocity. Ionizations are rare and, for our set of parameters, only occur in the case of encounters with a black hole. In all the other cases, the binaries are too hard to be broken apart by the incoming star (see Figure 4.7). In the case of encounters between equal mass stars, the binary is always too hard to be unbound by the incoming star.

Figure 4.7 gives the branching ratios, i.e. the fraction of all encounters resulting in a

Table 4.2: Dynamical encounters between a main-sequence stellar binary and a single star. Here MS indicates a main-sequence star, WD a white dwarf, NS a neutron star and BH a stellar mass black hole. Outcomes of interest for the ejection of one of the MS stars include flybys (F), exchanges (E) and ionizations (I).

Name	Encounter	Outcomes
E1	(MS, MS) + MS	F, E, I
E2	(MS, MS) + WD	E, I
E3	(MS, MS) + NS	E, I
E4	(MS, MS) + BH	E, I
E5	(BH, MS) + MS	F, E, I

particular outcome, as a function of the initial binary separation, for model E1 and E4. The relative importance of flybys, exchanges and mergers is a strong function of the binary semi-major axis, with mergers occurring in about 40% of the cases for the tightest binaries.

The average velocity of all main-sequence escapers is shown in Fig. 4.8 for all types of encounters. Encounters with a main-sequence star produce average recoil velocities significantly lower than required for the observed runaways, for all considered values of the binary semi-major axis. Encounters with white dwarfs and neutron stars produce only slightly larger velocities, and reach the required $45\,\mathrm{km\,s^{-1}}$ only for the tightest binaries. Encounters with a stellar mass black hole, on the other hand, result in typical ejection velocities in excess of $45\,\mathrm{km\,s^{-1}}$ for all values of $a \lesssim 0.4\,\mathrm{AU}$. Given that these are average velocities, large velocities can occasionally be achieved even for larger separations.

If encounters with stellar-mass black holes lead to exchanges, they are expected to produce a star-black hole binary that will then interact with the dominant population of single, main-sequence stars. We find that such binaries typically have large eccentricities. For this reason, when simulating encounters of type E5, we generate binaries with a suprathermal eccentricity distribution. The branching ratios for this process are shown in Figure 4.9. Most encounters of this kind result in simple flybys or mergers. The average velocity of escaping main-sequence stars is given in Fig. 4.8 for the case of a $30\,M_\odot$ black hole. Only binaries with separation $\lesssim 0.1\,\mathrm{AU}$ produce average velocities larger than $45\,\mathrm{km\,s^{-1}}$. On average, higher black holes masses do not result in larger ejection velocities, because a larger fraction of encounters results in a collision.

The rate of ejection of runaway stars like FS1 and FS2 by encounters with a compact object can be estimated as

$$\mathcal{R} = n\,\Sigma\,\mathrm{V}\,, \tag{4.7}$$

where n is number density of stars in the core, Σ is the cross-section for the process and V is the relative velocity between the binary and the black hole. The cross section can be

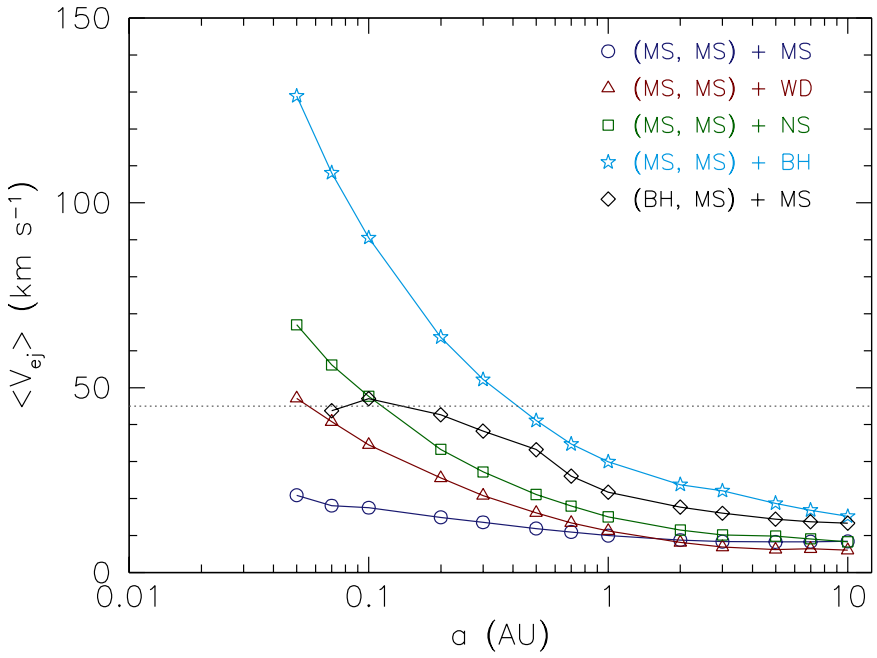

Figure 4.8: Average ejection velocities of all main-sequence escapers for the different types of encounters considered. For model E5, we adopt a black hole mass of 30 $M_{\odot}$. The dotted horizontal line marks the characteristic velocity of the runaways.

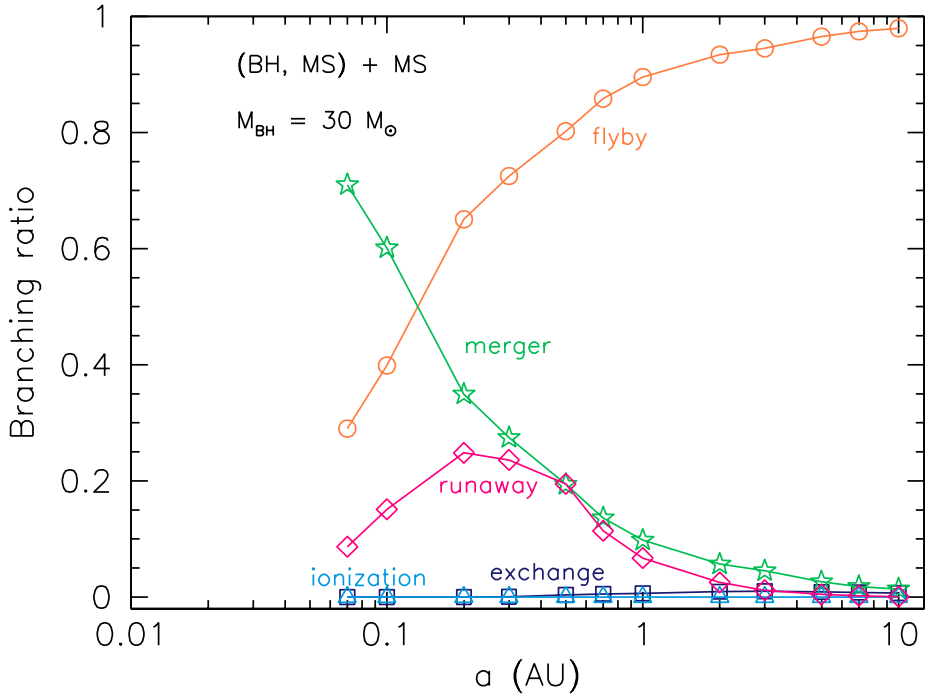

Figure 4.9: Branching ratios versus initial binary separation for the outcomes of encounters of type E5, in the case of a black hole of 30 $M_{\odot}$.

derived from the scattering experiments as

$$\Sigma = \pi\, b_{\rm max}^2\, f_r\,, \tag{4.8}$$

where $b_{\rm max}$ represents the maximum impact parameter for the process under consideration and f_r is the fraction of encounters resulting in escapers with velocity larger than $45\,{\rm km\,s^{-1}}$ (see Fig. 4.11). The rate for interactions is therefore

$$\mathcal{R} \approx 1.69\times10^{-9}\frac{1}{\rm yr}\left(\frac{n}{10^5\,{\rm pc^{-3}}}\right)\left(\frac{b_{\rm max}}{10\,{\rm AU}}\right)^2\left(\frac{\rm V}{10\,{\rm km\,s^{-1}}}\right)\,. \tag{4.9}$$

Finally, we multiply the event rate $\mathcal{R}$ as a function of the binary semi-major axis by the distribution function of the semi-major axis taken from Duquennoy & Mayor (1991). The final rates are shown in Figure 4.10, where we assume a relative velocity equal to the dispersion velocity in the core $V = 13\,{\rm km\,s^{-1}}$, and a stellar density $n = 10^5\,{\rm pc^{-3}}$. We obtain the central density by extrapolating our density profile ($n(0) = 10^6\,{\rm pc^{-3}}$) and multiplying this by a binary fraction of 10%. We caution that this is a mere working estimate derived from the total estimated stellar mass and the structural parameters of the cluster, and $\mathcal{R}$ scales linearly with the stellar density. The final rate is derived by integrating over all a.

The number of events producing runaway stars with velocity $\gtrsim 45\,{\rm km\,s^{-1}}$ is then

$$N_r = \mathcal{R}\, N_{\rm BH}\, T_{\rm rlx}\, f_b, \tag{4.10}$$

where $N_{\rm BH}$ is the number of BHs to be found in the core, $T_{\rm rlx}$ is the relaxation time of the core (the high velocity of the stars should decrease due to two-body relaxation within this time scale) and f_b the detection probability as obtained in Section 4.4.1.

Estimating the number of black holes in the cluster core is not straightforward. There are two factors which play a major role. The first one is the black hole retention fraction $f_{\rm ret}$, i.e. the fraction of black holes that does not escape the cluster due to kick velocities acquired during their formation. The second factor is how efficiently equal-mass black holes eject themselves from the cluster core by building a subcore through mass segregation. This process would leave only a few (0-3) black holes in the cluster (e.g. Sigurdsson & Hernquist 1993; Kulkarni et al. 1993; Miller & Hamilton 2002a; O'Leary et al. 2006). However, Mackey et al. (2007) find different results. In their N-body simulations, larger numbers of black holes are retained because the ejection rate of black holes decreases as the subcluster evolves. In order to estimate an appropriate number of black holes in the core of the globular cluster we use results from our own N-body simulations which are described in Lützgendorf et al. (2012, in preparation). Our results show that for a model with a retention fraction of $f_{\rm ret} = 0.3$ and $N = 128\,000$ particles there are only one or two black holes remaining after 12 Gyr. For higher retention fractions such as $f_{\rm ret} = 1.0$ this number increases to 20 black holes after 12 Gyr. With $N = 50\,000$ stars remaining, these values correspond to

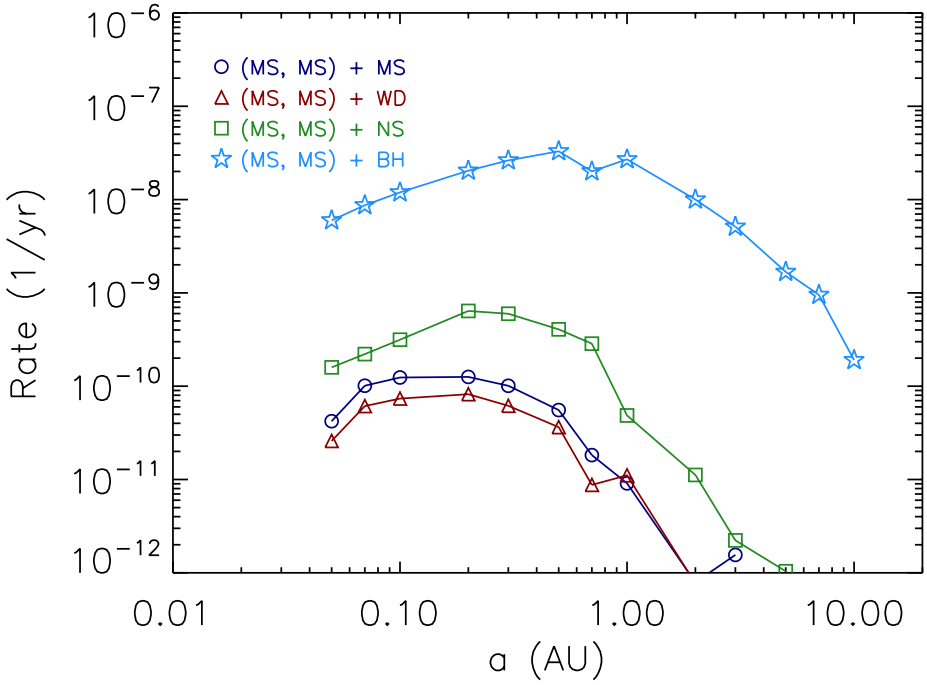

Figure 4.10: Event rates of the different encounters as a function of the separation multiplied by the distribution function of the semi-major axis. From this the final event rate can be achieved by integrating over the values for the semi-major axis.

black-hole fractions of $f_{BH} = N_{BH}/N_* = 2 \times 10^{-5}$ and 4×10^{-4} respectively, equivalent to 20 to 500 black holes in a cluster with 1×10^6 stars. These values are lower limits though, since we are not only interested in the number of black holes at the current time, but more so in the average number of black holes over the entire lifetime of the cluster. Therefore, an average black hole number of $N_{BH} \sim 100$ seems adequate as a first-order estimate.

Adopting a relaxation time $T_{\rm rlx} = 10^8\,$yr (Harris 1996), we find the expected number of runaway stars produced by encounters between a main-sequence binary and a stellar mass black hole to be:

$$N_{r,\rm FS1} = 0.3 \text{ stars} \quad (4.11)$$

$$N_{r,\rm FS2} = 3.4 \text{ stars} \quad (4.12)$$

The fact that the expected number of stars like FS1 is an order of magnitude lower than that of FS2 comes from the detection probabilities. A star like FS1 is less likely to be observed due to its brightness and the fact that its velocity vector has almost no tangential component. The expected number of stars like FS2 is in good agreement with our observation of the four other fast stars in NGC 2808.

Keeping in mind all the uncertainties that enter these estimates, we consider both of these numbers consistent with the observation of one star like FS1 and one like FS2.

Table 4.3: Dynamical encounters between a binary and a single star. FS1 and FS2 indicate the giant stars under consideration, MS indicates a main-sequence star, and BH a stellar mass black hole. Outcomes of interest for the ejection of one of the giant stars include flybys (F), exchanges (E) and ionizations (I).

Name	Encounter	Outcomes
G1	(FS1, FS1) + FS1	F, E, I
G2	(FS2, FS2) + FS2	F, E, I
M1	(FS1, FS1) + MS	E, I
M2	(FS2, FS2) + MS	E, I
M3	(FS1, MS) + MS	E, I
M4	(FS2, MS) + MS	E, I
B1	(FS1, FS1) + BH	E, I
B2	(FS2, FS2) + BH	E, I

4.5.2 The unbound case - Acceleration in the giant phase

The measured velocities for stars FS1 and FS2 are very close to the cluster escape velocity. This makes it hard to establish whether the two stars are bound or unbound to the cluster. Here we consider the case in which FS1 and/or FS2 received a recoil velocity during a recent dynamical encounter large enough to unbind them from the cluster.

We test the possibility that FS1 and FS2 were ejected from the cluster core by a dynamical encounter by performing numerical three-body scattering experiments similar to the ones described in Section 4.5.1. In this case, considering an ejection velocity of $45\,\mathrm{km\,s^{-1}}$ and the current projected distance of $\sim 0.3\,\mathrm{pc}$ from the cluster center, we can assume that the encounters that accelerated the two stars took place when the stars were already in the giant phase. This is an important assumption, and the one that distinguishes the encounters described in this Section from those in 4.5.1. Collisions in close encounters affect giant stars much more than they affect main-sequence stars due to the larger radii, and therefore larger cross-sections, of the giants.

We consider three main types of binary-single star encounters, which are detailed in Table 4.3: (1) encounters involving only giant stars (models G1, G2), (2) encounters involving giant and main-sequence stars (models M1, M2, M3, M4), and (3) encounters between a binary of giant stars and a black hole (BH) (of both the stellar and intermediate-mass kind). For each type of encounter listed in Table 4.3, we consider all outcomes resulting in the ejection of (at least) one giant star, and record the ejection velocity. Since we are interested in the ejection of giant stars with large velocities, we neglect all cases of collisions.

Encounters of star FS1 and FS2 with other giants (case G1 and G2), or main-sequence stars (case M1, M2, M3, M4) result in ejection velocities always much lower than $45\,\mathrm{km\,s^{-1}}$, for any value of the initial binary separation. It thus ruled out that any of the two high

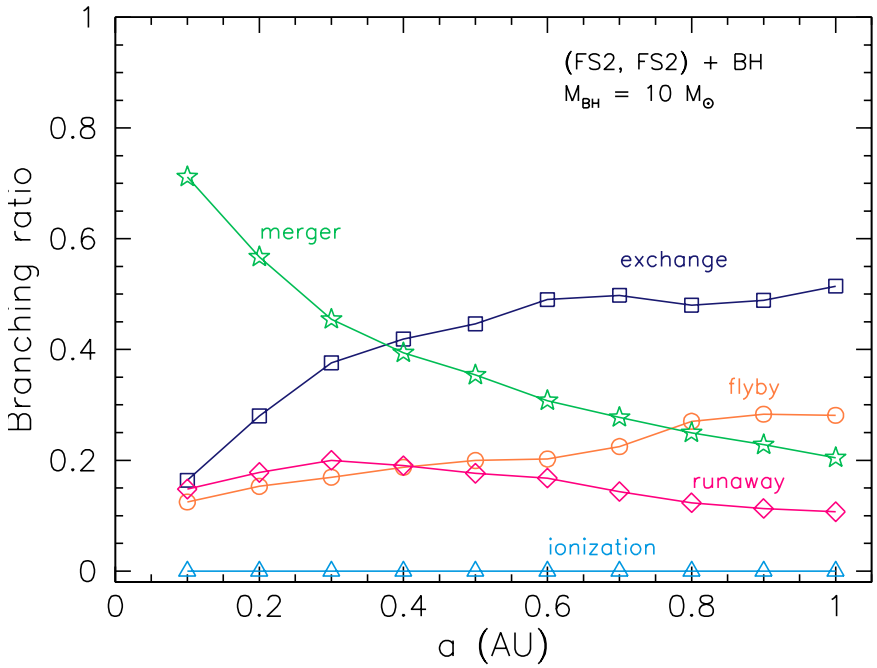

Figure 4.11: Branching ratios versus initial binary separation for the outcomes of encounters between a stellar binary and a black hole of 10 $M_\odot$ (model B2). The label "runaway" refers to encounters that produce an escaper with velocity larger than 45 km s^{-1}.

velocity giants were ejected by encounters with stars of the same mass, whether giants or main-sequence stars.

We also consider the case of encounters with black holes (BHs) of different masses. Figure 4.11 gives the branching ratios, as a function of the initial binary separation, for model B2. The relative importance of mergers and exchanges depends sensitively on the binary semi-major axis, with mergers occurring in more than 50% of the cases for $a \lesssim 0.2$ AU.

Average ejection velocities as a function of the initial binary semi-major axis are shown in Fig. 4.12, for models B1 and B2, and for different values of the BH mass $M_{\rm BH} = 10, 20, 50, 100\, M_\odot$. Velocity distributions for case B1 are shown in Fig. 4.13 for BH masses of $10, 50, 100\, M_\odot$ and the smallest value of the binary semi-major axis $a = 1$ AU. We find that stellar-mass BHs are sufficient to accelerate star FS2 to velocities of ~ 45 km s^{-1} for any value of the binary separation, and no BH of intermediate mass is required in the cluster to explain its velocity. Average ejection velocities for star FS1 are somewhat lower, due to the much larger size and therefore to the much larger number of close encounters that end with a collision. However, if we look at the distributions of ejection velocities for model B1, which are shown in Fig. 4.13 for the case $a = 1$ AU, we find that a 10 $M_\odot$ black hole is sufficient to produce ejection velocities of $40 - 45$ km s^{-1}.

We compute the ejection rates for this ejection mechanism in the same way as in Section 4.5.1. To obtain the final number of ejected stars, however, the relaxation time in Equation

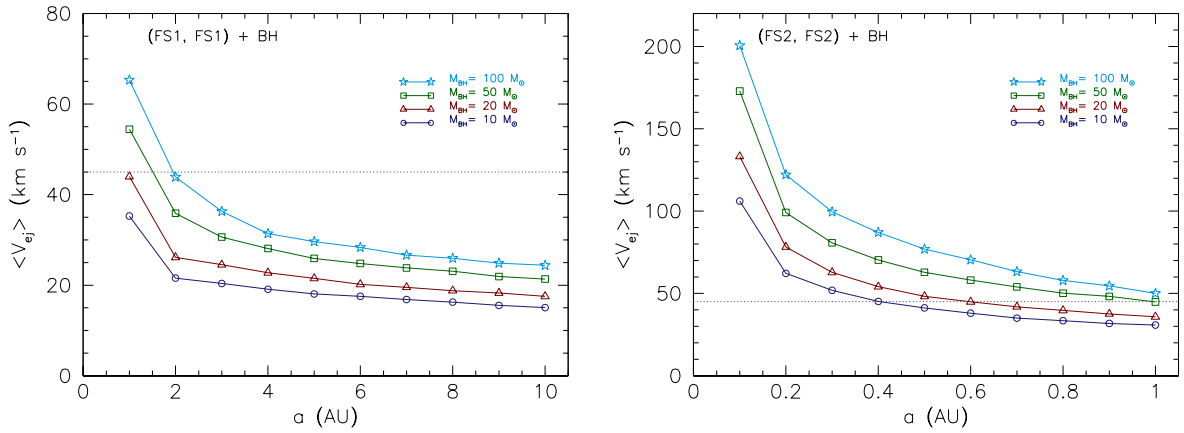

Figure 4.12: Average ejection velocity in runs B1 (left) and B2 (right) as a function of the initial binary semi-major axis. Different lines refer to different values of the BH mass, $M_{\rm BH} = 10, 20, 50, 100\,M_\odot$, respectively, from bottom to top. Dotted lines indicate the required ejection velocity of $45\,{\rm km\,s^{-1}}$.

Table 4.4: Expected numbers of stars if accelerated by an encounter of a giant and a massive black hole.

	NUMBER OF EXPECTED STARS			
	$10\ M_\odot$	$20\ M_\odot$	$50\ M_\odot$	$100\ M_\odot$
FS1	3.17×10^{-6}	1.46×10^{-5}	3.38×10^{-5}	3.77×10^{-4}
FS2	1.70×10^{-5}	2.21×10^{-5}	3.04×10^{-5}	6.37×10^{-5}

4.8 needs to be replaced with the crossing time of the core. With a typical velocity of $13\,{\rm km\,s^{-1}}$, the crossing time for a core diameter of 1.4 pc is $T_{\rm cr} \sim 10^5\,{\rm yr}$. This results in a final number of events as listed in Table 4.4. It is clear that the higher the black hole mass, the more stars with velocities larger than $45\,{\rm km\,s^{-1}}$ are produced. However, even a black hole of $10^3\ M_\odot$ would not be enough to produce an acceptable number of stars to explain the observations.

We conclude that a dynamical encounter between a binary of giant stars and a stellar-mass black hole of $\gtrsim 10\,M_\odot$ can produce giant stars with velocities $\sim 45\,{\rm km\,s^{-1}}$. However, the number of expected fast stars produced by this mechanism is one to three orders of magnitudes lower than our observations show. The reasons for this discrepancy are, on the one hand, the lower ejection rates due to the shorter timescales in which the stars will disappear from the field of view and, on the other hand, the fact that giant stars are less likely to achieve large velocities than main-sequence stars. For these reasons, this scenario is unlikely to have accelerated the observed runaways.

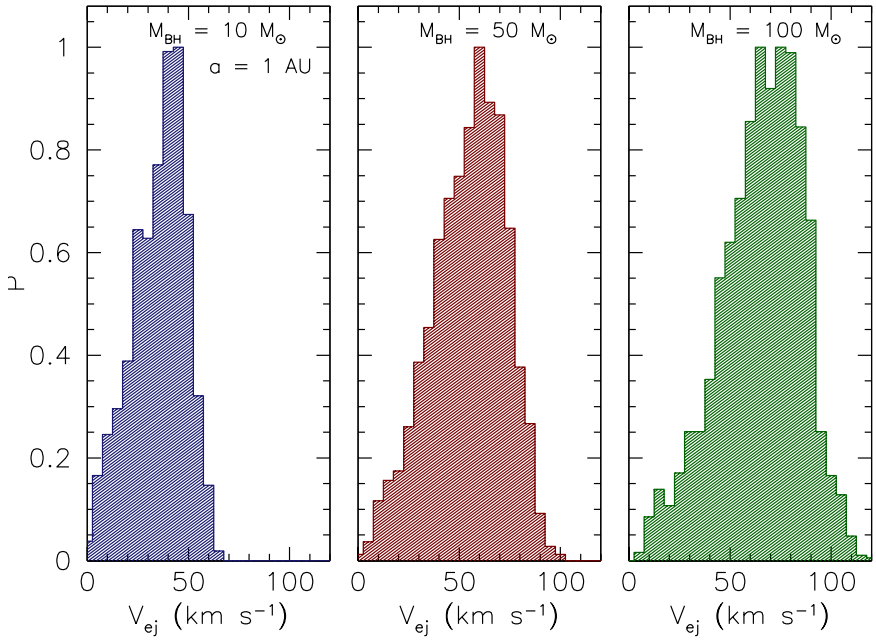

Figure 4.13: Distribution of ejection velocities in encounters between a binary of giant stars and a black hole (case B1). The three panels refer to BHs of different mass: $10, 50, 100\,M_{\odot}$, from left to right. The binary separation is set to 1 AU.

4.6 Comparison with other globular clusters

In Section 4.1 we mentioned the cases of M3 and 47 Tuc and their high-velocity stars. Meylan et al. (1991) argued that the two fast stars in 47 Tuc, which move with $3.6\sigma_c$ and $4.8\sigma_c$, must have been recently accelerated by encounters with a giant star, similar to our unbound case. The reason for this assumption is the fact that the velocities of these stars ($V_1 = -36.7$ km s^{-1}, $V_2 = 32.4$ km s^{-1}) are, within the errors, equal to the escape velocity $V_{esc} = 35.38$ km s^{-1} (Peterson & King 1975). This is a very similar situation to our case and therefore we would be more cautious in claiming the stars are bound or unbound. The argument of Meylan et al. (1991) that these stars could only recently have been accelerated is questionable. Furthermore, even if the velocities of the stars exceed the escape velocity by a few km s^{-1}, the probability that the stars are able to actually escape the cluster immediately remains low, since they are only able to escape by passing through small apertures near the Lagrange points L1 and L2. This can result in a significant delay of the escape of stars (Fukushige & Heggie 2000). For this reason it is a valid hypothesis that these stars also got accelerated in their main-sequence stage. Because the central density[1] $\log(\rho_0/\,\mathrm{pc}^{-3}) = 4.88$ and core relaxation time $\log(t_c/\,\mathrm{yr}) = 7.85$ (Harris 1996) of

[1]With the caveat that $\log(\rho_0)$ is measured with a different technique than our derived value and therefore lower than our actual central density for NGC 2808.

47 Tuc are very similar to the values of NGC 2808, the expected numbers of fast stars will be close to our derived numbers.

In the case of M3 the central velocity dispersion is lower than the one of NGC 2808 by 50 % ($\sigma_c = 4.9$ km s^{-1}). However, it is important to note that the absolute velocity dispersion is not the key factor, but rather its value relative to the velocities of the high-velocity stars. Gunn & Griffin (1979) measured velocities of 17.0 km s^{-1} and -22.9 km s^{-1} for two stars which are most likely cluster members. Again, these velocities lie in the same range as the escape velocity ($V_{esc} = 20.81$ km s^{-1}) but, as in the two previous cases, do not exceed this limit by much. The only difference with NGC 2808 and 47 Tuc is the central density of $\log(\rho_0) = 3.57$. This would lower othe expected number of high-velocity stars by an order of magnitude. Since this would most strongly affect the prediction for the unbound case, the most likely scenario for M3 is still that the stars are bound and were accelerated by a dynamical encounter with a massive object while they were in the main sequence phase.

The globular cluster NGC 6752 shows two millisecond pulsars outside the core: a recycled binary pulsar at more than three half-mass radii and a single pulsar at 1.4 half-mass radii. Such systems suggest the presence of a massive object in the center of the cluster. Colpi et al. (2002, 2003) show that the off-center location of the pulsars can be explained with scattering from a binary of stellar mass black holes or a single intermediate-mass black hole. This supports the idea that high-velocity stars in globular clusters may be produced by single or binary black holes.

4.7 Summary and conclusions

We detect five high-velocity stars in the globular cluster NGC 2808 using integral field unit spectroscopy as well as Fabry-Perot data for individual stars. All stars are $\sim 0.3 - 0.5$ pc away from the cluster center and their velocities correspond to $3.6 - 4.1\sigma_c$, where σ_c is the velocity dispersion in the core. All stars are very likely to be cluster members due to their positions in the CMD. Furthermore, we find that the proper motions of the stars are in good agreement with the proper-motion distribution.

For the case of the two fast stars found in the integral-field unit, we discuss various scenarios which could explain their peculiar motions. By performing a binary synthesis and looking at HST far UV and near UV images, we exclude the possibility of these stars being close binaries. Furthermore, we discuss the possibility of atmospherically active stars such as long period variables and conclude that this scenario can also be excluded due to a lack of spectroscopic evidence and general inconsistency with the observed velocity range.

The measured velocities of the stars are close to the estimated escape velocity from NGC 2808. For this reason, we consider two cases of acceleration: The bound case, in which the stars were accelerated while in the main-sequence stage; and the unbound case, in which the acceleration must have taken place recently. We perform numerical three-body

scattering experiments for both cases. In the bound case we also test the possibility that these stars belong to the tail of the Maxwellian velocity distribution by means of Monte Carlo simulations. In the case of three-body encounters of main-sequence stars and compact objects (the bound case) we consider four types of encounters: (1) encounters with a main-sequence star of the same mass, (2) encounters with a $0.8\,M_{\odot}$ white-dwarf, (3) encounters with a $1.4\,M_{\odot}$ neutron star and (4) encounters with a $\sim 10\,M_{\odot}$ black hole. To obtain the expected numbers of ejected stars, we calculate the event rates of each encounter producing a star with a velocity larger than 45 $\mathrm{km\,s^{-1}}$ as a function of the binary separation. Combining the rates with the log-normal orbital period distribution obtained by Duquennoy & Mayor (1991), we obtain the total event rate by integration.

Similarly, we test for the possibility of encounters with giant stars (the unbound case). As an input, we take the estimated properties of the two stars (radius and mass) and consider three main types of binary-single star encounters: encounters between giants, encounters of giant and main-sequence stars, and encounters including a black hole. We find that all encounters including only stars result in much lower escape velocities than the observed ones. Encounters between a binary of giants and a black hole, however, result in velocity distributions which peak at the observed velocities. Especially a black hole of $M_{BH} \sim 10\,M_{\odot}$ and a binary separation of $a = 1\,\mathrm{AU}$ predicts velocities around 40 $\mathrm{km\,s^{-1}}$ for star FS1. For star FS2, any separation produces large enough ejection velocities.

The scattering experiments show that no intermediate-mass black hole is needed in order to accelerate the stars to their velocities. Furthermore, only the encounters of main-sequence stars and compact objects have rates high enough to explain the observed stars. This leads us to the conclusion that the stars are bound and were accelerated by an encounter with a $\sim 10\,M_{\odot}$ stellar black hole. This cluster must thus have a high concentration of stellar-mass black holes in its center in order to make such an encounter likely enough to be observed. This is in agreement with the latest results on the central kinematics of NGC 2808 where no intermediate-mass black hole is detected Chapter 3. Such a retention of stellar remnants in evolving globular clusters is also in line with theoretical expectations, which allow up to $30\% - 50\%$ of the cluster mass to be constituted by remnants (Baumgardt & Makino 2003; Kruijssen 2009).

We compare our results with the two other known cases in which high velocity stars were detected in globular clusters, M3 and 47 Tuc. These cases are very similar to NGC 2808 and might therefore be explained with the same arguments. The high-velocity stars in these clusters are most probably products of encounters of main-sequence binaries with a massive black hole. For further analysis, N-body simulations could help verifying these results by running specific simulations dedicated to the statistics of fast stars and their origin. When combined with an analysis as carried out in this paper, this provides a general prediction for the origin of high-velocity stars in globular clusters.

Acknowledgements: *We thank Thomas Lebzelter, Mathieu Servillat and Dietrich Baade for sharing their knowledge and expertise. Also, special thanks go to Jay Anderson and his group for providing us with the proper motions and for the strong support of this project. This research was supported by the DFG cluster of excellence Origin and Structure of the Universe (www.universe-cluster.de). H.B. acknowledges support from the Australian Research Council through Future Fellowship grant FT0991052. We thank the referee, Steinn Sigurdsson, for constructive comments that helped improve the paper.*

CHAPTER 5

Limits on intermediate-mass black holes in six Galactic globular clusters with integral-field spectroscopy

Nora Lützgendorf, Markus Kissler-Patig, Karl Gebhardt, Holger Baumgardt, Eva Noyola, Tim de Zeeuw, Nadine Neumayer, Behrang Jalali, and Anja Feldmeier
Astronomy & Astrophysics, Volume 543, id.A82 (2012)

Abstract The formation of supermassive black holes (SMBHs) at high redshift still remains a puzzle to astronomers. No accretion mechanism can explain the fast growth from a stellar mass black hole to several billion solar masses in less than one Gyr. The growth of (SMBHs) becomes reasonable only when starting from a massive seed black hole with mass of the order of $10^2-10^5\ M_\odot$. Intermediate-mass black holes (IMBHs) are therefore an important field of research. Especially the possibility of finding them in the centers of globular clusters has recently drawn attention. We are investigating six galactic globular clusters for the presence of an intermediate-mass black hole at their centers. Based on their kinematic and photometric properties, we selected the globular clusters NGC 1851, NGC 1904 (M79), NGC 5694, NGC 5824, NGC 6093 (M80) and NGC 6266 (M62). We use integral field spectroscopy in order to obtain the central velocity-dispersion profile of each cluster. In addition we complete these profiles with outer kinematic points from previous measurements for the clusters NGC 1851, NGC 1094, NGC 5824 and NGC 6093. We also compute the cluster photometric center and the surface brightness profile using HST data. After combining these datasets we compare them to analytic Jeans models. We use varying M/L_V profiles for clusters with enough data points in order to reproduce their kinematic profiles in an optimal way. Finally, we vary the mass of the central black hole and test whether the cluster is better fitted with or without an IMBH. We present the statistical significance, including upper limits, of the black-hole mass for each cluster. NGC 1904 and NGC 6266 provide the highest significance for a black hole. Jeans models in combination with a M/L_V profile obtained from N-body simulations (in the case of NGC 6266) predict a central black hole of $M_\bullet = (3 \pm 1) \times 10^3\ M_\odot$ for NGC 1904 and $M_\bullet = (2 \pm 1) \times 10^3\ M_\odot$ for NGC 6266. Furthermore, we discuss the possible influence of dark remnants and mass segregation at the center of the cluster on the detection of an IMBH.

5.1 Introduction

The study of globular clusters has recently provided some fascinating new discoveries. Not long ago, globular clusters were assumed to be single population, isotropic stellar systems, formed by a single starburst in the early universe. With new generation instruments and space telescopes, however, this point of view has changed. Multiple stellar populations have been detected in many globular clusters and indicate a complicated formation mechanism (eg. Bedin et al. 2004; Piotto et al. 2007; Piotto 2008). Also, several clusters show rotation and high radial anisotropy in their outskirts (Ibata et al. 2011) and turned out to be more complicated dynamical systems than previously assumed. Further, over the last decade, hints were found that massive central black holes reside at the centers of some globular clusters (e.g. Gebhardt et al. 2005; Noyola et al. 2008, and Chapter 2), although other studies challenge these findings (e.g. van der Marel & Anderson 2010; Strader et al. 2012).

Intermediate-mass black holes are defined as covering a mass range of $10^2 - 10^5\ M_\odot$ and have become a promising field of research. With their existence it could be possible to explain the rapid growth of supermassive black holes, which are observed at large redshifts (Fan 2006) by acting as seed black holes (eg. Ebisuzaki et al. 2001; Tanaka & Haiman 2009). Further, detections of ultraluminous X-ray sources at off-center positions in distant galaxies (eg. Matsumoto et al. 2001; Fabbiano et al. 2001; Soria et al. 2010) suggest intermediate-mass black holes, supposedly originating from accreted and disrupted globular clusters or dwarf galaxies. Another motivation for searching for intermediate-mass black holes is the observed relation between the black-hole mass and the velocity dispersion of its host galaxy (e.g. Ferrarese & Merritt 2000; Gebhardt et al. 2000a; Gültekin et al. 2009). Exploring this relation in the lower mass range, where we find intermediate-mass black holes, will give important information about the origin and validation of this correlation.

The formation of intermediate-mass black holes can occur by the direct collapse of very massive first generation stars (Population III stars, Madau & Rees 2001), or runaway merging in dense young star clusters (Portegies Zwart et al. 2004; Gürkan et al. 2004; Freitag et al. 2006). This makes globular clusters excellent environments for intermediate-mass black holes. The currently best candidates for hosting an intermediate-mass black hole at their centers are the globular clusters ω Centauri (NGC 5139, Noyola et al. 2008, 2010; van der Marel & Anderson 2010; Jalali et al. 2012), G1 in M31 (Gebhardt et al. 2005), and NGC 6388 (Chapter 2). All of these very massive globular clusters show kinematic signatures of a central dark mass in their velocity-dispersion profiles. For ω Centauri, van der Marel & Anderson (2010) investigated a large dataset of HST proper motions and found less evidence for a central IMBH than proposed by Noyola et al. (2008). Using a new kinematic center, however, Noyola et al. (2010) and Jalali et al. (2012) confirmed the signature of a dark mass in the center of ω Centauri and proposed a $\sim 40\,000\,M_\odot$ IMBH.

Table 5.1: Properties of the six globular clusters from the references: NG=Noyola & Gebhardt (2006), H= Harris (1996), PM=Pryor & Meylan (1993), M=McLaughlin & van der Marel (2005) and L=this work (see Section 5.2.2).

Parameter	NGC 1851	NGC 1904	NGC 5694	NGC 5824	NGC 6093	NGC 6266	Ref.
RA (J2000)	05 : 14 : 06.7	05 : 24 : 11.0	14 : 39 : 36.3	15 : 03 : 58.6	16 : 17 : 02.4	17 : 01 : 13.0	L
DEC (J2000)	−40 : 02 : 49.3	−24 : 31 : 27.9	−26 : 32 : 19.6	−33 : 04 : 05.3	−22 : 58 : 32.6	−30 : 06 : 48.2	L
Galactic Longitude l	244.51	227.23	331.06	332.55	352.67	353.57	H
Galactic Latitude b	−35.04	−29.35	30.36	22.07	19.46	7.23	H
Distance from the Sun D	12.1 kpc	12.9 kpc	34.7 kpc	32.0 kpc	10.0 kpc	6.9 kpc	H
Core Radius r_c	2.00″	5.6″	2.2″	1.4″	4.5″	6.6″	NG
Central Concentration c	2.32	1.72	1.84	2.45	1.95	1.70	H
SB slope α	-0.38 ± 0.11	-0.03 ± 0.07	-0.19 ± 0.11	-0.36 ± 0.16	-0.16 ± 0.07	-0.13 ± 0.08	NG
Radial Velocity V_r	320.5 km/s	206.0 km/s	−144.1 km/s	−27.5 km/s	8.2 km/s	−70.1 km/s	H
Velocity Dispersion σ	10.40 km/s	4.81 km/s	5.5 km/s	12.8 km/s	13.3 km/s	13.7 km/s	PM
Metallicity [Fe/H]	−1.22 dex	−1.57 dex	−1.86 dex	−1.85 dex	−1.75 dex	−1.29 dex	H
Total Mass $\log M_{tot}$	5.50 ± 0.04	5.32 ± 0.08	5.40 ± 0.06	5.86 ± 0.04	5.44 ± 0.44	5.92 ± 0.07	M
Reddening E(B-V)	0.02	0.01	0.09	0.13	0.18	0.40	H
Absolute Magnitude M_{Vt}	−8.33 mag	−7.86 mag	−7.81 mag	−8.84 mag	−8.23 mag	−9.18 mag	H

For G1, X-ray and radio emission were detected at its center. They are consistent with a black hole of the same mass as derived by kinematic measurements (Pooley & Rappaport 2006; Kong 2007; Ulvestad et al. 2007). This result, however, was recently challenged by Miller-Jones et al. (2012) who found no radio signature at the center of G1 when repeating the observations. Also Strader et al. (2012) investigated a set of globular clusters in order to test for X-ray and radio signatures of intermediate-mass black holes. All of their fluxes lead to very low upper limits on a possible black-hole mass. Further, Cseh et al. (2010) and Lu & Kong (2011) investigated radio and X-ray emission in the globular clusters NGC 6388 and ω Centauri, respectively and found upper limits of $\sim 1500\,M_{\odot}$ for NGC 6388 and $1100 - 5200\,M_{\odot}$ for ω Centauri. However, various assumptions about the gas accretion process, such as clumpyness of the gas distribution, accretion efficiency and the translation of X-ray fluxes to bolometric fluxes to black hole masses, have to be made. Thus, non-detection in X-ray and radio are difficult to interpret in terms of a black hole mass upper limit.

Kinematic observations of individual stars in the central regions of globular clusters are not trivial. Without adaptive optics or space telescopes the central regions are not resolved due to their enormous stellar densities. Integrated light spectroscopy and proper motions from space telescope measurements (where the observations are not limited by the seeing) are therefore currently the only methods to derive the very central kinematics.

When selecting a globular cluster candidate for investigating the possible presence of an intermediate-mass black hole we consider the absolute brightness of the cluster (since this is an indicator of its mass), its central velocity dispersion and the inner slope of its surface brightness profile. A massive cluster is much more likely to host a massive black hole than a less massive cluster, according to formation scenarios such as runaway merging, that require many massive stars in a dense environment to form a black hole. Furthermore, it has been suggested that the most massive globular clusters are stripped cores of dwarf galaxies and therefore also more likely to host central black holes. In addition, a high central velocity dispersion indicates a high mass concentration in the center of the globular cluster and, according to the observed $M - \sigma$ correlation, also a high black-hole mass. However, as shown in the case of M15, a rising velocity-dispersion profile is not always a sign for an intermediate-mass black hole (e.g. Dull et al. 1997; Baumgardt et al. 2003, 2005; van den Bosch et al. 2006). The dynamical state of that cluster also needs to be considered. A collapsed core, as in the case of M15, indicates a high level of mass segregation, that can also rise the velocity-dispersion in the center profile without needing to invoke a black hole.

N-body simulations have shown that a shallow cusp in the surface brightness profile is expected for a cluster hosting an intermediate-mass black hole (Baumgardt et al. 2005). The simulations predict slopes in the surface brightness profiles between $\alpha = -0.1$ to -0.3 (where α is the slope of the surface luminosity density $I(r) \propto r^{\alpha}$). The values of the slope of the six globular clusters in our sample are taken from Noyola & Gebhardt (2006) and listed in Table 6.1 together with other properties. The Galactic globular clusters NGC 1851, NGC 1904 (M79), NGC 5694, NGC 5824, NGC 6093 (M80) and NGC 6266 (M62) have

distances of $\sim 7-35$ kpc and belong to the more massive clusters of our Galaxy. We note that not all clusters fulfill all three criteria (high mass, high dispersion and intermediate surface brightness slope). However, it is important to also investigate clusters which are, at this stage, considered unlikely to host IMBHs in order to verify the assumptions and to compare the 'good' with 'bad' candidate systems. Systematic differences might help to identify hosts of IMBHs candidate in the future.

This paper is structured in the following way: Section 5.2 describes the photometric datasets, the computation of the color-magnitude diagrams, center determinations and derivation of the surface-brightness profiles. In Section 5.3 we describe the spectroscopic data and the reduction and in Section 5.4 the computation of the velocity maps as well as the velocity-dispersion profiles. The kinematic data is then combined with the photometric data and compared to dynamical Jeans models in Section 5.5. In the final Section 7.5 we summarize our results and discuss the conclusions we derive from the data analysis.

5.2 Photometry

We first analyze the photometric properties of our six clusters. This Section describes the various methods used to measure the cluster center and the light profiles. Since the photometric data are from different observations it is crucial to keep the analysis as homogeneous as possible in order to compare the results of the different clusters with each other.

5.2.1 Photometric catalogs

For our photometric analysis we use data from the Hubble Space Telescope (HST) Archive. For the majority of the clusters (NGC 1904, NGC 5694, NGC 5824, NGC 6266) the data were obtained with the Wide Field and Planetary Camera 2 (WFPC2) within different projects (see Table 5.2 for more details). When available, we use images in the filters *I* (F814W) and *V* (F555W, F606W), since the kinematic data were obtained in a wavelength range close to the *I* filter. However, only half of the clusters were observed in both filters. For NGC 1904, NGC 5694 and NGC 5824, only observations in the *B* (F439W) and V filters are available.

For NGC 6266 we additionally use data obtained with the Advanced Camera for Surveys (ACS) in the Wide-Field Channel in the filters *B* and *R* (F625W). Unfortunately, the high exposure time of $t = 340$ s saturated the brightest stars in the pointing. Therefore, we did not use these images for most of our analysis since we need the brightest stars in order to register them in our IFU pointing. The large field of view of the ACS is nevertheless useful to check our center determination.

All images are analyzed using *daophot II*, *allstar* and *allframe* by Stetson (1987). The routines are ideally suited for globular clusters since they were developed for photometry in

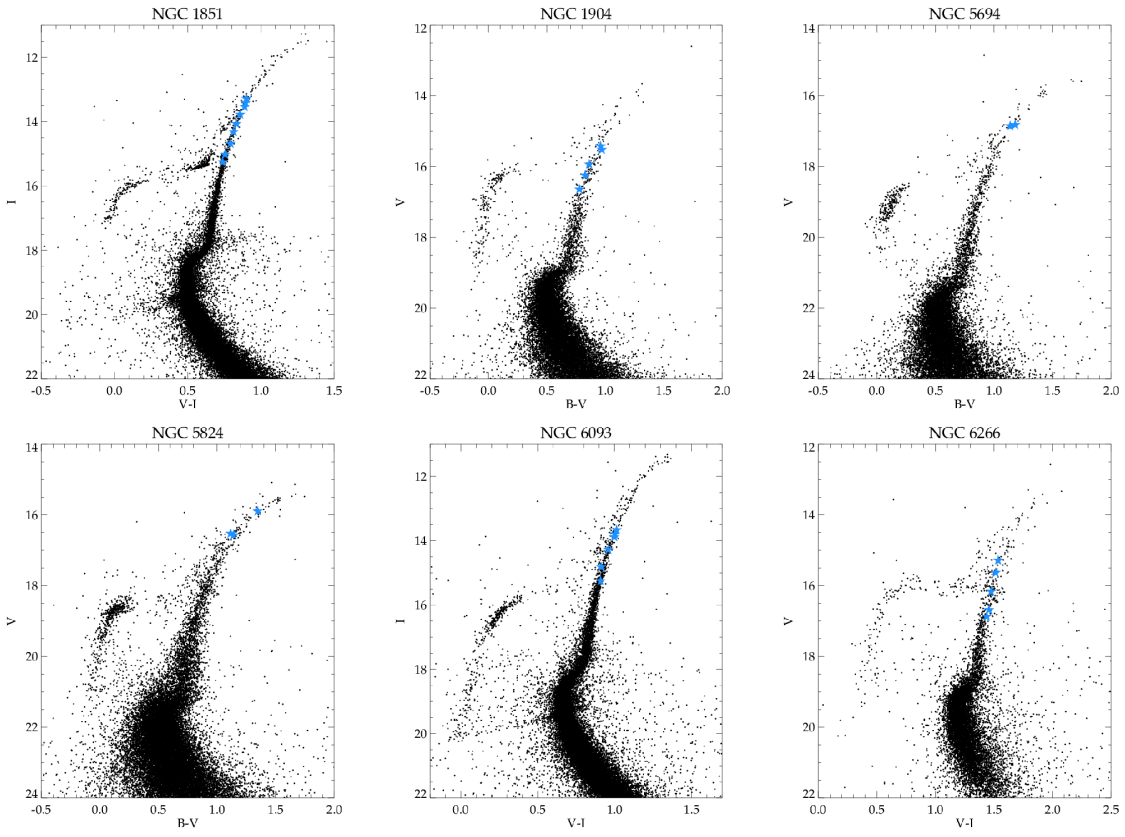

Figure 5.1: The color-magnitude diagrams of the six clusters of our sample. Overplotted are the stars which we used to create the combined template for the kinematic analysis (blue stars). For NGC 1851 and NGC 6093 the catalogs provided by Anderson et al. (2008) are used.

Table 5.2: HST observations of the clusters.

Cluster	Date	Pogram ID	Filters
NGC 1851	2006-05-01	GO-10775 (PI: Sarajedini)	F606W, F814W
NGC 1904	1995-10-14	GO-6095 (PI: Djorgovski)	F439W, F555W
NGC 5694	1996-01-08	GO-5902 (PI: Fahlman)	F439W, F555W
NGC 5824	1996-01-12	GO-5902 (PI: Fahlman)	F439W, F555W
NGC 6093	2006-04-09	GO-10775 (PI: Sarajedini)	F606W, F814W
NGC 6266	2000-08-21	GO-8709 (PI: Ferraro)	F555W, F814W
	2004-08-01	GO-10120 (PI: Anderson)	F439W, F625W

crowded fields. A detailed description of the individual steps can be found in Chapter 2. The stars are identified in the image and a point spread function (PSF) is fitted using the routines *find*, *phot* and *psf*. The task *allstars* then groups the neighboring stars to apply the multiple-profile-fitting routine simultaneously. Afterwards, the *find* task is applied again to find, in the star-subtracted image, stars which were not found in the first run. This procedure is performed in all bands independently and the catalogs are combined using the programs *daomaster* and *allframes*. After constructing the final catalog for the long and short exposures, we combine the two datasets and obtain the final catalog which is used for further analysis.

For NGC 1851 and NGC 6093 we use images and catalogs provided by the ACS Survey of Galactic Globular Clusters [1] (Anderson et al. 2008). The catalogs cover a large spatial area ($\sim 100''$) and provide very accurate photometry and astrometry for the clusters in the bands I and V. A high-quality science image (retrieved from the HST archive) which consists of the reduced, calibrated, and combined ACS images in the V-band is also available and is used for further analysis such as determining the surface brightness profile. Figure 5.1 shows the color-magnitude diagrams (CMD) of our six clusters overplotted with the template stars used for the kinematic analysis.

5.2.2 Cluster center determination

The center determination is critical for this work as errors in the center position can cause differences in the velocity-dispersion profile and the surface brightness profile as shown in the case of ω Centauri (Noyola et al. 2008; van der Marel & Anderson 2010), which is especially tricky due to its large core radius. Despite the small cores of the clusters in out sample, we find some differences in the position of the center with respect to previous measurements.

For the center determination we use the method described in Goldsbury et al. (2010). This method is based on isodensity contours which are fitted by ellipses to find the center. We overlay the star catalog with a grid of equally spaced points. The grid extends $20''$ in each direction for the WFPC2 images and $50''$ for the ACS images with a spacing of $2''$. On every point a circle is drawn with a radius of $4''$ (WFPC2) or $10''$ (ACS) and the density of stars in this circle is calculated. With this we create an isodensity contour plot of 8 contours. We flag and exclude grid points where the radius exceeds the image dimensions in order to avoid edge effects. Figure 5.2 shows the contour plots from the center determination for our six clusters. The gray shaded areas mark the grid points not affected by the image borders, while the pink shaded areas mark the ones we exclude from the analysis. Finally, we fit ellipses to the four innermost contours leaving out the central region since it is dominated by small number statistics. The center is derived by taking the average value of the different ellipse centers.

[1] available at http://www.astro.ufl.edu/~ata/public_hstgc/databases.html

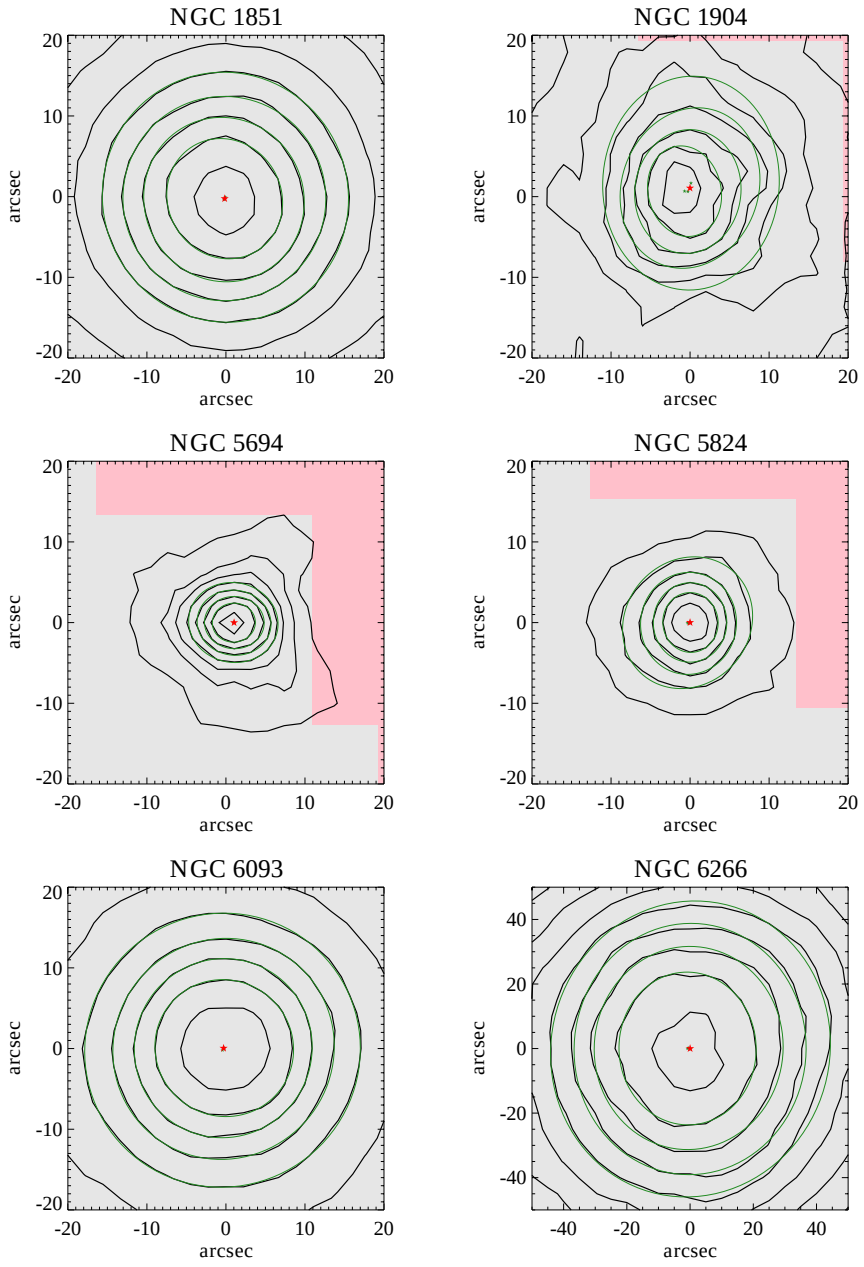

Figure 5.2: Isodensity contours for the center determination of our sample. The ellipses fitted to four of the contours are shown in green and the resulting center is marked by the red star. The different shades mark the area where the contours can be trusted (gray area) and where they are contaminated by edge effects (pink area).

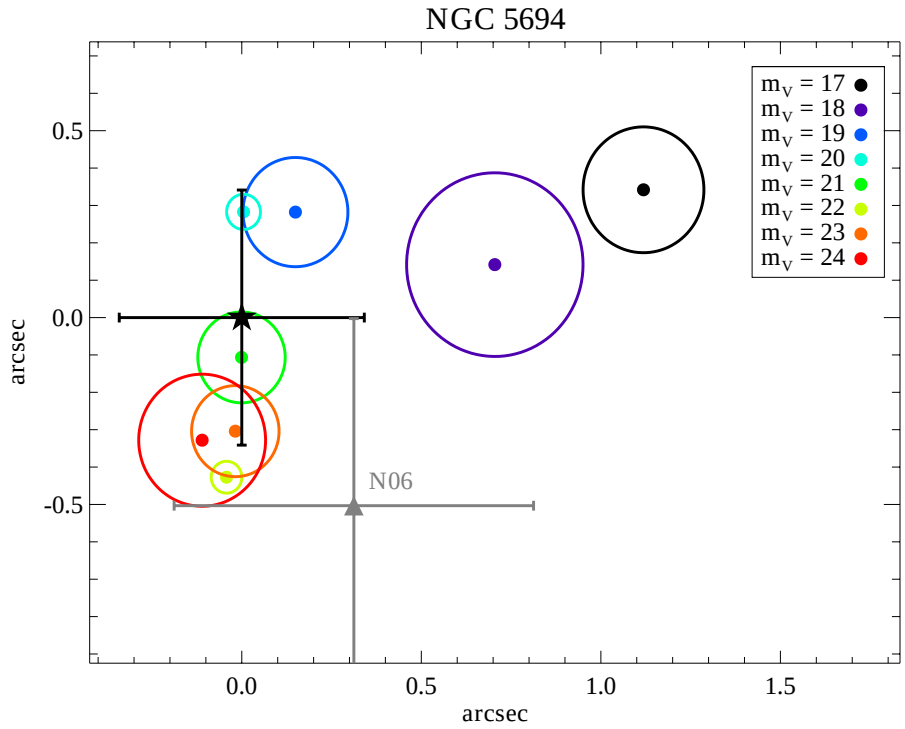

Figure 5.3: The center positions applying the isodensity method with different magnitude cuts for NGC 5694. The circles represent the error bars of the centers. Overplotted are also the final derived center (black star) and the center determined by Noyola & Gebhardt (2006) (gray triangle).

For the WFPC2 images, a larger grid and smoothing radius are desired in order to get wide and smooth isodensity contours. Our dataset for these clusters, however, is restricted to the small and asymmetric field of view of the WFPC2 chip. A larger smoothing radius than we use would enlarge the region of excluded points. The values listed above are the best compromise between smoothing and enough contours to fit.

We try different magnitude cuts on our catalog in order to investigate the effect on the center determination. We find that this changes the results by far more than the error bars would suggest. Figure 5.3 shows the different centers and their error bars for NGC 5694. The plot shows that the center moves depending on the magnitude cut. We observed this behavior in all of our clusters including the ones where we used ACS images. If the magnitude cut is too low and we include many faint stars then the analysis suffers from incompleteness in the center. This creates holes in the distribution of the faint stars where they are affected by bright stars (as described in Goldsbury et al. 2010). This biases the statistics towards these holes. On the other side, if the cut is too bright and we only have bright stars, the total statistics is dominated by shotnoise due to the small number of bright stars.

In order to get a stable estimate of the cluster center we use an error weighted mean of

the center positions for the cuts $m_V = 19, 20, 21, 22, 23$ (which show the smallest errors) and determine the error from the scatter. For the final result we adopt the maximum error for both dimensions. Figure 5.3 shows the final position of the center in comparison with the center obtained by Noyola & Gebhardt (2006).

In order to verify our results we tried further methods for the center determination. The first alternative method is using pie wedges instead of isodensity contours on the photometric catalog. For a grid of trial centers, a circle is applied to each center and divided into an even number of pie wedges. For each opposing wedge pair, the cumulative distribution of stars is derived and compared. From the differences between the wedges of one circle, each of the trial centers is assigned a value and a contour plot results. By deriving the minimum of this contour plot we derive the center of symmetry, thus the center of the cluster. This has been done for different numbers of pie wedges and orientations as well as the same magnitude cuts as in the previous method. We find the same behavior of the center position dependent on the magnitude cuts. After applying the same method for finding the average center position out of the different magnitude cut dependent centers, we have a very good agreement between the centers obtained with pie wedges and with isodensity contours.

As a third test we create isolight-density contours from the image. After masking out the brightest stars, the image is processed like the star catalogue by overlaying a grid with a spacing of $2''$, applying a circle with a radius $4''$, and evaluating the light per pixel evaluated for each grid point. From this, a contour plot is derived and ellipses fitted to find the center of the light distribution. Despite the masking, the contours are still very noisy due to contamination of bright stars. However, the centers derived from this method also agree within the errorbars with our previous centers. We use the isodensity contour center as our final result which is listed in Table 5.4. In addition, the finding charts for each cluster are shown in Figure 5.4.

We compare the derived center positions with the values obtained by Noyola & Gebhardt (2006). In Table 5.4 we list the distance of the two center positions. For all clusters the values agree well within our uncertainties and the uncertainty of Noyola & Gebhardt (2006, $\Delta = 0.5''$). The only exception is NGC 6266. For this clusters the two centers lie almost $3''$ apart from each other which is out of range for both uncertainties. Due to the unfortunate position of the center of NGC 6266 on the WFPC2 chip (close to the image boarder), the center position of Noyola & Gebhardt (2006) suffers from large uncertainties. We repeat the analysis of Noyola & Gebhardt (2006) with the new ACS image and find no discrepancy between the two centers. We therefore, conclude that the center derived in this work is more reliable due to the better quality of the ACS image.

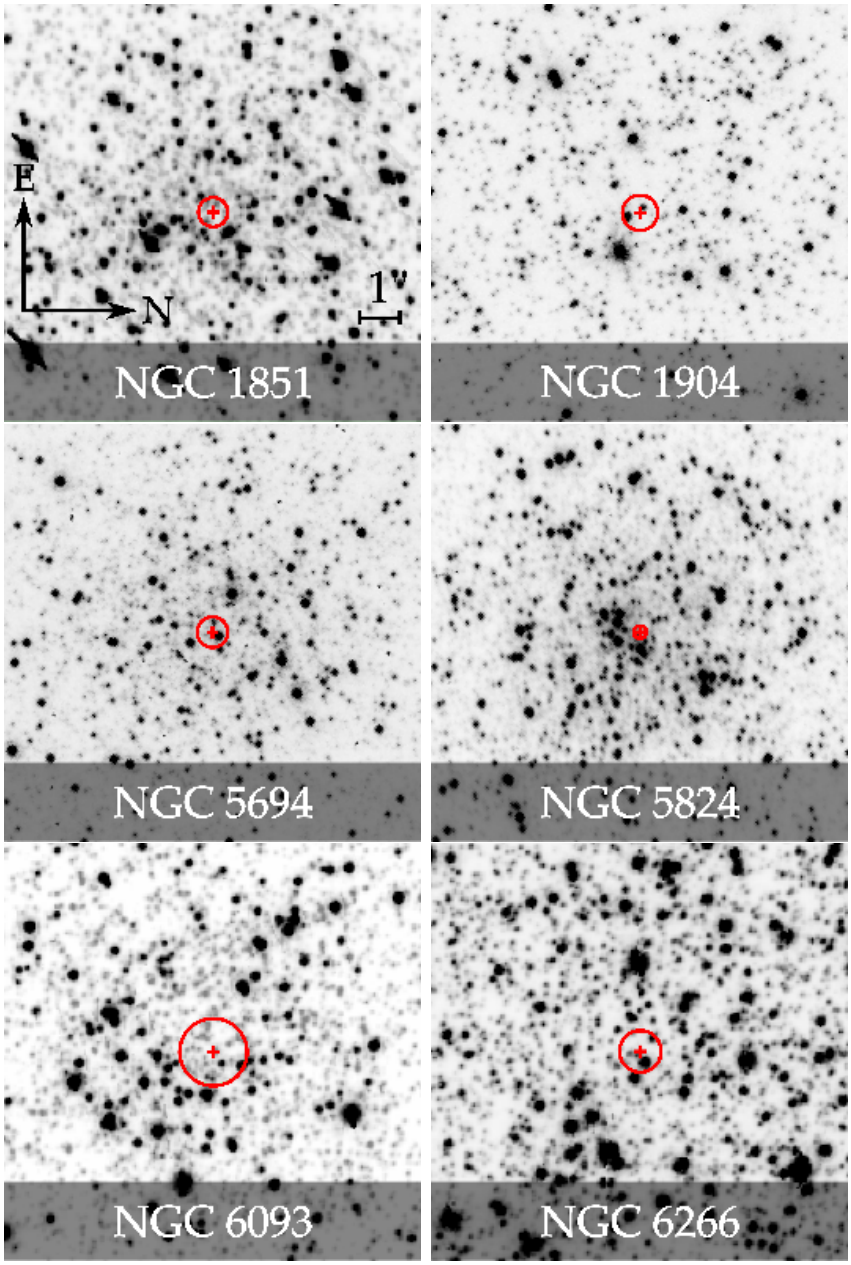

Figure 5.4: Finding charts for the centers of the six clusters. All images are orientated in the same way as the first one in the left panel. The size of the circle corresponds to the error of the center position.

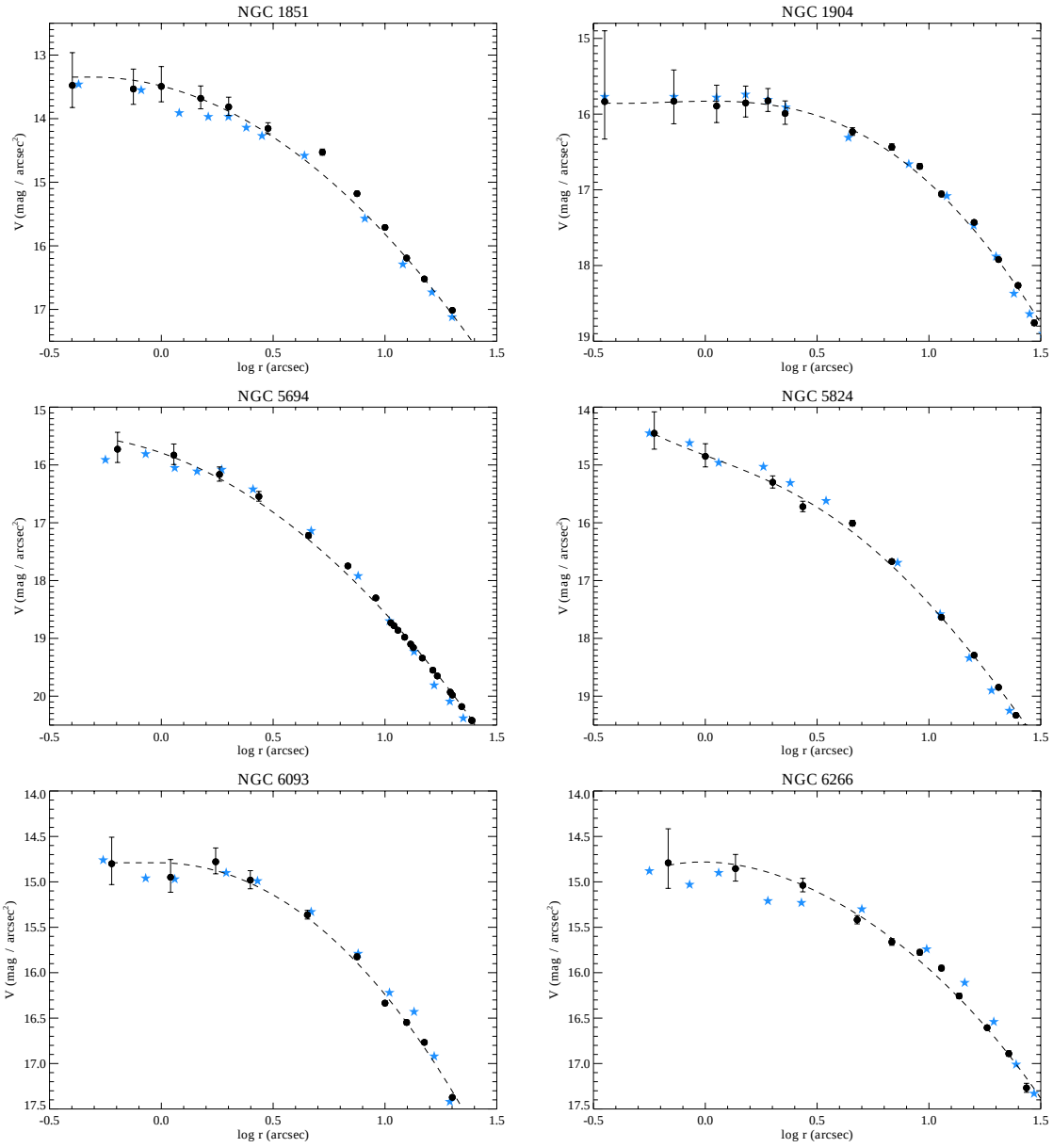

Figure 5.5: The surface brightness profiles of our six clusters. Black circles are the measured points with our method of combined pixel statistics and star counts, the blue stars show for a comparison the points from the profile obtained by Noyola & Gebhardt (2006). The dashed line shows our smoothed profiles.

5.2.3 Surface brightness profile

The next step in the photometric analysis is the computation of the surface brightness profile. This is needed as an input for the dynamical Jeans models and provides important information about the dynamical state of the cluster, e.g. if it is core collapsed or not. Due to the finite number of stars, a surface brightness profile is always affected by shotnoise. Therefore, deriving a smooth profile which can be easily deprojected is not straightforward.

As described in Chapter 3 we use a combination of pixel statistics and star counts. The pixel statistics are carried out by masking the bright stars in the image and drawing radial bins around the center. In each bin, the counts per pixel are estimated using a robust biweight estimator (Beers et al. 1990). The starcount profile is determined by taking the same bins and calculating the surface brightness density of the remaining bright stars which have been masked out in the previous method. The final profile is the combination of the two methods, scaled to the photometric points of Trager et al. (1995). The errors of the profile are derived from Poisson statistics of all stars in each bin. For radii larger than the extent of our images we complete the profile with the points from Trager et al. (1995). For NGC 1904 this method was not applicable, due to its low central stellar density. When splitting the area into individual stars and light, low number statistics cause large uncertainties. The surface brightness profile for this cluster was therefore derived by pixel statistics only.

Figure 5.5 shows the surface brightness profiles for all the clusters compared with the unsmoothed surface brightness profiles of Noyola & Gebhardt (2006, blue stars). The large difference between our SB profile and the one of Noyola & Gebhardt (2006) most probably occurs from the difference in the centers. However, except of two points, the profiles still agree within their errorbars. The profiles are not completely smooth. This is natural since a cluster with a finite number of stars never has a smooth profile. However, when deprojecting the profile, little uneven parts in the shape of the profile are enhanced and may create strong features in the resulting density profile. This then further affects the derived dynamical models. In order to avoid this we smooth our profiles before deprojecting them using Tschebychev polynomials (Noyola & Gebhardt 2006). The smoothed profiles are also shown in Figure 5.5 (dashed lines). From these profiles we derive the total luminosity in the V-band of each cluster using Multi-Gaussian-Expansions (Emsellem et al. 1994). The final photometric parameters are listed in Table 5.4.

In order to test how much the uncertainties in the center position affect the SB profile, we run Monte Carlo simulations on the center position and construct a new light profile on every generated center position. We find that the uncertainties produced from a center are within the errorbars of the SB profile and, as shown in Monte Carlo simulations in Chapter 3, will not effect the measurements on the black-hole mass.

Table 5.4: Photometric properties of the clusters in our sample. The columns are: (1) name of the cluster (2,3) position of the center on the image in pixel, (4) uncertainties in pixel, (5, 6) position of the center on the image in RA and DEC, (7) uncertainties in arcseconds, (8) reference image used for the center determination, (9) distance to the center derived in Noyola & Gebhardt (2006), and (10) total luminosity of the cluster.

Cluster	x_c (pix)	y_c (pix)	Δ (pix)	RA_c (J2000)	DEC_c (J2000)	$\Delta('')$	Reference Image	NG06 ($''$)	$\log L_{tot}(L_\odot)$
NGC 1851	2919	3011	7	05 : 14 : 06.7	−40 : 02 : 49.3	0.3	`ACS SURVEY`	0.1	5.25
NGC 1904	262	289	9	05 : 24 : 11.0	−24 : 31 : 27.9	0.5	`u2vo0402t_c0f.fits`	0.0	4.95
NGC 5694	453	367	8	14 : 39 : 36.3	−26 : 32 : 19.6	0.4	`u2y70105t_c0f.fits`	0.7	5.10
NGC 5824	365	313	3	15 : 03 : 58.6	−33 : 04 : 05.3	0.2	`u2y70205t_c0f.fits`	0.4	5.39
NGC 6093	3007	2943	16	16 : 17 : 02.4	−22 : 58 : 32.6	0.7	`ACS SURVEY`	1.0	5.18
NGC 6266	1764	3424	6	17 : 01 : 13.0	−30 : 06 : 48.2	0.3	`j92103050_drz.fits`	2.8	5.57

5.3 Spectroscopy

The inner kinematic data were obtained with the GIRAFFE spectrograph of the FLAMES (Fiber Large Array Multi Element Spectrograph, Pasquini et al. 2002) instrument at the Very Large Telescope (VLT) using the ARGUS mode (Large Integral Field Unit). NGC 6266 was observed in March 2010 and the other five clusters were observed in February 2011. The ARGUS unit was set to the 1 : 1.67 magnification scale (pixel size: 0.52″, 14×22 pixel array). Depending on the core radius and surface brightness the pointings were arranged symmetrically around the center with exposure times of either 600 s or 900 s. The orientation and placement of the individual pointings can be seen in Figure 5.6, where the final velocity maps are shown. For detailed information about the spectroscopic observations we refer to Table 5.5.

The observations were taken in the wavelength range of the Calcium Triplet ($\sim 850\,\mathrm{nm}$), a prominent absorption feature ideally suited for kinematic measurements (example spectra are shown in Figure 5.7). With the low spectral resolution mode set-up LR8 ($820 - 940\,\mathrm{nm}$, $R = 10400$) and sufficient S/N (~ 100) we can measure robust velocity dispersions down to $8\,\mathrm{km\,s^{-1}}$ with an accuracy of of 1-2 $\mathrm{km\,s^{-1}}$ using a nonparametric fitting algorithm. Below that value, we are sensitive to template mismatch and continuum placement. We report three velocity dispersions that are below $8\,\mathrm{km\,s^{-1}}$, where we have performed simulations in order to understand the uncertainties. While the uncertainties are measured robustly, bias in the values can be large comparatively. We do not attempt to estimate the bias for these low values since they will have little consequence for the enclosed mass profile given the other well-measured points.

The reduction of all clusters was done homogeneously using the GIRAFFE pipeline programmed by the European Southern Observatory (ESO) in combination with additional programs. The pipeline with its five recipes (*gimasterbias, gimasterdark, gimasterflat, giwavecalibration, giscience*) is described in more detail in Chapter 2. Before applying this pipeline, however, we use the program LA-Cosmic developed by van Dokkum (2001) to remove the cosmic rays from our raw spectra. The final routine *giscience* produces a reduced science frame as well as the extracted and rebinned spectra frame from the input observations. A reconstructed image of the respective field of view of the ARGUS observations is also produced by the pipeline. This is later used to match the observations with the HST image.

In order to subtract the sky from the spectra using the 14 skyfibres from the ARGUS observations, we use the IDL program *argus_specsub*[2] which uses the algorithm of a routine by Mike Irwin (Battaglia et al. 2008). The IDL version of the program does almost the same as the original program except the final cross correlation. For a detailed description of the routine see Battaglia et al. (2008) and Chapter 3. Due to cross talk between bright stars in object fibres and adjacent sky fibres, some of the sky fibres were contaminated and

[2]The IDL version can be found at http://nora.luetzgendorf.de

Table 5.5: Spectroscopic observations of the clusters. The columns list the cluster name, the Program ID of the individual observations, the exposure time of the ARGUS observation (t_{exp}), the numbers of exposures and the position angle of the ARGUS array (measured from North to East, the long axis aligned with North-South) for different pointings.

Cluster	Pogram ID	t_{exp} [s]	Exposures	Position Angle [degree]
NGC 1851	086.D-0573	600	24	0
NGC 1904	086.D-0573	600	12	0
		900	12	0
NGC 5694	086.D-0573	900	3	0
NGC 5824	086.D-0573	600	3	0
		900	6	0
NGC 6093	086.D-0573	600	12	0
NGC 6266	085.D-0928	600	9	0
		600	9	45
		600	9	90
		600	12	135

not usable for the analysis and therefore had to be excluded. In order to avoid bright stars dominating the averaged spectra when they are combined, we apply a normalization to the spectra by fitting a spline to the continuum and divide the spectra by it.

5.4 Kinematics

This section describes how the velocity map and the velocity-dispersion profile are derived and matched with the photometric data. The kinematic profile is later used to fit analytic Jeans models and set constraints on the mass of a possible black hole.

5.4.1 Registration of images

Before deriving the velocity for each spaxel, the single pointings need to be combined according to their relative shifts. This can be done by using the header information of each pointing and using their relative shifts to each other. This works well for pointings with the same position angle since the relative shifts are quite accurate. For rotated pointings and for absolute positions on the sky, the header information found in the reconstructed ARGUS pointings is not accurate enough. Due to the fact that ARGUS is not exactly rotated around its center, different rotation angles are offset from each other. For this reason, we have to reconstruct each ARGUS pointing on top of the HST image. This is

done by two-dimensional cross correlation. The HST image is convolved with a Gaussian according to the seeing of the VLT observations and iteratively cross-correlated with each of the ARGUS pointings. With this method we obtain an accurate position ($\sim 0.5''$) of the pointings on the HST images and thus, their absolute positions and relative shifts to each other. When available we used *I*-band images to do the cross correlation. For the ACS images no calibrated and combined *I*-band image was available. We therefore used the catalog to produce an artificial *I*-band image using the IRAF routine *mkobjects*.

5.4.2 Velocity map

The velocity map is computed by arranging the pointings according to their positions, overlaying a grid with a spaxel size of $0.52''$, and combining the spectra (e.g. in overlapping regions or multiple exposures) in each spaxel of the grid. The velocity of each spaxel is measured on the combined spectra using the penalized pixel-fitting (pPXF) program developed by Cappellari & Emsellem (2004).

In order to test individual spaxels for shot noise, we apply the same routines as described in Chapter 2. At every position of a star in the catalog, a two dimensional Gaussian is modeled with a standard deviation set to the seeing of the ground based observations (FWHM $\sim 0.8''$) and scaled to the total flux of the star. We measure the absolute amount and fraction of light that each star contributes to the surrounding spaxels. For each spaxel we then have the following information: a) how many stars contribute to the light of that spaxel, and b) which fraction of the total light is contributed by each star. As in the case of NGC 2808 (Chapter 3), we mask out spaxels for which either fewer than 10 stars contribute to the light, or a single star contributes more than 60 % of the light. This leaves us with 2/3 of the total number of spectra. We also test the effect of the mapping by comparing the velocity-dispersion profiles of the mapped and the unmapped spectra. The deviations are all within the uncertainties of the measurements and therefore not critical. However, in order to include any contribution by systematic errors we apply the mapping which also partly results in smoother profiles.

The template for measuring the velocities and velocity dispersions was taken from the same observations of each cluster in the following way: First, our shot noise routine calculates for each spaxel in the pointing how many stars contribute to the light of each spaxel. This is useful to mask spaxels which are dominated by a single star and to find the spaxels which could be used as templates. We select our template candidates by sorting out all spaxels where a single star contributes by more than 80 %. These are identified in the color magnitude diagram and excluded if they are possible foreground stars. For each of the clusters we select 6 - 10 template candidates, depending on how many stars are available.

The candidates are then divided into equal numbers of faint and bright stars. We bring all templates to the same velocity scale by measuring the relative velocities and shifting them and we combine the faint and the bright candidates to two master templates. We perform

the kinematic measurements with the faint and the bright master template. For most of the clusters we find that the combined faint template fits the data better than the bright template, except for NGC 1904 and NGC 5694 where the bright template fits better. We also fit the spectra using all individual templates where the weight on each template is a free parameter. This test results in high weights for the fainter templates. For all further analyses we use the best fitting master template (faint: NGC 1851, NGC 5824, NGC 6093, NGC 6266, bright: NGC 1904, NGC 5694). The positions of the stars used to create the master template for each cluster in the CMD are displayed in Figure 5.1 (blue star symbols).

The final velocity maps of all clusters are shown in Figure 5.6. The velocities are scaled to the reference frame of each cluster and the cluster centers are marked with the black crosses.

5.4.3 Inner velocity-dispersion profile

In order to fit our data with dynamical models and to estimate possible black-hole masses, we need a velocity dispersion profile. We obtain this profile by combining the spectra in radial bins around the center using a sigma clipping algorithm to remove any remaining cosmic rays. From the combined spectra we measure the velocity dispersion with the same template as for the velocity map using a non-parametric line of sight velocity distribution (LOSVD) fitting (Gebhardt et al. 2000b; Pinkney et al. 2003). In this method a LOSVD histogram is smoothed and convolved with the template spectrum and fitted to the observations using χ^2 statistics. In addition, the routine is able to fit for a continuum offset and an equivalent width. Several starting values such as the bin width of the LOSVD and the smoothing factor are tested by running Monte-Carlo simulations until the parameters are found which produce the smallest biases. This method turned out to be more stable at this resolution than pPXF which produces different results depending on whether one fits two (V, σ) or four (V, σ, h_3, h_4) Gauss-Hermite moments. We find that the pPXF results are consistent within the uncertainties with the non-parametric fits when fitting four moments. We also try different combinations of bins in order to find the smoothest profile for each cluster.

The errors are estimated in two ways: The first one originates from the kinematic measurements and is derived through Monte-Carlo simulations of the observed spectra for 100 different realizations. The scatter in the results is then determined using a robust biweight estimator. The second error is calculated from the shotnoise in each bin as described in Chapter 3. For each bin we run Monte Carlo simulations using the information from our shot noise routine described in Section 5.4.2. With this information we know how many stars contribute by what amount to each spaxel, and how many spaxels are added up in each bin. We simulate a spaxel by assigning random velocities, drawn from a Gaussian distribution ($\sigma = 10$ km s^{-1}), to each star contributing to a spaxel, shifting the template spectra by this velocity and averaging the spectra after weighting them by their luminosity. The resulting spaxels are normalized, combined and the kinematics measured. The shot-

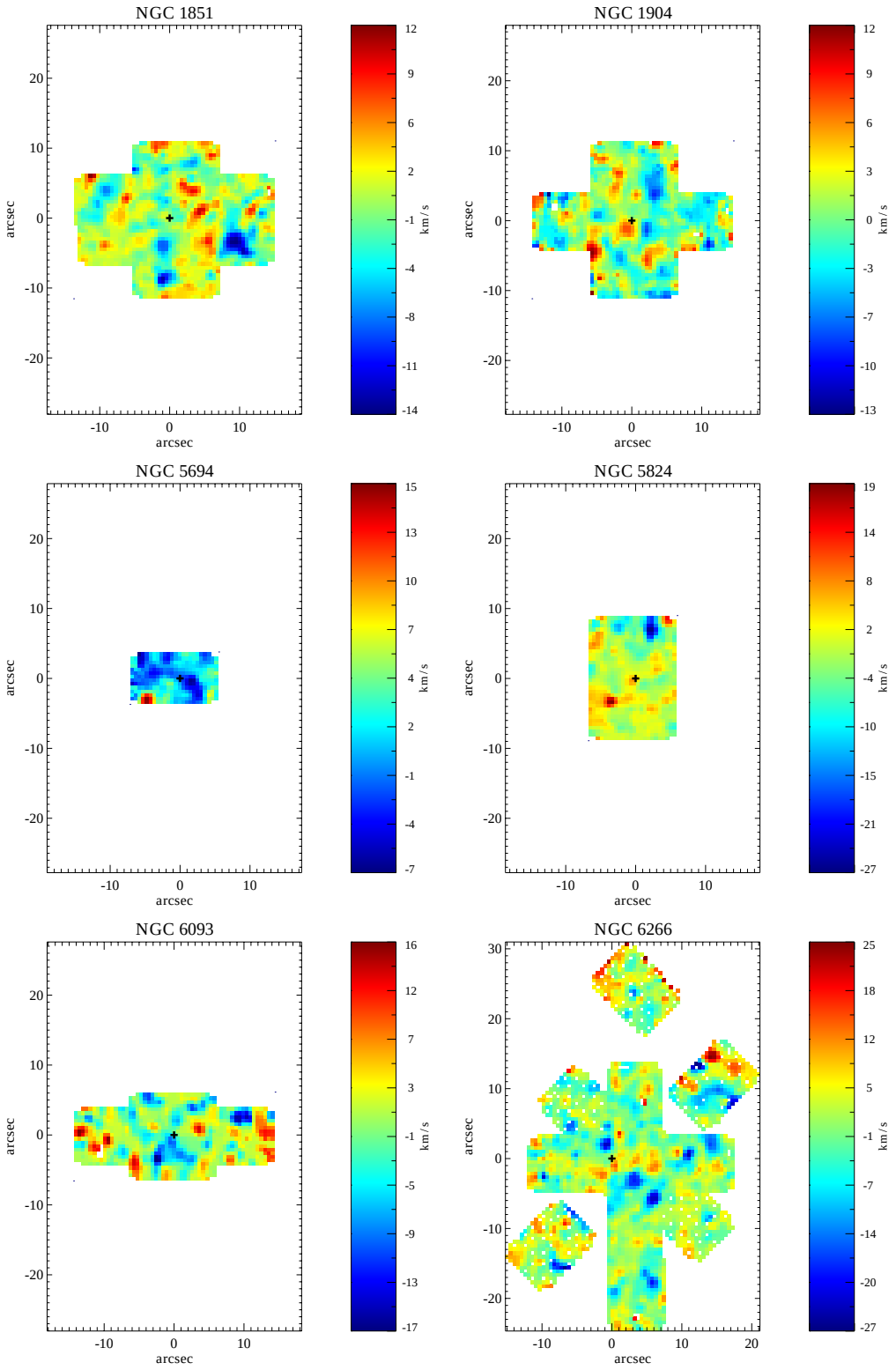

Figure 5.6: The final velocity maps of the clusters in our sample. The velocity scale has been adjusted to the mean velocity of each cluster. The black cross marks the center of the cluster. The orientation is the same as in Figure 5.4

noise error for each bin is derived from the spread in the dispersion measurements of the fake spaxel after 1000 realizations. The final value results from a quadratic summation of both errors assuming that they are independent of each other. Table A.1 lists the derived kinematic profiles for all clusters together with additional outer kinematics as described in the next section.

In addition to the velocity dispersion profile, we estimate the radial velocity of the cluster in a heliocentric reference frame and the effective velocity dispersion σ_e. The radial velocity is measured by combining all spectra in the pointing and measuring the total velocity relative to the velocity of the template. After correcting this value for the motion of the template and the heliocentric velocity, the absolute radial velocity of all clusters is derived. The values are listed in Table 5.7 together with the other results from the spectroscopic analysis. As in Chapter 3 we determine the effective velocity dispersion using equation (1) in Chapter 2 by adopting the half-mass radius as the effective radius. σ_e is also listed them in Table 5.7.

5.4.4 Outer kinematics

In addition to the inner velocity-dispersion points we use outer kinematic points, if available, to constrain the mass-to-light ratio of the clusters. Outer kinematics are available for NGC 1805, NGC 1904, NGC 6093 and NGC 5824. For NGC 1851 and NGC 1904 they are taken from the dataset obtained by Scarpa et al. (2011) using the FLAMES multi-object spectrograph. The dataset was obtained in order to test Newtonian gravity in globular clusters and therefore extends to large radii ($\sim$ 30 pc). The observations were carried out from November 2007 to March 2008 by using the HR9B setup of the FLAMES spectrograph which covers the wavelength range of the magnesium triplet (5143 Å $< \lambda <$ 5346 Å) at resolution $R = 25\,900$. For further description of the data and data reduction we refer to Scarpa et al. (2011).

The data set contains 199 stars for NGC 1851 and 173 stars for NGC 1904 with positions and radial velocities. We measure the outer velocity-dispersion profile by binning the data into bins containing $\sim$ 50 stars each and evaluating a velocity dispersion using a maximum likelihood method introduced by Pryor & Meylan (1993). The final profiles are shown in Figure 5.8 and 5.9 together with the inner kinematic points.

For NGC 5824, we use data obtained with the Rutgers Fabry-Perot on the Blanco 4-m telescope at Cerro Tololo Inter-American Observatory (CTIO) observed in March 1994. The Fabry-Perot velocities come from a very similar set of observations and reductions as presented in Gebhardt et al. (1997). These spectra are centered on a small region around the Hα absorption line, with absolute velocity calibration derived from comparison with published radial velocities. Due to the fact that the data set only contains $\sim$ 100 stars, only one kinematic point can be extracted from the sample. This data point, however, is still useful and included in the velocity dispersion profile of NGC 5824 (Figure 5.11).

The outer kinematics for NGC 6093 were taken with a different Fabry-Perot instrument. As

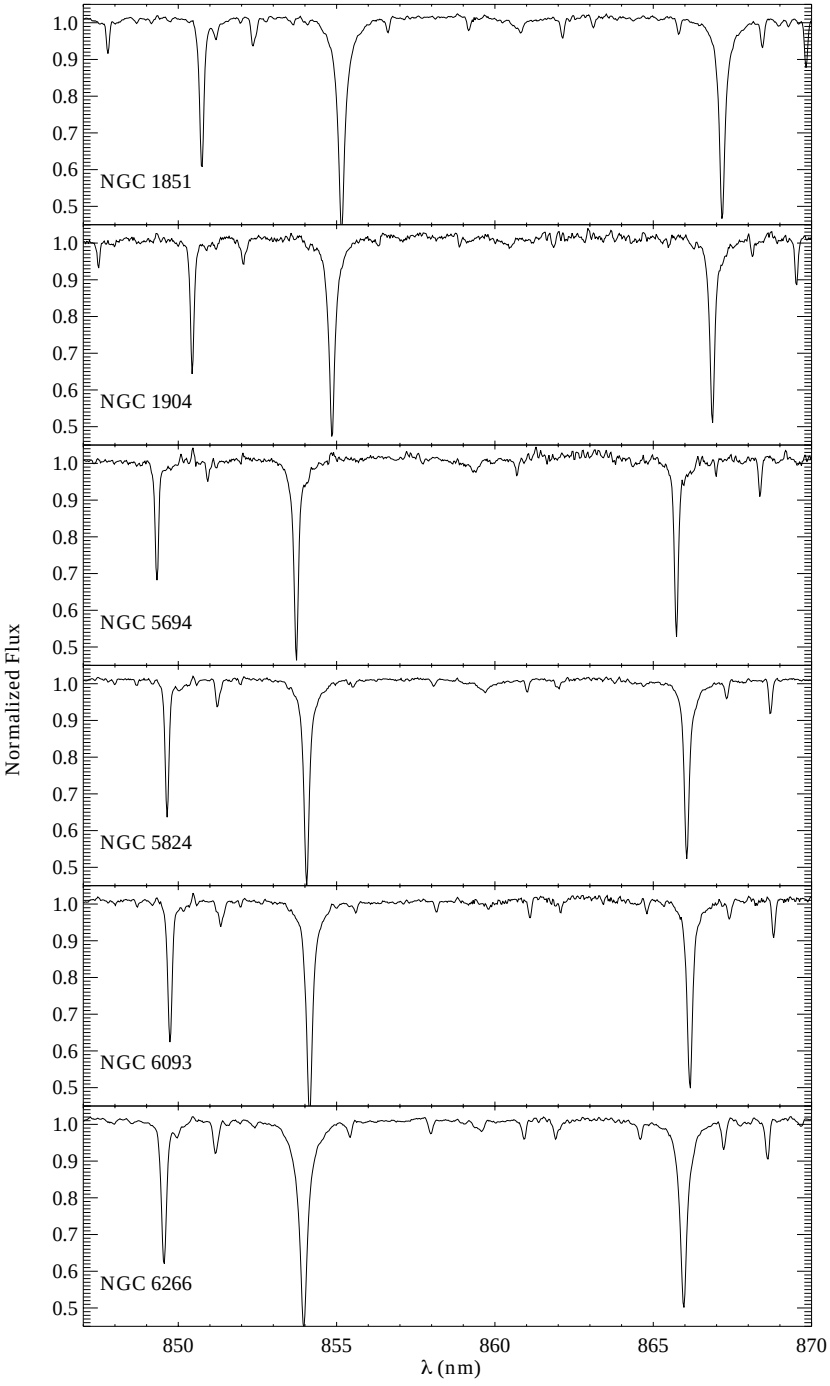

Figure 5.7: Combined spectra showing the Ca-triplet region, of the second radial bin of each cluster. The spectra are representative for the ones from which we derive the kinematic measurements.

described in Gebhardt et al. (1997) the data were taken in May 1995 using an imaging Fabry-Perot spectrophotometer with the Sub-arcsecond Imaging Spectrograph (SIS) mounted at the Canada-France-Hawaii Telescope (CFHT). Similar to the observations of NGC 5824, a series of exposures stepped by 0.33 Å were taken across the Hα line. For each star and each exposure, a photometric analysis was carried out and a spectrum across the Hα line was derived. From this, the kinematics of $\sim$ 875 stars were obtained. We combine these velocities in four bins with $\sim$ 200 stars each and derive the outer velocity-dispersion profile for NGC 6093.

5.4.5 Dynamical distance to NGC 6266

For NGC 6266 no outer kinematics are found in the literature but recent measurements of proper motions obtained by McNamara et al. (2012) can be used to verify the profile and determine the dynamical distance of NGC 6266. At first we compute the velocity-dispersion profile of the proper motions using our derived center position. The ideal way would be to apply the same bins as for our radial measurements to have a direct comparison. Unfortunately, there are only 5 stars in the central bin in the proper motions dataset. The maximum likelihood method from Pryor & Meylan (1993) which we apply to calculate the velocity dispersions is not reliable for bins with less than 20 stars, but necessary to account for the different errorbars of the velocity measurements. For this reason it is not possible to obtain a data point for the innermost bin from the proper motions. The data is binned in 5 bins containing $\sim 30-100$ stars and compared to the velocity-dispersion profile of the from the radial measurements. The proper motions profile is then scaled to the radial profile by applying χ^2 statistics. The final distance is then computed by:

$$d(pc) = 21.1 \frac{\sum_{i=0}^{N} (\sigma_{r,i}/\delta\sigma_{p,i})^2}{\sum_{i=0}^{N} (\sigma_{r,i}\sigma_{p,i})/\delta\sigma_{p,i}^2} \tag{5.1}$$

Where $\sigma_{r,i}$ and $\sigma_{p,i}$ are the datapoints of the interpolated N radial velocity-dispersion profile and the proper motions profile, respectively, and $\delta\sigma_{p,i}$ are the uncertainties of the proper motions. We derive a final distance of $d = (6.5 \pm 0.3)$ kpc. This is in good agreement with the value obtained by McNamara et al. (2012, $d = (7.2 \pm 0.6)$ kpc) as well as other published values: 7.9 ± 1.1 kpc (Illingworth 1976), 7.0 kpc (Ferraro et al. 1990), 6.6 ± 0.5 (Beccari et al. 2006), 6.7 ± 1.0 kpc (Contreras et al. 2010), and 6.9 ± 0.7 (Harris 1996). Figure 5.13 shows the final proper motion and radial velocity-dispersion profile compared to Jeans models.

5.5 Dynamical Models

After extracting photometric and kinematic data from the observations, the data are fed into dynamical models in order to find the best fitting parameters that describe the globular cluster. This Section describes the analytical Jeans models which we use for fitting the data and lists the results from the best fits.

5.5.1 Isotropic Jeans models

For our analysis we use spherical Jeans models as described by Cappellari (2002, 2008). The IDL routines provided by M. Cappellari[3] enable the modeling of the surface brightness profile and fitting the observed velocity data and the mass-to-light ratio at the same time. Using the surface-brightness profile as an input, the routine parametrizes it using a multi-Gaussian expansion (MGE) method developed by Emsellem et al. (1994). The advantage of this method is that the deprojection can be done analytically since a deprojection of a Gaussian surface brightness results again in a Gaussian luminosity density.

With the deprojected luminosity profile the code uses the spherical Jeans equation to calculate a velocity dispersion profile. This model profile is then scaled to the observed data using χ^2 statistics. From the scaling factor the global M/L_V is derived. In Chapter 2 we introduced a radial M/L_V profile (similar to the method described in Williams et al. 2009) in order to fit clusters with high mass segregation and therefore highly varying M/L_V. This can be done in two ways: 1) using a predefined M/L_V profile or 2) fitting the M/L_V profile to the data. For the latter, a M/L_V profile is computed by multiplying each of the Gaussian components of the luminosity profile with a different factor in order to derive a density profile. The ratio of the density profile to the luminosity profile then gives the M/L_V profile.

The first method is implemented by parametrizing the input M/L_V profile with an MGE fit. This is done by multiplying the individual gaussians of the MGE-luminosity profile with a set of factors in order to derive the MGE-mass-density profile. From this, an MGE-M/L_V profile is derived by dividing the mass-density profile by the luminosity profile, and compared to the input M/L_V profile. We vary the multiplication factors in order to derive the best fit to the input M/L_V profile. The final model-velocity-dispersion profile is then calculated from the best-fit mass-density profile.

Fitting an M/L_V profile directly to the kinematic data is done by finding the optimum multiplication factors for the luminosity-Gaussians which minimize the χ^2 of the resulting kinematic fit. The disadvantage of this procedure is that one can only use as many Gaussians as data points are available (otherwise the fit would be degenerate). For a small number of data points this method is therefore difficult to apply since a small number of Gaussians produces large variations in all profiles. A way around this would be a combination of both methods in two steps. In the first step the M/L_V profile is fitted to the data with a limited

[3]Available at http://www-astro.physics.ox.ac.uk/~mxc/idl

number of Gaussians and in the second step the noisy M/L_V profile is smoothed and fed again into the routine as a given profile, where a higher number of Gaussians can be used. The total M/L_V value is derived from the total luminosity L_{tot} and the total mass M_{tot}. The uncertainties of the total M/L_V value are derived from a combination of the uncertainties of the mass, obtained from the χ^2 fit to the kinematic data and the luminosity, calculated from the average errors on the distance (5 %) and the reddening (10 %) as taken from Harris (1996). In the following sections we discuss the modeling of the clusters individually. Every cluster is different. Every object is composed of different dataset combinations and therefore needs different treatment in terms of modeling.

Spherical symmetry is in general a valid assumption for globular clusters. Especially in our sample all clusters have observed axial ratios larger or equal to $b/a = 0.95$ (White & Shawl 1987). However, ignoring rotation in the outer regions of the cluster would lead to an overestimation of the M/L_V in the outskirts. For this reason we also test for axisymmetric models using the one-dimensional surface brightness profile and the axial ratios as listed in White & Shawl (1987). We find that even for the cluster with the highest flattening (NGC 1851, $b/a = 0.95$) the difference in the Jeans models in the outer regions does not exceed 0.1 $\mathrm{km\,s^{-1}}$. This corresponds to a difference in the maximum M/L_V value in the outskirts of ~ 0.7 causing a difference in the total M/L_V of 0.1 and a difference in the total mass of $\Delta \log M_{tot} = 0.03$. All deviations caused by the flattened models are still within the errorbars of the values measured with the spherical models. Consequently, it is not necessary to use axisymmetric models for these cluster for our purposes.

It is important to state that we do not directly include rotation in our Jeans models. However, since we measure the second moment in the data and models, we in fact do include the contribution of the rotation to the dynamics. Thus, we expect no difference when directly including the rotation. We treat the data and models consistently by integrating over full annulus so any rotation, if present, will be included in the second moment and thus the mass profile.

5.5.2 NGC 1851

The combined kinematic data of NGC 1851 covers a large radial range of the cluster. At first sight, the two datasets of the outer and inner kinematics seem to agree well with each other. However, when comparing the data to a Jeans model with constant M/L_V (Figure 5.8.a) the datasets seem to be shifted with respect to each other. Figure 5.8.a also shows a model where the M/L_V profile is fitted to the data (green line). The resulting M/L_V profile is shown in panel b) of the same Figure. The profile stays flat for a large range of radii and rises by a factor of five in the outskirts ($r > 3$ pc). The shape of the profile is expected since low-mass stars (with high M/L) move to the outskirts of the cluster due to mass segregation. The amount with which the M/L_V changes seems high but compared to the M/L_V profile derived from N-body simulations for NGC 6266 (Section 5.5.7), still

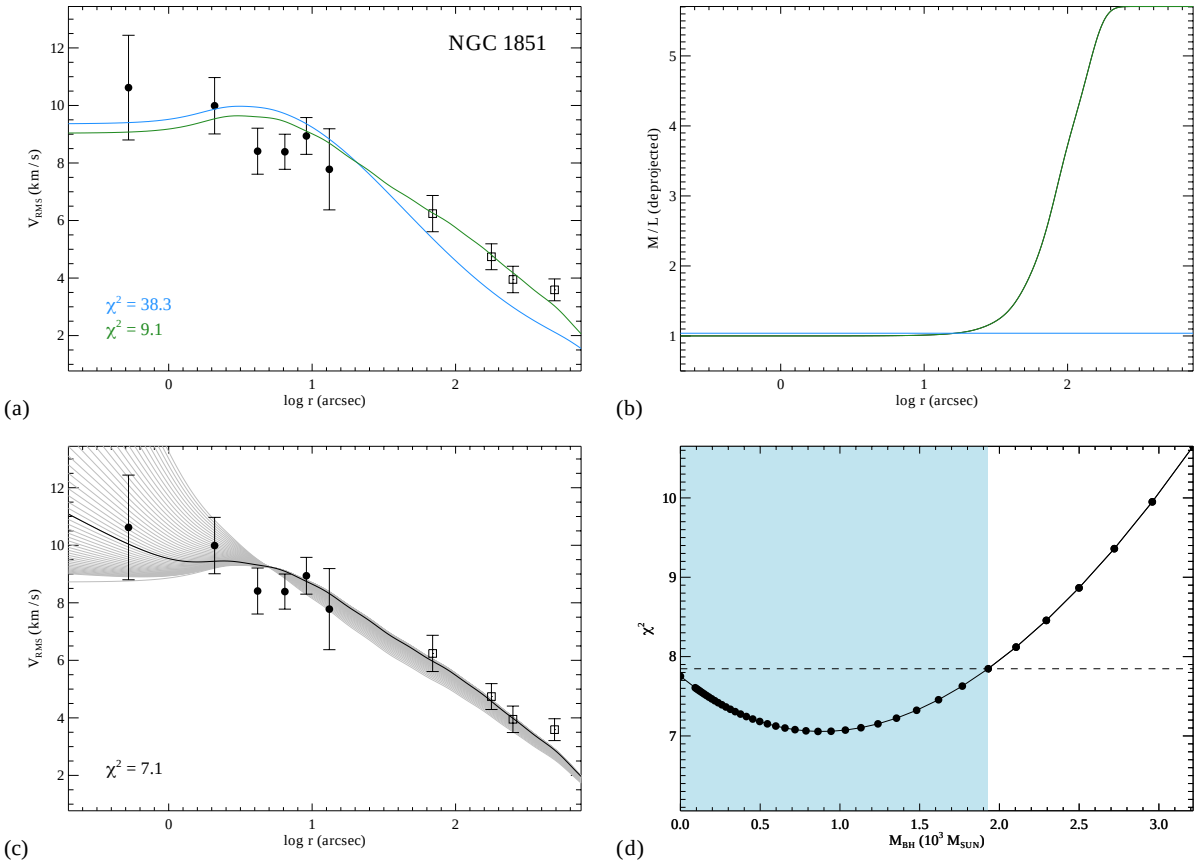

Figure 5.8: Jeans models for the globular cluster NGC 1851 compared to the datapoints obtained in this work (black bullets) and the outer data points obtained by Scarpa et al. (2011, open squares). Panel a) shows the comparison of a model with and without fitting a M/L_V profile. The corresponding M/L_V profiles are shown in panel b). The panels c) and d) show various Jeans models with the varying M/L_V profile and with different black-hole masses and their χ^2 values. The best fit model is plotted as a black solid line and the blue shaded area in panel d) indicates the 1σ error on the black-hole mass.

reasonable. When applying these fits to combined datasets one has to keep in mind that there could be still a systematic offset between the data. This could change the shape of the fitted M/L_V profile as explained in the following Section.

We also test models with different black-hole masses (Figure 5.8.c and d). For this we use the green model from Figure 5.8.a and include the potential of a central black hole. The χ^2 values of each model are shown in Figure 5.8.d as a function of the black-hole mass. It is shown that despite the fact that the best fit requires a black hole of about 1000 $M_\odot$, the data is still consistent with a no-black-hole model within the 1σ errors (blue shaded area in Figure 5.8.d).

5.5.3 NGC 1904

NGC 1904 is an interesting case. Similar to NGC 1851 the large radial coverage of kinematic data points allows to study the dynamic stage of that cluster very well. Figure 5.9 demonstrates that a simple isotropic Jeans model with a constant M/L_V over the entire cluster does not reproduce the data very well (blue line in Figure 5.9.a). The first question which arises immediately is whether either of the data sets suffers from a systematic shift between inner and outer measurements which causes this mismatch between the points. Since the points from Scarpa et al. (2011) were obtained from individual stars in the outer regions of the cluster, which usually is a safe method, the potential errors are most probable with the data points obtained with the IFUs.

In order to test for systematic offsets in our measurements we use different templates and different methods to extract the kinematics (as already explained in the previous section). Using the faint master template results in even higher velocity dispersions ($\sim 1-2$ km s^{-1}) and does not solve the problem. We also extract the brightest stars in the pointing by applying the shotnoise routines and construct a velocity histogram using these stars. By measuring the dispersion of this histogram we get an estimate of the velocity dispersion of the brightest stars in the cluster independent from the line fitting method. We obtain a total velocity dispersion of ~ 6 km s^{-1}. By testing different luminosity bins of the stars we find that the velocity dispersion drops the fainter the stars are. This arises from the contamination of the faint stars form cluster background cluster light and therefore a bias towards the cluster mean velocities. For this reason the actual velocity dispersion is probably higher than the 6 km s^{-1} measured from the bright stars, that are also contaminated by background light by a small percentage. This leads us to the conclusion that the measurement of the integrated light with $\sigma \sim 6-9$ km s^{-1} is most likely correct correct.

Modeling the final profile of NGC 1904 is not trivial. In order to fit both the inner and the outer data points we fit the M/L_V profile to the data. Figure 5.9.a shows the result of this fit (green line) and Figure 5.9.b the corresponding M/L_V profile. In order to reproduce the inner kinematics, the M/L_V profile needs to rise strongly towards the center, to drop further out and to rise again in the outskirts in order to fit the flat outer profile. The strong

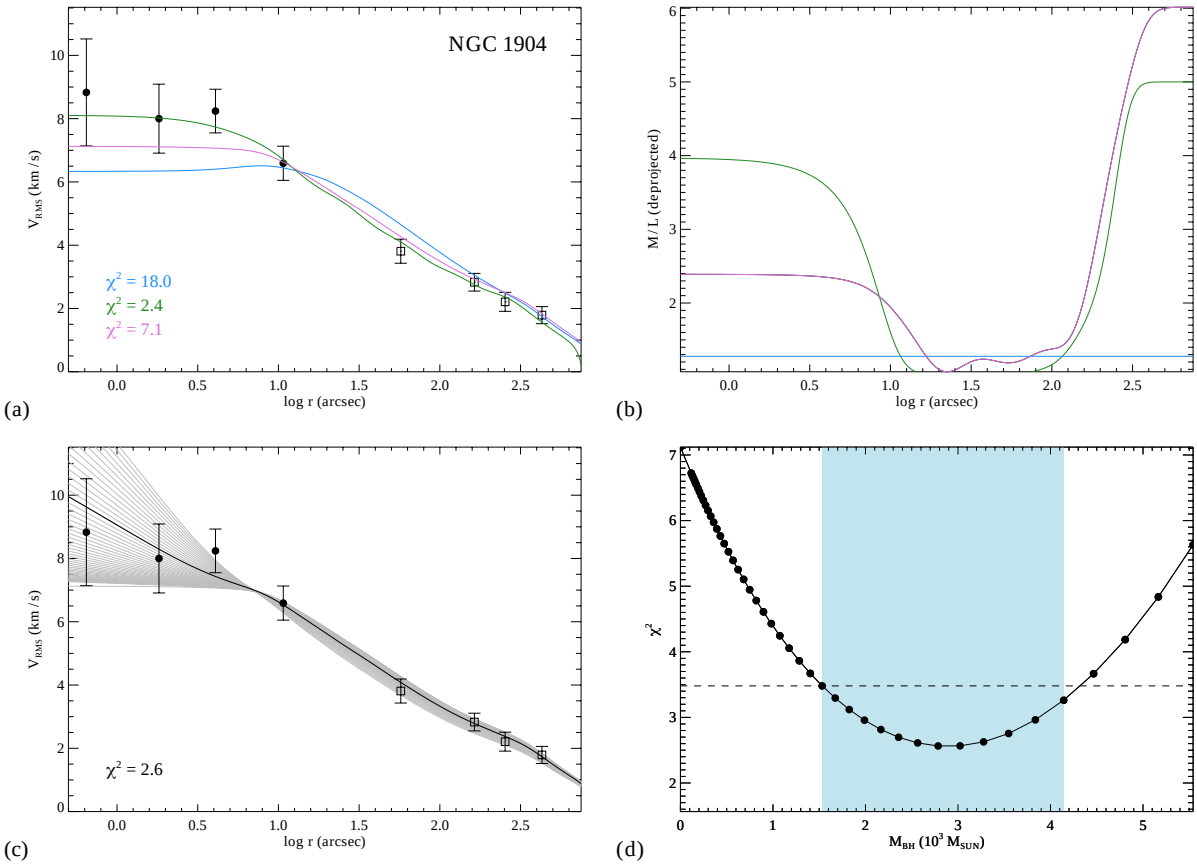

Figure 5.9: Jeans models for the globular cluster NGC 1904. All four panels and symbols are the same as in Figure 5.8. The purple line in Panel b) shows the intermediate M/L_V profile which is used also when fitting the black hole mass in Panel c) and d).

rise towards the center could be explained with a high concentration of remnants at the center of the cluster. However, this would imply that NGC 1904 is in a core collapse state, which is not supported by its flat surface brightness profile.

The strong rise towards the center is a sign for core collapse, where heavy remnants sink to the center of the cluster. However, for NGC 1904 this scenario is rather unlikely due to its large core and flat surface brightness profile (see Figure 5.5). For this reason the fitted M/L_V profile seems to be not a good descriptions of the clusters properties. We therefore use an intermediate M/L_V profile (Figure 5.9.a and b, purple line) which does not rise as strong as the previous profile. The shape of the intermediate M/L_V profile is in good agreement with what we find in N-body simulations.

Using the intermediate M/L_V profile we fit the kinematic profile by adding a black hole in the center of the cluster. In Figure 5.9.c we show different Jeans models computed for different black-hole masses (grey lines) and constant M/L_V. By performing χ^2 statistics (Figure 5.9.d) we find the model which fits the data best (black line). This model predicts a black hole of $M_\bullet = (3 \pm 1) \times 10^3 M_\odot$.

5.5.4 NGC 5694

The limited field of view of the ARGUS observations of NGC 5694 (see Figure 5.6) makes it difficult to unfold the kinematic properties of this cluster. Also, due to its low surface brightness the signal-to-noise of these observations is almost half the signal-to-noise of the other clusters and the uncertainties increase accordingly. Figure 5.10 shows the final datapoints as well as a grid of Jeans models with different black-hole masses. Due to the small coverage of the kinematic profile it is not possible to fit a M/L_V profile to the data and a constant M/L_V is assumed. For this reason the only free parameter we vary is the mass of the central black hole.

The best fit is provided by a model with a black-hole mass of $M_\bullet \sim 4 \times 10^3\ M_\odot$, the model with no black hole however, is not excluded. Unfortunately the errorbars are large and the datapoints too few. The cluster can be considered as a good candidate for hosting an intermediate-mass black hole at its center, but with the current data coverage and quality it is challenging to put strong constraints on the mass of a possible central black hole. For that reason we treat the result of the fit for NGC 5694 with care.

5.5.5 NGC 5824

For NGC 5824 we obtain one outer datapoint from the Fabry-Perot data. This adds up to five kinematic points out to a radius of 25″ (~ 3 pc). The observed profile is in very good agreement with a Jeans model with constant M/L_V (Figure 5.11.a), and does not require a M/L_V variation.

We also test for Jeans models with different IMBH masses for NGC 5824. In Figure 5.11.a

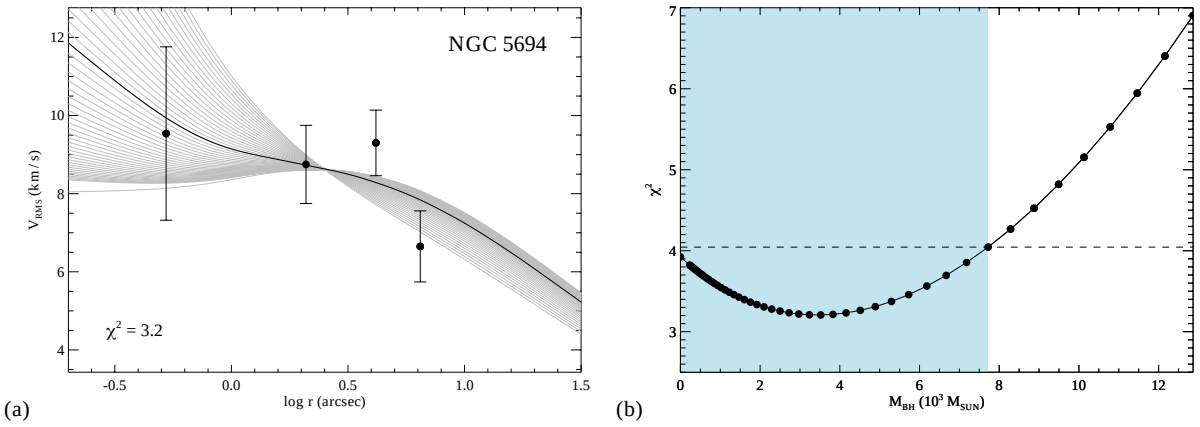

Figure 5.10: Dynamical models for the globular cluster NGC 5694. a) a grid of models with different black-hole masses. b) χ^2 as a function of black-hole mass. The blue shaded area marks the 1 σ error.

we plot the grid of models on top of the data and study their χ^2 values. We find a slightly better fit for a model with a black hole of $M_\bullet \sim 2000\ M_\odot$. However, due to the large uncertainty of the innermost point the data is still consistent with a no-IMBH model.

5.5.6 NGC 6093

For NGC 6093 the outer and inner kinematics seem to agree well within the errorbars. Considering the last data point of the Fabry-Perot data, however, a variable M/L_V profile is needed also for this cluster in order to fit the observational data in an optimal way. Figure 5.12.a and b show two Jeans models, one with constant (blue) and one with varying (green) M/L_V on top of the data. Note that the M/L_V profile shown in panel b is only reliable out to the last data point where the model was fitted. The outer drop of the profile for radii greater than 200″ is therefore meaningless.

The comparison with models of different black-hole masses in Figure 5.12.c and d shows that no black hole is needed in order to fit the kinematic data of NGC 6093 and the profile is flat in the center.

5.5.7 NGC 6266

The velocity-dispersion profile of NGC 6266 shows the most distinct rise in the center of all the clusters. McNamara et al. (2012) performed N-body simulations in order to reproduce the kinematic data of NGC 6266 obtained from HST proper motions. We match the proper motions with our radial velocity-dispersion profile and find good agreement in the general shape of the two datasets. For that reason we can use their derived N-body M/L_V profile as an input for our kinematic models.

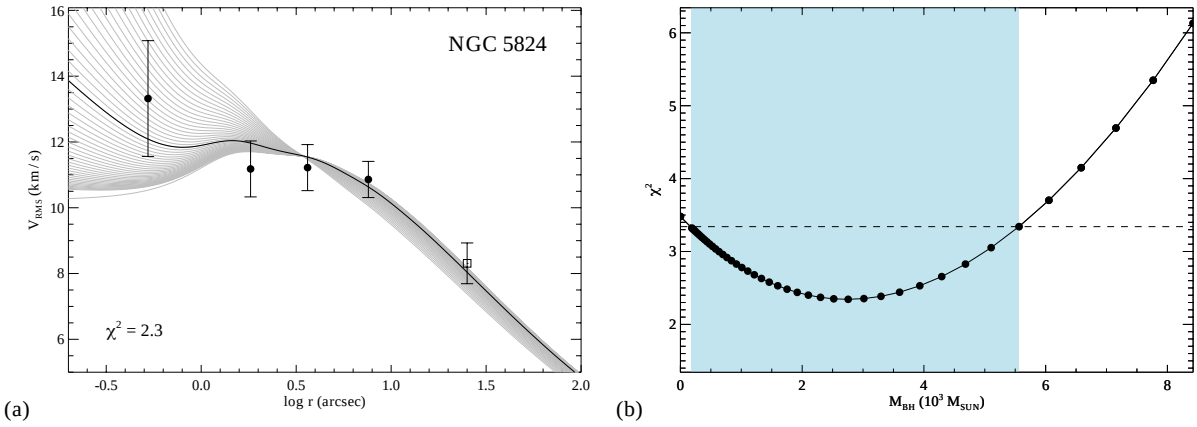

Figure 5.11: Kinematic profile of NGC 5824 in comparison with different Jeans models.The open square marks the one outer datapoint obtained from Fabry-Perot measurement. The rest of the symbols and panels are the same as in Figure 5.10.

The N-body simulations were carried out using the Graphical Processing Unit (GPU)-enabled version of the collisional N-body code NBODY6 (Aarseth 1999; Nitadori & Aarseth 2012) on the GPU cluster of the University of Queensland. All simulations started with $N = 50\,000$ stars distributed according to a King (1962) model using different initial concentrations c and half-mass radii r_h and masses following a Kroupa (2001) mass function. The metallicity was set to $[Fe/H] = -1.18$ as given by Harris (1996) and stellar evolution was included according to the routines of Hurley et al. (2000) during the cluster evolution time of 12 Gyr. With different retention fractions for white dwarfs (100%), neutron stars (10%) and black holes (10%), the final population of dark remnants in the cluster consists mainly of white dwarfs which make 30% of the total cluster mass. In general, most of the stellar-mass black holes got kicked out during the cluster lifetime and only $1-2$ black holes and about a dozen neutron stars remain.

Figure 5.13 shows this M/L_V profile and the corresponding Jeans model. The M/L_V rises strongly in the outer regions of the cluster which results from mass segregation of low-mass stars which migrate towards larger radii. However, due to the lack of outer kinematics for NGC 6266 we cannot validate this profile with great confidence since the rise of the M/L_V value occurs at radii larger than covered by our kinematic data points.

As for the previous clusters we also test Jeans models with different black-hole masses for NGC 6266. In Figure 5.13.a the different models (grey lines) and the best fit (solid line) to the data are visualized. Due to the strong rise of the profile in the inner regions the data requires a model with a central black hole of the mass $M_\bullet = (2.5 \pm 1.5) \times 10^3\ M_\odot$. Figure 5.13.c shows the χ^2 as a function of black-hole mass and the 1σ error of the best fit (blue shaded area).

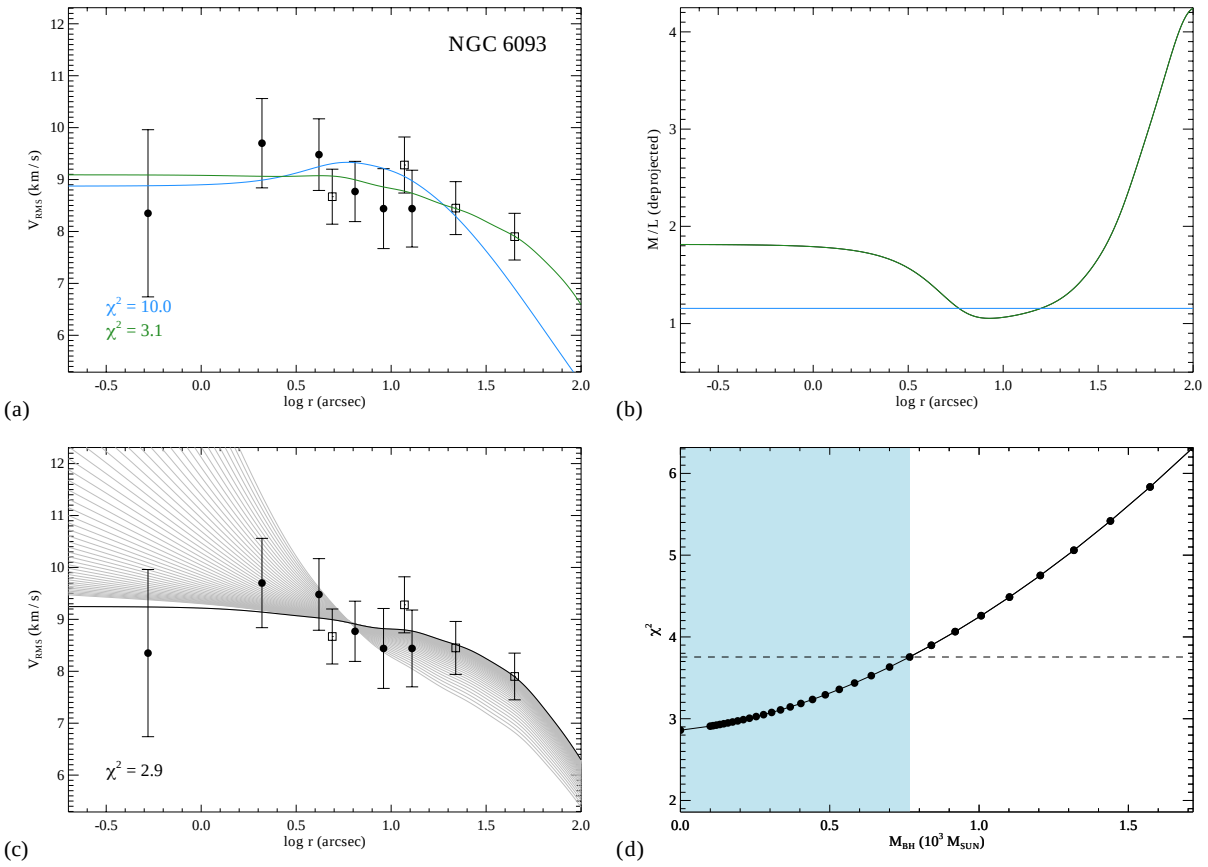

Figure 5.12: Jeans models for the globular cluster NGC 6093 compared to the datapoints obtained in this work (black bullets) and the outer data points obtained by with the CFHT Fabry-Perot instrument (open squares). Panel a) shows the comparison of a model with (green) and without (blue) fitting a M/L_V profile. The corresponding M/L_V profiles are shown in panel b). The panels c) and d) show various Jeans models with different black-hole masses and their χ^2 values. The best fit model is plotted as a black solid line.

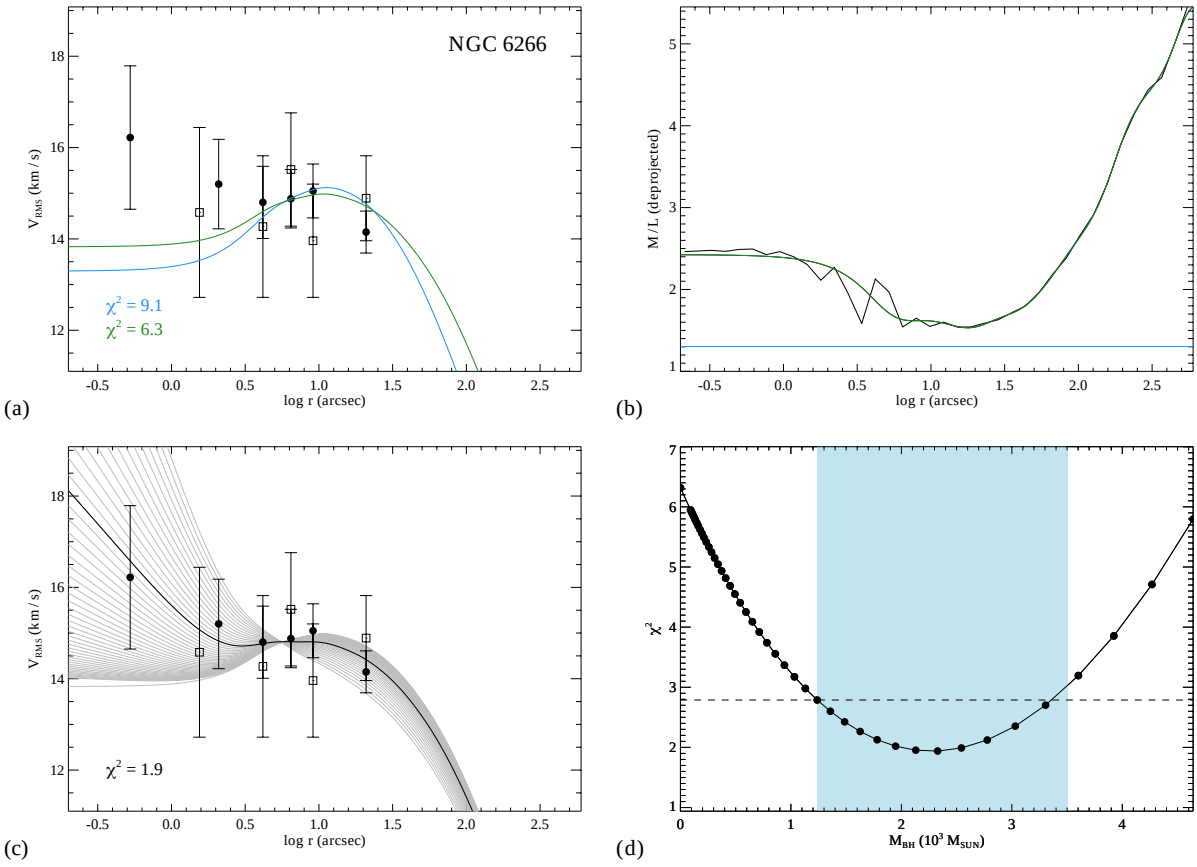

Figure 5.13: Jeans models, data, and M/L_V profile of NGC 6266. All panels and colors are the same as in the previous figures. The M/L_V profile (black line in panel b) is taken from N-body simulations and used as an input for the Jeans models. The green solid line in panel b) shows the parametrization of this profile. The 1σ area of the black-hole mass is visualized as blue shaded area in panel d) as in the previous figures.

5.6 Summary and Conclusions

We study the kinematic and photometric properties of the six Galactic globular clusters NGC1851, NGC 1904, NGC 5694, NGC 5824, NGC 6093 and NGC 6266. We use spectroscopic observations obtained with the large integral field unit ARGUS of the FLAMES instrument at the VLT as well as high resolution HST images to obtain the photometric properties. From these images we determine the light-weighted center of each cluster using an isodensity-contour method with different magnitude cuts. We find that the derived centers are in good agreement with Noyola & Gebhardt (2006) except for NGC 6266 where the centers lie more than 2″ apart from each other. We derive surface brightness profiles through a combination of star counts and integrated light and determine the central slope of the light profile.

The kinematic profiles are derived by fitting non-parametric LOSVDs to the spectra combined in radial bins. For NGC 1851 and NGC 1904 outer kinematics were also available from datasets obtained by Scarpa et al. (2011). Outer kinematics for NGC 5824 and NGC 6093 are taken from Fabry-Perot observations (Gebhardt et al. 1997). From the individual velocities of the stars an outer velocity-dispersion profile is derived using a maximum likelihood method. For NGC 6266 we compare our inner kinematic profile with proper motion data obtained by McNamara et al. (2012) and find very good agreement between these two datasets. We feed the surface brightness profile into analytical Jeans models and search for the best fitting model by varying the mass of the central black hole as well as the M/L_V values.

Table 5.7 lists the final results of the Jeans modeling. For the total masses and M/L_V values we use the results of the models which fit the data best, i.e. had the lowest χ^2 values. We indicate the values derived from models with a varying M/L_V profile with the index V. Comparing M_{tot} and M/L_V to the values presented in McLaughlin & van der Marel (2005), we find in general a good agreement of the total masses of the clusters. The only exception is NGC 5824 where our derived mass of $\log M = 5.65 \pm 0.03$ is lower than their value of $\log M = 5.81 \pm 0.04$. This originates in our value for the total luminosity which is already lower than the value of McLaughlin & van der Marel (2005) while for the other clusters the total luminosities are in good agreement with the values of McLaughlin & van der Marel (2005). The overall M/L_V ratios that we derive agree with the predictions of single-stellar population models following standard stellar mass functions at ages of 10 - 12 Gyr as shown in Figure 7 in Mieske et al. (2008) and McLaughlin & van der Marel (2005) and also agree with the predicted dynamical M/L_V values from McLaughlin & van der Marel (2005), partly due to the large uncertainties of the McLaughlin & van der Marel (2005) values. It is not surprising that our dynamical M/L_V values are similar to the stellar population models since our clusters are massive and the mass loss through low-mass stars ejections, which would cause a decrease of the initial M/L_V value (e.g. Baumgardt & Makino 2003; Kruijssen & Lamers 2008; Kruijssen 2009), is not yet efficient enough to lower the M/L_V value by more

Table 5.7: Kinematic results of the six clusters. Listed are the measured central velocity dispersion from the IFU data (σ_{tot}), the effective velocity dispersion measured from the kinematic profile (σ_e), the total M/L_V, the total mass M_{tot}, and the limits on the mass of the possible intermediate-mass black hole ($M_\bullet$). The result marked with an asterisk should be treated with care. The index V indicates when a model with varying M/L_V profile was applied instead of one with a constant value for M/L_V.

Cluster	V_r [km s^{-1}]	σ_{tot} [km s^{-1}]	σ_e [km s^{-1}]	M/L [$M_\odot/L_\odot$]	log M_{tot} [$M_\odot$]	$M_\bullet$ [$M_\odot$]
NGC 1851	322.7 ± 4.3	8.4 ± 0.8	9.3 ± 0.5	$2.1^V \pm 0.2$	$5.57^V \pm 0.03$	$< 2^V \times 10^3$
NGC 1904	205.2 ± 2.5	7.0 ± 0.4	8.0 ± 0.5	$1.6^V \pm 0.2$	$5.16^V \pm 0.03$	$(3 \pm 1)^V \times 10^3$
NGC 5694	-140.4 ± 1.4	8.5 ± 0.4	8.8 ± 0.6	2.1 ± 0.4	5.41 ± 0.05	$< 8 \times 10^3$*
NGC 5824	-25.0 ± 0.7	11.1 ± 0.5	11.2 ± 0.4	1.8 ± 0.2	5.65 ± 0.03	$< 6 \times 10^3$
NGC 6093	12.1 ± 0.5	9.4 ± 0.4	9.3 ± 0.3	$2.3^V \pm 0.3$	$5.53^V \pm 0.02$	$< 800^V$
NGC 6266	-75.0 ± 1.0	15.0 ± 2.8	15.5 ± 0.5	2.5 ± 0.4	5.97 ± 0.01	$(2 \pm 1)^V \times 10^3$

than 0.1 or 0.2.

For all of the clusters we also compared the data to models with different black hole masses. The final results of these fits are also listed in Table 5.7. For three clusters we only give an upper limit on the black-hole mass since the datapoints are consistent with a no-black-hole model within the 1σ errorbars. For NGC 1904, NGC 5694 and NGC 6266 the data require a model with a significant black-hole mass. In the case of NGC 1904 we perform tests in order to check whether the high black-hole mass could originate from a systematic offset between inner and outer kinematic profile. We find no evidence for a systematic shift of the inner kinematic profile. Assuming the outer kinematics, which are measured from individual stars, are correct, we conclude a black-hole mass of $(3 \pm 1) \times 10^3\, M_\odot$ for NGC 1904. The result of NGC 5694 has to be treated carefully because of the low radial coverage and needs to be confirmed with more data. For that reason we mark the result of this cluster with an asterisk in Table 5.7.

Also NGC 1851 might require more detailed analysis. NGC 1851 could be the merging product of two globular clusters as the presence of self-enrichment signatures in both populations of the cluster and its photometric properties suggest (Carretta et al. 2010; Gratton et al. 2012; Olszewski et al. 2009). Also, the recently discovered cold stream in the vicinity of NGC 1851 (Sollima et al. 2012) hints towards an accretion scenario where NGC 1851 is the remnant of a nuclear cluster located in a dwarf galaxy which was accreted and stripped by the Milky Way. For that reason Jeans models might not be sufficient to model a cluster with such a violent history.

The profile of NGC 6266 is very well reproduced by the model which is surprising considering its large error bars. From all the clusters in our sample NGC 6266 is by far the best candidate for hosting an intermediate-mass black hole. With $\sim 2000\, M_\odot$ it is, however, rather small compared to the black-hole masses found in clusters from previous studies. McNamara

et al. (2012) compared the proper motion data and the surface brightness profile of NGC 6266 with N-body simulations and found that a centrally located IMBH is not required to match these profiles but given the uncertainties in the position of the center, a black hole with a mass of a few thousand solar masses cannot be excluded. The fact that we use a different center than McNamara et al. (2012) might explain the stronger signature in our profile and the different, but still consistent results on the black hole masses.

Another topic which needs to be discussed is the influence of dark remnants to the velocity-dispersion profile and the probability of this mimicking the effect of a single IMBH at the center. It is known that due to mass-segregation, stars more massive than the mean sink to the center of the cluster, which causes a higher concentration of massive stars/remnants in the cluster's core. This would challenge the detection of an IMBH since the rise in the M/L_V causes a rise in the velocity-dispersion profile which could mimic the influence of an IMBH. The largest influence on the velocity-dispersion profile is produced by the most massive remnants such as black holes and neutron stars. However, the retention fraction of these objects is very poorly understood. Neutron stars are believed to get kicks of order a few hundred km/sec at birth (Lyne & Lorimer 1994), which would imply that only few of them are retained in a globular cluster. Hence, neutron stars are unlikely to dominate the mass budget at any radius in a globular cluster. In contrast, due to their higher mass, black holes are believed to get smaller kick velocities and therefore remain in a larger fraction in star clusters after their birth. However, recent population synthesis modeling of Galactic low-mass X-ray binaries by Repetto et al. (2012) has shown that black holes might get natal kicks that are of the same order as those of neutron stars. In addition, N-body simulations by Mackey et al. (2008) and Merritt et al. (2004) as well as our own unpublished simulations show that star clusters with many stellar mass black holes have very large cores that are best fit by low concentration King models. Since the clusters in our sample all follow high-concentration King profiles, it is unlikely that they contain a significant concentration of stellar mass black holes in their centres. In the case of white dwarfs, our N-body models assume a retention fraction of 100% and despite the central rise in M/L_V caused by the white dwarfs, we still need IMBHs to fit the velocity-dispersion profile in some of our clusters. We therefore have reasons to assume that remnants in the cluster center do not influence our results by a large amount and especially that our conclusions concerning the possible presence of IMBHs are not significantly effected. Nevertheless, this conclusion can not be exclusively proven and our derived IMBH masses have to be treated with care. Detailed N-body simulations should and will be applied in follow-up papers in order to finally answer this question and disentangle kinematic signatures of remnants and IMBHs.

The search for intermediate-mass black holes in globular clusters became a promising new field of research in the last decade. With new observational techniques such as integral-field spectroscopy and refined analysis methods for deriving proper motions it became possible to resolve the central kinematics where a possible black hole would start influencing the motions of the stars. With our current sample of ten Galactic globular clusters, including ω Centauri, NGC 6388, NGC 2808 and NGC 5286 (Feldmeier et al. in preparation) we have

the largest sample of clusters studied with integral field units up to date. A next step in terms of analysis will be a comparison study of all clusters. We plan to correlate black-hole masses with structural and kinematic properties of the host cluster in order to find possible links to formation scenarios and environments for intermediate-mass black holes. We are also currently running N-body simulations, which will help us understand the dynamical processes in clusters with massive central black holes and to plan future observations for revealing the secrets of intermediate-mass black holes.

Acknowledgements: *This research was supported by the DFG cluster of excellence Origin and Structure of the Universe (www.universe-cluster.de).*

CHAPTER 6

$M_\bullet - \sigma$ relation for intermediate-mass black holes in globular clusters

Nora Lützgendorf, Markus Kissler-Patig, Nadine Neumayer, Holger Baumgardt, Eva Noyola, Tim de Zeeuw, Karl Gebhardt,, Behrang Jalali, and Anja Feldmeier

Astronomy & Astrophysics, 2013 accepted

Abstract For galaxies hosting supermassive black holes (SMBHs), it has been observed that the mass of the cntral black hole ($M_\bullet$) tightly correlates with the effective or central velocity dispersion (σ) of the host galaxy. The origin of this $M_\bullet - \sigma$ scaling relation is assumed to lie in the merging history of the galaxies, but many open questions about its origin and the behavior in different mass ranges still need to be addressed. The goal of this work is to study the black-hole scaling relations for low black-hole masses, where the regime of intermediate-mass black holes (IMBHs) in globular clusters (GCs) is entered. We collected all existing reports of dynamical black-hole measurements in GC, providing black-hole masses or upper limits for 14 candidates. We plotted the black-hole masses versus different cluster parameters including total mass, velocity dispersion, concentration, and half-mass radius. We searched for trends and tested the correlations to quantify their significance using a set of different statistical approaches. For correlations with a high significance we performed a linear fit, accounting for uncertainties and upper limits. We find a clear correlation between the mass of the IMBH and the velocity dispersion of the globular cluster. As expected, the total mass of the globular cluster then also correlates with the mass of the IMBH. While the slope of the $M_\bullet - \sigma$ correlation differs strongly from the one observed for SMBHs, the other scaling relations $M_\bullet - M_{tot}$, and $M_\bullet - L$ are similar to the correlations in galaxies. Significant correlations of black-hole mass with other cluster properties were not found in the present sample.

6.1 Introduction

Empirical scaling relations between the masses of nuclear black holes and properties of their host galaxies in terms of total luminosity L, bulge mass $M_{\rm bulge}$ (Kormendy & Richstone 1995; Marconi & Hunt 2003; Häring & Rix 2004) or the effective (projected) velocity dispersion σ (Ferrarese & Merritt 2000; Gebhardt et al. 2000a; Ferrarese & Ford 2005; Gültekin et al. 2009) disclose a strong connection between the formation history of supermassive black holes (SMBHs) and galaxies. These scaling relations can be explained by gas-accreting black holes that drive powerful jets and outflows into the surrounding interstellar medium, thus affecting the star formation rate and regulating the subsequent supply of matter onto the SMBH (Silk & Rees 1998; Di Matteo et al. 2005; Springel et al. 2005; Hopkins et al. 2007). Alternative explanations reproduce these empirical correlations by large numbers of merger events in which extreme values of $M_\bullet/M_{\rm bulge}$ are averaged out.

While galaxies and central SMBHs in the most common mass range, $M_\bullet = 10^{6-9}\,M_\odot$, seem to closely follow the one-parameter power law $M_\bullet - \sigma$ and $M_\bullet - L$ relations, there is now some evidence for large scatter or an upward curvature trend for SMBH masses at the highest mass regime ($M_\bullet \approx 10^{10}\,M_\odot$, e.g. Gebhardt et al. 2011; McConnell et al. 2011; van den Bosch et al. 2012).

Given this puzzling behavior of the $M_\bullet - \sigma$ relation at high masses, the question arises if different laws apply for the low-mass end as well. Attempts of measuring lower black-hole masses in dwarf galaxies (e.g. Filippenko & Ho 2003; Barth et al. 2004; Xiao et al. 2011) sparsely populate the relation down to a black-hole mass of $\sim 10^5$, but not lower. The lower the black-hole mass, the fainter they appear in radio and X-ray emission and the weaker is the kinematic signature and the smaller the radius of influence. Therefore, detecting black-hole masses lower than $10^5\ M_\odot$ is challenging. Reaching for the mass range that currently is assigned to intermediate-mass black holes ($10^2 - 10^5\ M_\odot$, IMBHs) requires extending the search toward different stellar systems.

The possible existence of IMBHs in low-mass stellar systems such as globular clusters (GCs) was first suggested by Silk & Arons (1975) while studying X-ray sources in a large sample of GCs. These authors concluded that the observed X-ray fluxes could only be explained by mass accretion onto a $100 - 1000\ M_\odot$ central black hole. This discovery triggered a burst of black-hole hunting in GCs using X-ray and radio emission but also photometric and kinematic signatures.

Owing to the small amount of gas and dust in GCs, the accretion efficiency of a potential black hole at the center is expected to be low. This makes the detection of IMBHs at the centers of GCs through X-ray and radio emissions very challenging (Miller & Hamilton 2002c; Maccarone & Servillat 2008). However, several attempts were made to detect radio and X-ray emission of gas in the central regions and to provide a black-hole mass estimate (e.g. Maccarone et al. 2005; Ulvestad et al. 2007; Bash et al. 2008; Cseh et al. 2010). Recently, Strader et al. (2012) tested several Galactic GCs for the presence of possible

IMBHs by investigating radio and X-ray emission. They only found upper limits on the order of $10^2\ M_\odot$. However, the authors had to make various assumptions about the gas accretion process such as gas distribution, accretion efficiency, and transformation of X-ray fluxes to black-hole masses to derive those limits. Besides X-ray and radio emission, the central kinematics in GCs can reveal possible IMBHs.

Motivated by the results of Silk & Arons (1975), Bahcall & Wolf (1976) claimed the detection of an IMBH in M15 by measuring its light profile and comparing it with dynamical models. The first claim from kinematic measurements was made by Peterson et al. (1989), who found a strong rise in the velocity dispersion profile of M15. More recently, Gebhardt et al. (1997, 2000b) and Gerssen et al. (2002) estimated a black-hole mass in M15 of $(3.2 \pm 2.2) \times 10^3 M_\odot$ from photometric and kinematic observations. However, after more investigations this cluster no longer appears as a strong IMBH hosting candidate (e.g. Dull et al. 1997; Baumgardt et al. 2003, 2005; van den Bosch et al. 2006) and the previously detected X-ray sources turned out to be a large number of low-mass X-ray binaries, but new detections of IMBH candidates in other clusters followed.

Using integrated light near the center of the M31 cluster G1, Gebhardt et al. (2002, 2005) measured the velocity dispersion of this cluster and argued for the presence of a $(1.8 \pm 0.5) \times 10^4 M_\odot$ IMBH. Furthermore, X-ray and radio emission were detected at the cluster center, consistent with a black hole of the same mass (Pooley & Rappaport 2006; Kong 2007; Ulvestad et al. 2007). This result, however, was recently challenged by Miller-Jones et al. (2012), who found no radio signature at the center of G1 when repeating the observations.

Another good candidate for hosting an IMBH at its center is the massive GC ω Centauri (NGC 5139). Noyola et al. (2008, 2010) measured the velocity-dispersion profile with an integral-field unit and used dynamical models to analyze the data. Because of to the distinct rise in the velocity-dispersion profile they claimed a black-hole mass of $M_\bullet = 40\ 000\, M_\odot$. The same object was studied by Anderson & van der Marel (2010) using proper motions from HST images. They found less compelling evidence for a central black hole, but more importantly, they found a location for the center that differs from previous measurements. Both G1 and ω Centauri have been suggested to be stripped nuclei of dwarf galaxies (Freeman 1993; Meylan et al. 2001; Jalali et al. 2012) and therefore may not be the best representatives of GCs.

Further evidence for the existence of IMBHs is provided by the discovery of ultra-luminous X-ray (ULX) sources at non-nuclear locations in starburst galaxies (e.g. Fabbiano 1989; Colbert & Mushotzky 1999; Matsumoto et al. 2001; Fabbiano et al. 2001). The brightest of these compact objects (with $L \sim 10^{41}\ \mathrm{erg\,s^{-1}}$) imply masses larger than $10^3 M_\odot$ assuming no beaming of the X-ray emission and accretion at the Eddington limit. Probably one of the best IMBH candidates, the ULX source HLX-1, was discovered in an off-center position of the spiral galaxy ESO243-49 by Farrell et al. (2009) and Godet et al. (2009) and is most likely associated with a group of young stars remaining from the core of a stripped dwarf galaxy (e.g. Soria et al. 2010, 2013).

Table 6.1: Properties of the 14 GCs of our sample. The references for the measurements are a) Harris (1996), b) Chapter 2, c) Chapter 3, d) Chapter 5 e) Feldmeier et al. (2013), f) Gerssen et al. (2002), g) McLaughlin & van der Marel (2005), h) Ma et al. (2007) i) Meylan et al. (2001) j) Stephens et al. (2001), k) Noyola et al. (2010), l) Ibata et al. (2009), m) Gebhardt et al. (2005) n) Meylan et al. (1995). For clusters not provided with uncertainties in M_{tot} and L_{tot} we adopted a value of 0.02 dex.

ID		D_{SUN} [kpc]	D_{GC} [kpc]	[Fe/H]	e	c	r_h [pc]	$\log M_{tot}$ [$\log M_\odot$]	δM_{tot}	$\log L_{tot}$ [$\log L_\odot$]	δL_{tot}	σ [km s^{-1}]	$\delta\sigma$	$M_\bullet$ [$M_\odot$]
G1		675.0^i	36.8^j	-1.22^h	0.19^h	2.01^h	6.5^h	6.76^m	0.02	6.31^a	0.02	25.1^i	0.3	$(1.8 \pm 0.5) \times 10^{4\,g}$
NGC 104	47Tuc	4.5^a	7.4^a	-0.72^a	0.09^a	2.07^a	4.1^a	6.04^g	0.02	5.66^g	0.02	9.8^g	0.0	$< 1.5 \times 10^3$
NGC 1851		12.1^a	16.6^a	-1.18^a	0.05^a	1.86^a	1.8^a	5.57^d	0.04	5.25^d	0.04	9.3^d	0.5	$< 2.0 \times 10^{3\,d}$
NGC 1904	M79	12.9^a	18.8^a	-1.60^a	0.01^a	1.70^a	2.4^a	5.15^d	0.03	4.94^d	0.03	8.0^d	0.5	$(3.0 \pm 1.0) \times 10^{3\,d}$
NGC 2808		9.6^a	11.1^a	-1.14^a	0.12^a	1.56^a	2.2^a	5.91^c	0.04	5.59^c	0.04	13.4^c	0.2	$< 1.0 \times 10^{4\,c}$
NGC 5139	ω Cen	5.2^a	6.4^a	-1.53^a	0.17^a	1.31^a	7.6^a	6.40^k	0.05	5.97^a	0.05	22.0^n	4.0	$(4.7 \pm 1.0) \times 10^{4\,k}$
NGC 5286		11.7^a	8.9^a	-1.69^a	0.12^a	1.41^a	2.5^a	5.45^e	0.02	5.42^e	0.01	9.3^e	0.4	$(1.5 \pm 1.1) \times 10^{3\,e}$
NGC 5694		35.0^a	29.4^a	-1.98^a	0.04^a	1.89^a	4.1^a	5.41^d	0.05	5.09^d	0.05	8.8^d	0.6	$< 8.0 \times 10^{3\,d}$
NGC 5824		32.1^a	25.9^a	-1.91^a	0.03^a	1.98^a	4.2^a	5.65^d	0.03	5.40^d	0.03	11.2^d	0.4	$< 6.0 \times 10^{3\,d}$
NGC 6093	M80	10.0^a	3.8^a	-1.75^a	0.00^a	1.68^a	1.8^a	5.53^d	0.03	5.17^d	0.03	9.3^d	0.3	$< 8.0 \times 10^{2\,d}$
NGC 6266	M62	6.8^a	1.7^a	-1.18^a	0.01^a	1.71^a	1.8^a	5.97^d	0.01	5.57^d	0.01	15.5^d	0.5	$(2.0 \pm 1.0) \times 10^{3\,d}$
NGC 6388		9.9^a	3.1^a	-0.55^a	0.01^a	1.75^a	1.5^a	6.04^b	0.08	5.84^b	0.08	18.9^b	0.3	$(1.7 \pm 0.9) \times 10^{4\,b}$
NGC 6715	M54	26.5^a	18.9^a	-1.49^a	0.06^a	2.04^a	6.3^a	6.28^g	0.05	6.20^g	0.05	14.2^i	1.0	$(9.4 \pm 5.0) \times 10^{3\,l}$
NGC 7078	M15	10.4^a	10.4^a	-2.37^a	0.05^a	2.29^a	3.0^a	5.79^f	0.02	5.59^a	0.02	12.0^f	0.0	$< 4.4 \times 10^{3\,f}$

In this paper we take the latest results for IMBH measurements in GCs from the literature and search for correlations with properties of their host cluster. For the first time, enough datapoints on IMBHs are available to perform this analysis. Established relations for SMBHs and their host galaxies, such as the $M_\bullet - \sigma$ relation or the $M_\bullet - M_{tot}$, are the focus of this work. Probing the low-mass end of these correlations will provide important information about the origin and growth of SMBHs. In Section 6.2 we introduce the sample and the data from the literature used in this work. Section 6.3 describes the methods we applied for determining correlation coefficients and regression parameters, and in Section 6.4 we discuss the major correlations and their statistical significance. Finally, Section 7.5 summarizes our work and lists our conclusions.

6.2 The sample

The sample we chose for our analysis consists of 14 Galactic GCs for which we have kinematic measurements of their central regions. The majority of these measurements come from integral-field spectroscopy and were carried out by our group (Feldmeier et al. 2013, Chapter 2, 3, and 5) .

These clusters were observed with the GIRAFFE spectrograph of the FLAMES (Fiber Large Array Multi Element Spectrograph, Pasquini et al. 2002) instrument at the Very Large Telescope (VLT) using the ARGUS mode (Large Integral Field Unit). The velocity-dispersion profile was obtained by combining the spectra in radial bins centered around the adopted photometric center and measuring the broadening of the lines using a non parametric line-of-sight velocity-distribution fitting algorithm. For larger radii, the kinematic profiles were completed with radial velocity data from the literature, when available. In addition to the spectroscopic data, HST photometry was used to obtain the star catalogs, the photometric center of the cluster, and its surface brightness profile. For each cluster photometry and spectroscopy were combined to apply analytic Jeans models to the data. The surface brightness profile was used to obtain a model velocity-dispersion profile that was fit to the data by assuming different black-hole masses and M/L_V profiles. The final black-hole masses were obtained from a χ^2 fit to the kinematic data. Table 6.1 lists all clusters of the sample and their main properties.

In four clusters of our sample we found signatures of an IMBH. These clusters are NGC 6388, NGC 6266, NGC 1904, and NGC 5286. All of them show a rise in the velocity dispersion and require black-hole masses between $1.5 \times 10^3 - 2 \times 10^4$ $M_\odot$. A high radial anisotropy in the center of these clusters would also explain the rise in the velocity-dispersion profile. However, N-body simulations have shown that any anisotropy in the center of a GC would be smoothed out after several of relaxation times (Chapter 2). Since all these clusters are older than at least 5-10 relaxation times, we conclude that the best explanation for the rise of the kinematic profile is indeed a black hole. Nevertheless, the result of the cluster NCG 1904 has to be treated carefully since the rise might occur from a mismatch

of outer and inner kinematics. The rest of the clusters in our sample shows less evidence for a central black hole with shallow or even dropping velocity-dispersion profiles. For these we adopted the 1σ errors of the measurement as the upper limit.

ω Centauri, G1, and NGC 6715 are GCs with measured black-hole masses not obtained by our group. For ω Centauri we used the latest result of Noyola et al. (2010) for the black-hole mass of the IMBH in ω Centauri of $\sim 47\,000\,M_{\odot}$, which was derived by studying VLT/FLAMES integral-field spectroscopy data of the inner kinematics, similar to the method described above. This value was also confirmed through a comparison with N-body simulations by Jalali et al. (2012). The GC G1 in M31 was observed with the Space Telescope Imaging Spectrograph (STIS) by Gebhardt et al. (2002) and the velocity-dispersion profile compared with dynamical Schwarzschild models. For our analysis we used their derived mass of $M_{\bullet} = (1.8 \pm 0.5) \times 10^4\ M_{\odot}$. Ibata et al. (2009) measured the inner kinematics of the GC NGC 6715 (M54) using a combination of VLT/FLAMES MEDUSA and ARGUS data. They found a cusp in the inner velocity-dispersion profile consistent with a $\sim 9\,400\ M_{\odot}$ IMBH. Unfortunately, they did not provide any uncertainties on this measurement since they could not exclude a high amount of radial anisotropy in the center, which would also explain the rise of the profile. With our results obtained in Chapter 2 however, we are confident that high radial anisotropy is not very likely to reside long in the centers of GCs. We therefore adopted the IMBH measurement of Ibata et al. (2009) and a conservative uncertainty of 50% on the black-hole mass. We stress that high anisotropy in a GC is unlikely for undisturbed clusters, but considering the violent environment of some clusters in the sample (i.e., NGC 6388 and NGC 6266), disk and bulge shocking cannot be excluded. The uncertainty in the black-hole mass measurement might therefore be underestimated in some cases.

The last two clusters included in our sample are M15 and 47 Tuc. Both of them seem to have no IMBHs at their centers. M15, which was observed with several instruments over the past years, was one of the most popular objects for the studying IMBHs. Because it is a post-core collapse cluster, M15 is nowadays assumed to be a poor candidate for hosting an IMBH, since a massive black hole would enlarge the core of the cluster and prevent core collapse (Baumgardt et al. 2003; Noyola & Baumgardt 2011). 47 Tuc is a poor candidate for hosting a massive black hole at its center as well. McLaughlin et al. (2006) obtained HST proper motions for 47 Tuc and found no evidence for a rise in its velocity dispersion profile, i.e., an IMBH.

The final sample of GCs and their properties are listed in Table 6.1. The cluster parameters were taken from different sources (see references in Table 6.1) and their black-hole masses from the observations listed above.

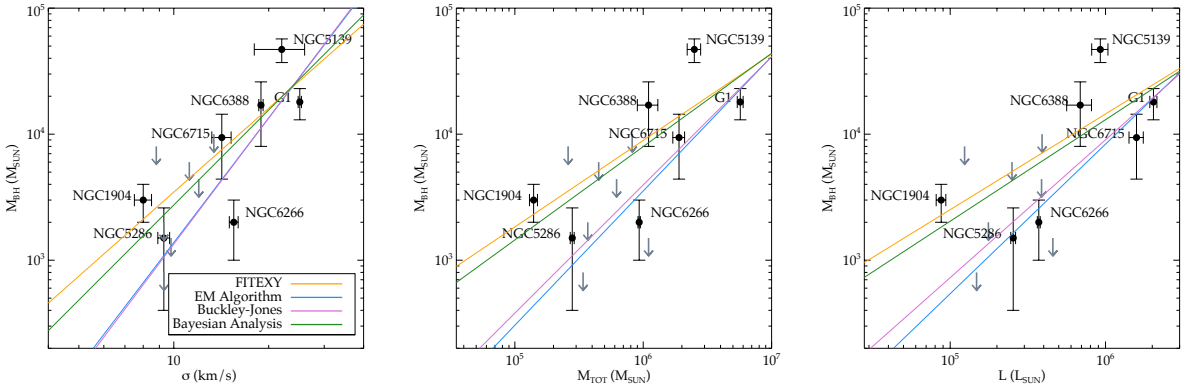

Figure 6.1: $M_\bullet - \sigma$ (left), $M_\bullet - M_{TOT}$ (middle) and $M_\bullet - L_{TOT}$ (right) relation for GCs with IMBHs. The gray arrows indicate upper limits. We compare the slopes of the best-fits from four different methods.

6.3 Dealing with censored data

With our current dataset we encountered several challenges. 1) The dataset is small. With $n = 14$ we enter statistical regimes ($n < 30$) where many statistical approaches are not reliable anymore i.e., the Spearman correlation test. 2) The dataset contains not only measurements, but also a large number of upper limits. The statistical method that deals with these so-called censored datasets is called survival analysis. Feigelson & Nelson (1985) and Isobe et al. (1986) proposed several techniques for applying survival analysis to astronomical datasets. Especially treating bivariate data (a dataset with two variables) with upper limits and determining correlation coefficients and linear regressions is described in detail in these papers. However, survival analysis does not treat uncertainties of the detected measurements. This would bias our result since our dataset 3) also contains large asymmetric uncertainties in both variables.

We are not aware of a heuristic method that treats all of these caveats properly. Therefore, we present several attempts at analyzing the data by accounting for each problem separately and discuss their differences. The goal is to test for possible correlations between two parameters of the dataset. For parameters with a significant correlation we obtain the linear regression parameters α, β and ϵ_0, where

$$y = \alpha + \beta x \tag{6.1}$$

and ϵ_0 indicates the intrinsic scatter, i.e.,the dispersion in y due to the objects themselves rather than to measurement errors.

6.3.1 Partly treating uncertainties

Since there are no correlation coefficients known that would include measurements uncertainties, we are limited to the standard statistical methods. Furthermore, because our dataset is small, we cannot perform a meaningful Spearman correlation test. This leaves us with the the Kendall-τ rank correlation coefficient as a measurement for the significance of the correlation. The τ parameter is calculated through the numbers of concordant (ranks of both elements agree) and discordant (ranks of both elements differ) datapairs and the total number of elements in the dataset. If the data x and y are independent of each other, then the correlation coefficient τ becomes zero. Positive and negative signs of the Kendall-τ imply a correlation and anticorrelation of the data, respectively. Table 6.2 lists the Kendall-τ and the significance of its deviation from zero (P) for several data combinations as calculated from the IDL routine R_CORRELATE.

As suggested from Table 6.2 and Figure 6.1, there are three correlations observed in our dataset: $M_\bullet - \sigma$, $M_\bullet - M_{tot}$, and $M_\bullet - L$, as observed for SMBHs in massive galaxies. To compare the correlation properties with measurements from galaxies we performed a power-law fit to the data defined as

$$\log_{10}(M_\bullet/M_\odot) = \alpha_\sigma + \beta_\sigma \log_{10}[\sigma/(200\,\mathrm{km s^{-1}})] \quad (6.2)$$

$$\log_{10}(M_\bullet/M_\odot) = \alpha_M + \beta_M \log_{10}[M_{tot}/(10^{11} M_\odot)] \quad (6.3)$$

$$\log_{10}(M_\bullet/M_\odot) = \alpha_L + \beta_L \log_{10}[L_{tot}/(10^{11} L_\odot)] \quad (6.4)$$

.

All three relations were fitted using the algorithm described by Tremaine et al. (2002), where the quantity

$$\chi^2 = \sum_{i=1}^{N} \frac{[\log_{10}(M_{\bullet,i}) - \alpha - \beta \log_{10}(\sigma/\sigma_0)]^2}{\epsilon_0^2 + \epsilon_{M,i}^2 + \beta^2 \epsilon_{\sigma,i}^2} \quad (6.5)$$

is minimized and the 68% confidence intervals of α and β are determined by the range for which $\Delta\chi^2 = \chi^2 - \chi^2_{min} \leqslant 1$. The uncertainties of $M_\bullet$ (ϵ_M) and σ (ϵ_σ) are considered asymmetrically in the power-law fit and the internal scatter ϵ_0 is set such that the reduced χ^2, i.e., the χ^2 per degree of freedom, is unity after minimization. σ_0 is chosen to be 200 $\mathrm{km\,s^{-1}}$ (as in Equation 6.2). For Equation 6.3 and 6.4, σ_0 becomes $M_0 = 10^{11} M_\odot$ and $L_0 = 10^{11} M_\odot$, respectively. We used the IDL routine PMFITEXY[1] (Williams et al. 2010) and extended it to account for asymmetric errorbars. The final values of the fit are given in Table 6.3, which compares the fit parameters from different methods.

[1]Available at: http://purl.org/mike/mpfitexy

6.3.2 Treating upper limits

The methods developed by Feigelson & Nelson (1985) and Isobe et al. (1986) combine survival analysis with astronomical applications such as determining correlation coefficients and linear regression parameters. The basic ingredients are the survival function $S(z_i)$ (the probability that the object is not detected until z_i) and the hazard function $\lambda(z_i)$ (the instantaneous rate of detection at z_i given that the object is undetected before z_i). These functions are used to construct statistical quantities and also consider the non-detections.

A package of Fortran routines called ASURV[2] is available for this purpose. The package contains routines for determining non-parametric correlation coefficients such as the Cox proportional hazard model (Equation 21 in Isobe et al. 1986), the generalized Kendall rank correlation (Equation 28), and linear regression methods such as the expectation-maximization (EM) algorithm with different distributions. We applied the routines to our data and list the results in Table 6.2 for the correlations and Table 6.3 for the linear regression parameters. For the generalized Kendall rank correlation the routine does not calculate τ itself but the number of standard deviations from zero ($z = \tau/[\mathrm{Var}(\tau)]^{\frac{1}{2}}$, where $\mathrm{Var}(\tau)$ is the variance of τ under the null hypothesis). From this value, the significance of a correlation between the two variables (P) can be found from a table of the integrated Gaussian distribution. For the Cox proportional hazard model (CPH) a χ^2 value is defined to test for the significance of a correlation and the probability is taken from χ^2 distribution tables.

We stress that survival analysis a) assumes detections to be exact measurements, i.e., does not treat uncertainties and b) treats upper limits as absolute values, above (or below) where the data are definitely not detected. Since neither is the case for our data, the results have to be treated with care.

6.3.3 Combining uncertainties and upper limits

To treat upper limits and uncertainties in a dataset simultaneously, Kelly (2007) developed a Bayesian method that accounts for measurement errors in linear regression. This method is based on a maximum likelihood approach that is generalized to deal with multiple independent variables, nondetections (upper limits), and selection effects.

The basic approach of the routine (available as IDL routine LINMIX_ERR in the Astrolib package) is to generate a random sample of the regression parameters drawn from the probability distribution of the parameters given the measured data using a Markov chain Monte Carlo algorithm. For each iteration the regression parameters and the parameters of the prior density are updated until the Markov chain converges to the posterior distribution. The saved parameter values can then be treated as a random draw from the posterior. The final values are derived through the mean or median of the random draw.

[2]Available at: http://astrostatistics.psu.edu/statcodes/asurv

Table 6.2: Correlation parameters and significance calculated with various methods.

	STANDARD STATISTICS		SURVIVAL ANALYSIS			
	Kendall		Generalized Kendall		Cox proportional hazard Model	
Relation	τ	P	z	P	χ^2	P
$M_\bullet - \sigma$	0.79	0.96	12.57	1.00	2.62	0.99
$M_\bullet - M_{TOT}$	0.82	0.98	5.50	0.98	2.48	0.99
$M_\bullet - L_{TOT}$	0.71	0.93	6.45	0.99	2.40	0.98
$M_\bullet - D_{SUN}$	−0.04	0.06	3.03	0.92	0.40	0.31
$M_\bullet - D_{GC}$	0.21	0.36	0.01	0.09	0.27	0.21
$M_\bullet - [Fe/H]$	0.32	0.52	0.37	0.46	1.00	0.68
$M_\bullet - e$	0.48	0.73	1.95	0.84	1.28	0.80
$M_\bullet - c$	0.11	0.18	0.96	0.67	0.40	0.31
$M_\bullet - r_h$	0.54	0.78	2.34	0.87	1.60	0.89

To perform the Markov chain, two methods are available: The first one is the Gibbs sampler, which simulates new values of the model parameters and missing data at each iteration depending on the values of the observed data, current model parameters, and missing data (Kelly 2007). The second method is the Metropolis-Hastings algorithm (e.g. Metropolis et al. 1953; Hastings 1970) which is used when the selection function is not independent of the dependent variables y, the measurement errors are large, or the sample size is small. Since this is the case for our sample, we used the Metropolis-Hastings algorithm to determine the regression parameters (for more details we refer to Kelly 2007). In Table 6.3 we list the parameters obtained with this method. For the subsequent analysis we adopted the results of the Bayesian method as the derived fit.

6.4 Discussion

In this section we discuss the results listed in Table 6.3 and compare the resulting correlations of IMBHs with the existing scaling relations of SMBHs in galaxies.

6.4.1 The three main scaling relations

The first correlations we studied are the ones observed in galaxies. Comparing these scaling relations with those obtained for GCs might shed light onto their origin and the evolution of GCs. Therefore, we first examined the relations $M_\bullet - \sigma$, $M_\bullet - M_{tot}$, and $M_\bullet - L$. We tested for the significance of a correlation by applying the methods described in the previous section. Table 6.2 lists the results of the Kendall τ test from standard statistics compared with the generalized Kendall τ and the results from the CPH model from survival analysis. The value P gives the probability of an existing correlation between the two values and

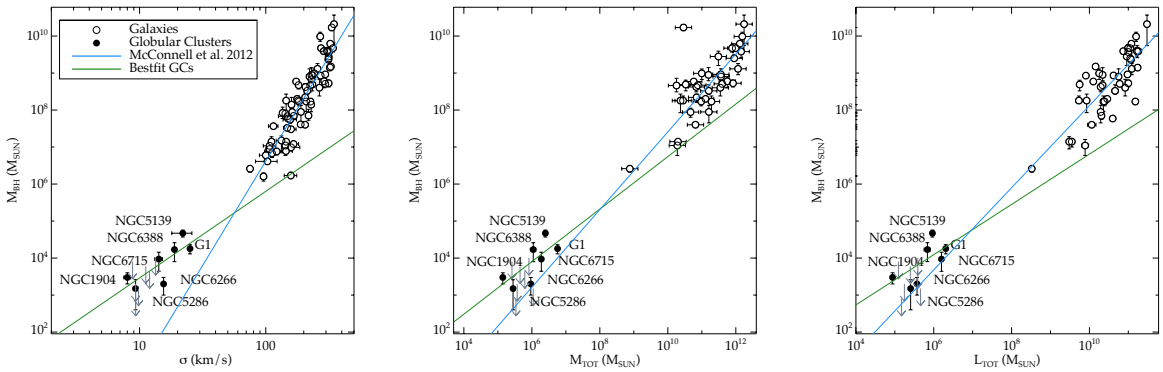

Figure 6.2: $M_\bullet - \sigma$, $M_\bullet - M_{tot}$, and $M_\bullet - L_{tot}$ relations of IMBHs and SMBHs in comparison. The slope of the best fit to the GCs (green line) is a factor of two shallower than the slope for the SMBHs in galaxies (blue line) for $M_\bullet - \sigma$, but very similar for the remaining two correlations.

shows high significance ($> 90\%$) for all three correlations with all methods. The highest probability is found for the $M_\bullet - \sigma$ relation when using the generalized Kendall τ, but when regarding only the standard statistics, the $M_\bullet - M_{tot}$ is given the highest significance. It is also the correlation with the most stable results over all three methods.

The existence of these correlations agrees with previous measurements of SMBHs in galaxies, where the same main scaling relations where found. We applied a linear regression to all three relations, using the methods described in the previous sections. In Figure 6.2 we show the three scaling relations, overplotted by the best fits from the Bayesian method (green line in Figure 6.1). For the $M_\bullet - \sigma$ relation, all parameters of the linear regression from the different methods agree within their errorbars. The parameters derived from the different survival analysis methods are almost identical. In general, the plots show that the values of the survival analysis do not differ much from each other for all correlations. The same is true for the FITEXY method and the Bayesian approach, which shows that the errorbars have a stronger effect on the fit than the upper limits.

Comparing these values with slopes obtained for SMBHs in galaxies (Figure 6.2, blue line) yields a significant difference for the slope of the correlation between galaxies and GCs in the $M_\bullet - \sigma$ relation. The most recent slope obtained from McConnell & Ma (2013) is $\beta_\sigma = 5.64 \pm 0.32$, a factor of two higher than the value that we measured for the GCs. This is also visible in Figure 6.2 where the values for the galaxies and the GCs are overplotted. The $M_\bullet - \sigma$ relation seems to be curved upward when reaching the very high-mass black holes and becomes more shallow when reaching the low-mass range.

Moreover, for the $M_\bullet - M_{tot}$ and $M_\bullet - L_{tot}$ correlation all IMBH masses lie above the correlation found for galaxies but, as shown in Figure 6.2, the slopes of the correlations do not differ as much as they do for the $M_\bullet - \sigma$ relation. In fact, with $\beta = 1.11 \pm 0.13$ for $M_\bullet - L_{tot}$ and $\beta = 1.05 \pm 0.11$ for $M_\bullet - L_{tot}$, the values obtained by McConnell & Ma (2013) agree with the values from Table 6.3 within their uncertainties.

One possible explanation for the difference in the scaling relations could be a strong mass-loss of GCs in the early stages of their evolution. Especially for ω Centauri, NGC 1851, and G1 this could have had a considerable effect because these objects were suggested to be cores of stripped dwarf galaxies (Freeman 1993; Meylan et al. 2001; Jalali et al. 2012; Sollima et al. 2012). A higher mass in the early stage of evolution of these objects would have shifted the points in all three plots to the right and therefore closer to the correlations observed for galaxies. The strongest difference in slopes is shown in the $M_\bullet - \sigma$ relation. Expansion due to mass loss and relaxation would lead to an decrease of the velocity dispersion and could explain the different effect on M_{tot} and σ.

Another explanation would be a different mass-radius relation for galaxies and GCs which complicates the comparison of the scaling relations as the velocity dispersion is measured from an effective radius in both systems. Since GCs and galaxies are different objects, formed in different environments and processes, this explanation seems reasonable and is discussed in Graham (2013) and references therein. The fact that our relations match with the results found for nuclear star clusters (Graham 2012; Neumayer & Walcher 2012), which are found to exhibit shallow slopes, similar to GCs, supports this theory. Furthermore, clusters in our sample with upper limits still have a probability of hosting smaller IMBHs not detected up to date. This would bias all the relations towards high IMBH masses and could partly explain the difference in slopes. In fact, this is indicated by the steeper slopes from the survival analysis (where we consider only upper limits but no errorbars) as shown in Figure 6.1.

6.4.2 Are there more correlations?

The three main scaling relations discussed above are known for galaxies that host SMBHs at their centers. Even for the cases where the slopes of the IMBH correlations agree with the SMBH, it does not imply a causal connection. Formation scenarios and co-evolution of host system and black hole are assumed to be quite different for galaxies and GCs. For this reason it is crucial to search for fundamental correlations of cluster-specific values with the mass of the IMBH. This has never been done before. This section is dedicated to describe the choice of parameters and the results on their correlation significance.

Distances

The first parameter we checked is the distance to the sun (D_{SUN}). No correlation is expected with this parameter, but it can be used to exclude observational biases that might be introduced to the measurements. The farther away the object, the larger one would expect the uncertainty on the black-hole mass to be. Panel a) of Figure 6.3 shows the black-hole mass as a function of distance for all Galactic GCs in our sample. We excluded G1 from the plot (but not from the analysis) because it is the only cluster outside the Milky Way and its large distance would distort the figure. From the plot no evident correlation

Table 6.3: Best-fit parameters for the three main scaling relations obtained form different fitting routines.

	$M_\bullet - \sigma$	$M_\bullet - M_{TOT}$	$M_\bullet - L_{TOT}$
	—FITEXY—		
α	6.42 ± 0.77	7.38 ± 1.40	7.96 ± 1.81
β	2.21 ± 0.69	0.69 ± 0.28	0.76 ± 0.34
ϵ	0.25	0.33	0.35
	—SURVIVAL ANALYSIS—		
	EM Algorithm		
α	7.41 ± 0.83	8.63 ± 2.03	9.84 ± 2.10
β	3.28 ± 0.72	1.01 ± 0.34	1.18 ± 0.37
σ	0.36	0.49	0.47
	Buckley-Jones Method		
α	7.45	8.42	9.47
β	3.32 ± 0.92	0.96 ± 0.32	1.10 ± 0.40
σ	0.42	0.43	0.46
	—BAYESIAN ANALYSIS—		
α	6.51 ± 1.94	7.45 ± 3.53	7.49 ± 6.08
β	2.34 ± 1.63	0.71 ± 0.59	0.68 ± 1.05

between D_{SUN} and $M_\bullet$ can be found, but the correlation coefficients in Table 6.2 show a wide spread, reaching from a slight anti-correlation for the standard Kendall τ to a significant correlation when using survival analysis. The reason for this mismatch might arise from the outlier position of G1 compared with the other distances.

As another parameter we studied the distance of the cluster to the Galactic center (in case of G1 to the center of M31), i.e., the position of the cluster in its host galaxy (D_{GC}). Finding a correlation or anticorrelation with galactocentric distance could invite speculations about a connection between environment and black-hole formation, although the clusters are most probably not at the same distance where they were formed. Panel b) and the results in Table 6.2 indicate no correlation with D_{GC}.

Metallicity

In Panel c) we correlate the black-hole mass with the metallicity of the cluster. A cluster with a low metallicity might be more likely to form a massive black hole through runaway merging of massive stars because of the lack of strong stellar winds at low metallicities (e.g. Vanbeveren et al. 2009). However, according to Figure 6.3.c and the values in Table 6.2, this does not seem to be the case.

Morphology

The lower panels in Figure 6.3 depict the black-hole mass as a function of the three structural parameters: ellipticity (e), concentration (c), and half-mass radius (r_h). The reason why we tested for correlations in these parameters lies in the possible connection between morphology and the cluster being the nucleus of an accreted dwarf galaxy. For example, a high ellipticity would speak against GCs, which are assumed to be spherical and dynamically relaxed systems and for a remnant of a dwarf galaxy where aspherical shapes are more common. In the same context, an IMBH in a dwarf galaxy is thought to be more massive than in a GC since more mass was available at its formation.

Furthermore, it has been shown that a black hole prevents core collapse and extends the inner regions of the cluster (e.g. Baumgardt et al. 2005). Therefore, a correlation of the central concentration with black-hole mass would be expected. Clusters with large half-mass radii have also been suggested to be good candidates of clusters hosting IMBHs at their centers. The highest correlation significance is found for the half-mass radius, but for the ellipticity a $1-2\,\sigma$ detection of correlation is present as well. For the concentration, the values of the different methods show strong variations ranging from 18% to 67%. In summary, the structural parameters and the black-hole mass show signs of correlations. However, the detection significance is low and needs to be confirmed with a larger data set.

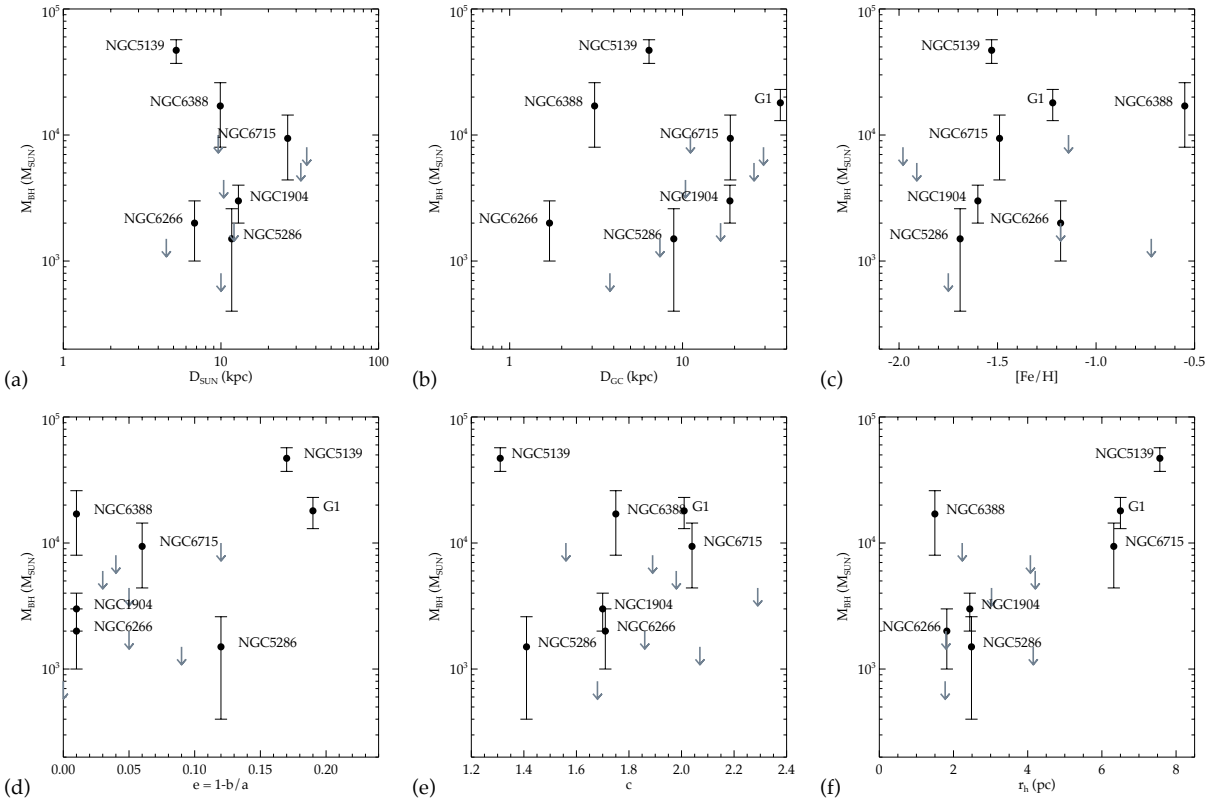

Figure 6.3: IMBH masses as a function of several cluster properties such as a) the distance of the cluster to the sun (D_{SUN}), b) the distance from the Galactic center (D_{GC}), c) the metallicity ([Fe/H]), d) the ellipticity ($e = 1 - b/a$), e) the concentration parameter (c), and f) the half-mass radius (r_h)

6.5 Summary and conclusions

We collected data from the literature from GCs that were examined for the existence of a possible IMBH at their center using stellar dynamics. Our sample consists of 14 GCs with kinematically measured black-hole masses: six of them are thought to host IMBHs, the remaining ones have only upper limits on black-hole masses. To take uncertainties and upper limits into account, we used different methods to derive the correlation coefficients and linear regression parameters. We plotted the masses of the central IMBH versus several properties of the host clusters, such as total mass, total luminosity, and velocity dispersion to verify existing correlations that are found in galaxies, but also in the attempt to find new correlations between black-hole mass and cluster properties. We found that the three main correlations that are observed in galaxies ($M_\bullet - \sigma$, $M_\bullet - M_{tot}$, and $M_\bullet - L_{tot}$) also hold for IMBHs. The slope of the $M_\bullet - \sigma$ relations differs by a factor of two from the fits made to the galaxy sample while the remaining correlations are more similar to those observed for galaxies.

Furthermore, we tested for possible correlations of the IMBH mass and other properties of the GC such as distance, metallicity, structural properties, and size. We found no evidence for a correlation as strong as the $M_\bullet - \sigma$ relation, but we found a trend of black-hole mass with the cluster size, i.e., the half-mass radius r_h and its ellipticity. This is reasonable since the central black hole leads the cluster to expand by accelerating stars in its vicinity.

We assume in the following that the $M_\bullet - \sigma$ relation is tight, has a physical origin, and extends to the lowest masses. These assumptions have not rigorously been demonstrated to date. We also assume that the IMBHs in GCs formed at high redshifts and did not evolve much since then, unlike the GCs themselves, which will have suffered mass loss during their evolution. With these assumptions, a proposed explanation for this behavior is the process of stripping, which might have occurred to these stellar systems when accreted to the Milky Way. If they were more massive and luminous in the past, they would have fit to the correlation of the galaxies instead of being shifted to the low-mass end. These stripping scenarios have previously been suggested for clusters like G1 and ω Centauri, as mentioned in Section 6.1. In particular, because clusters most probably lost most of their mass during their lifetime and galaxies gained mass during their merging history, it would be very surprising to find both objects on the same scaling relation.

The fact that the $M_\bullet - \sigma$ shows higher discrepancies when comparing the relation of galaxies than $M_\bullet - M_{tot}$ and $M_\bullet - L_{tot}$ might arise from either different mass-radius relations of these very different black-hole host systems or from the expansion-driven decrease of the velocity dispersion in GCs. This is supported by the fact that the scaling relations agree with the upper limits for nuclear clusters, which are stellar systems similar to GCs. N-body simulations and semi-analytic expansion models are needed to quantitatively study these theories. We note that a bias toward higher black-hole masses due to detection limits cannot be excluded either.

For the future we aim to extend this sample and confirm the reported correlations and their slopes. With integral-field units combined with adaptive optics, the search for IMBHs can be extended to extragalactic sources. Nevertheless, a complete search of Galactic GCs will provide a larger sample and help to additionally constrain critical observables that hint at the presence of an IMBH in the center of a GC.

Acknowledgements: *This research was supported by the DFG cluster of excellence Origin and Structure of the Universe (www.universe-cluster.de). N.L. thanks Eric Feigelson, Brandon Kelly and Michael Williams for their friendly support and for providing the essential software used in this work. We thank the referee for constructive comments and suggestions that helped to improve this manuscript.*

CHAPTER 7

N-body simulations of globular clusters in tidal fields: Effects of intermediate-mass black holes.

Nora Lützgendorf, Holger Baumgardt, and J. M. Diederik Kruijssen
Astronomy & Astrophysics, submitted (2013)

Abstract Intermediate-mass black holes (IMBHs) may provide the missing link in order to understand the growth of supermassive black holes in the early universe. Some formation scenarios predict that IMBHs could have formed by runaway collisions in globular clusters (GCs). However, it is challenging to put observational constraints on the mass of a black hole in a largely gas-free (and hence accretion-free) stellar system such as a GC. Understanding the influence of an IMBH in the center of a GC on its environment might provide indirect detection methods. Our goal is to test the effects of different initial compositions of GCs on their evolution in a tidal field. We pin down the crucial observables which indicate the presence of an IMBH at the center of the cluster. Besides central IMBHs, we also consider the effects of different stellar-mass black hole retention and stellar binary fractions. We perform a set of 22 *N*-body simulations and vary particle numbers, IMBH masses, stellar-mass black-hole retention fractions and stellar binary fractions. These models are all run in an external tidal field in order to study the effect of black holes on the cluster mass loss, mass function and life times. Finally, we compare our results with observational data. We find that a central massive black hole increases the escape rate of high-mass stars from a star cluster, implying that the relative depletion of the mass function at the low-mass end proceeds less rapidly. Furthermore, we find a similar behavior when a cluster hosts a high number of stellar-mass black holes instead of one massive central IMBH. The presence of an IMBH also weakly affects the fraction of the cluster mass that is constituted by stellar remnants, as does the presence of primordial binaries. We compare our simulations with observational data from the literature and find good agreement between our models and observed mass functions and structural parameters of GCs. We exploit this agreement to identify GCs that could potentially host IMBHs.

7.1 Introduction

The dynamical evolution of globular clusters (GCs) in a tidal field causes them to gradually dissolve (e.g. Ambartsumian 1938; Spitzer 1958; Baumgardt 2001). After GCs have migrated out of their gas-rich birth environment (Shapiro et al. 2010; Elmegreen 2010; Kruijssen et al. 2012), this dissolution is driven by two-body relaxation, i.e. the repeated effect of soft encounters between stars, which leads to energy equipartition and populates the high-velocity tail of the Maxwellian velocity distribution (e.g. Portegies Zwart et al. 2010). Because escape is driven by a tendency towards energy equipartition between stars of different masses and a mass-dependent encounter rate, the escape probability is not the same for all stars and generally decreases with mass (Hénon 1969; Vesperini & Heggie 1997; Takahashi & Portegies Zwart 2000; Baumgardt & Makino 2003; Kruijssen 2009). As a result of mass segregation, high-mass stars sink to the center of a star cluster while low-mass stars are pushed to the outskirts, where they are easily removed by the galactic tidal field. This changes the slope of the mass function (MF) and the mass-to-light ratio (M/L) of the GC (e.g. Richer et al. 1991; De Marchi et al. 2007; Mandushev et al. 1991; Kruijssen & Mieske 2009; Baumgardt & Makino 2003).

How the content of evaporating clusters evolves exactly depends on their initial composition and global properties. Kruijssen (2009) showed that the most massive objects in a cluster play a key role in determining which bodies escape. It is therefore important when the bulk of the dynamical mass loss occurs, i.e. early on (when massive stars are still present) or after ~ 1 Gyr (when all stars with masses $m > 2\ M_\odot$ will have ended their lives). In the latter case, the cluster evolution will be dominated by stellar remnants, because at such old ages they generally have masses that exceed the masses of the most massive luminous stars. During their formation process, remnants receive velocity kicks (e.g. Lyne & Lorimer 1994; Pfahl et al. 2002; Moody & Sigurdsson 2009; Fregeau et al. 2009), and hence the fraction of remnants that is retained depends on the depth of the potential well M/r_h (see Kruijssen 2009 for a quantitative analysis), as well as the magnitude of the kick velocity.

If the central density of a young GC is high enough, runaway collisions between stars may be able to produce an intermediate-mass black hole (IMBH, see Portegies Zwart et al. 2004; Gürkan et al. 2004). In the context of the above discussion, it is clear that the presence of an IMBH could potentially have an observable influence on the evolution of the GC composition. Thus far, the search for IMBHs has focused on direct detection through kinematics (e.g. Baumgardt et al. 2003; van den Bosch et al. 2006; Noyola et al. 2008, and Chapter 2), surface brightness profiles (e.g. Noyola & Gebhardt 2006), or the search for Bondi-Hoyle accretion in the centers of GCs (e.g. Strader et al. 2012). An analysis of how the presence of IMBHs changes the stellar composition of GCs would provide an independent tracer, or at the very least facilitate better criteria for the selection of target GCs in observational work.

Previous numerical work on IMBHs in GCs has had a natural emphasis on the internal evolution of GCs. Baumgardt et al. (2005) and Noyola & Baumgardt (2011) found that the surface brightness profiles of clusters hosting an IMBH exhibit weak central cusps, in contrast to core-collapsed clusters with very steep profiles and pre-core collapsed systems with no cusp at all. However, Trenti et al. (2010) and Vesperini & Trenti (2010) showed that the shallow cusp may also form as a transition state of GCs undergoing core collapse and therefore cannot be a sufficient criterion for a GC hosting an IMBH. Furthermore, it has been shown that IMBHs prevent a cluster from undergoing core collapse and reduce the degree of mass segregation compared to non-IMBH clusters (Baumgardt et al. 2004; Gill et al. 2008). Trenti et al. (2007) predict that clusters with a large ratio of core radius to half-mass radius are good candidates for hosting an IMBH. This was challenged by Hurley (2007) who showed that the ratios observed for Galactic GCs can be explained without the need for an IMBH when treating model data as if they were observational data. Most of these studies focused on internal observables such as the surface brightness profile and hence did not consider tidal effects. Because of the importance of a tidal boundary for the eventual composition of a GC, our simulations do include a tidal field. A first effort in this direction was made by Trenti et al. (2010), who included a single *N*-body run with an IMBH in their model grid of tidally dissolving clusters.

In this paper, we address the dynamical evolution of GCs with direct *N*-body simulations, serving two particular aims. Firstly, we study the evolution of the composition of dissolving clusters itself, covering a substantial part of the parameter space. In doing so, we vary quantities that are important but have not received much prior attention, such as the remnant retention fraction and the initial binary fraction. Secondly, we intend to identify global tracers of the presence of IMBHs or massive remnants. We discuss the evolution of the characteristics of GCs and compare them to observational results. Wherever possible, we identify potential targets for future observational searches for IMBHs.

The structure of the paper is as follows: In Section 7.2, we introduce the *N*-body code and the initial conditions of the simulations. Section 7.3 is dedicated to the influence of different IMBH masses, black-hole retention fractions, and binary fractions on the properties of tidally dissolving clusters. In Section 7.4, we compare our numerical results to the observed distribution of GCs in the mass function slope versus concentration plane. The paper is concluded with Section 7.5, where we summarize our work and present our conclusions.

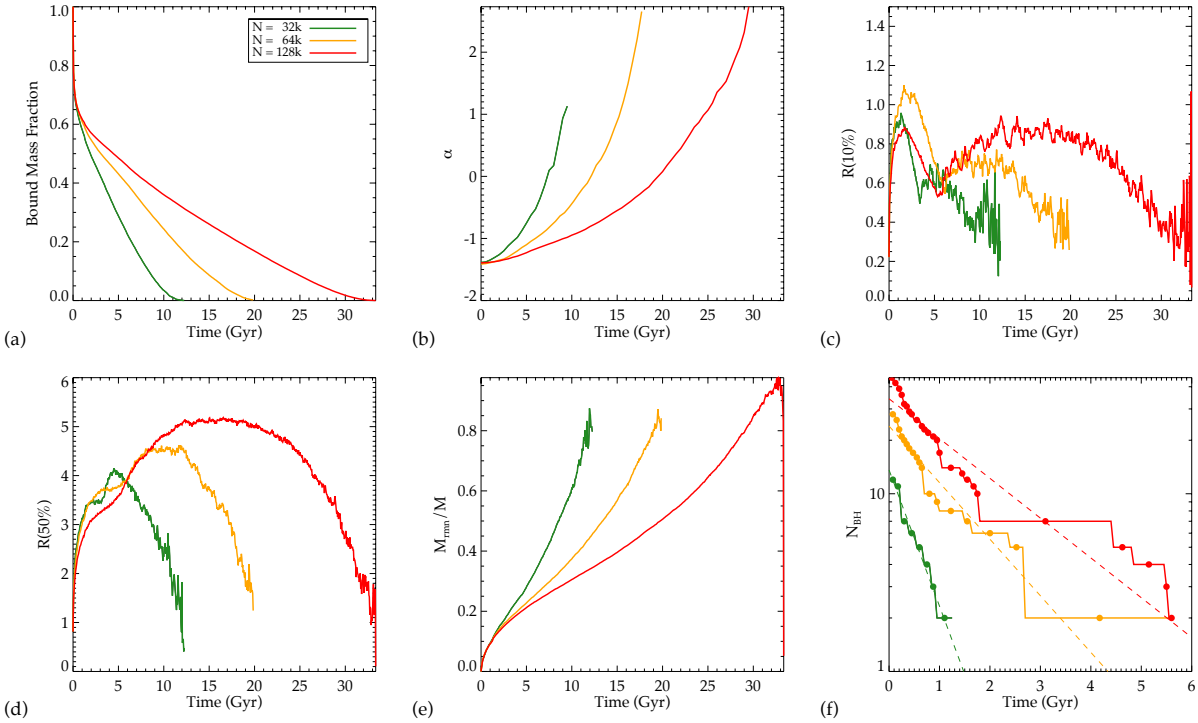

Figure 7.1: Evolution of the reference models. Shown are: a) the bound mass fraction, b) the slope of the mass function α (for $0.3\,M_\odot < m < 0.8\,M_\odot$), c) the Lagrangian radii $r_{10\%}$ and d) $r_{50\%}$, e) the remnant mass fraction, and f) the number of stellar-mass black holes as a function of time. We stress that the absolute time on the x-axis is arbitrary as it depends on the total mass and the galactocentric distance and is therefore only shown for relative comparison. Dashed lines in Panel f) mark the logarithmic fits to the evolution of the black hole numbers.

7.2 Models

In this section we describe the survey of *N*-body simulations that are treated in this paper.

7.2.1 *N*-body simulations

We run *N*-body simulations based on the GPU (Graphic Processing Unit)-enabled version of the collisional *N*-body code NBODY6 (Aarseth 1999; Nitadori & Aarseth 2012) on GPU graphic cards at the Headquarters of the European Southern Observatory (ESO) in Garching and the University of Queensland in Brisbane. This code uses a Hermite integration scheme with variable time steps. Furthermore it treats close encounters between stars by applying KS (Kustaanheimo & Stiefel 1965) and chain regularizations and accounts for stellar evolution (Hurley et al. 2000). The regularization procedures are crucial in order to follow orbits of tightly-bound binaries over a cluster life time accurately and treat strong binary-single and binary-binary interactions properly. The simulations are carried out with particle numbers of $N = 32\,768$ (32k), 65 536 (64k), and 131 072 (128k) stars.

The initial density profile is given by a King (1966) model with a central concentration $W_0 = 7$ and an initial half-mass radius of $r_h = 1$pc. This is preferable to a tidally limited cluster where the tidal radius from the King model is set equal to the Jacobi radius of the tidal field, which has proven to be unrealistic for modeling GC-like densities, since the resulting initial half-mass radii are of the order of 4-5 pc. This has the effect that the clusters are too extended at the beginning of their evolution and undergo core collapse only at the very end of their evolution. Furthermore, after expansion due to mass loss through stellar evolution, these clusters attain half-mass radii of 8-10 pc, much larger than what is observed in GCs today. For this reason we fix the initial half-mass radius to 1 pc. This is more time-consuming due to the increase of the numbers of time steps caused by the smaller crossing times.

All models start with a Kroupa (2001) initial mass function (IMF, $\xi(m)\,\mathrm{d}m \sim m^{\alpha}\,\mathrm{d}m$) which has a Salpeter-like power law slope of $\alpha = -2.3$ for stars more massive than $0.5 M_{\odot}$ and a slope of $\alpha = -1.3$ for stars between 0.08 and $0.5 M_{\odot}$. For the lower and upper mass limit we choose 0.1 and $100\,M_{\odot}$, respectively. This configuration leads to an initial mean mass of $\langle m \rangle = 0.63 M_{\odot}$.

Our clusters are put on a circular orbit around an external galaxy that follows the potential of an isothermal sphere ($\Phi(r) \propto \ln r$). The distance to the Galactic center is chosen to be 8.5 kpc and the circular velocity of the galaxy V_G is set to 220 $\mathrm{km\,s^{-1}}$ for all our simulations as we study Galactic GCs only. The particle integration is done in an accelerated, but non-rotating reference frame where the cluster remains in the center and the galaxy moves around the cluster on a circular orbit. The forces due to the Galactic potential and the stellar gravity are both applied to each star when it is advanced on its orbit through the cluster.

Table 7.1: Initial parameters of the N-body simulations. The similar masses of some of the models are due to an error in the randomizing routine but do not affect the individuality of each model.

N	M_0 ($M_\odot$)	$M_\bullet/M_0$	$f_{\rm ret}$	$f_{\rm bin}$	$T_{\rm diss}$ (Gyr)
- REFERENCE MODELS -					
32768.....	20887	0.00	0.30	0.00	9.55
65536.....	41678	0.00	0.30	0.00	16.55
131072.....	84050	0.00	0.30	0.00	27.35
- FAMILY 1: IMBH MASSES -					
32768.....	20686	0.01	0.30	0.00	9.25
65536.....	41678	0.01	0.30	0.00	16.20
131072.....	84050	0.01	0.30	0.00	28.25
32768.....	20686	0.03	0.30	0.00	7.90
65536.....	41678	0.03	0.30	0.00	13.80
131072.....	84000	0.03	0.30	0.00	24.50
- FAMILY 2: BH RETENTION FRACTION -					
32768.....	20686	0.00	0.00	0.00	9.10
65536.....	41678	0.00	0.00	0.00	15.45
131072.....	83037	0.00	0.00	0.00	26.60
32768.....	20686	0.00	0.50	0.00	10.10
65536.....	41678	0.00	0.50	0.00	16.55
131072.....	83754	0.00	0.50	0.00	28.35
32768.....	20686	0.00	1.00	0.00	10.90
65536.....	41678	0.00	1.00	0.00	18.20
131072.....	84050	0.00	1.00	0.00	30.85
- FAMILY 3: BINARY FRACTION -					
32768.....	20686	0.00	0.30	0.10	9.20
65536.....	41589	0.00	0.30	0.10	15.30
32768.....	20872	0.00	0.30	0.30	8.45
65536.....	41760	0.00	0.30	0.30	13.75

Table 7.1 lists the initial parameters for our set of models, which from left to right are the particle number (N), IMBH-mass fraction ($M_\bullet/M_0$), black-hole retention fraction ($f_{\rm ret}$), binary fraction ($f_{\rm bin}$), and dissolution time ($t_{\rm diss}$, defined as the time the cluster needs to lose 95% of its initial mass, see Section 7.3.1). Due to an error in our mass-randomizing routine, some of the models with the same particle number contain the exact same mass. However, since every model starts with different initial parameters, this does not affect the individuality of each model.

7.2.2 Reference Models

In Figure 7.1 we depict the evolution of our reference models with N = 32k, 64k and 128k stars. Shown are the bound mass fraction (a), the mean slope of the mass function α in the mass interval $0.3\,M_\odot < m < 0.8\,M_\odot$ (b), the Lagrangian radii $r_{10\%}$ (c) and $r_{50\%}$ (d) which include 10 % and 50 % of the cluster mass, respectively (the latter is the half-mass radius r_h), the remnant mass fraction (e), and the number of stellar-mass black holes (f) as a function of time.

The evolution of the bound mass fraction in Figure 7.1.a shows a similar behavior for all models. After a steep drop from 1.0 to 0.7 in the first Gyr, which results mainly from the mass loss due to stellar evolution, the mass fraction drops almost linearly until the last few Gyrs of the cluster lifetime. After this, the mass loss slows down. Besides the increasing lifetime with particle number we do not find significant differences among these models in terms of their mass evolution.

The next quantity we show is the evolution of the mass function slope α. This is done by binning the mass intervals logarithmically going from $m = 0.2\ M_\odot$ to $10\ M_\odot$ in 20 bins. We determine the slope of the mass function by fitting a power law to the points with $0.3\,M_\odot < m < 0.8\,M_\odot$, as this is the same fitting area used for the observational data. The result is shown in Figure 7.1.b. As expected, the slope of the mass function increases with the age of the cluster as the cluster loses low-mass stars through two-body relaxation. As with the bound mass fraction there are no significant differences between models with different particle numbers other than the time scaling (when plotting these values as a function of the fraction of the total lifetime t/t_{diss} all three models agree).

The plots 7.1.c and d depict the evolution of the two Lagrangian radii that include 10 % and 50 % of the cluster mass, respectively. The core collapse is indicated by a drop in the 10 % Lagrangian radius followed by an immediate rise due to binary heating. Surprisingly, the exact occurrence of that event does not seem to depend on the particle number. While the 32k model undergoes core collapse first, the 128k core collapse still occurs before the 64k model reaches this point. However, the slightly different occurrences of the core collapse might be due to noise in the models with low particle numbers.

The last two plots (Figure 7.1.e and f) show the evolution of the stellar remnants in the clusters. In Figure 7.1.e the remnant mass fraction increases with time. This is due to the

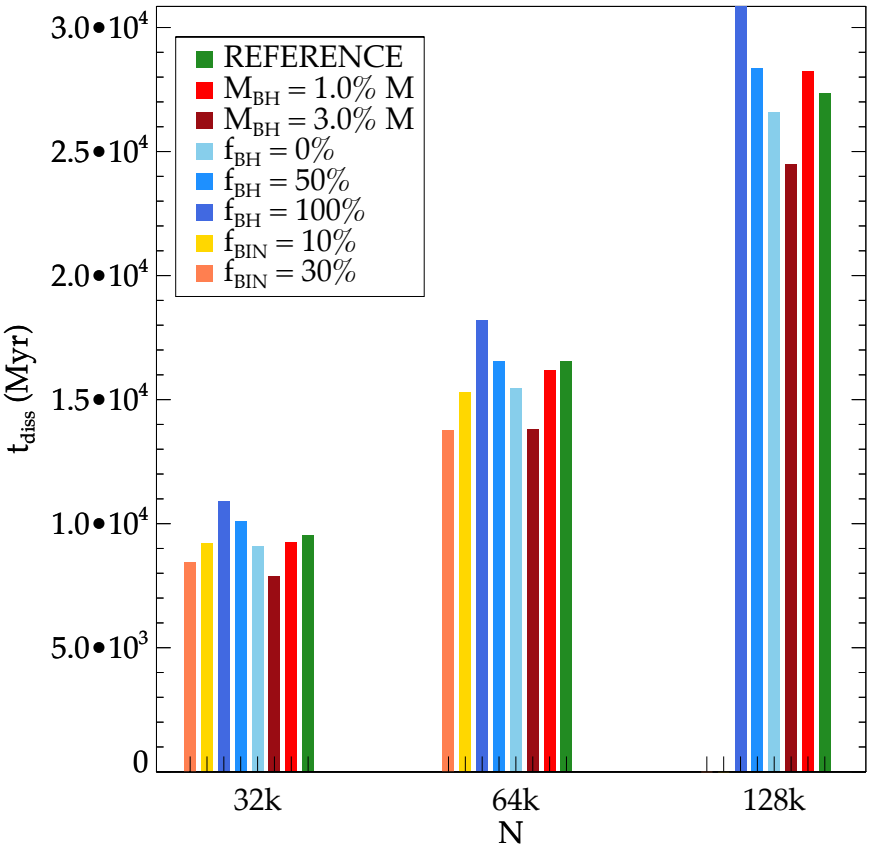

Figure 7.2: Lifetimes of all clusters as a function of their initial particle number.

fact that low-mass stars get ejected more efficiently than high-mass stars. Consequently, the fraction of high-mass stars to low-mass stars increases constantly. The steep rise at the beginning is due to initially rapid stellar evolution and the consequent formation of stellar remnants. The evolution of the stellar-mass black hole numbers in the clusters in Figure 7.1.f shows a roughly exponential behavior. For a model with 128k stars, the number of black holes already drops to half of the initial value within 1 Gyr. After 5 Gyr all black holes have been ejected from the cluster. To lead the eye, we apply rough logarithmic fits to the evolution of black-hole numbers (dashed lines). This is in good agreement with previous results (e.g. Sigurdsson & Hernquist 1993; Kulkarni et al. 1993; Miller & Hamilton 2002b; O'Leary et al. 2006) which show that stellar mass black holes eject themselves from the cluster core by building a dynamically decoupled sub core through mass segregation (Spitzer 1969). A comparison of Panel c) with Panel f) indicates that the core collapse in all models occurs after the cluster has lost its stellar-mass black holes.

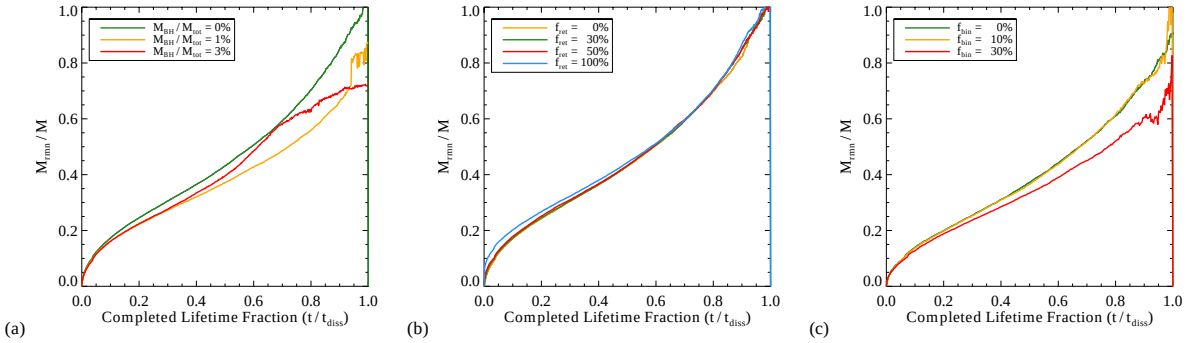

Figure 7.3: Remnant mass fractions as a function of completed lifetime fraction for simulations with different a) IMBH masses, b) black-hole retention fractions and c) primordial binary fractions. All models contain 128k particles, except for the binary-fraction models which are limited to 64k stars.

7.2.3 Model Families

We run models with different IMBH masses, black-hole retention fractions and binary fractions which we categorize in three different families. In order to use realistic values for the IMBH masses we consider several scaling relations such as the $M_\bullet - M_{\rm bulge}$ relation (Magorrian et al. 1998; Häring & Rix 2004) and the $M_\bullet - \sigma$ relation (Ferrarese & Merritt 2000; Gebhardt et al. 2000a; Gültekin et al. 2009). When extrapolating these empirical correlations, they predict IMBH masses of $M_\bullet \sim 0.001 - 0.03\ M_{\rm tot}$ in GCs (Goswami et al. 2012). This corresponds to black-hole masses $M_\bullet \sim 10^2 - 5 \times 10^3\ M_\odot$ in an average GC with a mass of $M_{\rm tot} = 1.5 \times 10^5\ M_\odot$. These masses were found by Portegies Zwart et al. (2004) who used *N*-body simulations to model the runaway merging of massive stars in the dense star cluster MGG-11. Their values, however, should be treated as upper limits, since stellar mass loss of the 'runaway' star was not included. Taking into account these predictions, we use two different black-hole masses: 1% and 3% of the total cluster mass. For models with black-hole masses $< 1\%$ the actual black-hole mass is $< 800\ M_\odot$ even in simulations of N = 128k stars and the central black hole has a high chance of getting ejected by encounters with massive stars.

The retention fraction gives the fraction of stellar remnants that stay in the cluster after their formation. It is assumed that very compact objects such as black holes and neutron stars suffer a kick velocity during their formation which is often higher than the escape velocity of the cluster (Lyne & Lorimer 1994). Theoretical estimates for the retention fraction of neutron stars range from 5 % to 20 % (Drukier 1996). For black holes, however, the range of possible values is not well-constrained since the physics of the formation of black holes is still not fully understood. For this reason, we assume a constant retention fraction of 10 % for neutron stars and vary the retention fractions of the black holes from 0 % (no black hole remains in the cluster) to 100 % (all black holes that are formed remain in the cluster). For white dwarfs we always assume a retention fraction of 100% since they

do not suffer any kick velocities (Davis et al. 2008).

Binaries are important for the dynamical evolution of GCs and need to be considered in our models. In order to test how primordial binaries affect the models, we introduce a third family in which we vary the fraction of binaries in the initial conditions of the model from 10 % to 30 %. This covers the current typical binary fraction in GCs, which is about 10 % (e.g. Rubenstein & Bailyn 1997; Davis et al. 2008; Dalessandro et al. 2011). Since the calculation of the individual time steps of the binary systems is very time-consuming we are limited to a maximum particle number of 64k for the models with primordial binary fractions.

7.3 Observables

The main goal of this study is to find observables in GCs which give information about the presence of a possible intermediate-mass black hole at their centers. In this Section we study the effects of IMBHs on their environment in order to pin down important tracers for central black holes in GCs. We especially concentrate on mimicking observations, i.e., measuring cluster properties in the same way as observers would do in order to compare our results with observational studies.

7.3.1 Life Times

The lifetime, or dissolution time $t_{\rm diss}$ gives information about the dynamical evolution of the model as a function of its internal properties. In this work, we define the dissolution time as the time when the cluster has lost 95% of its initial mass.

In Figure 7.2 we compare the lifetimes of our model families with the reference models (green bars). As expected, there is a clear trend with particle number and slight differences (of the order of $\sim 10-20\%$) between models with different initial conditions. The higher the mass of the central IMBH, the shorter is the lifetime of the cluster. The opposite trend is observed for models with different black-hole retention fractions. The model with the longest lifetime is the model with a black-hole retention fraction of 100 %. However, it is remarkable that the difference in lifetimes is only of the order of 20% and therefore does not show a strong dependence on whether the cluster hosts an IMBH, a large number of stellar-mass black holes or primordial binaries.

The primordial binary fraction affects the lifetime of the cluster model slightly. Encounters with binaries can result in flybys, exchanges, ionizations, and sometimes mergers (see Chapter 4). Some of these encounters result in high-velocity stars which exceed the escape velocity of the cluster. This can lead to a higher ejection rate than in clusters without tight binaries.

We compare our results to the lifetimes of Baumgardt & Makino (2003) who studied *N*-body

simulations of GCs in tidal fields with different galactocentric distances and eccentricities. With a neutron star retention fraction of 100% and no stellar-mass black holes, their initial conditions slightly differ from ours. However, since their stellar masses are cut off at 15 $M_{\odot}$, the effective retention fraction of neutron stars is lower and the models from their family II are comparable to our $f_{\rm ret} = 0\%$ models (see Table 7.1). Except for the 32k model, the lifetimes of the models in this study are $\sim 10\%$ longer than the ones of Baumgardt & Makino (2003). These discrepancies are most likely caused by the under-filling initial conditions of our simulations in contrast to the tidally filling clusters of Baumgardt & Makino (2003).

7.3.2 Remnant fractions

Another quantity that we consider is the fraction of the cluster mass that is constituted by stellar remnants. As remnants we count all stars within one tidal radius that are classified as either a white dwarf, neutron star or black hole. The results are displayed in Figure 7.3 where we compare the remnant fractions for models with different black-hole masses, retention fractions, and primordial binary fractions as a function of the completed lifetime fraction (i.e. t/t_{diss}). The remnant fractions increase monotonically. This occurs because of the increasing number of remnants due to stellar evolution and also to the fact that low-mass stars get ejected first. For all models, this increase continues until the end of the cluster's lifetime. For models with non-zero IMBH masses and primordial binary fractions, however, the remnant fraction shows a slower increase compared to the reference model. For models with a high fraction of stellar-mass black holes, the remnant fraction does not exhibit a strong variation. An explanation for the lower remnant fraction in models with IMBHs and primordial binaries could be that the lower degree of mass segregation caused by the IMBH distributes massive stars and remnants further outside in the cluster where they can be easier ejected. For binaries, the effect might be caused by the higher survival chance of low-mass stars in binaries. Due to their higher total mass, they remain in the cluster longer compared to single low-mass stars and the remnant fraction increases more slowly.

In summary, remnants are ejected more efficiently in a cluster with a central massive black hole, while no notable effect is found for clusters with different black-hole retention fractions. This is in contrast with the result found by Kruijssen (2009), who used semi-analytic models in order to study the evolution of the stellar mass function in star clusters. There it was proposed that the remnant fraction can also decrease towards the end of a cluster's lifetime if a large fraction of stellar-mass black holes is retained.

7.3.3 Mass function slope

The slope of the mass function is a measure for the evolutionary state (or dynamical age) of a GC since it gives information about how many stars and which kind of stars were

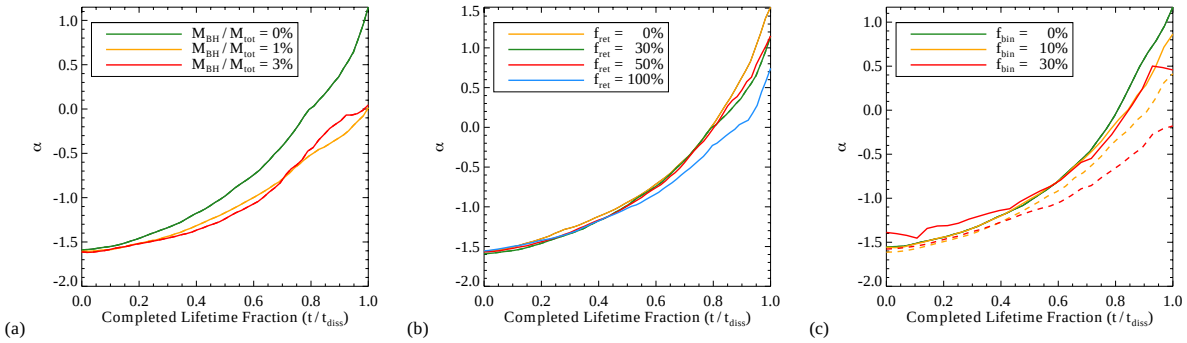

Figure 7.4: Mass-function slopes (for $0.3\,M_\odot < m < 0.8\,M_\odot$) as a function of the completed lifetime fraction for simulations with different a) IMBH masses, b) black-hole retention fractions and c) primordial binary fractions. All models contain 128k particles, except for the binary-fraction models which are limited to 64k stars. The dashed lines indicate the true mass function slope, while the solid lines indicate the mass function slopes as measured by an observer, i.e., counting binaries as single stars.

ejected. We use the method described in Section 7.2.2 to derive the mass function slopes in the mass range of $0.3\,M_\odot < m < 0.8\,M_\odot$ for our models. We stress that our goal is to compare the derived properties of the simulations with observations. For binaries, we therefore take the total luminosity of the system and transfer this into a mass using the existing $M(L)$ relation of single stars in the cluster. In this way we make sure that the binaries contribute to the mass function as they would in observations where the binary components can not be separated. In Figure 7.4 we plot the slope of the mass function as a function of the completed lifetime fraction (solid lines). For comparison we over plot the 'true' evolution of α (dashed lines) as it would be measured if all binary stars can be resolved. As expected, low-mass stars gain high velocities due to two-body relaxation and escape the cluster. Therefore, the slope of the mass function at the low-mass end changes from negative to positive and increases monotonically. This behavior is observed for all our simulations. However, the details of the change in the slope differ from model to model.

As shown in panel a) of Figure 7.4, the IMBH mass has a significant influence on the mass function slope. This most probably arises from the fact that a central black hole ejects high-mass stars more efficiently than the non-IMBH model, as already demonstrated in the previous section. In panel b) of Figure 7.4 the evolution of α seems to be very similar irrespective of how many stellar-mass black holes are retained by the cluster. Only for a retention fraction of 100% a slight difference in α becomes noticeable.

Also binaries cause a slower rise of the mass function slope and therefore a lower depletion in low-mass stars. As shown in panel c) of Figure 7.4, the simulation that starts with a primordial binary fraction of 30% ends up with the lowest *true* value of α of all simulations (dashed lines). As described in the previous section this can be explained by the lower ejection rate of low-mass stars that reside in binaries. However, this is only measurable

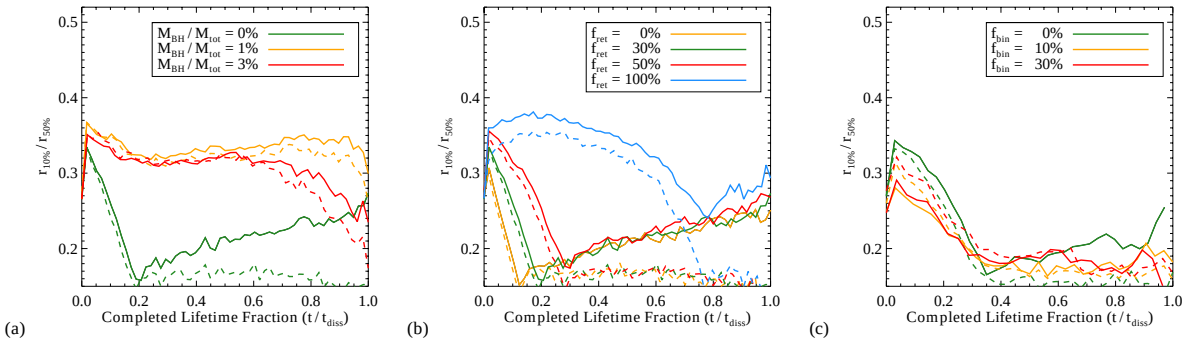

Figure 7.5: Characteristic radii ratios ($r_{10\%}/r_{50\%}$, i.e., deprojected radii containing 10% and 50% of the stars) as a function of completed lifetime fraction for simulations with different a) IMBH masses, b) black-hole retention fractions and c) primordial binary fractions. All models contain 128k particles, except for the binary-fraction models which are limited to 64k stars. The dashed lines indicate the $r_{L,10\%}/r_{L,50\%}$ (deprojected radii containing 10% and 50% of the mass) evolution when taking the Lagrangian radii.

when resolving all the binaries. A large fraction of binaries can bias the observed value of the mass function slope to higher values (solid lines). The differences increase with cluster lifetime and range from $\Delta\alpha = 0.05 - 0.5$ and $\Delta\alpha = 0.2 - 0.7$ for the 10% and the 30% binary fraction model, respectively.

7.3.4 Structural properties

The final quantities of interest are the cluster's structural properties, such as the characteristic radii containing 10% and 50% of its stars. Again, we aim to compare these quantities with observations and therefore derive the values in the same way as we do for the observed clusters. In order to obtain these observables in a non-parametric and consistent way, we apply several steps: First, we derive a projected surface brightness profile for stars brighter than $M_v = 8.5$ mag in 15 logarithmic bins from $r_{min} = 1''$ (by placing all our clusters at a distance of 10 kpc this corresponds to ~ 0.05 pc) out to the tidal radius of the cluster. In each bin the stellar number density is computed for three orthogonal projected directions. For the final density we take the average of the three projected directions and use the scatter as the error. With this method we derive a projected density profile similar to that observed for a real cluster. As a next step we deproject the stellar density profile of each cluster using the projected profiles and a multi-Gaussian expansion method (Emsellem et al. 1994) in order to be comparable to observations. This parametrization has the advantage that a smooth deprojected profile can be easily obtained since the deprojection of any Gaussian results again in a Gaussian. By integrating the deprojected profiles, we obtain radii which include different percentages of the total number of stars such as $r_{50\%}$ and $r_{10\%}$.

In Figure 7.5 we show the evolution of the ratio $r_{10\%}/r_{50\%}$ with time. One prominent feature

of this plot is the strong dip in the ratio at about $t/t_{\rm diss} = 0.2$ ($\sim$ 5 Gyr) which indicates core collapse. The plots demonstrate that for the standard model with a conservative black-hole retention fraction of 30 % and no primordial binaries or IMBH, core collapse is a very prominent feature in the evolution of the structural parameters (see Figure 7.5.a, green line). The presence of an intermediate-mass black hole at the center of the cluster entirely prevents core collapse and $r_{10\%}/r_{50\%}$ is nearly constant over the cluster's lifetime (Figure 7.5.a). A similar effect arises if a large number of stellar-mass black holes is present. As shown in Figure 7.5.b, the model with a retention fraction of 100 % undergoes core expansion rather than core collapse which is delayed until the final stages of its evolution. This underlines the dependence on the time of core collapse on the black-hole retention fraction. Surprisingly, the binary fraction does not seem to have a strong effect on the concentration of the cluster. Core collapse occurs at the same time as for the model without any primordial binaries and the overall evolution of $r_{10\%}/r_{50\%}$ is very similar. However, this result should be treated with care because of the the low-number statistics of the 64k models.

In order to estimate the degree of mass segregation in our models, we further consider the evolution of the Lagrangian radii $r_{L,10\%}$ and $r_{L,50\%}$. These quantities indicate the radii that contain 10% and 50% of the total cluster mass (i.e., also including remnants), respectively. Due to two-body relaxation and mass segregation, remnants sink to the center of the cluster causing a higher concentration of mass. This causes the ratio of $r_{L,10\%}$ and $r_{L,50\%}$ to be lower than $r_{10\%}$ and $r_{50\%}$ that were derived from the stellar distribution only. Therefore, studying the difference between the two ratios gives an estimation of the degree of mass segregation. In Figure 7.5 the evolution of $r_{L,10\%}/r_{L,50\%}$ is indicated by the dashed lines. It is notable that the ratios of the characteristic radii differ for all our models after some time of cluster evolution. This indicates that mass segregation is present in all the clusters but its degree differs from model to model. Especially after core collapse the segregation of remnants is much higher than observed in the visible stars for clusters without IMBHs or low stellar-mass black hole retention fractions. The lowest mass segregation is observed for models with non-zero IMBH masses. This result is of great interest for understanding the connection between observed quantities and actual dynamical stage of the globular cluster.

7.4 Comparison to observed GCs

This section describes the comparison of globular cluster N-body simulations with observed properties. This may help to explain empirical correlations and identify new cluster candidates for hosting IMBHs.

7.4.1 $\alpha - c$ plane

De Marchi et al. (2007) and Paust et al. (2010) studied the mass function slopes α as a function of the concentration parameter c for a total sample of 36 Galactic GCs. As mentioned in the previous section, the slope of the mass function is a measure for the dynamical age of the cluster. The higher the slope (i.e. larger value of α), the more low-mass stars where already lost due to two-body relaxation in the external tidal field. Therefore, one would expect a direct correlation between this slope and other quantities that are correlated with the dynamical time scale of the cluster (see Figure 7.4). One of these quantities is the concentration c that is a measure for the central density of the cluster. The more advanced cluster evolution is, the closer it gets to core-collapse, thus, the higher is its central concentration. The observations, however, contradict this picture by showing the opposite relation between mass-function slope and concentration [1].

To measure the concentration parameter c that we can compare to the observations, we compute a projected density profile (as described in Section 7.3.4) and fit an isotropic King (1966) model to the simulation data. This allows us to derive the structural parameters (e.g. c, r_c and r_h) from the best fit.

To compare with the work of De Marchi et al. (2007) and Paust et al. (2010), we derive α (for $0.3\,M_\odot < m < 0.8\,M_\odot$) and c at points in time spaced by 500 Myr from the cluster models. Figure 7.6 (left panels) displays the tracks on top of the observed data of De Marchi et al. (2007, filled circles) and Paust et al. (2010, open circles). As before, we compare models with different IMBH masses, black-hole retention fractions and primordial binary fractions. The figure shows that our standard model (without an intermediate-mass black hole and retention fraction of 30 %) undergoes core collapse after several Gyr and moves back to lower concentrations during its evolution (green line). Furthermore, the figure shows that the cluster without a black hole behaves in the expected way and c increases with α before it undergoes core collapse. After core collapse, however, the dependence of these two values is reversed as the cluster core slowly expands again due to binary heating. Comparing the green line with the data, it seems plausible that clusters with medium-to-high concentrations and relatively unevolved mass functions can be represented by a no-IMBH model with a medium retention fraction. Clusters with central massive black holes are presented by the yellow and the red lines. These models do not undergo core collapse and represent the data points with low concentrations very well. A similar agreement was found by Trenti et al. (2010) for a single IMBH run.

The suppression of core collapse can also be produced by many stellar-mass black holes as demonstrated by the model with the 100 % black-hole retention fraction (Figure 7.6.c, blue line). The large concentration of black holes in the center also enlarges the core of the visible stars and prevents core collapse as it functions as an extra heating source. As

[1] Note that the authors measured the mass function slope for the mass range $0.3\,M_\odot < m < 0.8\,M_\odot$. This includes the *break* of the mass function that is usually located at $0.5\,M_\odot$. For this reason, the measurements are very sensitive to uncertainties in total magnitudes and distances and should therefore be treated with care.

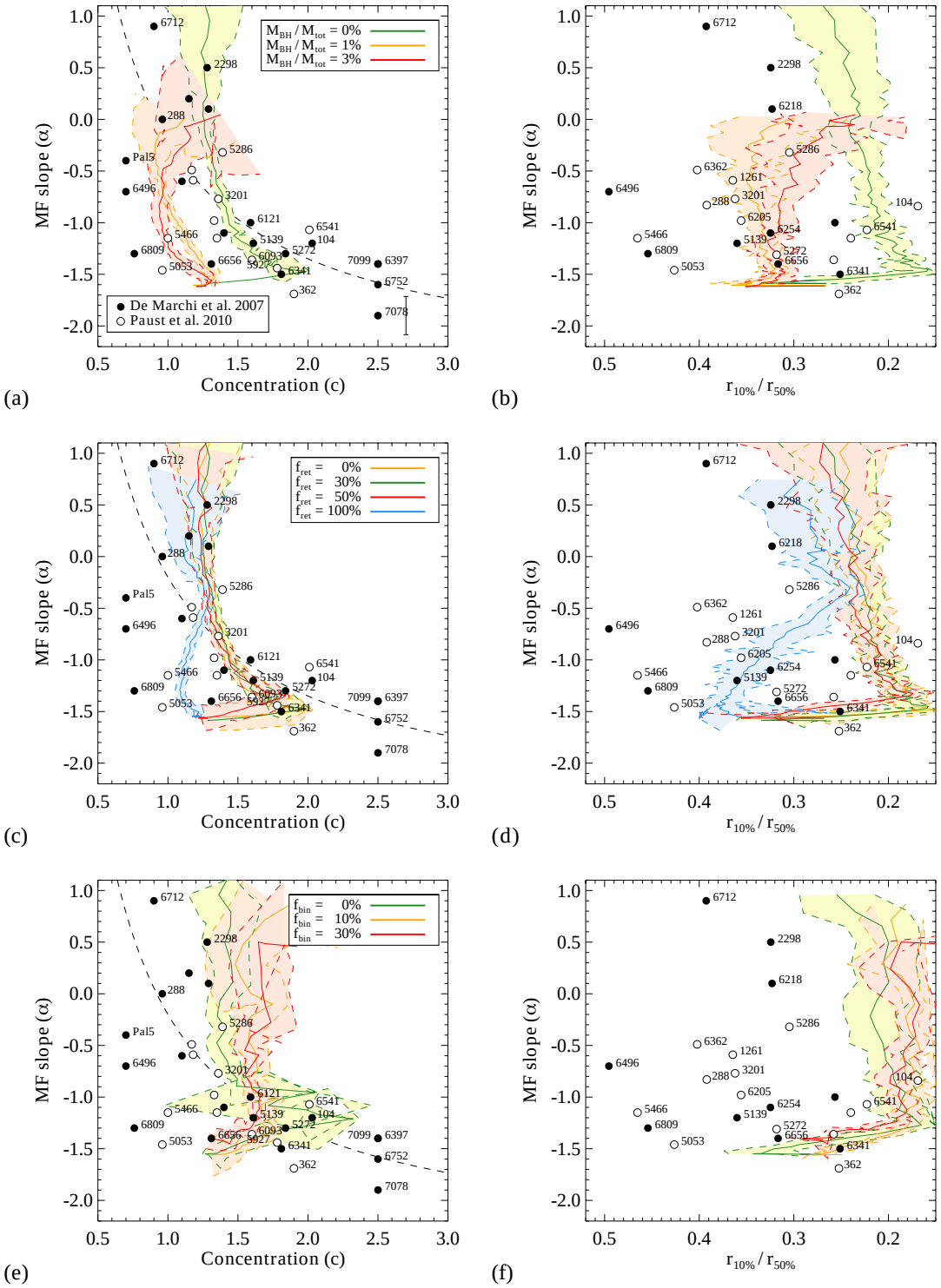

Figure 7.6: α - c plane (left panels) and $\alpha - r_{10\%}/r_{50\%}$ plane (right panels) of observed GCs in comparison with *N*-body simulations. Shaded areas mark the 3σ limit of the simulations. Clusters falling within these limits and not overlapping with other models are considered to be well-represented by these models. The error bar in panel a) is representative for the uncertainties in α for the observed clusters. The clusters that are labeled are discussed in Section 7.5.

already observed for the structural properties, binaries do not affect the concentration of the cluster and the tracks are similar for binary and non-binary models.

7.4.2 $\alpha - r_c/r_h$ plane

Another and preferable way of comparing these data to the models is by using the derived non-parametric structural parameters $r_{10\%}$ and $r_{50\%}$ instead of the concentration parameter. The ratio of these radii is a more reliable indicator than that provided by the parametric approach, because a King model does not always provide a good fit to the data after core collapse.

In order to extract the characteristic radii from the observational data we take all clusters which are included in the sample of Paust et al. (2010) and De Marchi et al. (2007) and apply the same procedure as for the *N*-body data. We match their clusters with the sample of Trager et al. (1995) and McLaughlin & van der Marel (2005) in order to obtain surface-brightness profiles and masses for as many clusters as possible. The overlap is substantial and we obtain a sample of 22 clusters. For each cluster we then deproject the surface brightness profile using the smoothed profiles from Trager et al. (1995) and the multi-Gaussian expansion method as described in Section 7.3.4. We integrate the deprojected surface-brightness profiles in order to obtain the radii $r_{10\%}$ and $r_{50\%}$ and use the total masses obtained by McLaughlin & van der Marel (2005).

From Figure 7.6 (right panels) we conclude that the ratio of the two characteristic radii is a good replacement for the concentration parameter. The observed data follow a similar distribution as in the $\alpha - c$ plot (i.e., there appears to be a lack of clusters with low $r_{10\%}/r_{50\%}$ value and high α). As already concluded from the $\alpha - c$ analysis, models with large cores and low values for the mass function slope are good candidates to host a central IMBH. However, the degeneracy with the models with a 100 % black-hole retention fraction needs to be treated with caution. The agreement between the observations and the different *N*-body runs can be exploited to identify candidate GCs for hosting an IMBH. This is done in the next section.

7.5 Summary and discussion

We have investigated the effect of intermediate-mass black holes, stellar-mass black hole retention fractions and primordial binary fractions on the properties of GCs evolving in a tidal field. We run *N*-body simulations using the GPU-enabled version of NBODY6 with 32k, 64k, and 128k stars. We study the effect of the different initial conditions on the cluster lifetime, remnant fraction, mass function, and structural parameters. In addition, we compare the results of the simulations with observational data from the literature and find good agreement. Due to the specific shape of the King profile, the concentration

parameter c is not a good representation of the cluster's internal properties. For that reason we also compute the ratio of the radius containing 10% and 50% of the stars in the cluster $r_{10\%}$ and $r_{50\%}$, which is a more accurate quantity than the parametric King fit.

When comparing the different models we find that a cluster with central IMBH has a shorter lifetime than the rest of the models. This is caused by the enhanced ejection of stars due to lower mass segregation. On the other hand, models with high black-hole retention fractions live the longest among all simulations. A possible explanation for the extended lifetimes is that large number of stellar-mass black holes would make the core expand and prevent core-collapse, thereby slowing down dynamical evolution. We stress that the difference in cluster lifetime are of the order of 20% and the effects of IMBHs, stellar-mass black holes and binaries are therefore modest.

Our study also shows that a central IMBH in a GC causes the remnant fraction to increase more slowly compared to a cluster without a central black hole. However, a similar effect is reached with a high (30%) fraction of primordial binaries. Again, the reason of this behavior might be found in the lower degree of mass-segregation that causes high-mass stars and remnants to be distributed in the outskirts of the cluster where they can be easily ejected. For the evolution of the mass function in the simulations, we find that the central IMBH as well as a primordial binary fraction of 30% lead to a delay of the depletion of low-mass stars due to ejections of high-mass stars. Therefore, the mass function slope has a lower value (i.e. less depleted in low-mass stars) at the end of the cluster's lifetime than for models without an IMBH or binaries.

When comparing the models to the observations in the plane of the mass function slope versus the cluster's concentration, we find that the IMBH models well-explain the observed data with low concentrations. By contrast, the models without an IMBH undergo core collapse immediately. Our more extensive parameter survey thus confirms the initial suggestion by Trenti et al. (2010). The analysis also shows that the same effect can be achieved when considering a black-hole retention fraction of 100%. In this case the black holes in the cluster center survive long enough to prevent core collapse over a long timescale. However, it seems very unrealistic to retain all black holes in the cluster after formation. We therefore conclude that GCs which lie in the upper left side of Figure 7.6, i.e. with low concentrations but depleted mass functions, are good candidates for hosting (or having hosted) an IMBH at their center.

In order to find the best candidates for clusters hosting an IMBH we select those which agree within 3σ (derived from the spread in the values of α and c within 500 Myr) with one of the IMBH runs. Figure 7.6 shows the comparison with the models. The color shaded areas mark the 3σ limits of the simulations. Only a few clusters can be identified as clear IMBH or non-IMBH candidates. The majority of the clusters lie in the white areas and are therefore not clearly defined. For the $\alpha - c$ plot, the best IMBH candidates are: NGC 288, NGC 5466, and NGC 6656 since they overlap with the 3σ regions of the IMBH simulations directly. But also NGC 5053, NGC 6809, NGC 6496 and Pal 5, are promising

since their values are closer to the ones predicted from the IMBH models than the non-IMBH models. Furthermore, NGC 6712 could be considered if scaling up the lifetime of the IMBH models to reach higher values for α. NGC 5272, NGC 6341, NGC 5927, NGC 6093, and NGC 3201 agree with the non-IMBH model if considering their values of α and c. Analogous to the IMBH candidates, also the high concentration models to the right of the no-IMBH models, e.g., NGC 6397 or NGC 7078, can be considered as clusters that most likely do not host an IMBH at their center. NGC 5286 agrees with all three models which makes it challenging to compare with previous studies. Feldmeier et al. (2013) found the inner kinematics of NGC 5286 to be consistent with a 15 000$M_{\odot}$ black hole at its center. However, as mentioned earlier, the $\alpha - c$ plane for GCs might not be the best values to compare to our simulations since the King model is not a good representation of an evolved cluster's structural parameters.

When making the same comparison for the non-parametric radii $r_{10\%}$ and $r_{50\%}$ we find NGC 1261 , NGC 3201, NGC 5286, NGC 5272, NGC 6254 and NGC 6656 overlapping with the 3σ regions of the IMBH models. The IMBH candidates NGC 5286 and NGC 5139 (ω Centauri) both are more consistent with models that host an IMBH. Also clusters with high $r_{10\%}/r_{50\%}$ to the left of the IMBH models can be considered as possible candidates. We note that this is almost the entire sample for which surface brightness profiles were available. However, as shown in Panel d), some of the clusters are equally well reproduced by a model that contains a high black-hole retention fraction. This degeneracy may be lifted with more detailed *N*-body simulations for both clusters in order to be able to distinguish between the two possible explanations. As mentioned before, a black-hole retention fraction of 100%, i.e, when none of the formed stellar-mass black hole are ejected, does not agree with our knowledge of the violent process of black hole formation. At least some fraction of the black holes will be ejected due to high kick velocities and the model with the black-hole retention fraction of 100% should therefore be treated as an extreme case.

In order to test the results of this study, more kinematic observations have to be performed for the clusters that are considered IMBH candidates. A new sample of inner kinematics for Galactic GCs is desired and planned for the future. Also, a larger sample of GCs with available mass function slopes and surface brightness profiles would help to further constrain the behavior of GCs in the $\alpha - c$ and $\alpha - r_{10\%}/r_{50\%}$ plane. As we have shown, such observations may provide a powerful diagnostic for identifying GCs that possibly host IMBHs. Furthermore, future *N*-body simulations with an extended parameter space are needed in order to reproduce the observations that were not covered by the simulations presented in this study.

Acknowledgements: *This research was supported by the DFG cluster of excellence Origin and Structure of the Universe (www.universe-cluster.de).*

APPENDIX A

Surface Brightness Profiles

Table A.1: Derived surface brightness profiles of all clusters in the V-band. ΔV_h and ΔV_l are the high and low values of the errors, respectively

Name	r [arcsec]	V [mag/arcsec^2]	ΔV_l [mag/arcsec^2]	ΔV_h [mag/arcsec^2]	Name	r [arcsec]	V [mag/arcsec^2]	ΔV_l [mag/arcsec^2]	ΔV_h [mag/arcsec^2]
NGC 1851	−0.40	13.48	0.52	0.35	NGC 5824	1.06	17.64	0.02	0.02
NGC 1851	−0.12	13.53	0.31	0.24	NGC 5824	1.20	18.29	0.02	0.02
NGC 1851	0.00	13.49	0.31	0.24	NGC 5824	1.31	18.85	0.02	0.02
NGC 1851	0.18	13.68	0.20	0.17	NGC 5824	1.39	19.33	0.02	0.02
NGC 1851	0.30	13.82	0.15	0.13	NGC 5824	1.43	19.54	0.02	0.02
NGC 1851	0.48	14.15	0.09	0.08	NGC 5824	1.47	19.73	0.02	0.02
NGC 1851	0.72	14.53	0.05	0.05	NGC 5824	1.50	19.91	0.02	0.02
NGC 1851	0.88	15.18	0.04	0.03	NGC 5824	1.52	20.01	0.02	0.02
NGC 1851	1.00	15.71	0.03	0.03	NGC 5824	1.57	20.24	0.02	0.02
NGC 1851	1.10	16.19	0.03	0.03	NGC 5824	1.61	20.49	0.02	0.02
NGC 1851	1.18	16.52	0.03	0.03	NGC 5824	1.64	20.67	0.02	0.02
NGC 1851	1.30	17.01	0.02	0.02	NGC 5824	1.66	20.78	0.02	0.02
NGC 1851	1.40	17.69	0.02	0.02	NGC 5824	1.71	21.05	0.02	0.02
NGC 1851	1.48	18.05	0.02	0.01	NGC 5824	1.75	21.28	0.02	0.02
NGC 1851	1.60	18.72	0.01	0.01	NGC 5824	1.77	21.37	0.02	0.02
NGC 1851	1.70	19.32	0.01	0.01	NGC 5824	1.77	21.38	0.02	0.02
NGC 1851	1.78	19.79	0.01	0.01	NGC 5824	1.82	21.67	0.02	0.02
NGC 1851	1.85	20.18	0.01	0.01	NGC 5824	1.86	21.89	0.02	0.02
NGC 1851	1.90	20.39	0.01	0.01	NGC 5824	1.86	21.90	0.02	0.02
NGC 1851	1.95	20.61	0.01	0.01	NGC 5824	1.87	21.94	0.02	0.02
NGC 1851	2.00	20.78	0.01	0.01	NGC 5824	1.91	22.19	0.02	0.02
NGC 1851	2.08	21.61	0.01	0.01	NGC 5824	1.93	22.32	0.02	0.02
NGC 1851	2.12	21.88	0.01	0.01	NGC 5824	1.95	22.41	0.02	0.02
NGC 1851	2.16	22.19	0.01	0.01	NGC 5824	1.95	22.42	0.02	0.02
NGC 1851	2.22	22.62	0.01	0.01	NGC 5824	1.99	22.69	0.02	0.02
NGC 1851	2.23	22.69	0.01	0.01	NGC 5824	2.01	22.82	0.02	0.02
NGC 1851	2.30	23.14	0.01	0.01	NGC 5824	2.02	22.86	0.02	0.02
NGC 1851	2.31	23.24	0.01	0.01	NGC 5824	2.03	22.91	0.02	0.02
NGC 1851	2.38	23.73	0.01	0.01	NGC 5824	2.05	23.03	0.02	0.02
NGC 1851	2.46	24.38	0.01	0.01	NGC 5824	2.08	23.25	0.02	0.02
NGC 1851	2.48	24.52	0.01	0.01	NGC 5824	2.09	23.33	0.02	0.02
NGC 1851	2.48	24.54	0.01	0.01	NGC 5824	2.13	23.59	0.02	0.02
NGC 1851	2.54	24.93	0.01	0.01	NGC 5824	2.16	23.74	0.02	0.02
NGC 1851	2.62	25.64	0.01	0.01	NGC 5824	2.18	23.90	0.02	0.02
NGC 1851	2.78	26.95	0.01	0.01	NGC 5824	2.23	24.18	0.02	0.02
NGC 1904	−0.45	15.83	0.94	0.49	NGC 5824	2.23	24.21	0.02	0.02
NGC 1904	−0.14	15.83	0.41	0.30	NGC 5824	2.23	24.23	0.02	0.02
NGC 1904	0.05	15.89	0.27	0.22	NGC 5824	2.27	24.44	0.02	0.02
NGC 1904	0.18	15.85	0.22	0.18	NGC 5824	2.29	24.62	0.02	0.02
NGC 1904	0.28	15.82	0.16	0.14	NGC 5824	2.32	24.80	0.02	0.02
NGC 1904	0.36	15.99	0.17	0.14	NGC 5824	2.35	24.98	0.02	0.02
NGC 1904	0.66	16.23	0.05	0.05	NGC 5824	2.38	25.18	0.02	0.02
NGC 1904	0.83	16.44	0.04	0.04	NGC 5824	2.38	25.22	0.02	0.02
NGC 1904	0.96	16.69	0.04	0.04	NGC 5824	2.43	25.59	0.02	0.02
NGC 1904	1.06	17.06	0.04	0.03	NGC 5824	2.48	25.93	0.02	0.02
NGC 1904	1.20	17.43	0.03	0.03	NGC 5824	2.57	26.54	0.02	0.02
NGC 1904	1.31	17.92	0.03	0.03	NGC 5824	2.64	27.06	0.02	0.02
NGC 1904	1.40	18.26	0.03	0.03	NGC 5824	2.73	27.74	0.02	0.02
NGC 1904	1.47	18.76	0.04	0.03	**NGC 6093**	−0.22	14.80	0.29	0.23
NGC 1904	1.53	18.97	0.03	0.03	NGC 6093	0.04	14.95	0.20	0.17
NGC 1904	1.56	19.10	0.03	0.03	NGC 6093	0.24	14.78	0.15	0.13

continued.

Name	r [arcsec]	V [mag/arcsec^2]	ΔV_l [mag/arcsec^2]	ΔV_h [mag/arcsec^2]	Name	r [arcsec]	V [mag/arcsec^2]	ΔV_l [mag/arcsec^2]	ΔV_h [mag/arcsec^2]
NGC 1904	1.56	19.11	0.03	0.03	NGC 6093	0.40	14.98	0.10	0.10
NGC 1904	1.59	19.25	0.03	0.03	NGC 6093	0.65	15.36	0.05	0.05
NGC 1904	1.64	19.52	0.03	0.03	NGC 6093	0.88	15.82	0.03	0.03
NGC 1904	1.65	19.55	0.03	0.03	NGC 6093	1.00	16.33	0.03	0.03
NGC 1904	1.69	19.76	0.03	0.03	NGC 6093	1.10	16.55	0.03	0.03
NGC 1904	1.73	19.98	0.03	0.03	NGC 6093	1.18	16.77	0.02	0.02
NGC 1904	1.74	20.02	0.03	0.03	NGC 6093	1.30	17.37	0.02	0.01
NGC 1904	1.77	20.19	0.03	0.03	NGC 6093	1.40	17.75	0.01	0.01
NGC 1904	1.80	20.40	0.03	0.03	NGC 6093	1.48	18.15	0.01	0.01
NGC 1904	1.82	20.52	0.03	0.03	NGC 6093	1.60	18.69	0.01	0.01
NGC 1904	1.87	20.76	0.03	0.03	NGC 6093	1.70	19.34	0.01	0.01
NGC 1904	1.91	21.04	0.03	0.03	NGC 6093	1.78	19.59	0.01	0.01
NGC 1904	1.95	21.26	0.03	0.03	NGC 6093	1.85	20.23	0.01	0.01
NGC 1904	2.00	21.59	0.03	0.03	NGC 6093	1.90	20.20	0.01	0.01
NGC 1904	2.00	21.60	0.03	0.03	NGC 6093	1.95	20.76	0.01	0.01
NGC 1904	2.01	21.69	0.03	0.03	NGC 6093	2.00	20.99	0.01	0.01
NGC 1904	2.03	21.78	0.03	0.03	NGC 6093	2.05	21.47	0.01	0.01
NGC 1904	2.07	22.08	0.03	0.03	NGC 6093	2.07	21.59	0.01	0.01
NGC 1904	2.09	22.18	0.03	0.03	NGC 6093	2.09	21.76	0.01	0.01
NGC 1904	2.09	22.18	0.03	0.03	NGC 6093	2.12	21.96	0.01	0.01
NGC 1904	2.12	22.43	0.03	0.03	NGC 6093	2.13	22.04	0.01	0.01
NGC 1904	2.17	22.76	0.03	0.03	NGC 6093	2.16	22.24	0.01	0.01
NGC 1904	2.21	23.06	0.03	0.03	NGC 6093	2.16	22.27	0.01	0.01
NGC 1904	2.23	23.24	0.03	0.03	NGC 6093	2.17	22.31	0.01	0.01
NGC 1904	2.25	23.34	0.03	0.03	NGC 6093	2.21	22.63	0.01	0.01
NGC 1904	2.31	23.84	0.03	0.03	NGC 6093	2.22	22.71	0.01	0.01
NGC 1904	2.38	24.33	0.03	0.03	NGC 6093	2.23	22.80	0.01	0.01
NGC 1904	2.40	24.51	0.03	0.03	NGC 6093	2.23	22.83	0.01	0.01
NGC 1904	2.48	25.21	0.03	0.03	NGC 6093	2.25	22.93	0.01	0.01
NGC 1904	2.57	25.94	0.03	0.03	NGC 6093	2.25	22.94	0.01	0.01
NGC 5694	−0.20	15.73	0.29	0.23	NGC 6093	2.29	23.30	0.01	0.01
NGC 5694	0.06	15.83	0.19	0.16	NGC 6093	2.31	23.47	0.01	0.01
NGC 5694	0.26	16.16	0.13	0.12	NGC 6093	2.32	23.53	0.01	0.01
NGC 5694	0.44	16.55	0.09	0.08	NGC 6093	2.35	23.75	0.01	0.01
NGC 5694	0.66	17.22	0.05	0.05	NGC 6093	2.38	24.00	0.01	0.01
NGC 5694	0.83	17.75	0.03	0.03	NGC 6093	2.38	24.05	0.01	0.01
NGC 5694	0.96	18.30	0.03	0.03	NGC 6093	2.40	24.19	0.01	0.01
NGC 5694	1.03	18.73	0.03	0.03	NGC 6093	2.43	24.51	0.01	0.01
NGC 5694	1.04	18.78	0.03	0.03	NGC 6093	2.47	24.81	0.01	0.01
NGC 5694	1.06	18.86	0.03	0.03	NGC 6093	2.48	24.94	0.01	0.01
NGC 5694	1.09	18.98	0.03	0.03	NGC 6093	2.53	25.37	0.01	0.01
NGC 5694	1.12	19.10	0.03	0.03	NGC 6093	2.55	25.53	0.01	0.01
NGC 5694	1.13	19.16	0.03	0.03	NGC 6093	2.57	25.73	0.01	0.01
NGC 5694	1.17	19.34	0.03	0.03	NGC 6093	2.59	25.88	0.01	0.01
NGC 5694	1.21	19.55	0.03	0.03	NGC 6093	2.64	26.41	0.01	0.01
NGC 5694	1.23	19.65	0.03	0.03	NGC 6093	2.68	26.75	0.01	0.01
NGC 5694	1.29	19.93	0.03	0.03	NGC 6093	2.73	27.31	0.01	0.01
NGC 5694	1.30	19.98	0.03	0.03	**NGC 6266**	−0.17	14.79	0.37	0.28
NGC 5694	1.34	20.18	0.03	0.03	NGC 6266	0.14	14.85	0.16	0.14
NGC 5694	1.39	20.42	0.03	0.03	NGC 6266	0.44	15.04	0.08	0.07
NGC 5694	1.39	20.42	0.03	0.03	NGC 6266	0.68	15.42	0.05	0.05
NGC 5694	1.43	20.64	0.03	0.03	NGC 6266	0.83	15.66	0.04	0.04
NGC 5694	1.47	20.85	0.03	0.03	NGC 6266	0.96	15.78	0.03	0.03
NGC 5694	1.48	20.89	0.03	0.03	NGC 6266	1.06	15.95	0.03	0.03
NGC 5694	1.50	21.04	0.03	0.03	NGC 6266	1.14	16.26	0.03	0.03
NGC 5694	1.55	21.31	0.03	0.03	NGC 6266	1.26	16.61	0.02	0.02
NGC 5694	1.56	21.38	0.03	0.03	NGC 6266	1.36	16.89	0.03	0.03
NGC 5694	1.57	21.39	0.03	0.03	NGC 6266	1.44	17.27	0.05	0.05
NGC 5694	1.64	21.86	0.03	0.03	NGC 6266	1.52	17.46	0.02	0.02
NGC 5694	1.65	21.89	0.03	0.03	NGC 6266	1.53	17.51	0.02	0.02
NGC 5694	1.71	22.27	0.03	0.03	NGC 6266	1.56	17.62	0.02	0.02
NGC 5694	1.74	22.43	0.03	0.03	NGC 6266	1.59	17.70	0.02	0.02
NGC 5694	1.77	22.63	0.03	0.03	NGC 6266	1.59	17.74	0.02	0.02
NGC 5694	1.82	22.96	0.03	0.03	NGC 6266	1.60	17.74	0.02	0.02
NGC 5694	1.82	22.99	0.03	0.03	NGC 6266	1.61	17.78	0.02	0.02
NGC 5694	1.85	23.17	0.03	0.03	NGC 6266	1.63	17.89	0.02	0.02
NGC 5694	1.87	23.27	0.03	0.03	NGC 6266	1.64	17.94	0.02	0.02
NGC 5694	1.91	23.54	0.03	0.03	NGC 6266	1.65	17.97	0.02	0.02
NGC 5694	1.91	23.57	0.03	0.03	NGC 6266	1.69	18.14	0.02	0.02
NGC 5694	1.95	23.80	0.03	0.03	NGC 6266	1.71	18.24	0.02	0.02
NGC 5694	2.00	24.17	0.03	0.03	NGC 6266	1.73	18.32	0.02	0.02
NGC 5694	2.00	24.20	0.03	0.03	NGC 6266	1.74	18.34	0.02	0.02
NGC 5694	2.01	24.27	0.03	0.03	NGC 6266	1.77	18.48	0.02	0.02
NGC 5694	2.06	24.61	0.03	0.03	NGC 6266	1.77	18.49	0.02	0.02
NGC 5694	2.09	24.79	0.03	0.03	NGC 6266	1.77	18.51	0.02	0.02
NGC 5694	2.17	25.44	0.03	0.03	NGC 6266	1.80	18.65	0.02	0.02
NGC 5694	2.27	26.18	0.03	0.03	NGC 6266	1.82	18.75	0.02	0.02
NGC 5824	−0.23	14.45	0.37	0.28	NGC 6266	1.86	18.91	0.02	0.02
NGC 5824	0.00	14.85	0.22	0.18	NGC 6266	1.87	18.96	0.02	0.02
NGC 5824	0.30	15.30	0.11	0.10	NGC 6266	1.88	19.04	0.02	0.02
NGC 5824	0.44	15.72	0.09	0.09	NGC 6266	1.91	19.19	0.02	0.02
NGC 5824	0.66	16.01	0.05	0.05	NGC 6266	1.91	19.19	0.02	0.02

continued.

Name	r [arcsec]	V [mag/arcsec^2]	ΔV_l [mag/arcsec^2]	ΔV_h [mag/arcsec^2]	Name	r [arcsec]	V [mag/arcsec^2]	ΔV_l [mag/arcsec^2]	ΔV_h [mag/arcsec^2]
NGC 5824	0.83	16.67	0.03	0.03	NGC 6266	1.95	19.38	0.02	0.02
NGC 5824	1.06	17.64	0.02	0.02	NGC 6266	1.95	19.41	0.02	0.02
NGC 5824	1.20	18.29	0.02	0.02	NGC 6266	1.97	19.50	0.02	0.02
NGC 5824	1.31	18.85	0.02	0.02	NGC 6266	2.00	19.67	0.02	0.02
NGC 5824	1.39	19.33	0.02	0.02	NGC 6266	2.01	19.76	0.02	0.02
NGC 5824	1.43	19.54	0.02	0.02	NGC 6266	2.04	19.92	0.02	0.02
NGC 5824	1.47	19.73	0.02	0.02	NGC 6266	2.06	20.03	0.02	0.02
NGC 5824	1.50	19.91	0.02	0.02	NGC 6266	2.07	20.08	0.02	0.02
NGC 5824	1.52	20.01	0.02	0.02	NGC 6266	2.07	20.11	0.02	0.02
NGC 5824	1.57	20.24	0.02	0.02	NGC 6266	2.09	20.20	0.02	0.02
NGC 5824	1.61	20.49	0.02	0.02	NGC 6266	2.10	20.30	0.02	0.02
NGC 5824	1.64	20.67	0.02	0.02	NGC 6266	2.12	20.43	0.02	0.02
NGC 5824	1.66	20.78	0.02	0.02	NGC 6266	2.14	20.58	0.02	0.02
NGC 5824	1.71	21.05	0.02	0.02	NGC 6266	2.15	20.66	0.02	0.02
NGC 5824	1.75	21.28	0.02	0.02	NGC 6266	2.17	20.74	0.02	0.02
NGC 5824	1.77	21.37	0.02	0.02	NGC 6266	2.17	20.78	0.02	0.02
NGC 5824	1.77	21.38	0.02	0.02	NGC 6266	2.20	20.99	0.02	0.02
NGC 5824	1.82	21.67	0.02	0.02	NGC 6266	2.21	21.02	0.02	0.02
NGC 5824	1.86	21.89	0.02	0.02	NGC 6266	2.21	21.03	0.02	0.02
NGC 5824	1.86	21.90	0.02	0.02	NGC 6266	2.22	21.09	0.02	0.02
NGC 5824	1.87	21.94	0.02	0.02	NGC 6266	2.25	21.31	0.02	0.02
NGC 5824	1.91	22.19	0.02	0.02	NGC 6266	2.28	21.55	0.02	0.02
NGC 5824	1.93	22.32	0.02	0.02	NGC 6266	2.29	21.61	0.02	0.02
NGC 5824	1.95	22.41	0.02	0.02	NGC 6266	2.31	21.82	0.02	0.02
NGC 5824	1.95	22.42	0.02	0.02	NGC 6266	2.31	21.83	0.02	0.02
NGC 5824	1.99	22.69	0.02	0.02	NGC 6266	2.32	21.90	0.02	0.02
NGC 5824	2.01	22.82	0.02	0.02	NGC 6266	2.33	21.97	0.02	0.02
NGC 5824	2.02	22.86	0.02	0.02	NGC 6266	2.36	22.18	0.02	0.02
NGC 5824	2.03	22.91	0.02	0.02	NGC 6266	2.38	22.37	0.02	0.02
NGC 5824	2.05	23.03	0.02	0.02	NGC 6266	2.39	22.44	0.02	0.02
NGC 5824	2.08	23.25	0.02	0.02	NGC 6266	2.40	22.53	0.02	0.02
NGC 5824	2.09	23.33	0.02	0.02	NGC 6266	2.40	22.55	0.02	0.02
NGC 5824	2.13	23.59	0.02	0.02	NGC 6266	2.42	22.74	0.02	0.02
NGC 5824	2.16	23.74	0.02	0.02	NGC 6266	2.46	23.11	0.02	0.02
NGC 5824	2.18	23.90	0.02	0.02	NGC 6266	2.47	23.17	0.02	0.02
NGC 5824	2.23	24.18	0.02	0.02	NGC 6266	2.47	23.20	0.02	0.02
NGC 5824	2.23	24.21	0.02	0.02	NGC 6266	2.50	23.45	0.02	0.02
NGC 5824	2.23	24.23	0.02	0.02	NGC 6266	2.53	23.80	0.02	0.02
NGC 5824	2.27	24.44	0.02	0.02	NGC 6266	2.62	24.63	0.02	0.02
NGC 5824	2.29	24.62	0.02	0.02	NGC 6266	2.70	25.59	0.02	0.02

Bibliography

Aarseth, S. J. 1999, PASP, 111, 1333

Ambartsumian, V. A. 1938, in translated form, 1985, IAU Symposium, Vol. 113, Dynamics of Star Clusters, ed. J. Goodman & P. Hut, 521

Anderson, J., Sarajedini, A., Bedin, L. R., et al. 2008, AJ, 135, 2055

Anderson, J. & van der Marel, R. P. 2010, ApJ, 710, 1032

Bahcall, J. N. & Wolf, R. A. 1976, ApJ, 209, 214

Barth, A. J., Ho, L. C., Rutledge, R. E., & Sargent, W. L. W. 2004, ApJ, 607, 90

Bash, F. N., Gebhardt, K., Goss, W. M., & Vanden Bout, P. A. 2008, AJ, 135, 182

Battaglia, G., Irwin, M., Tolstoy, E., et al. 2008, MNRAS, 383, 183

Baumgardt, H. 2001, Astronomical and Astrophysical Transactions, 20, 43

Baumgardt, H., Gualandris, A., & Portegies Zwart, S. 2006, MNRAS, 372, 174

Baumgardt, H., Hut, P., Makino, J., McMillan, S., & Portegies Zwart, S. 2003, ApJ, 582, L21

Baumgardt, H. & Makino, J. 2003, MNRAS, 340, 227

Baumgardt, H., Makino, J., & Ebisuzaki, T. 2004, ApJ, 613, 1143

Baumgardt, H., Makino, J., & Hut, P. 2005, ApJ, 620, 238

Beccari, G., Ferraro, F. R., Possenti, A., et al. 2006, AJ, 131, 2551

Bedin, L. R., Piotto, G., Anderson, J., et al. 2004, ApJ, 605, L125

Beers, T. C., Flynn, K., & Gebhardt, K. 1990, AJ, 100, 32

Bowyer, S., Byram, E. T., Chubb, T. A., & Friedman, H. 1965, Sience, 147, 394

Bruntt, H., Grundahl, F., Tingley, B., et al. 2003, A&A, 410, 323

Cappellari, M. 2002, MNRAS, 333, 400

Cappellari, M. 2008, MNRAS, 390, 71

Cappellari, M. & Emsellem, E. 2004, PASP, 116, 138

Carretta, E., Gratton, R. G., Lucatello, S., et al. 2010, ApJ, 722, L1

Colbert, E. J. M. & Mushotzky, R. F. 1999, ApJ, 519, 89

Colpi, M., Mapelli, M., & Possenti, A. 2003, ApJ, 599, 1260

Colpi, M., Possenti, A., & Gualandris, A. 2002, ApJ, 570, L85

Contreras, R., Catelan, M., Smith, H. A., et al. 2010, AJ, 140, 1766

Cseh, D., Kaaret, P., Corbel, S., et al. 2010, MNRAS, 406, 1049

Dalessandro, E., Lanzoni, B., Beccari, G., et al. 2011, ApJ, 743, 11

Davis, D. S., Richer, H. B., Anderson, J., et al. 2008, AJ, 135, 2155

De Marchi, G., Paresce, F., & Pulone, L. 2007, ApJ, 656, L65

Di Matteo, T., Springel, V., & Hernquist, L. 2005, Nature, 433, 604

Drukier, G. A. 1996, MNRAS, 280, 498

Dull, J. D., Cohn, H. N., Lugger, P. M., et al. 1997, ApJ, 481, 267

Duquennoy, A. & Mayor, M. 1991, A&A, 248, 485

Ebisuzaki, T., Makino, J., Tsuru, T. G., et al. 2001, ApJ, 562, L19

Einstein, A. 1916, Annalen der Physik, 354, 769

Elmegreen, B. G. 2010, ApJ, 712, L184

Elmegreen, B. G. & Efremov, Y. N. 1997, ApJ, 480, 235

Emsellem, E., Monnet, G., & Bacon, R. 1994, A&A, 285, 723

Fabbiano, G. 1989, ARA&A, 27, 87

Fabbiano, G., Zezas, A., & Murray, S. S. 2001, ApJ, 554, 1035

Fan, X. 2006, New A Rev., 50, 665

Farrell, S. A., Webb, N. A., Barret, D., Godet, O., & Rodrigues, J. M. 2009, Nature, 460, 73

Feigelson, E. D. & Nelson, P. I. 1985, ApJ, 293, 192

Feldmeier, A., Lützgendorf, N., Neumayer, N., et al. 2013, ArXiv e-prints

Ferrarese, L. & Ford, H. 2005, Space Sci. Rev., 116, 523

Ferrarese, L. & Merritt, D. 2000, ApJ, 539, L9

Ferraro, F. R., Beccari, G., Dalessandro, E., et al. 2009, Nature, 462, 1028

Ferraro, F. R., Clementini, G., Fusi Pecci, F., Buonanno, R., & Alcaino, G. 1990, A&AS, 84, 59

Filippenko, A. V. & Ho, L. C. 2003, ApJ, 588, L13

Freeman, K. C. 1993, in Astronomical Society of the Pacific Conference Series, Vol. 48, The Globular Cluster-Galaxy Connection, ed. G. H. Smith & J. P. Brodie, 608–+

Fregeau, J. M., Richer, H. B., Rasio, F. A., & Hurley, J. R. 2009, ApJ, 695, L20

Freitag, M., Gürkan, M. A., & Rasio, F. A. 2006, MNRAS, 368, 141

Fukushige, T. & Heggie, D. C. 2000, MNRAS, 318, 753

Gebhardt, K., Adams, J., Richstone, D., et al. 2011, ApJ, 729, 119

Gebhardt, K., Bender, R., Bower, G., et al. 2000a, ApJ, 539, L13

Gebhardt, K., Pryor, C., O'Connell, R. D., Williams, T. B., & Hesser, J. E. 2000b, AJ, 119, 1268

Gebhardt, K., Pryor, C., Williams, T. B., Hesser, J. E., & Stetson, P. B. 1997, AJ, 113, 1026

Gebhardt, K., Rich, R. M., & Ho, L. C. 2002, ApJ, 578, L41

Gebhardt, K., Rich, R. M., & Ho, L. C. 2005, ApJ, 634, 1093

Gerssen, J., van der Marel, R. P., Gebhardt, K., et al. 2002, AJ, 124, 3270

Gill, M., Trenti, M., Miller, M. C., et al. 2008, ApJ, 686, 303

Godet, O., Barret, D., Webb, N. A., Farrell, S. A., & Gehrels, N. 2009, ApJ, 705, L109

Goldsbury, R., Richer, H. B., Anderson, J., et al. 2010, AJ, 140, 1830

Goswami, S., Umbreit, S., Bierbaum, M., & Rasio, F. A. 2012, ApJ, 752, 43

Graham, A. W. 2012, MNRAS, 422, 1586

Graham, A. W. 2013, Planets, Stars and Stellar Systems (Berlin:Springer), 6, 91

Gratton, R. G., Lucatello, S., Carretta, E., et al. 2012, A&A, 539, A19

Gualandris, A., Portegies Zwart, S., & Eggleton, P. P. 2004, MNRAS, 350, 615

Gualandris, A., Portegies Zwart, S., & Sipior, M. S. 2005, MNRAS, 363, 223

Gültekin, K., Richstone, D. O., Gebhardt, K., et al. 2009, ApJ, 698, 198

Gunn, J. E. & Griffin, R. F. 1979, AJ, 84, 752

Gürkan, M. A., Freitag, M., & Rasio, F. A. 2004, ApJ, 604, 632

Gvaramadze, V. V. & Gualandris, A. 2011, MNRAS, 410, 304

Gvaramadze, V. V., Gualandris, A., & Portegies Zwart, S. 2008, MNRAS, 385, 929

Gvaramadze, V. V., Gualandris, A., & Portegies Zwart, S. 2009, MNRAS, 396, 570

Habets, G. M. H. J. & Heintze, J. R. W. 1981, A&AS, 46, 193

Häring, N. & Rix, H. 2004, ApJ, 604, L89

Harris, W. E. 1974, ApJ, 192, L161+

Harris, W. E. 1996, AJ, 112, 1487

Hastings, W. 1970, Biometrika, 97

Heggie, D. C. 1975, MNRAS, 173, 729

Heggie, D. C., Hut, P., & McMillan, S. L. W. 1996, ApJ, 467, 359

Hénon, M. 1969, A&A, 2, 151

Hills, J. G. & Fullerton, L. W. 1980, AJ, 85, 1281

Hinkle, K., Hall, D., & Ridgway, S. 1982, ApJ, 252, 697

Hinkle, K. H. 1978, ApJ, 220, 210

Hinkle, K. H., Lebzelter, T., & Scharlach, W. W. G. 1997, AJ, 114, 2686

Holmberg, E. 1941, ApJ, 94, 385

Hopkins, P. F., Hernquist, L., Cox, T. J., Robertson, B., & Krause, E. 2007, ApJ, 669, 45

Hurley, J. R. 2007, MNRAS, 379, 93

Hurley, J. R., Pols, O. R., & Tout, C. A. 2000, MNRAS, 315, 543

Hut, P. & Bahcall, J. N. 1983, ApJ, 268, 319

Ibata, R., Bellazzini, M., Chapman, S. C., et al. 2009, ApJ, 699, L169

Ibata, R., Sollima, A., Nipoti, C., et al. 2011, ApJ, 738, 186

Illingworth, G. 1976, ApJ, 204, 73

Illingworth, G. & Freeman, K. C. 1974, ApJ, 188, L83+

Isobe, T., Feigelson, E. D., & Nelson, P. I. 1986, ApJ, 306, 490

Jalali, B., Baumgardt, H., Kissler-Patig, M., et al. 2012, A&A, 538, A19

Kelly, B. C. 2007, ApJ, 665, 1489

King, I. 1962, AJ, 67, 471

King, I. R. 1966, AJ, 71, 64

Kong, A. K. H. 2007, ApJ, 661, 875

Kormendy, J. & Richstone, D. 1995, ARA&A, 33, 581

Kroupa, P. 2001, MNRAS, 322, 231

Kruijssen, J. M. D. 2009, A&A, 507, 1409

Kruijssen, J. M. D. & Lamers, H. J. G. L. M. 2008, A&A, 490, 151

Kruijssen, J. M. D. & Mieske, S. 2009, A&A, 500, 785

Kruijssen, J. M. D., Pelupessy, F. I., Lamers, H. J. G. L. M., et al. 2012, MNRAS, 421, 1927

Kulkarni, S. R., Hut, P., & McMillan, S. 1993, Nature, 364, 421

Kustaanheimo, P. & Stiefel, E. 1965, J. Reine Angew. Math., 218, 204

Lamers, H. J. G. L. M. & Cassinelli, J. P. 1999, Introduction to Stellar Winds, ed. Lamers, H. J. G. L. M. & Cassinelli, J. P.

Lanzoni, B., Dalessandro, E., Ferraro, F. R., et al. 2007, ApJ, 668, L139

Lebzelter, T., Kiss, L. L., & Hinkle, K. H. 2000, A&A, 361, 167

Lebzelter, T., Wood, P., Hinkle, K., Joyce, R., & Fekel, F. 2005, A&A, 432, 207

Lebzelter, T. & Wood, P. R. 2011, A&A, 529, A137

Lu, T.-N. & Kong, A. K. H. 2011, ApJ, 729, L25

Lynden-Bell, D. 1969, Nature, 223, 690

Lyne, A. G. & Lorimer, D. R. 1994, Nature, 369, 127

Ma, J., de Grijs, R., Chen, D., et al. 2007, MNRAS, 376, 1621

Maccarone, T. J., Fender, R. P., & Tzioumis, A. K. 2005, MNRAS, 356, L17

Maccarone, T. J. & Servillat, M. 2008, MNRAS, 389, 379

Mackey, A. D., Wilkinson, M. I., Davies, M. B., & Gilmore, G. F. 2007, MNRAS, 379, L40

Mackey, A. D., Wilkinson, M. I., Davies, M. B., & Gilmore, G. F. 2008, MNRAS, 386, 65

Madau, P. & Rees, M. J. 2001, ApJ, 551, L27

Magorrian, J., Tremaine, S., Richstone, D., et al. 1998, AJ, 115, 2285

Mandushev, G., Staneva, A., & Spasova, N. 1991, A&A, 252, 94

Mapelli, M., Colpi, M., Possenti, A., & Sigurdsson, S. 2005, MNRAS, 364, 1315

Marconi, A. & Hunt, L. K. 2003, ApJ, 589, L21

Matsumoto, H., Tsuru, T. G., Koyama, K., et al. 2001, ApJ, 547, L25

McConnell, N. J. & Ma, C.-P. 2013, ApJ, 764, 184

McConnell, N. J., Ma, C.-P., Gebhardt, K., et al. 2011, Nature, 480, 215

McLaughlin, D. E. 1999, AJ, 117, 2398

McLaughlin, D. E., Anderson, J., Meylan, G., et al. 2006, ApJS, 166, 249

McLaughlin, D. E. & van der Marel, R. P. 2005, ApJS, 161, 304

McMillan, S. L. W. & Hut, P. 1996, ApJ, 467, 348

McNamara, B. J., Harrison, T. E., Baumgardt, H., & Khalaj, P. 2012, ApJ, 745, 175

Merritt, D., Piatek, S., Portegies Zwart, S., & Hemsendorf, M. 2004, ApJ, 608, L25

Metropolis, N., Rosenbluth, A. W., Rosenbluth, M. N., Teller, A. H., & Teller, E. 1953, J. Chem. Phys., 21, 1087

Meylan, G., Dubath, P., & Mayor, M. 1991, ApJ, 383, 587

Meylan, G., Mayor, M., Duquennoy, A., & Dubath, P. 1995, A&A, 303, 761

Meylan, G., Sarajedini, A., Jablonka, P., et al. 2001, AJ, 122, 830

Mieske, S., Hilker, M., Jordán, A., et al. 2008, A&A, 487, 921

Miller, M. C. & Hamilton, D. P. 2002a, ApJ, 576, 894

Miller, M. C. & Hamilton, D. P. 2002b, ApJ, 576, 894

Miller, M. C. & Hamilton, D. P. 2002c, MNRAS, 330, 232

Miller-Jones, J. C. A., Wrobel, J. M., Sivakoff, G. R., et al. 2012, ApJ, 755, L1

Miocchi, P. 2007, MNRAS, 381, 103

Misner, C. W., Thorne, K. S., & Wheeler, J. A. 1973, Gravitation, ed. Misner, C. W., Thorne, K. S., & Wheeler, J. A.

Moody, K. & Sigurdsson, S. 2009, ApJ, 690, 1370

Moretti, A., Piotto, G., Arcidiacono, C., et al. 2009, A&A, 493, 539

Neumayer, N. & Walcher, C. J. 2012, Advances in Astronomy, 2012

Nitadori, K. & Aarseth, S. J. 2012, MNRAS, 424, 545

Noyola, E. & Baumgardt, H. 2011, ApJ, 743, 52

Noyola, E. & Gebhardt, K. 2006, AJ, 132, 447

Noyola, E., Gebhardt, K., & Bergmann, M. 2008, ApJ, 676, 1008

Noyola, E., Gebhardt, K., Kissler-Patig, M., et al. 2010, ApJ, 719, L60

O'Leary, R. M., Rasio, F. A., Fregeau, J. M., Ivanova, N., & O'Shaughnessy, R. 2006, ApJ, 637, 937

Olszewski, E. W., Saha, A., Knezek, P., et al. 2009, AJ, 138, 1570

Pasquini, L., Avila, G., Blecha, A., et al. 2002, The Messenger, 110, 1

Paust, N. E. Q., Reid, I. N., Piotto, G., et al. 2010, AJ, 139, 476

Peterson, C. J. & King, I. R. 1975, AJ, 80, 427

Peterson, R. C., Seitzer, P., & Cudworth, K. M. 1989, ApJ, 347, 251

Pfahl, E., Rappaport, S., Podsiadlowski, P., & Spruit, H. 2002, ApJ, 574, 364

Pinkney, J., Gebhardt, K., Bender, R., et al. 2003, ApJ, 596, 903

Piotto, G. 2008, in HST Proposal, 11739–+

Piotto, G., Bedin, L. R., Anderson, J., et al. 2007, ApJ, 661, L53

Pooley, D. & Rappaport, S. 2006, ApJ, 644, L45

Portegies Zwart, S. F., Baumgardt, H., Hut, P., Makino, J., & McMillan, S. L. W. 2004, Nature, 428, 724

Portegies Zwart, S. F., McMillan, S. L. W., & Gieles, M. 2010, ARA&A, 48, 431

Pryor, C. & Meylan, G. 1993, in Astronomical Society of the Pacific Conference Series, Vol. 50, Structure and Dynamics of Globular Clusters, ed. S. G. Djorgovski & G. Meylan, 357–+

Ratnatunga, K. U. & Bahcall, J. N. 1985, ApJS, 59, 63

Repetto, S., Davies, M. B., & Sigurdsson, S. 2012, MNRAS, 425, 2799

Richer, H. B., Fahlman, G. G., Buonanno, R., et al. 1991, ApJ, 381, 147

Robin, A. C., Reylé, C., Derrière, S., & Picaud, S. 2004, A&A, 416, 157

Rubenstein, E. P. & Bailyn, C. D. 1997, ApJ, 474, 701

Scarpa, R., Marconi, G., Carraro, G., Falomo, R., & Villanova, S. 2011, A&A, 525, A148

Schödel, R., Ott, T., Genzel, R., et al. 2002, Nature, 419, 694

Scholz, M. 1992, A&A, 253, 203

Schwarzschild, K. 1916, Abh. Konigl. Preuss. Akad. Wissenschaften Jahre 1906, 92, Berlin, 1907, 189

Servillat, M., Dieball, A., Webb, N. A., et al. 2008, A&A, 490, 641

Shapiro, K. L., Genzel, R., & Förster Schreiber, N. M. 2010, MNRAS, 403, L36

Sigurdsson, S. & Hernquist, L. 1993, Nature, 364, 423

Sigurdsson, S. & Phinney, E. S. 1993, ApJ, 415, 631

Silk, J. & Arons, J. 1975, ApJ, 200, L131

Silk, J. & Rees, M. J. 1998, A&A, 331, L1

Sirianni, M., Jee, M. J., Benítez, N., et al. 2005, PASP, 117, 1049

Sollima, A., Gratton, R. G., Carballo-Bello, J. A., et al. 2012, MNRAS, 426, 1137

Sommariva, V., Piotto, G., Rejkuba, M., et al. 2009, A&A, 493, 947

Soria, R., Hau, G. K. T., Graham, A. W., et al. 2010, MNRAS, 405, 870

Soria, R., Hau, G. K. T., & Pakull, M. W. 2013, ApJ, 768, L22

Spitzer, Jr., L. 1958, ApJ, 127, 17

Spitzer, Jr., L. 1969, ApJ, 158, L139

Springel, V., Di Matteo, T., & Hernquist, L. 2005, MNRAS, 361, 776

Stephens, A. W., Frogel, J. A., Freedman, W., et al. 2001, AJ, 121, 2597

Stetson, P. B. 1987, PASP, 99, 191

Strader, J., Chomiuk, L., Maccarone, T. J., et al. 2012, ApJ, 750, L27

Takahashi, K. & Portegies Zwart, S. F. 2000, ApJ, 535, 759

Tanaka, T. & Haiman, Z. 2009, ApJ, 696, 1798

Trager, S. C., King, I. R., & Djorgovski, S. 1995, AJ, 109, 218

Tremaine, S., Gebhardt, K., Bender, R., et al. 2002, ApJ, 574, 740

Trenti, M., Ardi, E., Mineshige, S., & Hut, P. 2007, MNRAS, 374, 857

Trenti, M., Vesperini, E., & Pasquato, M. 2010, ApJ, 708, 1598

Ulvestad, J. S., Greene, J. E., & Ho, L. C. 2007, ApJ, 661, L151

van den Bosch, R., de Zeeuw, T., Gebhardt, K., Noyola, E., & van de Ven, G. 2006, ApJ, 641, 852

van den Bosch, R. C. E., Gebhardt, K., Gültekin, K., et al. 2012, Nature, 491, 729

van der Marel, R. P. & Anderson, J. 2010, ApJ, 710, 1063

van der Marel, R. P. & Franx, M. 1993, ApJ, 407, 525

van Dokkum, P. G. 2001, PASP, 113, 1420

Vanbeveren, D., Belkus, H., van Bever, J., & Mennekens, N. 2009, Ap&SS, 324, 271

Vesperini, E. & Heggie, D. C. 1997, MNRAS, 289, 898

Vesperini, E. & Trenti, M. 2010, ApJ, 720, L179

White, R. E. & Kraft, T. T. 1972, PASP, 84, 298

White, R. E. & Shawl, S. J. 1987, ApJ, 317, 246

Williams, M. J., Bureau, M., & Cappellari, M. 2009, MNRAS, 400, 1665

Williams, M. J., Bureau, M., & Cappellari, M. 2010, MNRAS, 409, 1330

Wood, P. R. 1979, ApJ, 227, 220

Wyller, A. A. 1970, ApJ, 160, 443

Xiao, T., Barth, A. J., Greene, J. E., et al. 2011, ApJ, 739, 28

Yoon, S., Lee, C., & Lee, Y. 2000, in Bulletin of the American Astronomical Society, Vol. 32, Bulletin of the American Astronomical Society, 739–+

Yungelson, L. R., van den Heuvel, E. P. J., Vink, J. S., Portegies Zwart, S. F., & de Koter, A. 2008, A&A, 477, 223

Acknowledgements

Ever since I started doing science I was exceedingly lucky to have *Markus Kissler-Patig* as my supervisor, mentor and friend. Everything I know about processing science, working with other people, making decisions and solving problems I learned from him. I cannot thank him enough for being the best supervisor in the world, for always having time for me regardless of his busy schedule, for giving hope and motivation in moments where I was frustrated, for being a role model inside and outside science and for teaching me patience.

I further deeply thank my second referee and mentor *Tim de Zeeuw* who supported me from the very beginning with his advice and motivation. I thank him for always having an open ear and for always being one of the first replying with comments to my papers. I would also like to thank *Nadine Neumayer* who has become one of my biggest role models and close friend over the last four years. Her positive attitude and ability of finding a solution to everything, whether it is science related or not, gave me strength during our numerous coffees and chats.

Big thanks also go to my group of collaborators. To *Holger Baumgardt*, for his incredibly fast answers from the other side of the world and sharing his fascination for astronomy with me. To *Karl Gebhardt* for his emails that made me laugh and cry, his critical eye on my papers that never overlooked the smallest errors and his steady support during the job hunt. To *Eva Noyola* for her support and answers despite her busy times at home and to *Diederik (D.) Kruijssen* for his inspiring ideas, numerous discussions with pen and paper, his advise in all areas, for tees, coffees and tequilas!

Keep being motivated is not always easy and I would not have been able to be as productive as I was without the proper distraction on the other side. Therefore, I want to thank all my amazing friends at ESO for their kindness, the science coffees, the Biergarten days, the BBQs at the lake, the international food parties and many more dinners and clubbing nights. In particular I want to thank my fellow mentor *Giacomo Beccari* for the lessons in Italian, his professional and private support, and great collaboration. Further, I thank my lovely office mates *Margherita Bonzini* and *Alvaro Iribarrem* for listening to my complaints, the little coffee brakes, the multilingual swearing and just for being the best office mates in the world! I also thank my amazing "Girls" *Anna Feltre*, *Gráinne Costigan* and *Leticia Ferreira* for making me laugh during our endless Skype and Whatsapp chats, making me drunk in our nights out, and for an unforgettable week in Chile.

There were people that could distract me, there were people that could motivate and advise me but there was only one person that fully understood me and my strange way of seeing the world. I therefore deeply thank *Oscar Gonzalez* that he was there for me whenever I needed him, that he loved me and believed in me, that he gave me strength and self confidence and that he taught me to stand up again no matter how often I fall.

Zu guter Letzt danke ich meiner *Familie* und *Freunden*, hier ganz besonders *Maria Meissner*, aus tiefsten Herzen. Dafür das sie in guten wie in schlechten Zeiten für mich da waren, mich motiviert und angespornt haben, für ihr aufrichtiges Interesse in meine Arbeit und ihren unübersehbaren Stolz für mich. Danke an meine *Mutter* für ihre Bemühungen meine Sprache zu erhalten, die tollen Urlaube zusammen, ihre Stärke und ihr gefährliches Halbwissen. Danke an meinen *Vater* für die unzähligen Skype und Telefongespräche, *Norman* für die vielen freuchtfröhlichen Abende und seine Gastfreundlichkeit zu meinen Freunden, *Ludi*, *Vincent* und *Max* dafür das sie mir Cocktails gemixt und mich zur Weißglut getrieben haben und danke an meine *Großeltern* deren Hingabe und Interesse mich immer wieder zu neuen Taten beflügelt hat.